MPM SCIENTIFIC JOURNAL

ISSN 1605-2730
E-ISSN 1605-8119

MATERIALS PHYSICS AND MECHANICS

Vol. 54, N. 2, 2026

MATERIALS PHYSICS AND MECHANICS

"Materials Physics and Mechanics" Editorial Office:
Phone: +7(812)552 77 78, ext. 224 **E-mail:** mpmjournal@spbstu.ru **Web-site:** http://www.mpm.spbstu.ru

International scientific journal "**Materials Physics and Mechanics**" is published by Peter the Great St. Petersburg Polytechnic University in collaboration with Institute for Problems for Mechanical Engineering in the Russian Academy of Sciences in both hard copy and electronic versions. The journal provides an international medium for the publication of reviews and original research papers written in English and focused on the following topics:

- Mechanics of composite and nanostructured materials.
- Physics of strength and plasticity of composite and nanostructured materials.
- Mechanics of deformation and fracture processes in conventional materials (solids).
- Physics of strength and plasticity of conventional materials (solids).
- Physics and mechanics of defects in composite, nanostructured, and conventional materials.
- Mechanics and physics of materials in coupled fields.

Owner organizations: Peter the Great St. Petersburg Polytechnic University; Institute of Problems of Mechanical Engineering RAS.

Materials Physics and Mechanics is indexed in Chemical Abstracts, Cambridge Scientific Abstracts, Web of Science Emerging Sources Citation Index (ESCI) and Elsevier Bibliographic Databases (in particular, SCOPUS).

МЕХАНИКА И ФИЗИКА МАТЕРИАЛОВ

Materials Physics and Mechanics

Том 54, номер 2, 2026 год

Учредители:
ФГАОУ ВО «Санкт-Петербургский политехнический университет Петра Великого»
ФГБУН «Институт проблем машиноведения Российской академии наук»

Тел.: +7(812)552 77 78, доб. 224 **E-mail:** mpmjournal@spbstu.ru **Web-site:** http://www.mpm.spbstu.ru

Тематика журнала

Международный научный журнал "Materials Physics and Mechanics" издается Санкт-Петербургским политехническим университетом Петра Великого в сотрудничестве с Институтом проблем машиноведения Российской академии наук в печатном виде и электронной форме. Журнал публикует обзорные и оригинальные научные статьи на английском языке по следующим тематикам:

- Механика композиционных и наноструктурированных материалов.
- Физика прочности и пластичности композиционных и наноструктурированных материалов.
- Механика процессов деформации и разрушения в традиционных материалах (твердых телах).
- Физика прочности и пластичности традиционных материалов (твердых тел).
- Физика и механика дефектов в композиционных, наноструктурированных и традиционных материалах.
- Механика и физика материалов в связанных полях.

Редколлегия принимает статьи, которые нигде ранее не опубликованы и не направлены для опубликования в другие научные издания. Все представляемые в редакцию журнала "Механика и физика материалов" статьи рецензируются. Статьи могут отправляться авторам на доработку. Не принятые к опубликованию статьи авторам не возвращаются.

Журнал "Механика и физика материалов" ("Materials Physics and Mechanics") включен в систему цитирования Web of Science Emerging Sources Citation Index (ESCI), SCOPUS и РИНЦ.

Contents

MATERIALS PHYSICS AND MECHANICS RESEARCH ARTICLE

Submitted: December 12, 2025 **Revised: February 19, 2026** **Accepted: March 25, 2026**

Numerical study of the influence of the reverse martensitic transformation completion degree on the cyclic stability of a shape memory alloy-based actuator

F.S. Belyaev [1]✉, A.E. Volkov [2], D.F. Gorbachenko [1], M.E. Evard [2]

[1] Institute for Problems of Mechanical Engineering RAS, St. Petersburg, Russia

[2] St. Petersburg State University, St. Petersburg, Russia

✉ belyaev_fs@mail.ru

ABSTRACT

Despite all the advantages of shape memory alloy-based actuators, their widespread adoption is hampered by a significant drawback: a gradual decline in performance with repeated actuation. The ways to overcome this drawback are explored. Based on microstructural modeling, the influence of the degree of completion of the reverse martensitic transformation on the operational stability of a torsion actuator with a working body made of a TiNi alloy was investigated. The existence of a critical transformation threshold (~ 75 %) has been identified: exceeding it leads to significant loss of work output, while limiting the transformation to this level ensures practical stabilization of the working cycle parameters. A compromise in the influence of the transformation degree was revealed: reducing it improves the stability of the actuator parameters but reduces the work output per cycle. Based on the obtained results, criteria for selection of an optimal operating mode for actuators intended for long-term cyclic operation were formulated.

KEYWORDS

shape memory alloys • thermomechanical actuator • functional fatigue • martensitic transformations microstructural modeling

Funding. *This work has been supported by the grant of the Russian Science Foundation, RSF 25-21-00361, https://rscf.ru/project/25-21-00361/.*

Citation: Belyaev FS, Volkov AE, Gorbachenko DF, Evard ME. Numerical study of the influence of the reverse martensitic transformation completion degree on the cyclic stability of a shape memory alloy-based actuator. *Materials Physics and Mechanics*. 2026;54(2): 1–16.
http://dx.doi.org/10.18149/MPM.5422026_1

Introduction

Currently, there is active development and implementation of actuators using shape memory alloys (SMA) as working bodies [1–7]. The growing interest in such drives is due, first of all, to increasingly stringent requirements for weight, energy efficiency and reliability of modern advanced systems, such as aircraft, robotic systems and spacecraft. The wide potential of the technology finds practical application in various industries: in aerospace engineering — for controlling structural elements with minimal weight [8–12], in robotics — for creation of powerful and miniature artificial muscles [13–15], in the automotive industry — as actuators for comfort systems and valve mechanisms [16,17], in microelectronics — for precision positioning devices [18,19], and also in medicine — in the development of surgical instruments with controlled deformation [1,20]. The key functional advantages of SMA-based actuators include:

1. High specific force and performance. This property is due to the specific nature of the SMAs, which induces significant reactive stresses and produces useful work through reversible deformation associated with a martensitic transformation. This enables the creation of compact actuators with high power. SMA-based actuators can achieve a weight reduction of up to 80 % compared to conventional electric and hydraulic actuators [21].
2. Structural reliability. High reliability is a consequence of the simple design of such actuators. The absence of complex kinematic units and a small number of moving parts minimize the risk of mechanical failure.
3. Silent operation and low vibration. The smooth nature of SMA deformation ensures almost silent operation and minimal vibration. This makes this technology promising for precision systems, such as optical circuit elements and astronomical instrumentation.
4. Scalability. The physical principles underlying the operation of the SMAs are scale-invariant, which allows them to be successfully applied both in large-scale power drives [12,22] and in microactuators [3,19,23].

The operating principle of a thermomechanical SMA-actuator is based on the eponymous effect – the ability of a material to recover its original shape when heated. Constraining this restoration leads to significant reactive stresses in the material, which enables it to perform useful work. To ensure cyclic operation, the return to the original deformed state upon cooling is achieved by applying an external load. Consequently, the actuator's operating cycle consists of two stages: the cocking stage (accumulation of deformation under load during cooling) and the actuation stage (shape recovery and work output during heating).

Based on their architecture, SMA-actuators are divided into two main types: double-acting and single-acting. Double-acting actuators are capable of generating force in two opposite directions [11,19,24,25]. Typically, this design contains two SMA working bodies, which are alternately heated and cooled. The heated body, restoring its shape, performs a working stroke and simultaneously deforms the other cooled body, thus cocking it for the next cycle. Single-acting actuators perform a working stroke in only one direction [26–32]. This is the most common design, consisting of a SMA working body and an elastic counterbody (e.g., a spring). During the actuation stage, the heated SMA element, overcoming the resistance of the counterbody, restores its shape and performs useful work. At the cocking stage, the cooled working body is deformed by the return force of the elastic counterbody, which has stored energy during the working stroke, thereby closing the thermomechanical cycle.

Despite the listed advantages, SMA-based actuators have a significant drawback that limits their use: instability of the material's functional properties under cyclic loading. During repeated thermomechanical cycling (cocking - actuation), the material exhibits degradation of its characteristics, manifested in the accumulation of residual strain, a shift in the temperatures of the forward and reverse martensitic transformations, and a decrease in the recoverable strain and the developed force [33]. This phenomenon, to varying degrees, is inherent in all SMAs; however, the intensity of degradation is determined by a combination of factors. These include the chemical composition of the alloy, the type of martensitic transformation, the parameters of the preliminary thermomechanical treatment, and the magnitude and nature of the applied load [34–38].

The consequences of property instability are a gradual decrease in work output in the working cycle and incomplete actuation, which can ultimately lead to functional failure.

The main factor responsible for instability of the SMA functional properties is accommodative plastic deformation (microplastic deformation) accompanying the growth of martensite crystals in the austenitic matrix. This process causes irreversible shifts in the crystal lattice, leading to increased macroscopic irreversible deformation. It also generates deformation defects that form internal stress fields. These fields, in turn, have a significant impact on subsequent martensitic transformations.

Experimental research has shown that the final stage of the reverse transformation is responsible for a significant portion of the overall microplastic deformation [39]. Therefore, one method for reducing instability during cyclic actuation is to limit the heating temperature of the working body, which reduces the degree of completion of the reverse martensitic transformation. However, this approach has an obvious drawback: a decrease in the heating temperature leads to a decrease in the generated stresses and, consequently, to a drop in the useful work per cycle. This compromise defines the core objective of this numerical study, which is to explore pathways for enhancing the cyclic stability of the actuator's working cycle without incurring a significant degradation in its performance. To this end, a series of computational experiments was conducted using a microstructural model of SMAs. This model accounts for the accumulation of microplastic deformation, a feature critical for simulating cyclic degradation, and has been successfully applied to actuator simulation problems in prior studies.

Mechanical model of SMA

Due to the complex nature of the SMA deformation behavior, characterized by the absence of a clear relationship between stress, strain, and temperature, mechanical models are required for adequate description of this behavior. There are many different approaches to modeling SMAs, some of which have also been used to describe the operation of SMA actuators [28,30,40–42]. However, to address the objectives of this study, a microstructural model previously developed by the authors [43–48] is used. This model has a key advantage: the ability to correctly account for the main deformation mechanisms of SMA, including the development of microplastic accommodation, which is critical for modeling cyclic degradation. The applied microstructural approach exhibits universality and high predictive ability, as confirmed by its successful application to describe a wide range of phenomena in SMAs, such as fatigue failure [43], transformation and ordinary plasticity [44], deformation during isothermal holding [45], the effect of martensite stabilization [46], as well as heat exchange with the environment [47]. Of particular relevance to the present work is the validation of this model for calculating the work of an SMA specimen under thermomechanical actuator conditions [48]. Thus, the chosen model is a proven tool applicable to solving engineering problems, in particular, for modeling the cyclic operation of SMA-based actuators. Below, the main features of the model and its governing equations, proposed and justified earlier in [49,50], are presented.

Basic model principles.

The model describes the behavior of a representative volume of material, which is considered as a material point. The key principle lies in the multi-level description of the microstructure. The representative volume consists of numerous grains with different crystallographic orientations. Each grain, in turn, can contain austenite and/or several orientational variants of martensite.

According to the Reuss hypothesis, the macroscopic strain of the representative volume ε is calculated as the average over all orientations ω of the strains of individual grains $\varepsilon^{gr}(\omega)$:

$$\varepsilon = \sum_{\omega} f(\omega)\varepsilon^{gr}(\omega), \quad (1)$$

where $f(\omega)$ is the volume fraction of grains with orientation ω.

Kinematics of deformation at the grain level

The strain of an individual grain is represented as the sum of contributions from various physical mechanisms:

$$\varepsilon^{gr} = \varepsilon^{E} + \varepsilon^{T} + \varepsilon^{Ph} + \varepsilon^{MP}, \quad (2)$$

where ε^{E} is elastic strain (according to Hooke's law), ε^{T} is thermal strain (due to thermal expansion), ε^{Ph} is phase strain (associated with the martensitic transformation), ε^{MP} is microplastic strain (associated with plastic accommodation of martensite).

Description of phase transformation

To describe the phase strain, internal variables Φ_n are introduced, where $\frac{\Phi_n}{N}$ represents the volume fraction of the n-th orientational variant of martensite (*N* is the total number of variants). The phase strain of a grain is calculated as the averaged contribution of all martensite variants:

$$\varepsilon^{Ph} = \frac{1}{N}\sum_{n=1}^{N} \Phi_n D^n, \quad (3)$$

where D^n is the Bain strain tensor for the n-th martensite variant.

The condition determining the onset and course of martensitic transformation is formulated through the balance of thermodynamic forces:

$$F_n = \pm F^{fr}, \quad (4)$$

where F_n is the generalized thermodynamic force causing the growth of the n-th variant of martensite, F^{fr} is the dissipative force that prevents the movement of interphase boundaries and causes the presence of temperature-phase hysteresis. The "+" sign in Eq. (4) corresponds to the forward transformation (austenite → martensite), and the "−" sign to the reverse transformation (martensite → austenite).

The thermodynamic forces F_n and F^{fr} are calculated as follows:

$$F_n = \frac{q_0}{T_0}(T - T_0) + \sigma_{ij} : D_{ij}^n - \mu \sum_{m=1}^{N} A_{mn} (\Phi_m - b_m), \quad (5)$$

$$F^{fr} = q_0 \frac{M_s - T_0}{T_0}. \quad (6)$$

The first expression follows from the Gibbs potential and the second follows from the condition of the onset of direct martensitic transformation at temperature M_s. In these expressions q_0 is the latent heat of transformation, T_0 is the temperature of thermodynamic phase equilibrium (austenite and martensite), *T* is the temperature of the

representative volume, σ is applied stress, b is the density of oriented defects, A is the matrix that determines the interaction of martensite variants described in detail in [49,50]. The coefficient μ and the equilibrium temperature T_0 depend on the material constants and can be calculated as follows:

$$\mu = -\frac{q_0(M_s - M_f)}{T_0(1-2\alpha)}, \quad (7)$$

$$T_0 = \frac{M_s + A_f}{2}, \quad (8)$$

where M_f and A_f are the finish temperatures of the forward and reverse martensitic transformations respectively, α is a material constant characterizing the coherency of the martensitic phases. The choice of the value of μ in the form (7) follows from the condition that the direct martensitic transformation is completed at the temperature M_f upon cooling under no load.

Description of martensite reorientation.

The reorientation (twinning) of martensite is described using a specialized approach. This process is interpreted as a shift within the space of internal variables $\Phi_1, \cdots, \Phi_N$, under the constraint that the total volume fraction of martensite Φ^{gr} remains constant. The following hypotheses are postulated:

1. Any variant of martensite can transform into any other variant.
2. Reorientation proceeds in the direction within the space $\Phi_1, \cdots, \Phi_N$ that corresponds to the steepest decrease of the Gibbs potential G.
3. Reorientation is initiated when the thermodynamic driving force reaches a critical value.

To find the direction of reorientation we use vector $\tilde{F}$:

$$\tilde{F} = \left\{-\frac{\partial G}{\partial \Phi_1}, \cdots, -\frac{\partial G}{\partial \Phi_N}\right\}. \quad (9)$$

The projection L of a vector $\tilde{F}$ onto the plane $\Phi_1 + \cdots + \Phi_N = \text{const}$ corresponds to the direction of the steepest decrease of the Gibbs potential during reorientation. However, moving in this direction may violate the geometrical constraints requiring the non-negativity of volume fractions. To address this issue, if for some component n we have $\Phi_n = 0$ and $L_n < 0$, we replace L with its projection L' onto the intersection of the planes defined by $\Phi_n = 0$ and $\Phi_1 + \cdots + \Phi_N = \text{const}$. This procedure is repeated for other components of L as necessary. Finally, after normalizing the resulting vector, we obtain the unit direction l. This direction satisfies the hypothesis 2 and ensures that the conditions $\Phi^{gr} = \text{const}, \Phi_n \geq 0,\ n = 1, \ldots, N$ are not violated.

In accordance with the hypothesis 3, the condition for the onset of reorientation in the direction l is postulated as:

$$F^{tw}(l) = F^{frtw}, \quad (10)$$

where F^{frtw} is a material constant representing the critical force required to initiate reorientation, $F^{tw}(l)$ is the thermodynamic driving force for reorientation, defined by the directional derivative of the Gibbs potential:

$$F^{tw}(l) = -\frac{\partial G}{\partial l} = -\sum_{n=1}^{N} l_n \frac{\partial G}{\partial \Phi_n} = N \sum_{n=1}^{N} l_n \tilde{F}_n, \quad (11)$$

where $\tilde{F}_n$ denotes the thermodynamic force conjugate to the internal variable Φ_n.

It follows from hypotheses 1 and 2 that the increments $d\Phi_n$ are proportional to the components l_n:

$$d\Phi_n = l_n d\phi, \quad (12)$$

where $d\phi$ is a proportionality factor to be determined from condition (10).

Accounting for microplastic deformation

The growth of a martensite crystal causes deformation incompatibility with the surrounding austenite matrix and with crystallographically non-corresponding martensite variants, generating internal stresses and, consequently, microplastic slip. A key assumption in describing this deformation mechanism is that the microplastic deformation associated with the growth of a particular martensite variant is proportional to its Bain strain deviator:

$$\varepsilon^{MP} = \frac{1}{N}\sum_{n=1}^{N} \kappa \varepsilon_n^{mp} dev(D^n), \quad (13)$$

where ε_n^{mp} is the scalar measure of microplastic deformation associated with the growth of the n-th martensite variant, κ is a scaling coefficient.

To calculate the values of ε_n^{mp}, microplastic flow conditions are introduced into the model. These conditions are similar to the condition of plastic flow in the one-dimensional case, taking into account kinematic (translational) and isotropic hardening, where the role of stress is played by the generalized thermodynamic force F_n^p, and the kinematic and isotropic hardening correspond to the thermodynamic forces F^y and F_n^ρ:

$$\left|F_n^p - F_n^\rho\right| = F^y, \ \left(F_n^p - F_n^\rho\right) dF_n^p > 0. \quad (14)$$

The generalized thermodynamic force causing microplastic deformation is calculated as follows:

$$F_n^p = \mu \sum_{m=1}^{N} A_{mn}(\Phi_m - b_m). \quad (15)$$

Evolution of defects and hardening

Microplastic deformation causes material hardening through the generation of deformation-induced defects. While many types of defects exist, accounting for each individually is impractical. To simplify, all deformation-induced defects are classified into two types depending on whether they create long-range oriented internal stress fields: oriented defects, which produce such fields, and scattered defects, which do not.

The growth of the n-th martensite variant generates specific defects (e.g., dislocations on certain slip planes) that create internal stress fields with a distinct orientation. Consequently, the model distinguishes the densities of oriented defects, $b_1, \ldots, b_N$, produced by each martensite variant. The increase in the density b_n is assumed to be proportional to the microplastic strain ε_n^{mp} caused by the growth of the n-th martensite variant. However, this density cannot grow indefinitely. As microplastic deformation intensifies, the density is reduced by the annihilation of dislocations at grain boundaries. We assume that the generation of new defects and their annihilation eventually reach equilibrium, defining a maximum density β^*. This saturation behavior is described by the following equation:

$$\dot{b_n} = k_b \left(\dot{\varepsilon}_n^{mp} - \frac{|b_n|}{\beta^*} \dot{\varepsilon}_n^{mp} H\left(b_n \dot{\varepsilon}_n^{mp}\right) \right), \quad (16)$$

where *H* is the Heaviside function, k_b is a scaling factor. In this equation the first term in parentheses represents defect generation and the second term represents annihilation at the grain boundary.

In contrast, scattered defects generated by microplastic deformation are qualitatively indistinguishable regardless of which martensite variant caused the deformation. They are therefore described by a single scalar density *f*. This density is assumed to be proportional to the total accumulated microplastic strain from all variants. Furthermore, the density of scattered defects can decrease over time due to thermally activated processes. This evolution is governed by the following equation:

$$\dot{f} = \sum_{m=1}^{N} |\dot{\varepsilon}_m^{mp}| + r_0 e^{-\frac{U_f}{kT}} (f - f_0), \quad (17)$$

where r_0 is the recovery coefficient, U_f is the activation energy, k is the Boltzmann constant, f_0 is the equilibrium density of scattered defects.

To obtain a closed system of equations, it is necessary to introduce hardening laws. The model assumes that scattered defects impede dislocation movement, thereby increasing the yield stress. Consequently, their density is related to isotropic hardening. Clusters of oriented defects create internal stress fields, the effect of which is combined with external stress, shifting the center of the yield surface. Consequently, their density is related to kinematic hardening. Linear dependencies are proposed to relate hardening to defect densities:

$$F_n^{\rho} = a_{\rho} b_n, \quad (18)$$

$$F^{y} = a_y f, \quad (19)$$

where a_{ρ} and a_y are material constants determining the intensity of the corresponding types of hardening.

Computational algorithm

The model describes the behavior of a representative volume subjected to external thermomechanical loading. The input (control) parameters are stress σ, temperature *T*, and time *t*; the outputs are the macroscopic strain and the evolution of the internal variables.

The simulation procedure is divided into stages, each corresponding to an interval of monotonic variation of the control parameters. Within each stage, the system of evolution equations is integrated numerically. If the boundary conditions are prescribed in terms of strain (or as a stress-strain relationship, e.g., to account for the counterbody stiffness) rather than stress, the stress at the stage is determined iteratively to satisfy the required strain.

Each stage is further subdivided into increments (in time or another control parameter). For a given increment, the algorithm proceeds as follows:

1. The increments of all control parameters $\Delta\sigma, \Delta T, \Delta t$ are computed.
2. The thermodynamic driving forces F_n are evaluated using Eq. (5), and the martensitic transformation criteria (4) are checked. If the criteria are met, the changes in martensite volume fractions $\Delta\Phi_n^{tr}$ are calculated.
3. The reorientation driving force F^{tw} is calculated using Eq. (11), and the reorientation condition (10) is verified. If it is active, the contribution of reorientation to the changes in martensite volume fractions $\Delta\Phi_n^{tw}$ are computed.

4. Using the updated volume fractions, i.e., $\Phi_n + \Delta\Phi_n^{tr} + \Delta\Phi_n^{tw}$, the driving forces for microplastic strain F_n^p are calculated from Eq. (15), and the flow conditions (14) are evaluated. For all active flow systems, a system of equations is solved, comprising the flow conditions (14), the evolution equations for defect densities (16)–(17), and the hardening relations (18)–(19). The solution gives the corresponding increments of microplastic strain $\Delta\varepsilon_n^{mp}$, defect densities Δb_n, Δf, and hardening variables ΔF_n^{ρ}, ΔF^{y}.
5. The total grain strain ε^{gr} is then calculated using Eqs. (2), (3) and (13).
6. Steps 2 through 5 are performed independently for each grain. Finally, the averaged strain of the representative volume ε is obtained using Eq. (1).

The proposed algorithm numerically captures the essential features of the mechanical behavior of shape memory alloys required for the analysis of actuator applications.

Actuator

Schematic of the actuator

The object of this study is a single-acting torsion actuator. Its design (Fig. 1) comprises a working element (a rod made of a TiNi alloy), connected in series with an elastic counterbody (a return spring). Upon actuation, the working rod restores its shape, generating a torque that rotates a lever fixed to its end.

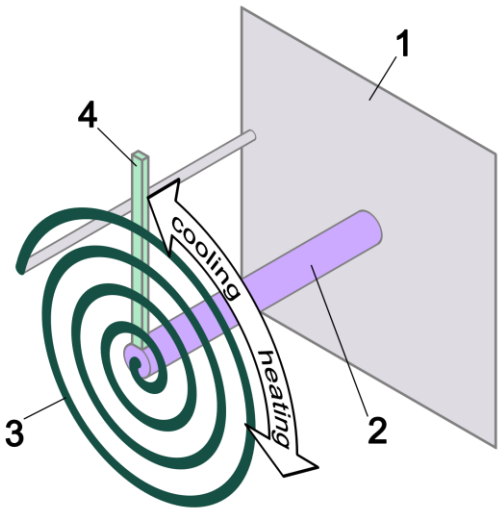

Fig. 1. Schematic diagram of the single-acting torsion actuator. Key components: 1 – base frame; 2 – SMA working body (TiNi rod); 3 – elastic counterbody (spring); 4 – output lever

System parameters

The TiNi alloy was selected as the working body material owing to its status as a widely used SMA and the combination of high functional properties, which include a significant recoverable strain. For the numerical simulation, the set of material constants given in Table 1 was adopted. This set, originally calibrated in [48], was validated against experimental data for actuators with elastic counterbodies of varying stiffness [33], confirming its adequacy for the present study.

Table 1. Material constants for TiNi alloy

Material constant	Symbol	Value
Number of martensite variants	N	12.00
Latent heat (enthalpy) of the direct martensitic transformation, MJ/m^3	q_0	-160.00
Characteristic temperatures of martensite transformation, K	M_f M_s A_s A_f	310.00 332.00 340.00 363.00
Temperature of the thermodynamic equilibrium, K	T_0	347.50
interaction coefficient of martensite variants	α	0.20
Microplastic strain scaling factor	κ	1.00
Coefficient of isotropic hardening, MPa	a_y	1.00
Coefficients of kinematic hardening, MPa	a_p	10.00
Maximum value of the oriented defects density	β^*	0.60
Oriented defects scaling factor	k_b	2.00
Initial value of scattered defects	f_0	0.00
Scattered defects recovery coefficient	r_0	0.09
Activation energy, kJ/mol	U_f	40.00

The counteraction is provided by an elastic counterbody; therefore, the increment in strain upon heating $\Delta\gamma$ is proportional to the increase in stress $\Delta\tau$. Hence, one may write $\Delta\tau = K \cdot \Delta\gamma$, where K is the linear coefficient characterizing the stiffness of the counterbody. In this work, the coefficient K was set to 11.3 GPa. This value is optimal for the actuator configuration under consideration, as it corresponds to the maximum work output per cycle, a finding established in prior research [33,48].

Working cycle

The working cycle of the actuator is based on the ability of a pre-deformed SMA element to recover its original shape upon heating due to the shape memory effect. Consequently, the actuator requires a preparatory step to introduce an initial deformation into the working body. A schematic of the preparation procedure and the subsequent working cycle is presented in Fig. 2.

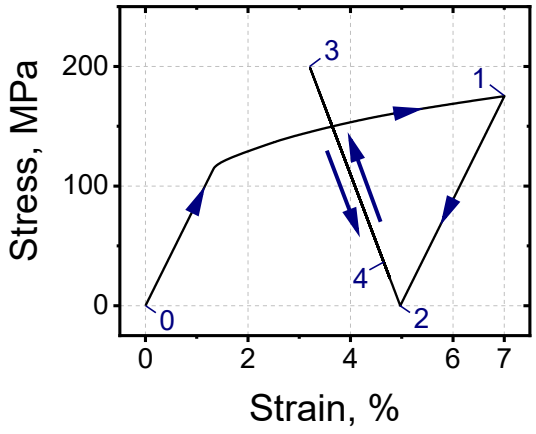

Fig. 2. Schematic of the initial preparation of the actuator's working body via torsional deformation (0–1) and unloading (1–2), followed by the working cycle consisting of the working stroke during heating (2–3) and the cocking phase during cooling (3–4)

The preparation of the TiNi working rod was simulated according to the following sequence. First, at the point (0), the rod is in a fully martensitic state. This state is achieved by cooling the unstressed rod from the austenitic state to a temperature below the martensite finish temperature M_f. Under such stress-free cooling conditions, the martensite forms in a self-accommodated manner, meaning that all variants are present in nearly equal volume fractions. From this initial state, the rod was subjected to torsional loading up to a shear strain of 7 % (segment 0–1). During this stage, the martensite variants undergo reorientation: those variants whose Bain strain is the most aligned with the applied stress grow at the expense of others, increasing their volume fraction. This process results in a textured martensitic structure. The rod was then unloaded (segment 1–2). The unloading is purely elastic, meaning that the reoriented martensite structure remains unchanged, leaving a residual strain of approximately 5 %. The prepared rod was subsequently installed in the actuator assembly with one end rigidly fixed and the other connected to the elastic counterbody (spring), after which the system was ready for cyclic operation.

The working cycle consists of two phases. During the working stroke (2–3), the working body is heated. When the temperature rises above the reverse transformation start temperature, A_s, the martensite begins to transform into austenite. As a result, the rod starts to recover its shape due to the shape memory effect, inducing a rising mechanical stress in the system by working against the elastic counterbody. During the subsequent cocking phase (3–4), the working body is cooled. The austenite formed in the previous stage now begins to transform back into martensite. However, since this transformation occurs under the stress applied by the pre-strained spring, the martensite formed is oriented, with preferential selection of variants whose orientations are aligned with the spring-induced stress. Consequently, the rod deforms back towards state 2, resulting in a drop in stress (usually not to zero). After completing the cocking phase, the actuator is reset for the next cycle. In stress-strain coordinates, the trajectory of the cycle follows along a straight line whose slope is defined by the stiffness of the elastic counterbody.

Simulation results

The actuator produces work output during the working stroke. The magnitude of this work is directly dependent on the heating temperature, reaching its maximum when the reverse martensitic transformation is complete. The objective of this study is to investigate the potential for enhancing the stability of the actuator's parameters by intentionally limiting the degree of reverse transformation completion. To this end, a series of numerical experiments simulating working cycles with incomplete transformation was conducted. Four heating temperatures were chosen, corresponding to work output levels of 90, 75, 50, and 25 % of the work produced in the first cycle with full reverse transformation. This approach enables a quantitative evaluation of the influence of transformation degree on the characteristic degradation. In all simulated cases, cooling was modeled until complete transformation to the martensitic state.

The simulation results for the first 15 cycles demonstrate a degradation of the actuator's key functional characteristics with an increasing number of cycles in all

regimes. This is evidenced by a simultaneous reduction in both the maximum cycle stress (Fig. 3(a)) and the magnitude of recoverable shape memory strain (Fig. 3(b)). Given that the specific work of the actuator is governed by the product of these parameters, their simultaneous decline leads to a corresponding drop in the work per cycle (Fig. 4, solid symbols).

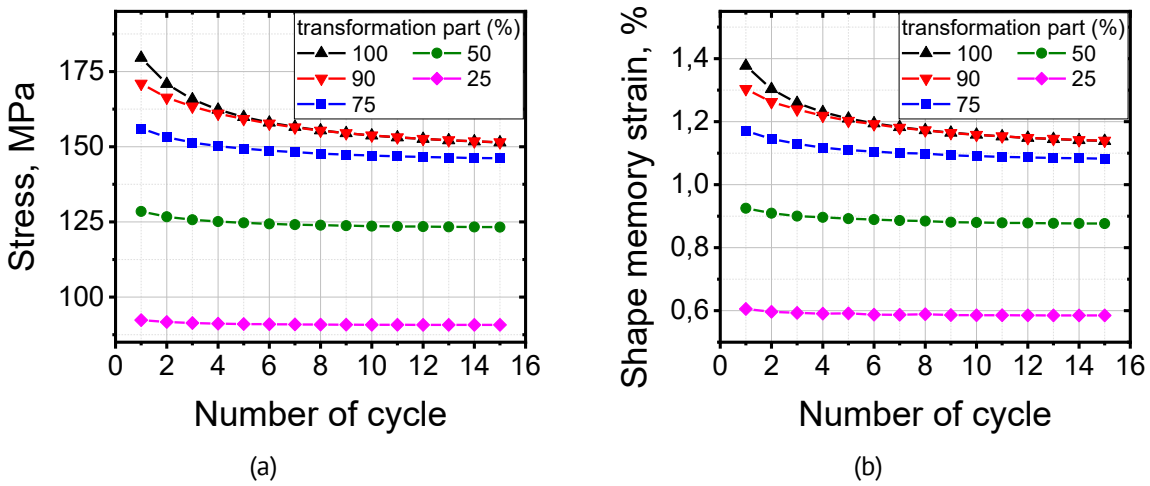

Fig. 3. Evolution of the maximum cycle stress (a) and shape memory strain (b) with the number of cycles for different degrees of reverse transformation completion

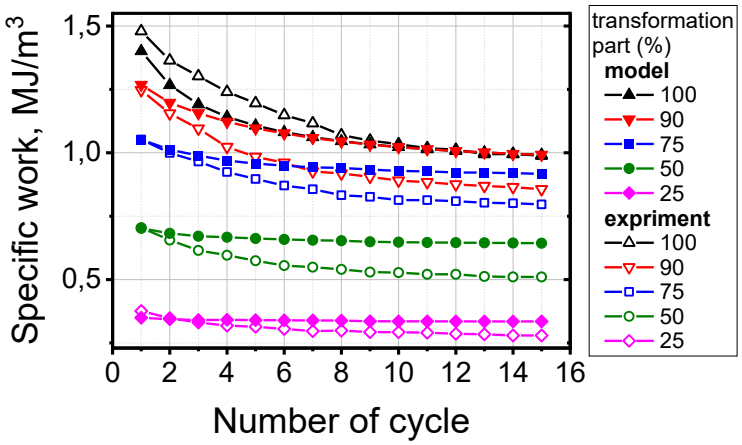

Fig. 4. Specific work per cycle on the cycle number for different degrees of reverse transformation completion. Simulation results (solid symbols) and experimental data from [51] (open symbols)

A clear dependence of the degradation dynamics on the degree of reverse transformation completion was identified. When the transformation is limited to 50 and 25 % of the maximum value, the actuator exhibits high stability, with the specific work remaining nearly constant. In contrast, regimes with complete (100 %) and near-complete (90 %) transformation are characterized by intense degradation: the work output declines rapidly, and by the 15-th cycle its value approaches the value of the 75 %-transformation regime. This observed trend is in qualitative agreement with the experimental data reported in [51], shown for comparison in Fig. 4 (open symbols).

Following the validation of the model against experimental data, a predictive simulation of the actuator's operation over 100 cycles was conducted for the same heating levels. The obtained dependences of the specific work per cycle on the cycle number are presented in Fig. 5. The analysis reveals two distinct stages of performance degradation:

1. Initial stage (up to ~ 30 cycles): characterized by a rapid but gradually slowing decrease in the work output.
2. Steady-state degradation stage (beyond 30 cycles): marked by a linear decrease in the work output.

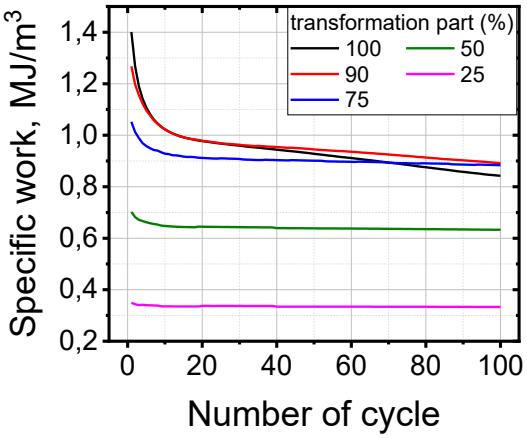

Fig. 5. Specific work per cycle on the cycle number for varying reverse transformation completion levels

The decisive influence of transformation completeness on long-term stability is evident. For regimes with complete (100 %) and near-complete (90 %) transformation, the slope in the second stage remains large, indicating a significant continued decline in performance. In contrast, for regimes with a transformation degree of 75 % or lower, the curves in the second stage become almost horizontal, exhibiting only a slight slope. This indicates a transition to a quasi-stable operating state with minimal gradual degradation of performance.

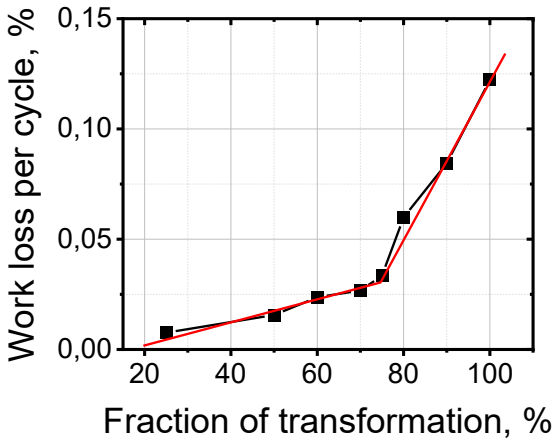

Fig. 6. Specific work loss per cycle in the steady-state degradation regime as a function of the reverse transformation fraction. The bilinear approximation reveals a critical transition near 75 % completion

To quantify the boundary between stable and unstable operational regimes, additional calculations were performed for various heating limits. Based on these results, a dependence of the work loss per cycle during the steady-state degradation stage on the reverse transformation fraction was obtained (Fig. 6). This dependence is well approximated by a bilinear function with a breakpoint near 75 %, which quantitatively confirms the previously identified transition.

Based on the simulation results, the following practical recommendations for actuators intended for long-term cyclic operation are proposed:

1. To ensure long-term parameter stability, it is recommended to select an operating cycle with a reverse transformation degree not exceeding 75 %. The predictive modeling results (Figs. 5 and 6) demonstrate that exceeding this threshold leads to a significantly higher degradation rate. For instance, with complete transformation, the work output falls below that of the 75 % regime after only ~ 70 cycles; for a 90% transformation, this occurs after ~ 100 cycles. Consequently, the higher initial work output in the early cycles is negated by its accelerated decline.
2. During the design phase, the performance loss over the actuator's target service life must be estimated. This assessment should account for the linear degradation in the steady-state regime to guarantee that the work output remains above the minimum required threshold.
3. The significant performance drop during the initial cycling stage (approximately the first 30 cycles) must be considered. To mitigate this problem in practice, it is recommended to conduct thermal cycling (training) of the working element before use.

For a comparative overview of the actuator's performance across the studied thermal regimes, Table 2 summarizes the key quantitative metrics: the work output in the first cycle, the cumulative work loss during the initial cycling stage (cycles 1 – 30), and the specific work loss per cycle in the steady-state regime.

Table 2. Actuator's work output and its degradation across simulated thermal regimes

Part of reverse transformation, %	Specific work at the first cycle, MJ/m^3	Work loss in the Initial stage of degradation, %	Work loss per cycle in the stage of steady-state degradation, %
100	1.401	31.5	0.122
90	1.268	24.1	0.084
80	1.122	16.1	0.06
75	1.052	13.7	0.033
70	0.977	12.8	0.027
60	0.834	9.8	0.024
50	0.702	8.4	0.016
25	0.349	3.5	0.0076

Conclusions

1. Microstructural modeling has identified accommodative microplastic deformation, predominantly occurring at the final stage of the reverse martensitic transformation, as the primary mechanism behind the degradation of key functional characteristics (maximum stress, recoverable strain, and specific work) in SMA-based thermomechanical actuators under cyclic loading.

2. The long-term degradation process exhibits two distinct stages: an initial stage (up to ~ 30 cycles) with rapid, non-linear deterioration of parameters, followed by a steady-state stage characterized by a linear decrease in specific work.
3. A critical threshold for the degree of completion of the reverse martensitic transformation has been quantitatively established at approximately 75 %. Exceeding this threshold leads to intense degradation, including during the steady-state stage. Conversely, limiting the transformation to 75 % or less enables an operational regime with minimal parameter instability.
4. A fundamental compromise between performance and stability has been demonstrated. While reducing the degree of transformation completion enhances cycle-to-cycle stability by decreasing the relative work loss, at the same time it reduces the absolute work output per cycle.

Based on these findings, the following practical guidelines for designing stable SMA actuators for long-term cycling are proposed:
1. Adopt an operating regime with a degree of reverse transformation not exceeding 75 %.
2. Account for performance losses during the initial cycling stage (first ~ 30 cycles), which can be mitigated by thermal cycling (training) of the working element before use.
3. Perform a service life prediction based on the linear degradation rate observed in the steady-state regime to ensure that the work output remains above the required minimum throughout the operational lifetime.

CRediT authorship contribution statement

Fedor S. Belyaev: conceptualization, investigation, writing – original draft; **Aleksandr E. Volkov**: writing – review & editing, supervision; **Daniil F. Gorbachenko**: investigation; **Margarita E. Evard**: writing – review & editing, supervision.

Conflict of interest

The authors declare that they have no conflict of interest.

References

1. Gangil N, Siddiquee AN, Maheshwari S. Towards applications, processing and advancements in shape memory alloy and its composites. *Journal of Manufacturing Processes.* 2020;59: 205–222.
2. Kim M, Heo J, Rodrigue H, Lee H, Pané S, Han M, Ahn SH. Shape Memory Alloy (SMA) Actuators: The Role of Material, Form, and Scaling Effects. *Advanced Materials.* 2023;35(33): 2208517.
3. Kohl M. *Shape Memory Microactuators.* Berlin: Springer; 2004.
4. Mertmann M, Vergani G. Design and application of shape memory actuators. *The European Physical Journal Special Topics.* 2008;158(1): 221–230.
5. Mohd Jani J, Leary M, Subic A, Gibson MA. A review of shape memory alloy research, applications and opportunities. *Materials & Design.* 2014;56: 1078–1113.
6. Mohd Jani J, Leary M, Subic A. Designing shape memory alloy linear actuators: A review. *Journal of Intelligent Material Systems and Structures.* 2017;28(13): 1699–1718.
7. Yadav SK. Shape Memory Alloy Actuators: A Review. *IJRASET.* 2019;7(5): 799–802.
8. Ameduri S, Concilio A. A shape memory alloy torsion actuator for static blade twist. *Journal of Intelligent Material Systems and Structures.* 2019;30(17): 2605–2626.

9. Hartl DJ, Lagoudas DC. Aerospace applications of shape memory alloys. *Proceedings of the Institution of Mechanical Engineers, Part G: Journal of Aerospace Engineering.* 2007;221(4): 535–552.
10. Liu R, Zhang C, Ji H, Zhang C, Qiu J. Training, Control and Application of SMA-Based Actuators with Two-Way Shape Memory Effect. *Actuators.* 2023; 12(1): 25.
11. Yang J, Zhang Y, Gu X, Li J, Fang P, Yang X, et al. Bi-direction and flexible multi-mode morphing wing based on antagonistic SMA wire actuators. *Chinese Journal of Aeronautics.* 2024;37(12): 373–387.
12. Nam C, Chattopadhyay A, Kim Y Application of shape memory alloy (SMA) spars for aircraft maneuver enhancement. In: *Proc. SPIE 4701, Smart Structures and Materials 2002: Smart Structures and Integrated Systems.* 2002. p.226–236.
13. Kheirikhah MM, Rabiee S, Edalat ME. A Review of Shape Memory Alloy Actuators in Robotics. In: Ruiz-del-Solar J, Chown E, Plöger PG. (Eds.) *RoboCup 2010: Robot Soccer World Cup XIV.* Berlin: Springer; 2011. p.206–217.
14. Lu Y, Xie Z, Wang J, Yue H, Wu M, Liu Y. A novel design of a parallel gripper actuated by a large-stroke shape memory alloy actuator. *International Journal of Mechanical Sciences.* 2019;159: 74–80.
15. Sreekumar M, Nagarajan T, Singaperumal M, Zoppi M, Molfino R. Critical review of current trends in shape memory alloy actuators for intelligent robots. *Industrial Robot.* 2007;34(4): 285–294.
16. Jani JM, Leary M, Subic A. Shape Memory Alloys in Automotive Applications. *Applied Mechanics and Materials.* 2014;663: 248–253.
17. Stoeckel D. Shape Memory Actuators for Automotive Applications. *Materials & Design.* 1990;11(6): 302–307.
18. Liu Q, Ghodrat S, Huisman G, Jansen KMB. Shape memory alloy actuators for haptic wearables: A review. *Materials & Design.* 2023;233: 112264.
19. Xu J, Kimura Y, Tsuji K, Abe K, Shimizu T, Hasegawa H, Mineta T. Fabrication and characterization of SMA film actuator array with bias spring for high-power MEMS tactile display. *Microelectronic Engineering.* 2020;227: 111307.
20. Hamid QY, Wan Hasan WZ, Azmah Hanim MA, Nuraini AA, Hamidon MN, Ramli HR. Shape memory alloys actuated upper limb devices: A review. *Sensors and Actuators Reports.* 2023;5: 100160.
21. Kamlet M. *NASA tests new alloy to fold wings in flight - NASA*. Available from: https://www.nasa.gov/centers/armstrong/feature/nasa-tests-new-alloy-to-fold-wings-in-flight.html [Accessed 30th November 2025].
22. Park HB, Kim DR, Kim HJ, Wang W, Han MW, Ahn SH. Design and Analysis of Artificial Muscle Robotic Elbow Joint Using Shape Memory Alloy Actuator. *Int J Precis Eng Manuf.* 2020;21(2): 249–256.
23. Liu Q, Wang W, Reynolds MF, Cao MC, Miskin MZ, Arias TA, Muller DA, McEuen PL, Cohen I. Micrometer-sized electrically programmable shape-memory actuators for low-power microrobotics. *Science Robotics.* 2021;6(52): eabe6663.
24. Priadko AI, Pulnev SA, Nikolaev VI, Rogov AV, Shmakov OA, Golyandin SN, Chikiryaka AV. Investigation of single crystal Cu-Al-Ni alloy bending force elements for linear motors. *Materials Physics and Mechanics.* 2016;29(2): 158–165.
25. Pei YC, Wang XY, Yao ZY, Wang BH, Liao Z hui, Lu H. The driving characteristics of bidirectional SMA wire actuators - Theoretical modeling and experimental testing. *Sensors and Actuators A: Physical.* 2024;372: 115328.
26. Movchan AA, Ekster NM. Actuator with a series connection of a shape memory alloy's rod and an elastic bias element. *Journal on Composite Mechanics and Design.* 2021;27(2): 169–190. (In Russian)
27. Movchan AA, Ekster NM. Selection of materials for creating bias bodies in force actuator with a working body made of a shape memory alloy. Part 1. Metal bias bodies. *Journal on Composite Mechanics and Design.* 2025;31(3): 351–372.
28. Khan AM, Bijalwan V, Shin B, Kim Y. Adaptive Neural Network Control Design and Analysis for Sma Actuators Having Dominant Shape Memory Effect. [Preprint] 2023. Available from: https://www.ssrn.com/abstract=4577203 [Accessed 30th November 2025].
29. Khan AM, Bijalwan V, Shin B, Kim Y. Adaptive neural network controller for the rotating SMA actuator. *Sensors and Actuators A: Physical.* 2024;370: 115240.
30. Mohd Jani J, Huang S, Leary M, Subic A. Numerical modeling of shape memory alloy linear actuator. *Computational Mechanics.* 2015;56: 443–461.
31. Ostropiko E, Razov A, Cherniavsky A. Investigation of TiNi shape memory alloy for thermosensitive wire drive. *MATEC Web Conf.* 2015;33: 03021.
32. Ostropiko ES, Razov AI. Functional properties of TiNi conical workingelements in the holding and release device. *Cybernetics and Physics.* 2018;7: 216–219.
33. Sibirev A, Belyaev S, Resnina N. The influence of counter-body stiffness on working parameters of NiTi actuator. *Sensors and Actuators A: Physical.* 2021;319: 112568.
34. Belyaev S, Resnina N, Zhuravlev R. Deformation of Ti–51.5at.%Ni alloy during thermal cycling under different thermal-mechanical conditions. *Journal of Alloys and Compounds.* 2013;577: S232–S236.

35. Furuya Y, Park YC. Thermal cyclic deformation and degradation of shape memory effect in Ti-Ni alloy. *Nondestructive Testing and Evaluation.* 1992;8–9(1–6): 541–554.
36. Hamilton RF, Sehitoglu H, Efstathiou C, Maier HJ. Mechanical response of NiFeGa alloys containing second-phase particles. *Scripta Materialia.* 2007;57: 497–499.
37. Morgan NB, Friend CM. A review of shape memory stability in NiTi alloys. *J. Phys. IV France.* 2001;11(PR8): Pr8-325-Pr8-332.
38. Sehitoglu H, Wu Y, Patriarca L. Shape memory functionality under multi-cycles in NiTiHf. *Scripta Materialia.* 2017;129: 11–15.
39. Sibirev A, Belyaev S, Resnina N. Softening process during reverse martensitic transformation in TiNi shape memory alloy. *Journal of Alloys and Compounds.* 2016;661: 155–160.
40. Movchan AA, Ekster NM. Geometrically Nonlinear Analysis of the Operation of a Shape Memory Alloy Force Actuator. *Russ Metall.* 2025;2025(4): 717–726.
41. Movchan AA, Ekster NM. Theoretical Analysis of the Operation of a Force Actuator with a Working Body Consisting of a Shape Memory Alloy Rod and an Elastic Displacement Body. *Russ Metall.* 2023;2023(4): 389–397.
42. Mirzaeifar R, Elahinia MH. Mathematical Modeling and Simulation. In: Elahinia MH. (Ed.) *Shape memory alloy actuators: design, fabrication, and experimental evaluation.* Wiley; 2015. p.45–84.
43. Belyaev FS, Evard ME, Volkov AE. Microstructural modeling of fatigue fracture of shape memory alloys at thermomechanical cyclic loading. *AIP Conference Proceedings.* 2018;1959: 070003.
44 Belyaev FS, Evard ME, Volkov AE. Simulation of the plastic deformation of shape memory alloys considering shear anisotropy on the slip plane. *Materials Physics and Mechanics.* 2023;51(1): 61–67.
45. Resnina N, Ivanov A, Belyaev F, Volkov A, Belyaev S. Simulation of recoverable strain variation during isothermal holding of the $Ni_{51}Ti_{49}$ alloy under various regimes. *Letters on Materials.* 2023;13(1): 33–38.
46. Volkov AE, Belyaev FS, Volkova NA, Vukolov EA, Evard ME, Rebrov TV. The effect of martensite stabilization in titanium nickelide after various methods of pre-deformation: simulation with a single set of constants. *Materials Physics and Mechanics.* 2024;52(4): 91–99.
47. Belyaev F, Volkov AE, Vukolov E, Evard M, Kudrina KV, Starodubova M. Influence of latent heat and heat exchange conditions on tension behavior of shape memory alloy specimen. *Materials Physics and Mechanics.* 2024;52(5): 18–28.
48. Belyaev FS, Volkov AE, Gorbachenko DF, Evard ME. Modeling of working cycles of thermomechanical actuators based on shape memory alloys at repeated actuation. *Materials Physics and Mechanics.* 2024;52(6): 89–90.
49. Belyaev F, Evard M, Volkov A, Volkova N. A Microstructural Model of SMA with Microplastic Deformation and Defects Accumulation: Application to Thermocyclic Loading. *Materials Today: Proceedings.* 2015;2: S583–S587.
50. Volkov AE, Belyaev FS, Evard ME, Volkova NA. Model of the Evolution of Deformation Defects and Irreversible Strain at Thermal Cycling of Stressed TiNi Alloy Specimen. *MATEC Web of Conferences.* 2015;33: 03013.
51. Sibirev A, Belyaev S, Resnina N. Improvement of the NiTi actuator performance stability by decreasing its operating temperature range. *Sensors and Actuators A: Physical.* 2023;363: 114743.

MATERIALS PHYSICS AND MECHANICS RESEARCH ARTICLE

Submitted: February 4, 2026 **Revised: March 10, 2026** **Accepted: March 16, 2026**

Partitioning of a microstructure produced during laser powder bed fusion of 17-4 PH steel

S.I. Borisov [1], P.D. Dolzhenko [1], I.S. Nikitin [1], A.A. Kalinenko [1], I.S. Zuiko [1], E.V. Kaliuzhnaya [1], L. Shi [2], Ch. Wu[2], S.Yu. Mironov [1]✉

[1] Belgorod National Research University, Belgorod, Russia

[2] Shandong University, Jinan, China

✉ mironov@bsuedu.ru

ABSTRACT

This study focused on the characterization of a complex microstructure in 17-4 PH martensitic steel produced during laser powder bed fusion. Due to the specific nature of the LPBF process, the additive material undergoes an extremely high cooling rate (~ 10^6 K/s) and pronounced thermal cycling. This usually gives rise to the complex microstructures consisting of δ-ferrite, austenite, and martensite. In this work, a two-step approach was developed for the partitioning of the δ-ferrite and martensite phases. The elaborated method was based on the electron backscatter diffraction technique and involved a two-factor filtration of the electron backscatter diffraction data using the distinct differences between the δ-ferrite and martensite in stored energy and grain size. From experimental observations, it was shown that the proposed technique was highly effective for an analysis of the complex microstructures produced during LPBF of 17-4 PH martensitic steel.

KEYWORDS

martensitic steel • additive manufacturing • electron backscatter diffraction • microstructure • martensite δ-ferrite

***Funding**. The work was supported by the government assignment FZWG-2026-0005 "Development of scientific foundations for optimization of selective laser melting and subsequent heat treatment of precipitation-hardening martensitic steel 17-4 PH", Ministry of Science and Higher Education of the Russian Federation. The experimental works were conducted using equipment of the Joint Research Center "Technology and Materials" at Belgorod State National Research University.*

Citation: Borisov SI, Dolzhenko PD, Nikitin IS, Kalinenko AA, Zuiko IS, Kaliuzhnaya EV, Shi L, Wu Ch, Mironov SYu. Partitioning of a microstructure produced during laser powder bed fusion of 17-4 PH steel. *Materials Physics and Mechanics*. 2026;54(2): 17–25.
http://dx.doi.org/10.18149/MPM.5422026_2

Introduction

Owing to a good balance of strength and corrosion resistance, 17-4 PH martensitic steel is widely used in aerospace, petrochemical, and marine industries. Moreover, a recent invention of the additive laser powder bed fusion (LPBF) technology may further broaden the application range of this material for the fabrication of complex-shaped parts.

The LPBF technology involves the incremental, layer-by-layer melting and fusion of an atomized metal powder by a laser beam following an appropriate computer model [1,2]. Due to the specific nature of the LPBF process, the manufactured material experiences a non-trivial thermal history involving an extremely high cooling rate (~10^6 K/s) and a pronounced thermal cycling, including several melting-to-solidification sequences. In the 17-4 PH steel, LPBF often gives rise to the complex microstructures consisting of

an intermixture of δ-ferrite, austenite, and martensite [3–20]. To ascertain the key microstructural mechanisms involved in the LPBF process as well as to predict the service properties of LPBFed parts, a quantification of these phases is necessary. However, while a detection of the austenitic phase is rather straightforward, the differentiation between the δ-ferrite and martensite is challenging because of the similarity of the crystal structure of the phases.

To surmount this issue, several approaches based on the electron backscatter diffraction (EBSD) technique have been proposed in the scientific literature [15,16,21–30]. Typically, those are based on the presumed distinction of the stored energy between the ferrite and martensite and the concomitant difference in the lattice imperfections. Hence, the distribution of a related EBSD metric (which is sometimes referred to as the image quality index[1]) should be either bimodal or exhibit a clear transition from one phase to another.

From the authors' experience, however, the experimental distributions of image quality (IQ) index are often smooth and show no clear transition between the phases. Therefore, the resulting microstructure partitioning is not always perfect.

To enhance the efficiency of this procedure, a two-step approach was suggested in the present study. In this case, the conventional IQ-based partitioning technique is complemented by an additional filtration step, which is based on another distinct characteristic of the martensitic phase. The latter one may include a relatively low confidence index of diffraction patterns, a broader grain orientation spread, or a finer grain size. It was assumed that such a two-factor data filtration strategy would increase the efficiency of phase partitioning. This work was undertaken to investigate the validity of this concept.

Materials and Methods

The program material used in this work was a commercial 17-4 PH martensitic steel with the nominal chemical composition shown in Table 1. The material was produced by 3D Systems Inc. using the nitrogen-gas atomization technique and supplied as an atomized metallic powder. The powder particles had a nearly spherical morphology and often contained satellites. The particle size distribution was relatively broad, spanning from ~ 1 to ≈ 30 μm.

Table 1. Nominal chemical composition of 17-4 PH martensitic steel (wt. %)

Fe	Cr	Ni	Cu	Mn	Si	Ta + Nb	C	P	S
Balance	15.0–17.5	3.0–5.0	3.0–5.0	⩽ 1.0	⩽ 1.0	0.15–0.45	⩽ 0.07	⩽ 0.04	⩽ 0.03

The LPBF process was carried out on a ProX DMD 200 machine (3D Systems). To minimize porosity, LPBF variables were selected to provide a relatively high volumetric energy density. Those included a laser power of 180 W, a laser scanning speed of 1 m/s, a hatch distance of 50 μm, and a powder layer thickness of 30 μm (the volumetric energy density of 120 J/mm^3). A cuboidal-shaped sample with dimensions 10 × 10 × 20 mm^3 was built vertically using a nitrogen atmosphere. A simple parallel scan strategy was employed

[1]In TSL OIM software, the image quality (IQ) index characterizes the sharpness of the Kikuchi bands in a digitized diffraction pattern and thus serves as a qualitative measure of stored energy.

with a 90° rotation of the laser scan direction from layer to layer. No heat treatment was applied after the LPBF procedure.

For EBSD observations, the built sample was sectioned in half along the building direction, mounted into a conductive KonductoMet resin, and mechanically polished using standard metallographic procedures. A final surface finish was achieved using 24-h vibratory polishing with OP-S colloidal silica suspension.

EBSD analysis was performed employing an FEI Quanta 600 field-emission-gun scanning electron microscope (FEG-SEM) equipped with TSL OIM™ software and operated at an accelerated voltage of 20 kV. Microstructural observations were focused on the central part of the built sample. To provide both a necessary spatial resolution and sufficient sampling statistics, an intermediate EBSD scan step size of 0.2 μm was applied. Given the above-mentioned difficulty of discriminating ferrite from martensite in EBSD, these two phases were indexed as the generic body-centered cubic (BCC) phase; accordingly, the austenite was indexed as the generic face-centered cubic (FCC) phase. To enhance the reliability of EBSD data, the fine grains comprising two or one pixel were automatically "cleaned" from the acquired EBSD map using the standard grain-dilation option of EBSD software.

Results and Discussion

Preliminary analysis

The EBSD IQ map of a typical microstructure evolved in the central part of the built sample[2] is shown in Fig. 1(a). In the map, the FCC phase is highlighted with red, while the BCC component is shown in gray.

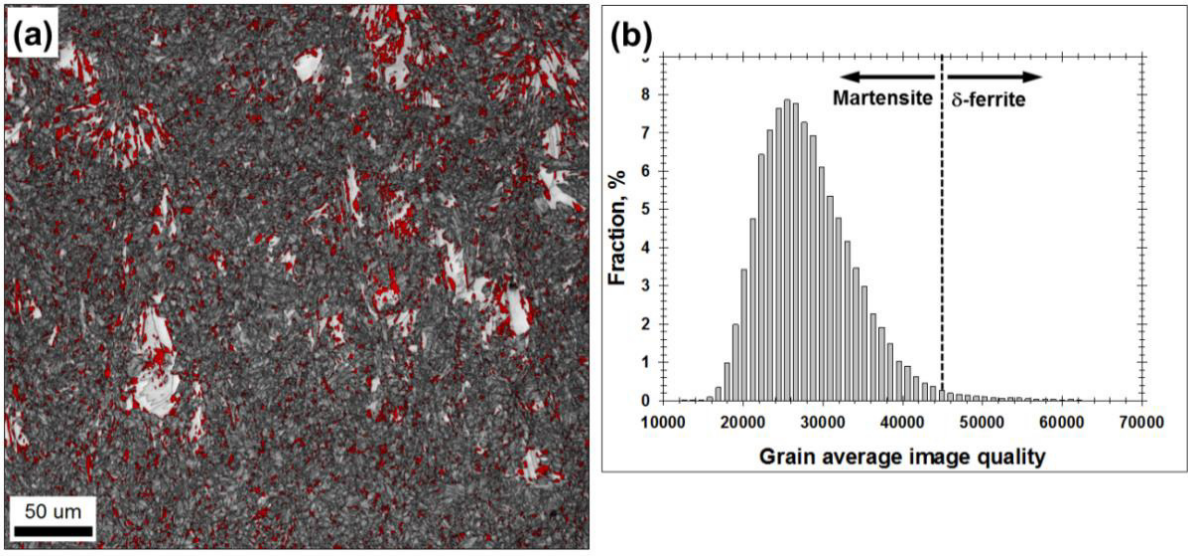

Fig. 1. (a) EBSD image-quality map of evolved microstructure (austenitic phase is highlighted with red) and (b) the distribution of the grain average image-quality index derived from the BCC microstructural component and used for the separation of martensite and d-ferrite. In (b), a presumed transition from martensite to d-ferrite is shown

[2]The volume fraction of the retained porosity within the LPBD'ed sample was measured to be ≈ 0.2 %.

The FCC constituent was obviously austenite. Remarkably, the austenite volume fraction was measured at ≈ 12.6 %, thus being comparatively high for 17-4 PH martensitic steel. Moreover, given the fine-scale nature of the produced microstructure (Fig. 1(a)), it is likely that some fraction of the austenite particles was "missed" during EBSD mapping, and thus the real proportion of this phase was even higher. The increased austenite content was likely attributable to both the relatively high cooling rate during LPBF and the influence of the nitrogen atmosphere.

In the context of the present study, of particular interest was the BCC microstructure. To a first approximation, it consisted of two distinct components, viz., coarse-grained and fine-grained ones.

The coarse-grained BCC component often exhibited columnar grain morphology and a comparatively bright IQ contrast (i.e., the low stored energy). Hence, this microstructural constituent was likely δ-ferrite. The preservation of the metastable δ-ferrite in the microstructure suggested the extremely high cooling rate during the LPBF. Remarkably, the δ-ferrite grains were not distributed uniformly throughout the microstructure but tended to cluster in local areas. Those presumably represented the remnants of the local molten pools, which are characteristic of the LPBF process.

Contrarily, the fine-grained BCC component showed a lath-shaped morphology and a comparatively dark IQ contrast (i.e., the high stored energy). From a broad perspective, therefore, this microstructural constituent reflected martensite. Noteworthy, the martensite was the dominant phase in the produced material, as is normally expected for the 17-4 PH martensitic steel.

Thus, in agreement with the scientific literature [3–20], the produced microstructure represented a complex mixture of δ-ferrite, austenite, and martensite. While the austenitic phase was readily recognizable, the unbiased distinguishing of δ-ferrite and martensite was challenging.

Microstructure partitioning. Step 1

To discriminate the δ-ferrite and martensite phases, the conventional IQ-based technique was first applied. The distribution of the grain average IQ indexes derived from the BCC microstructural constituent is presented in Fig. 1(b). The distribution was not bimodal but exhibited a distinct asymmetry. Specifically, it consisted of a pronounced peak at a comparatively low IQ index and an extreme end ("tail") in the high IQ range. It was highly likely that the former characteristic represented martensite, while the latter one reflected δ-ferrite. However, the transition between the phases was smooth, and no clear threshold could be found. The broadly similar IQ distributions for ferrite-martensite microstructures have been reported in a number of works, e.g. [21–24].

Using a trial-and-error approach, the approximate threshold was defined at IQ = 45,000. For clarity, this presumed borderline between the phases was indicated by a dotted line in Fig. 1(b). Based on this threshold, the IQ map[3] for the BCC crystals (Fig. 2(a)) was partitioned into two microstructural components, as shown in Fig. 2(b,c). It was found that the grains with relatively low IQ index (IQ < 45,000) exhibited lamellar

[3]The grayscale IQ maps are often similar to the corresponding optical (or SEM) images of a microstructure. Accordingly, those can be simple for comparison with conventional metallography.

morphology and comparatively fine sizes (Fig. 2(b)). On the other hand, the data with a higher IQ index (IQ ⩾ 45,000) encompassed all coarse columnar-shaped grains but also included a fraction of fine-scale grains (Fig. 2(c)).

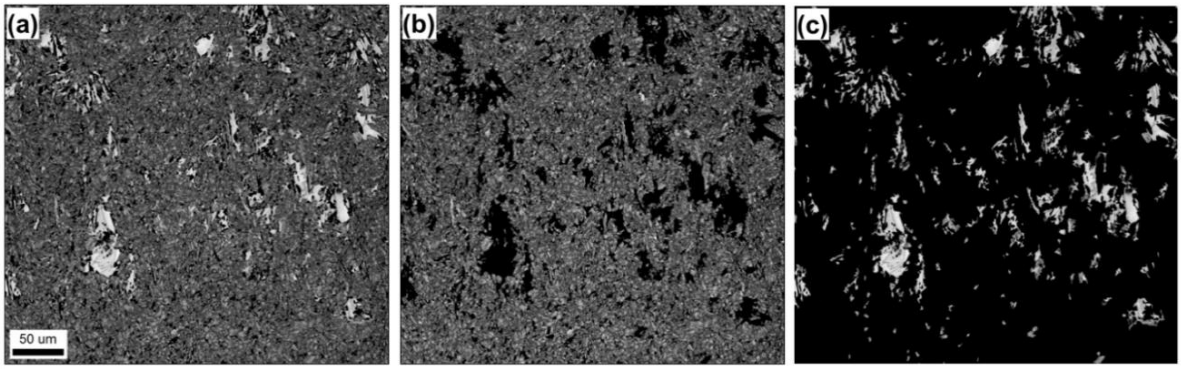

Fig. 2. EBSD image-quality maps showing microstructure partitioning of bcc phases (first step): (a) initial map, (b) "low-IQ" constituent, and (c) "high-IQ" constituent

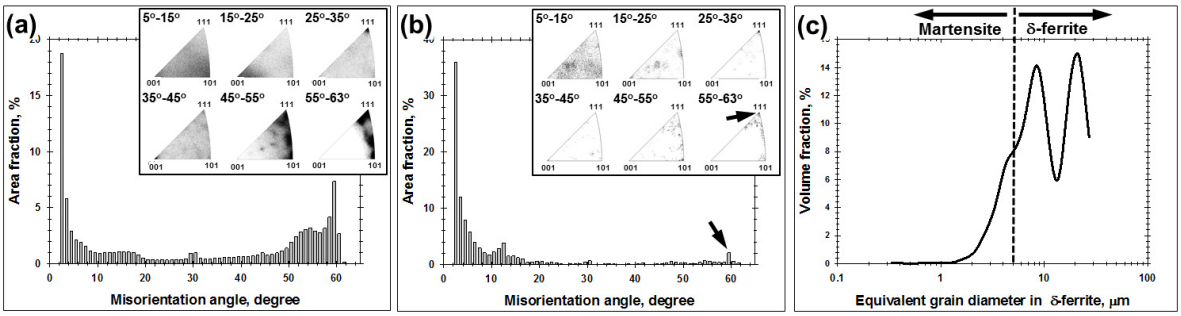

Fig. 3. Misorientation distributions derived from the partitioned phases (first step): (a) "low-IQ" microstructural constituent, (b) "high-IQ" microstructural constituent, and (c) grain-size distribution of the "high-IQ" microstructural constituent. In (a) and (b), misorientation-axis distributions are shown as inserts in the top right corners. In (b), arrows show an increased fraction of nearly-60° <111> boundaries, which presumably belonged to martensitic phase. In (c), a presumed transition from martensite to δ-ferrite is shown

To get additional insight into the partitioning results, misorientation distributions for both microstructural constituents were measured, as shown in Fig. 3(a,b). Due to the limited angular accuracy of EBSD, the lower-limit misorientation cut-off of 2° was applied in all cases.

The "low IQ" constituent showed a bimodal misorientation-angle distribution with a pronounced low-angle maximum and a broad peak in the range of 50–60° (Fig. 3(a)). Importantly, the misorientation axes of low-angle boundaries (LABs) tended to cluster near <101>, while those of the 50–60° boundaries preferentially concentrated near <111> and <101> (insert in the top right corner of Fig. 3(a)). The broadly similar misorientation distributions are normally observed in martensitic structures, e.g. [31–37] and are usually attributable to the dominance of the boundaries between martensite variants. Therefore, almost certainly, the "low IQ" microstructural constituent represented martensite.

The misorientation-angle distribution of the "high-IQ" microstructural constituent was dominated by low-angle boundaries but also included a subtle fraction of nearly 60° <111> boundaries (Fig. 3(b)). While the increased LAB content could readily be

associated with the dendritic origin of δ-ferrite, e.g. [15], the 60° <111> misorientations are hard to attribute to this phase. Moreover, a closer inspection showed that those boundaries were typically located within the relatively fine grains with relatively dark IQ contrast (Fig. 2(c)). Hence, those likely belonged to martensite, and therefore the partitioned δ-ferrite was probably contaminated by some fraction of this phase.

Microstructure partitioning. Step 2

Therefore, in accordance with expectations, the IQ-based approach was not entirely efficient. One probable reason for this effect could be the high residual stresses, which were presumably produced within the δ-ferrite phase due to an extremely high cooling rate during the LPBF process. This should degrade Kikuchi patterns and thus reduce the IQ index.

Accordingly, the second partitioning step was applied. From a series of preliminary experiments, it was found that the partitioning techniques based on either confidence index or grain orientation spread were not effective. Therefore, the grain size approach was used hereafter as the second data filtration step. This method was grounded on the presumed distinction in grain size between the δ-ferrite dendrites and martensite laths. The grain size was measured using the equivalent-grain diameter approach, i.e., by measurements of the grain area in the EBSD map and calculating the circle-equivalent diameter [38]. A 5-degree criterion was applied to define grain boundaries.

The grain size distribution derived from the partitioned δ-ferrite structure was shown in Fig. 3(c)[4]. Considering the specific character of the distribution, the grains below 5 μm in size were assumed to belong to the martensitic phase. For clarity, this presumed borderline between the martensite and δ-ferrite was indicated by a dotted line in Fig. 3(c). Based on this threshold, the IQ map for the BCC crystals (Fig. 4(a)) was partitioned into two microstructural components, as shown in Fig. 4(b,c). The misorientation distributions for the partitioned components were given in Fig. 5.

The second filtration step provided no apparent changes in either morphology or misorientation distribution of the presumed martensitic phase (Figs. 4(b) and 5(a)). In δ-ferrite, in contrast, the finest grains were filtered out (compare Figs. 4(c) and 2(c)). This eliminated the 60° <111> peak in the misorientation distribution (compare Figs. 5(b) and 3(b)).

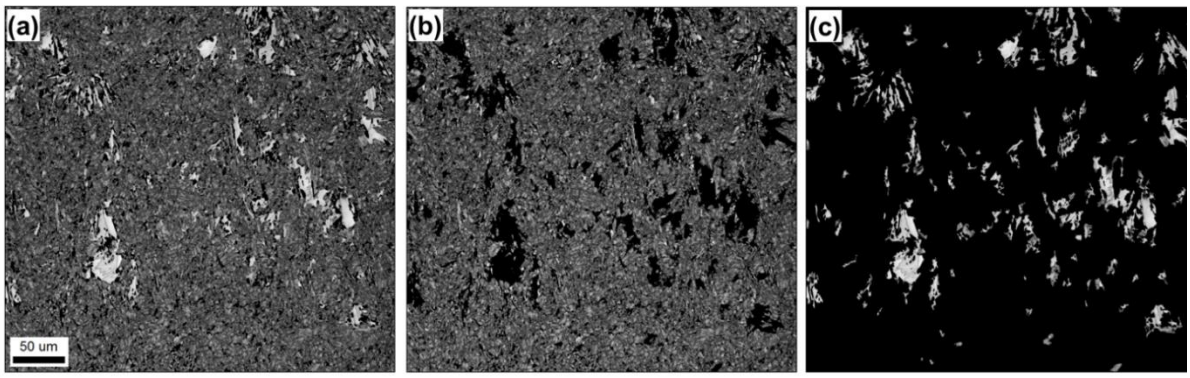

Fig. 4. EBSD image-quality maps showing microstructure partitioning of bcc phases (second step): (a) initial map, (b) partitioned martensite, and (c) partitioned δ-ferrite

[4]Given the scan step size of 0.2 μm applied during EBSD mapping, the finer grains (that may potentially exist in the microstructure) were not included in the grain-size distribution in Fig. 3(c).

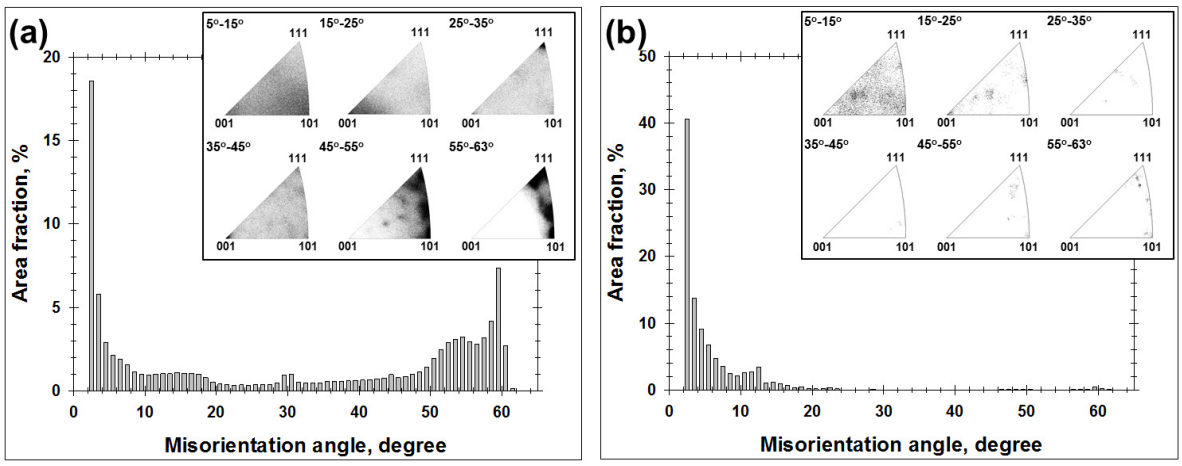

Fig. 5. Misorientation distributions derived from the partitioned phases (second step): (a) martensite and (b) δ-ferrite. In both cases, misorientation-axis distributions are shown as inserts in the top right corner

Premised on the latter observation, it was suggested that the δ-ferrite was filtered out from the martensite contaminations. Hence, it was concluded that the proposed two-step approach was effective for the partitioning of the δ-ferrite/martensite microstructure produced during LPBF of 17-4 PH martensitic steel.

It is worth noting that the conventional "one-step" IQ method is applicable to a wide range of ferrite-martensite structures [15,16,21–30]. It is likely, therefore, the relevance of the "two-step" technique developed in this study is not limited to the LPBF'ed 17-4 PH steel but also extends to a broader class of materials. On the other hand, the stress-relief annealing, which is often used for the LPBF'ed products, may reduce the difference in the stored energy between the martensite and δ-ferrite. This may obstruct the implementation of the approach.

Conclusions

This study was undertaken to provide an insight into the complex microstructure developed during LPBF of 17-4 PH steel. To this end, a two-step approach was proposed for the partitioning of the constituent δ-ferrite and martensite phases. This method was based on EBSD and involved a two-factor data filtration according to the distinct differences between the δ-ferrite and martensite in stored energy and grain size. The stored energy within the phases was evaluated employing a so-called image quality index, i.e., the EBSD metric characterizing the sharpness of the Kikuchi bands in digitized diffraction patterns. It was found the microstructure partitioning based on the stored energy only was not entirely effective. This observation was attributed to the high residual stresses, which were presumably produced within the δ-ferrite phase due to an extremely high cooling rate during the LPBF process. In contrast, the second-step partitioning on the basis of the grain size difference between the δ-ferrite and martensite was found to be effective for distinguishing these phases.

CRediT authorship contribution statement

Sergei I. Borisov: investigation, writing – review & editing; **Pavel D. Dolzhenko**: investigation, writing – review & editing; **Ivan S. Nikitin**: investigation, writing – review & editing; **Alexander A. Kalinenko**: investigation, writing – review & editing; **Ivan S. Zuiko**: investigation, writing – review & editing; **Elena V. Kaliuzhnaya**: writing – review & editing; **Lei Shi**: conceptualization, writing – review & editing; **Chuasong Wu**: conceptualization, writing – review & editing; **Sergei Yu. Mironov**: conceptualization, data curation, supervision, writing – original draft.

Conflict of interest

The authors declare that they have no conflict of interest.

References

1. Agarwala M, Bourell D, Beaman J, Marcus H, Barlow J. Direct selective laser sintering of metals. *Rapid Prototyping Journal.* 1999;1(1): 26–36.
2. Popovich AA, Sufiiarov VS, Borisov EV, Polozov IA, Masaylo DV. Design and manufacturing of tailored microstructure with selective laser melting. *Materials Physics and Mechanics.* 2018(1); 38: 1–10.
3. Murr LE, Gaytan SM, Ramirez DA, Martinez E, Hernandez J, Amato KN, Shindo PW, Medina FR, Wicker RB. Metal fabrication by additive manufacturing using laser and electron beam melting technologies. *Journal of Materials Science and Technology.* 2012;28(1): 1–14.
4. Akita M, Uematsu Y, Kakiuchi T, Nakajima M, Kawaguchi R. Defect-dominated fatigue behavior in type 630 stainless steel fabricated by selective laser melting. *Materials Science and Engineering: A.* 2016;666: 19–26.
5. Pasebani S, Ghayoor M, Badwe S, Irrinki H, Atre SV. Effects of atomizing media and post processing on mechanical properties of 17-4 PH stainless steel manufactured via selective laser melting. *Additive Manufacturing.* 2018;22: 127–137.
6. Vunnam S, Saboo A, Sudbrack C, Starr TL. Effect of powder chemical composition on the as-built microstructure of 17-4 PH stainless steel processed by selective laser melting. *Additive Manufacturing.* 2019;30: 100876.
7. Hsu TH, Chang YJ, Huang CY, Yen HW, Chen CP, Jen KK, Yeh AC. Microstructure and property of a selective laser melting process induced oxide dispersion strengthened 17-4 PH stainless steel. *Journal of Alloys and Compounds.* 2019;803: 30–41.
8. Wang X, Liu Y, Shi T, Wang Y. Strain rate dependence of mechanical property in a selective laser melted 17–4 PH stainless steel with different states. *Materials Science and Engineering: A.* 2020;792: 139776.
9. Sun Y, Hebert RJ, Aindow M. Effect of laser scan length on the microstructure of additively manufactured 17-4PH stainless steel thin-walled parts. *Additive Manufacturing.* 2020;35: 101302.
10. Yadollahi A, Mahmoudi M, Elwany A, Doude H, Bian L, Newman JC. Effects of crack orientation and heat treatment on fatigue-crack-growth behavior of AM 17-4 PH stainless steel. *Engineering Fracture Mechanics.* 2020;226: 106874.
11. Lee HJ, Dao VH, Ma YW, Yu JM, Yoon KB. Effects of process parameters on the high temperature strength of 17-4PH stainless steel produced by selective laser melting. *Journal of Mechanical Science and Technology.* 2020;34(8): 3261–3272.
12. Sabooni S, Chabok A, Feng SC, Blaauw H, Pijper TC, Yang HJ, Pei YT. Laser powder bed fusion of 17–4 PH stainless steel: A comparative study on the effect of heat treatment on the microstructure evolution and mechanical properties. *Additive Manufacturing.* 2021;46: 102176.
13. Ponnusamy P, Sharma B, Masood SH, Rahman Rashid RA, Rashid RR, Palanisamy S, Ruan D. A study of tensile behavior of SLM processed 17-4 PH stainless steel. *Materials Today: Proceedings.* 2021;45: 4531–4534.
14. Aripin MA, Sajuri Z, Syarif J, Baghdadi AH, Mohamed IF. Evaluation of microstructure and porosity for 3D printed stainless steel. *Materials Today: Proceedings.* 2022;66: 3082–3086.
15. Vysotskiy I, Malopheyev S, Zuiko I, Mironov S, Kaibyshev R. Crystallographic aspects of 17–4 PH martensitic steel produced by laser-powder bed fusion. *Materials Characterization.* 2022;194: 112405.
16. Vysotskiy I, Malopheyev S, Zuiko I, Mironov S, Kaibyshev R. Microstructure distribution in 17-4 PH martensitic steel produced by selective laser melting. *Metallurgical and Materials Transactions A.* 2022;53: 4143–4147.

17. Yasa E, Atik I, Kandemir I. Material-specific phenomena and developing higher yield process parameters in laser powder bed fusion of 17-4 PH stainless steel. *Journal of the Brazilian Society of Mechanical Sciences and Engineering.* 2023;45: 38.
18. Mazruee Sebdani R, Bilan HK, Gale JD, Wanni J, Madireddy G, Sealy MP, Achuthan A. Ultrasonic impact treatment (UIT) combined with powder bed fusion (PBF) process for precipitation hardened martensitic steels. *Additive Manufacturing.* 2024;84: 104078.
19. Fields B, Amiri M, Lim J, Purstl JT, Begley MR, Apelian D, Valdevit L. Microstructural control of a multi-phase PH steel printed with laser powder bed fusion. *Advanced Materials Technologies.* 2024;9: 2301037.
20. Kugelmeier CL, Unti LFK, Júnior ELS, Souza NM, Jardini AL, Avila JA, Cintho OM, Zilnyk K. Microstructure evolution and corrosion resistance evaluation of 17-4 precipitation hardening stainless steel processed by laser powder bed fusion. *Journal of Materials Engineering and Performance.* 2025;34: 10537–10547.
21. Wilson AW, Madison JD, Spanos G. Determining phase volume fraction in steels by electron backscattered diffraction. *Scripta Materialia.* 2001;45: 1335–1340.
22. Wu J, Wray PJ, Garcia CI, Hua M, De AJ. Ardo Image quality analysis: A new method of characterizing microstructures. *ISIJ International.* 2005;45: 254–262.
23. Nowell MM, Wright SI, Carpenter JO. Differentiating ferrite and martensite in steel microstructures using electron backscatter diffraction. In: *Proc. Materials Science and Technology Conference and Exhibition.* 2009.
24. Calcagnotto M, Ponge D, Raabe D. Microstructure control during fabrication of ultrafine grained dual-phase steel: Characterization and effect of intercritical annealing parameters. *ISIJ International.* 2012;52(5): 874–883.
25. Kang JY, Park SJ, Moon MB. Phase analysis on dual-phase steel using band slope of electron backscatter diffraction pattern. *Microscopy and Microanalysis.* 2013;19: 13–16.
26. Im YR, Kim EY, Song T, Lee JS, Suh DW. Tensile properties and stretch-flangeability of TRIP steels produced by quenching and partitioning (Q&P) process with different fractions of constituent phases. *ISIJ International.* 2021;61(2): 572–581.
27. Shen C, Wang C, Huang M, Xu N, Zwaag S, Xu W. A generic high-throughput microstructure classification and quantification method for regular SEM images of complex steel microstructures combining EBSD labeling and deep learning. *Journal of Materials Science & Technology.* 2021;93: 191–204.
28. Ostormujof TM, Purohit RRPPR, Breumier S, Gey N, Salib M, Germain L. Deep learning for automated phase segmentation in EBSD maps. A case study in dual phase steel microstructures. *Materials Characterization.* 2022;184: 111638.
29. Kang JY. Qualities of electron backscatter diffraction patterns and image contrast from a ferritic-martensitic steel microstructure. *Materials Characterization.* 2022;187: 111826.
30. Kozlowska A., Radwanski K., Grajcar A. Identification of structural constituents in advanced multiphase high-strength steels using electron back-scattered diffraction. *Symmetry.* 2024;16(12): 1630.
31. Stormvinter A, Mitsche S, Cerjak H. Martensite laths in creep resistant martensitic 9-12% Cr steels – calculation and measurement of misorientations. *Materials Characterization.* 2007;58(10): 874–882.
32. Govindaraj V, Farabi E, Kada S, Hodgson PD, Singh RP, Rohrer GS, Beladi H. Effect of manganese on the grain boundary network of lath martensite in precipitation hardenable stainless steels. *Journal of Alloys and Compounds.* 2021;886: 161333.
33. Kim JH, Miyamoto G, Shibata A, Hojo T, Koyama M, Zhang Y, Furuhara T. Influence of austenite grain boundary misorientation on hydrogen-induced intergranular crack propagation in a medium carbon martensitic steel. *Acta Materialia.* 2024;274: 120036.
34. Moura AN, Favarato LNO, Amorim DSC, Alcantara CM, Marques MCS, Orlando MTD, Vieira EA, Labiapari WS, Cunha MA, Oliveira TR. Effect of austenitization temperature on microstructure, crystallographic aspects, and mechanical properties of AISI 420 martensitic stainless steel. *Materials Science and Engineering: A.* 2024;909: 146835.
35. Sun Y, Wu Z, Ji Y, Wang P, Wu S, Cao G, Liu Z. Cryogenic impact toughness of 5.5 % Ni steel at −196 °C: synergy of a dual-phase heterogeneous lamellar structure and the stability of reversed austenite. *Materials Science and Engineering: A.* 2025;943: 148740.
36. Sun H, Shao M, Lu N, Li X, Li L, Wang Z, Jiang J, Zhang H. The morphology and crystallography of lath martensite via high pressure martensitic transformation in Fe-0.45 wt.% C steel. *Acta Materialia.* 2025;284: 120624.
37. Aletdinov AF, Mironov S, Korznikova GF, Zaripova RG, Konkova TN, Myshlyaev MM. EBSD analysys of austenite steel microstructure after cryogenic rolling. *Materials Physics and Mechanics.* 2017;33(1): 29–40. (In Russian)
38. Humphreys FJ. Quantitative metallography by electron backscatter diffraction. *Journal of Microscopy.* 1999;195: 170–185.

MATERIALS PHYSICS AND MECHANICS RESEARCH ARTICLE

Submitted: March 24, 2025 **Revised: October 15, 2025** **Accepted: March 5, 2026**

B_4C reinforced Al nanocomposite development by powder metallurgy route: revolutionizing material for the future

N. Mohanty [1], T.K. Patnaik [1], T. Dash [2]✉, S. Bajpai [3], S.K. Biswal [2]

[1] GIET University, Gunpur, Odisha, India

[2] International PranaGraf Mintech Research Centre (IGMRC), Bhubaneswar, Odisha, India

[3] CSIR-Institute of Minerals and Materials Technology, Bhubaneswar, Odisha, India

✉ tapanphy@gmail.com

ABSTRACT

An effective powder metallurgy route has been used to develop new Al/B_4C (0, 0.5, and 1 wt. %) nanocomposites. Following 4 h of optimized mechanical milling, particle size measurements verified for the pure Al, Al/B_4C (0.5 wt. %), and Al/B_4C (1 wt. %) samples as 65, 54, and 51 nm, respectively and these values are well corroborated to the crystal size measurement by XRD for the respective samples. Then the compacted (at 200 MPa) samples were sintered at an argon atmosphere at 550 °C for 3 h. Because of the homogeneous dispersion of 1 wt. % B_4C in Al, the intensity of the Al peaks is significantly reduced in the XRD pattern of Al/1 wt. % B_4C composite, which indicates the proper composite formation between Al and B_4C. It is marked that the reinforcement of B_4C enhanced the morphology of pure Al. Reinforcement of only 1 wt. % B_4C in Al was found to enhance its microhardness value from 45 to 112 VHN (about 148 % increment).

KEYWORDS

aluminium • boron carbide • XRD • microhardness

Citation: Mohanty N, Patnaik TK, Dash T, Bajpai S, Biswal SK. B_4C reinforced Al nanocomposite development by powder metallurgy route: revolutionizing material for the future. *Materials Physics and Mechanics*. 2026;54(2): 26–40. http://dx.doi.org/10.18149/MPM.5422026_3

Introduction

Aluminium (Al) is a very popular material, mainly due to its low density, ductility, and good electrical conductivity [1,2]. Still, its application is limited because of its poor hardness. Aluminium is potentially used in its alloy or composite forms. Different metals like magnesium (Mg), copper (Cu) [3], ceramics like magnesium oxide(MgO) [1], aluminium oxide (Al_2O_3), boron carbide (B_4C), silicon carbide (SiC) [3,4], and carbonaceous materials like graphene [2] and carbon nano tubes (CNT) [5] are generally added to Al to improve its various properties. Reinforcing aluminum with graphene [2] and CNT is widely used to enhance its microhardness and electrical properties. The enhancement of aluminum properties through the reinforcement of graphene/rGO and carbon nanotubes is not economically feasible. This is primarily because graphene and CNT [6] are quite expensive, which include challenges in developing aluminum-based composites using these materials. On the other hand, generally ceramic-reinforced Al matrix-based composites show good strength-to-weight ratio, corrosion, and tribological properties, enhancing their application to aviation, automobile, aerospace, marine, infrastructure, recreation, and defense [7–12].

Al with mono-, binary-, multiple-, or tri- ceramics reinforcement have been developed by different researchers [13–16]. As the number of reinforcing agents change, the behavior of composites changes with the change of kinematics and mechanism of composite formation. The process becomes challenging and difficult with the increase of number of reinforcements. Notably, among the ceramic class of carbides, boron carbide (B_4C) is the super ceramic material that shows excellent mechanical properties, low density, thermal, anti-corrosion, wear resistance, excellent impact strength, and ultimate tensile strengths, etc. [17–19].

Aluminum/boron carbide with lightweight, high hardness, and excellent thermal and chemical stability can be used for various industrial lightweight with high strength applications. Research is ongoing on B_4C-reinforced aluminium composites, but challenges include adding the right amount of B_4C, homogenous dispersion, and appropriate processing techniques. Al based composites (AMCs) can be prepared by various methods such as stir casting, powder metallurgy, squeeze casting, infiltration, spray deposition, mechanical alloying, direct metal deposition, extrusion, and hot pressing [20–23].

Each of these methods have their own Merits and demerits that are linked to specific application requirements of the composites. The powder metallurgy route is an effective method for preparing Al/B_4C composites, which involves powder composite formation, compaction, and sintering [24]. Hasan et al. [25] fabricated Al/B_4C (2.5, 5, 7.5, 10, and 12.5 wt. %) and Al/TiC (2.5, 5, 7.5, 10, and 12.5 wt. %) nanocomposites by powder metallurgy route sintered at 500 °C for 3.5 h under inert gas (argon). The micro-hardness for Al/B_4C (12.5 wt. %) nanocomposites and Al/TiC (12.5 wt. %) are 92 and 87.4 HRC, respectively, against pure Al about 40 HRC. A significant improvement in the hardness of the Al/B_4C composite was observed for the 12.5 wt. % reinforced B_4C composite. Khan et al. [23] prepared composites of AA7075 metal matrix of Al with reinforcement other ceramic like SiC, RHA (rice husk ash), and CES (carbonized eggshell) as reinforcing agents. Four samples, including AA7075, AA7075-5 wt. % SiC (MMC), AA7075-5 wt. % SiC-3 wt. % RHA (s-HMMC), and AA7075-5 wt. % SiC-3 wt. % RHA-1 wt. % CES (n-HMMC) were developed using the stir casting liquid metallurgy route, followed by the heat treatment. Stir casting of samples was carried out at 800 °C. Magnesium ribbons were added to enhance the wettability between the molten matrix and reinforcements. The cast samples underwent heat-treatment, heating at 400 °C for 3 h, quenching in a water bath, homogenization at 450 °C for 2 h, and aging at 120 °C for 24 h. The study reveals that the maximum experimental density of AA7075 was 2769 kg/m^3, with a decrease in densities with increasing reinforcements. The minimum experimental density of 2714 kg/m^3 was recorded for n-HMMC, which is about 1.18 % less than the base alloy. The reinforced composites showed higher porosity than the base alloy, with n-HMMC having the highest porosity at 3.11 %, followed by MMC, s-HMMC, and the base alloy. Scanning electron microscopy (SEM) images reveal base alloy AA7075 has coarse grains with minimal porosity, while the typical n-HMMC sample has a mixture of fine and coarse grains, with pores likely due to improper mixing, pouring issues, and trapped gases. In the work the n-HMMC alloy has the highest hardness at *HR* = 81.2 and *HBN* = 143.55, while the base alloy AA7075 has the lowest hardness at *HR* = 61.13 and *HBN* = 98.5.

Another study [26] investigates various Al-B_4C composite fabrication methods, including stir casting, powder metallurgy, melt-infiltration, and rolling. It compares their microstructural, mechanical, and physical properties. Powder metallurgy achieves uniform reinforcement particle distribution, while stir casting faces challenges like inhomogeneous distribution and low wetting behavior. Melt-infiltration is difficult to control pore size, and rolling reduces tensile strength. In our cases, heat treatment was simple and samples were sintered at relatively low temperature of 580 °C for 3 h. In our case, there is negligible reduction of density for the typical 1 wt. % B_4C reinforced Al composite in compared to base matrix of pure Al. But the microhardness value of Al was significantly increased from 45 to 112 VHN, a 148 % increase, due to the reinforcement of only 1 wt. % B_4C in Al.

Kumar et al. [27] prepared cast pure Al and Al/B_4C composites through the stir-casting method. He determined the microhardness of pure cast Al about 72 VHN. But upon addition of 6 wt. % B_4C to pure Al, it has been observed that there is an increment of about 21 VHN of composite. In [28], it is reported the effect of adding boron carbide (B_4C) reinforcement to an aluminium (Al) matrix at different volume fractions of B_4C particles, ranging from 2 to 12 %, fabricated by solid-state powder metallurgy using the hot-pressing process. The samples were processed at hot-pressing for 30 min at 620 °C, using induction heating and under uniaxial compressive stress of 60 MPa in a vacuum chamber. The hardness of the Al matrix was observed as 24 VHN. By reinforcing B_4C up to 12 vol. %, the microhardness value of the composite reached 50 VHN. No significant improvement in microhardness was observed, even when sintering was carried out at 620 °C in a vacuum chamber. Whereas the plastic deformation capacity of the Al matrix decreases as B_4C content increases. For pure Al, the material can undergo 31 % plastic deformation, which indicates a relatively high degree of ductility. However, when 12 % of B_4C is added, the plastic deformation drops significantly to 6 %. This suggests that the B_4C particles are stiffer and more brittle than Al, and their presence in the matrix inhibits the ability of the material to undergo plastic deformation. It was also marked that pure Al tends to fracture in a ductile manner, meaning it can deform plastically and absorb more energy before failure. However, with B_4C reinforced Al, the fracture becomes brittle. This transition from ductile to brittle fracture is attributed to the B_4C reinforcement. The B_4C particles are very hard and brittle, and they can act as stress concentrators within the Al matrix. When subjected to stress, these particles do not deform plastically like the Al matrix, but rather they promote crack initiation and propagation, leading to brittle fracture. In summary, while the addition of B_4C improves the hardness of the Al matrix, it also leads to a reduction in plastic deformation and a shift in fracture behavior from ductile to brittle. This makes the composite more rigid but less tough, meaning it can withstand higher stresses but is more prone to fracture under certain conditions. Hence, more additions of ceramics like B_4C are not suitable for the metallic behavior of Al.

The presented study investigates the effect of B_4C wt.% reinforcement (less or equal 1 wt. %) on the microstructural, physical and micro hardness properties of aluminium composites. Generally, B_4C more than 1 wt. % is added in pure Al to enhance its properties [17,24,25,27–29]. However, this research fills a gap in the exploration of the Al/B_4C composites synthesis by typical powder metallurgy route with sintering temperature below 600 °C. with minimum reinforcement of B_4C (preferably less than 1 wt. %) with

improved microstructural and microhardness behavior. More addition of B_4C to Al will not also be economically feasible on an industrial, commercial scale. Hence, in this work, we have made an attempt to develop pure Al and Al/B_4C (0.5 and 1 wt. %) composite materials by powder metallurgy route and evaluated their microstructural and microhardness properties for various future applications.

Materials and Methods

Aluminium (particle size ⩽ 30 μm, purity ⩾ 99 % μm, and density 2.78 g/cc) and boron carbide (particle size < 10 μm, purity 98 % and density 2.52 g/cc) powder samples were procured from Sigma-Aldrich and used as the starting materials. The typical process flowsheet adopted for preparation of Al/B_4C composites with actual photographs taken during experiments are presented in Fig. 1.

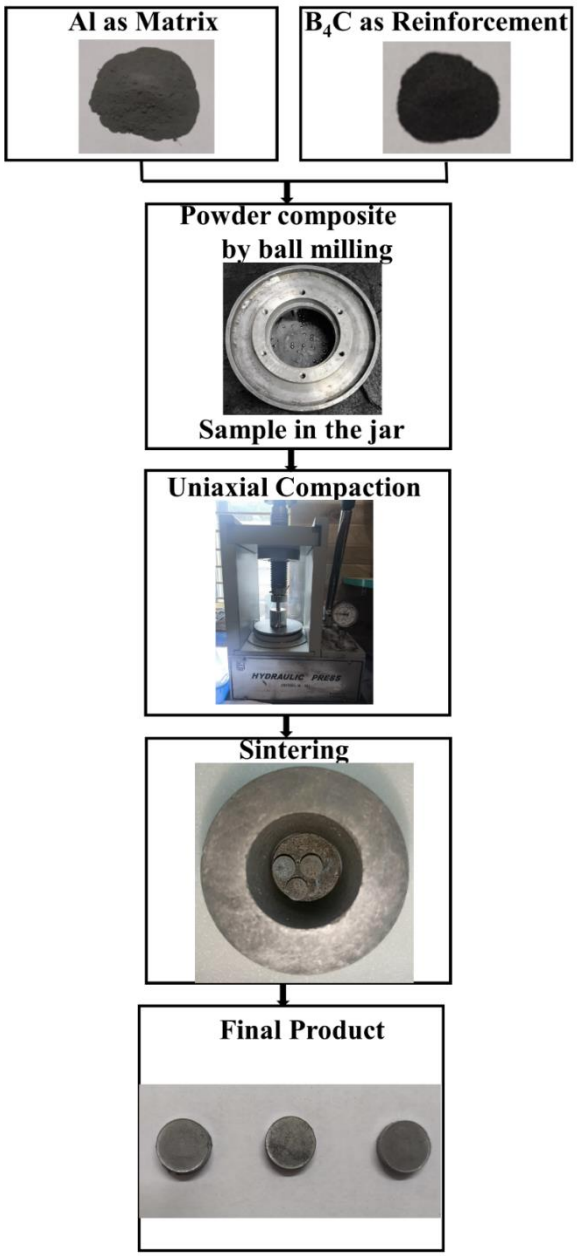

Fig. 1. The typical process flowsheet adopted for preparation of Al/B_4C composites

First, Al/B_4C (0.5 and 1 wt. %) composite powder was prepared using the mechanical planetary ball milling route. The ball mill was operated at a frequency of 30 Hz at 200 rpm (revolution per minute). Using tungsten carbide balls, the ball mill was carried in a stainless-steel jar. A charge-to-ball ratio of 1:10 was maintained during the ball milling. The milling of samples was done under an argon environment for 1–4 h. From the particle size analysis, it is observed that after 4 h of milling, the particle of power composite samples significantly reduced. The optimized powder composite samples produced after 4 h of milling were taken for cold uniaxial compaction at 200 MPa for powder samples of pure Al and Al/B4C (0.5 and 1 wt. %) composite samples added with polyvinyl alcohol (2–3 drops) as a binder. By cold compaction pellets were prepared with a diameter of 13 mm and thickness of 20 mm. Then, the pellets were air-dried. The compacted pellets were taken for sintering under an inert atmosphere (argon) in a controlled furnace. Sintering experiments were conducted at 550 °C for 180 min. After sintering over and obtaining the room temperature of the samples, they were taken out from the furnace for their properties evaluation.

The properties of the samples were evaluated using various techniques. The size distribution of mechanically ball-milled powder samples was quantified by a laser scattering particle size distribution analyzer (LA-960V2, Horiba Scientific). X-ray diffraction (XRD) (PANalytical X'Pert Pro diffractometer) was used to determine the crystalline behavior of sintered samples. Field emission scanning electron microscopy (FESEM) (model ZEISS SUPRA 55) with attached energy-dispersive X-ray spectroscopy (EDS) was employed to evaluate morphological and elemental compositions of samples after sintering. The microhardness of sintered samples was determined by taking an average of seven indentions carried out by equipment Fisher-Cripps, Australia, with diamond Berkovich indenter.

Results and Discussion

The variation of the median size (D_{50}) of mechanical ball-milled pure Al and Al/B_4C (0.5 and 1 wt. %) particles as a function of milling time (1–4 h), quantified by laser particle size analyzer is presented in Fig. 2. It has been observed that as the milling time increases from 1 to 4 h, it causes a shape decrease in particle size. From Fig. 2, it can be seen that up to 2 h of milling, there is a sharp decrease in particle size compared to the initial size of Al (particle size ⩽ 30 μm and B_4C (particle size < 10 μm). However, the rate of particle size reduction gradually decreases after 2 h of milling. In this work, we have obtained optimized particle size (D_{50}) for pure Al, Al/B_4C(0.5 wt. %), and Al/B_4C (1 wt. %) as 65, 54, and 51 nm, respectively, after 4 h mechanical milling. From Fig. 2, it can also be seen that adding B_4C particles to the Al powders resulted in a decreased size of the powder mixture. Hence, the addition of B_4C particles in Al is found to accelerate the milling process to reduce particle size. These results can be attributed to the hard ceramic behavior and finer particles of B_4C compared to Al. These results are found to be supported by other investigators regarding Al/B_4C nanocomposite powder synthesis by mechanical alloying [28].

The pure Al and Al/B_4C (0.5 and 1 wt. %) composites synthesized after 4 h of planetary ball milling were considered as the optimized nanomaterials produced in this work and then taken for cold compaction, followed by sintering experiments. The above

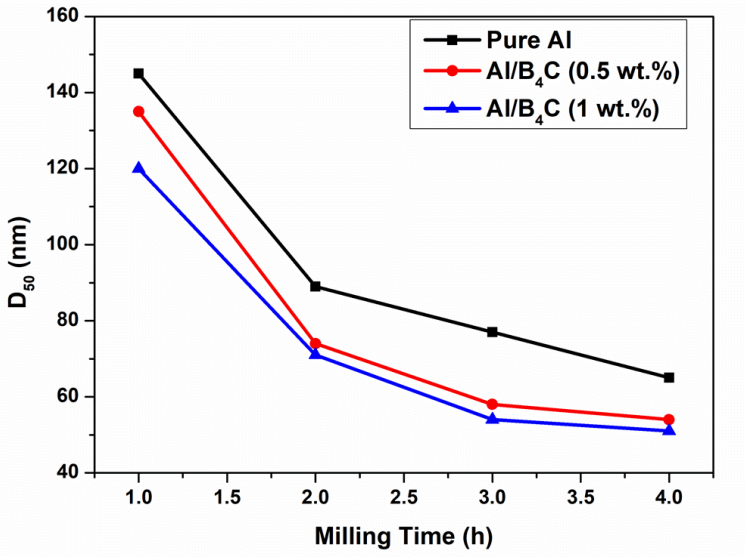

Fig. 2. The variation of the average particle size (D_{50}) of pure Al and Al/B_4C (0.5 and 1 wt. %) composites as a function of milling time

nanopowder samples added with polyvinyl alcohol (2 – 3 drops) as a binder are compacted at 200 MPa in a 13 mm die for one minute. Then, the samples were taken for sintering. In the first stage of the sintering cycle, the samples were heated from room temperature up to 550 °C with a heating rate of 5 °C per min. The samples were kept at 550 °C for 3 h in the second stage. Finally, the samples were allowed to cool up to 100 °C with a heating rate of 5 °C per min, and at last, the samples follow*ed in situ* cooling in the furnace till room temperature was achieved.

The X-ray diffraction (XRD) study of pure sintered aluminum (Al) and Al/B_4C composites with 0.5 and 1 wt. % B_4C reinforcement reveals important insights into the structural changes and crystallinity of the materials. The typical fundamental parameters obtained from XRD are presented in detail in Table 1. The diffracted peaks with their relative intensities are observable from Fig. 2. The peaks obtained in the XRD analysis are identified by comparing their Bragg's angle (2θ), d-spacing, and full width at half maximum (FWHM) values with that of inorganic crystal structure database (ICSD) of Al (Reference code: 98-006-2688) and B_4C (Reference code: 98-001-1179). In the XRD of pure sintered Al (Fig. 3(a)), distinct peaks corresponding to the (111), (002), (022), and (113) planes of aluminum are observed.

Table 1. Peak positions and corresponding FWHM and *d*-spacing values of XRD peaks of sintered pure Al and Al/B_4C composite samples

Pure Al			Al/0.5 wt.% B_4C			Al/1 wt.% B_4C			Peak assignment
Bragg's angle (2θ)	FWHM (2θ)	*d*-spacing, Å	Bragg's angle (2θ)	FWHM (2θ)	*d*-spacing, Å	Bragg's angle (2θ)	FWHM (2θ)	*d*-spacing, Å	
-	-	-	35.705210	0.048000	2.51264	35.072180	0.122803	2.55865	B_4C (104)
38.544210	0.149760	2.33562	38.518680	0.157760	2.33727	38.513900	0.185139	2.33578	Al(111)
44.806730	0.124800	2.02269	44.770120	0.192000	2.02287	44.765830	0.184205	2.02279	Al(002)
65.165870	0.149760	1.43040	65.150440	0.144000	1.43070	65.152500	0.163738	1.43106	Al(022)
78.312720	0.149760	1.21997	78.307950	0.168000	1.21991	78.299330	0.184205	1.22110	Al(113)

The XRD patterns for the Al/B_4C composites (Fig. 3(b,c)) show the presence of an additional peak at the 2θ position corresponding to the B_4C (104) plane, indicating the incorporation of B_4C particles into the Al matrix. The B_4C reinforcement does not introduce any impurity phases, confirming that the Al/B_4C composites are homogeneous. The XRD patterns of the Al/B_4C composites exhibit a shift of the aluminum peaks to lower 2θ values compared to pure Al. This could indicate lattice expansion due to the incorporation of B_4C, which is a harder material than Al. The FWHM of the peaks in Al/B_4C composites is higher than that in pure Al. The broader peaks typically suggest a reduction in crystallite size and increased lattice strain in the composite material. The FWHM is found to be the highest for the Al/B_4C (1 wt. %) composite, confirming the presence of finer grains and more internal strain. This results in a lower peak intensity for the composites. There is no significant difference in the *d*-spacing values for the corresponding peaks between pure Al and Al/B_4C composites, suggesting that the addition of B_4C does not significantly alter the crystal structure of Al at the atomic scale. The intensity of the aluminum peaks is observed to decrease with the addition of B_4C, especially in the Al/B_4C (1 wt. %) composite. This reduction in intensity is most significant for the Al (111) peak, indicating that the crystal orientation may be altered, or that there is a reduction in the size of the Al crystallites. As the B_4C content increases from 0.5 to 1 wt. % in the composites, the intensity of the B_4C (104) peak increases, confirming a higher volume fraction of B_4C in the Al matrix. This suggests that the reinforcement content has a measurable impact on the overall crystallographic structure of the composite.

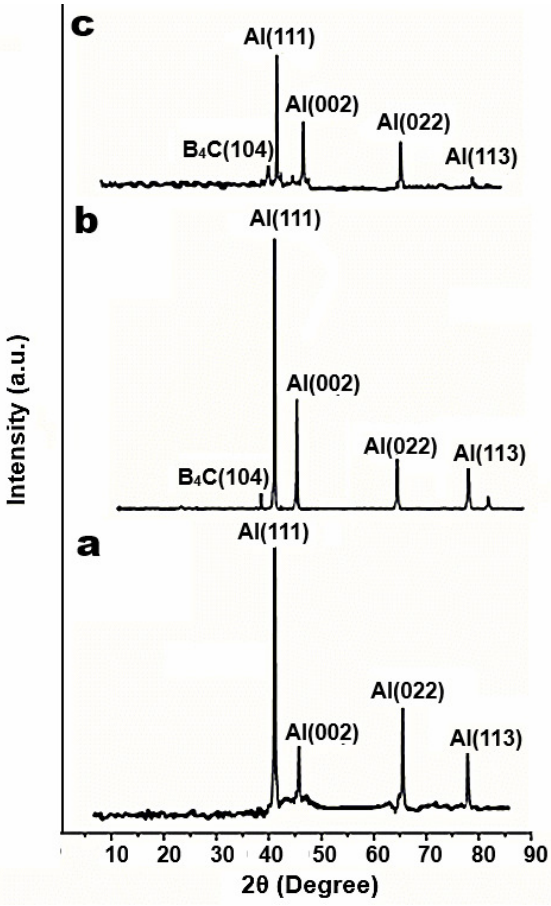

Fig. 3. XRD study of sintered samples (a) pure Al, (b) Al/B_4C (0.5 wt.%) composite, (c) Al/B_4C (1 wt.%) composite

From XRD spectra, the average crystallite size has been calculated for Al and B_4C phases considering only their highly intense peaks by applying the Scherer equation [30]:

$$\delta = \frac{0.9\lambda}{\beta cos\theta}, \quad (1)$$

where λ is a X-ray wavelength, β is FWHM (full width at half maximum) in radian for the peak observed at 2θ diffracting angle.

Pure sintered Al has a crystallite size of ~ 65.02 nm. Al/B_4C sintered composites (with 0.5 and 1 wt. % B_4C) show crystallite sizes ranging from ~ 63.88 to 64.75 nm for the Al phase and ~52.75 to 54.43 nm for the B_4C phase. The crystallite size of Al in the composites is quite similar to that of pure Al, with a slight decrease (~ 1–2 nm), suggesting that the addition of B_4C does not significantly affect the crystallite size of Al. However, the B_4C phase itself exhibits a smaller crystallite size compared to Al, which may be due to its different nature or the role of B_4C in stabilizing or refining the grains during processing. The fact that the crystallite sizes measured are consistent with the median particle sizes (D_{50}) after 4 h of milling indicates that the milling process likely contributed to refining the particles to a certain size. The lack of significant change in particle size after sintering supports the idea that milling is the dominant process for controlling particle size, rather than the sintering process itself. No significant agglomeration, grain growth, or nucleation is observed after the sintering process. This is an interesting observation, as typically, sintering can lead to particle coarsening or grain growth depending on the temperature and time. The absence of these phenomena suggests that the milling process, along with the particular sintering conditions used, was well-controlled to prevent unwanted changes in particle and grain size. It may also imply that the Al and B_4C particles were sufficiently fine and stable during milling, so no substantial changes were induced during sintering. The addition of B_4C seems to not only reduce the crystallite size of the B_4C phase but also helps to stabilize the crystallite size of the Al phase. This is likely due to the reinforcing role of B_4C particles, which may hinder excessive grain growth during the sintering process. B_4C is known for its hardness and stability, and in composites, it could act as a grain refiner, reducing the tendency of Al to grow its grains during sintering.

FESEM was used to assess the microstructure of the sintered pure Al and B_4C (0.5 and 1 wt. %) added Al composite samples (Fig. 4). There are noticeable microstructure cracks in pure sintered aluminum (Fig. 4(a)). The sample's surface morphology reveals a dip valley. After sintering, the Al/B_4C (0.5 and 1 wt. %) composite was observed to be extremely dense (Fig 4(b,c)). The microstructure shows no discernible dips or fissures. In particular, the Al/1 wt. % B_4C exhibits improved microstructure without any remarkable defects. The improvement of microhardness is greatly impacted by such superior microstructure. The study of the sintered pure Al and Al/B_4C (1 wt. %) composite phases was conducted through EDS analysis on the microstructures observed in FESEM images. The EDS analysis of sintered pure aluminium, as shown in Fig. 5(a) corresponding to the FESEM micrograph in Fig. 4(a), reveals only a peak associated with aluminium (Al). This indicates that the sintered pure Al consists solely of the aluminium phase, without any detectable impurities or additional phases. The EDS analysis of the phase 1 in the sintered Al/B_4C composite, indicated in Fig. 4(c), shows the presence of an aluminium peak (Fig. 5(b)). This confirms that phase 1 consists of aluminium, as expected in the

composite material. The EDS analysis of phase 2, marked on the FESEM image in Fig. 4(c), reveals peaks corresponding to boron (B) and carbon (C) (Fig. 5(c)). These peaks confirm the presence of the boron carbide (B_4C) phase within the composite. No peaks indicative of oxide or aluminium carbide phases were detected in the EDS analysis. The purity of the sintered samples is verified by the absence of any impurities in the EDS results, as no unexpected elements were detected, confirming the purity of the materials.

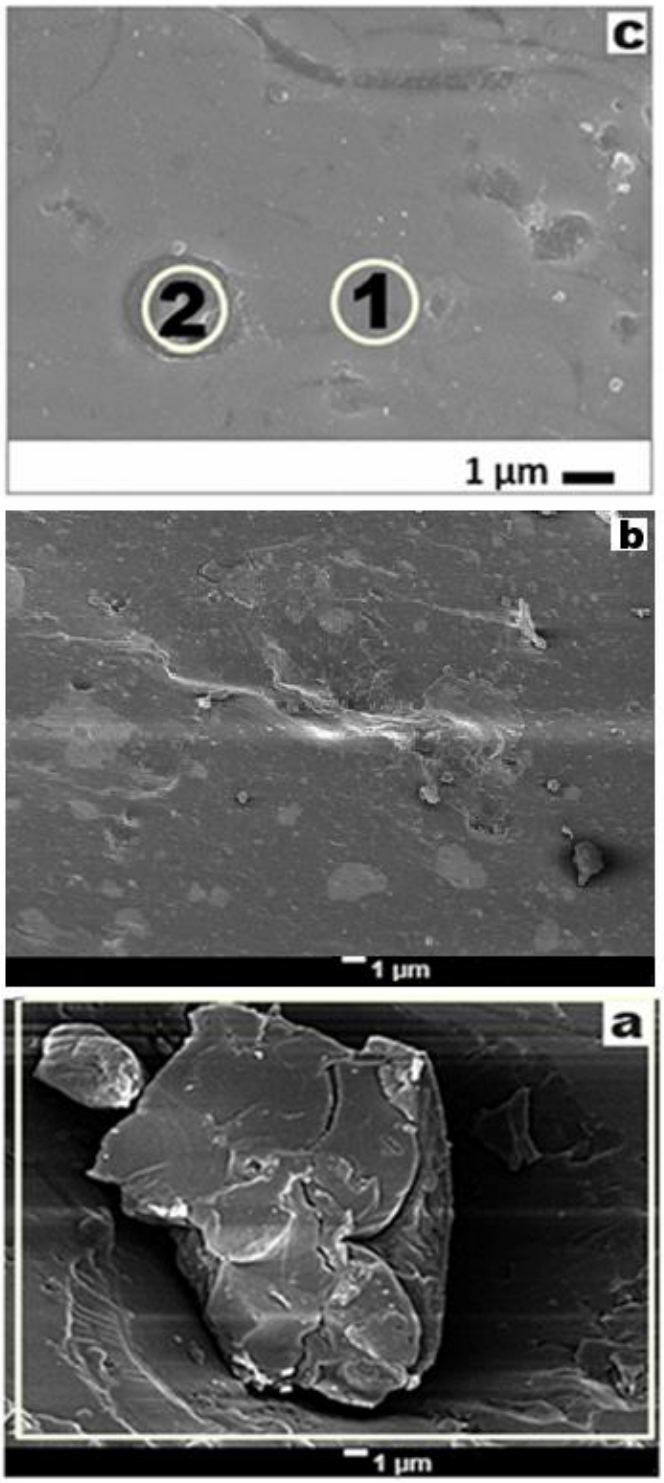

Fig. 4. FESEM analysis: (a) pure sintered Al, (b) sintered Al/B_4C (0.5 wt. %) composite sample, (c) sintered Al/B_4C (1 wt. %) composite sample

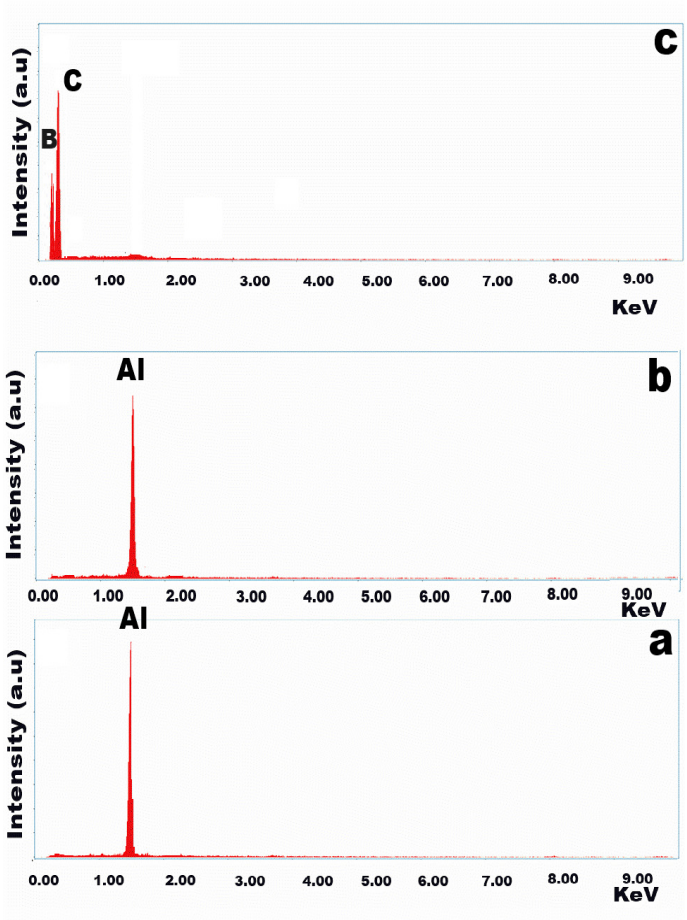

Fig. 5. (a) EDS result obtained on the total FESEM microstructure marked by the rectangular box shown in Fig. 4(a) of sintered pure Al; (b,c) EDS results obtained on the FESEM microstructure marked by phase 1 and phase 2 respectively in Fig. 4(c) of sintered Al/B_4C (1 wt. %) composite

The transmission electron microscopy (TEM) analysis result of sintered pure Al, Al/B_4C (0.5 wt. %) and Al/B_4C (1 wt. %) samples are presented in Fig. 6. Pure Al shows spheroidal kind of Al particles, which is typical for pure Al, where the particles are relatively uniform without any reinforcement. When B_4C (0.5 and 1 wt. %) reinforced in the matrix of Al, the dispersion of the B_4C particles is observed in the TEM images. The TEM results suggest that as the B_4C content increases, the particles are more evenly distributed within the Al matrix. The composite with 1 wt. % B_4C shows the relatively better dispersion, where the B_4C particles are well distributed in the Al matrix. This result could imply a stronger bond or interaction between the Al and B_4C. This analysis seems to indicate that increasing the B_4C content enhances the dispersion and potentially improves the structural integration between the phases, which might lead to improved hardness properties in the composite.

The microhardness of sintered pure Al and Al/B_4C (0.5 and 1 wt. %) composite samples were determined by calculating seven average values. The pure sintered Al exhibited a microhardness of 45 ± 5 Vickers hardness number (VHN), while the Al/B_4C (0.5 wt. %) composite demonstrated a microhardness of 75 ± 7 VHN. The microhardness of aluminum was further improved with the addition of 1 wt. % B_4C, resulting in the Al/1 wt. % B_4C composite achieving a microhardness exceeding 148 % (112 ± 8 VHN) compared to pure

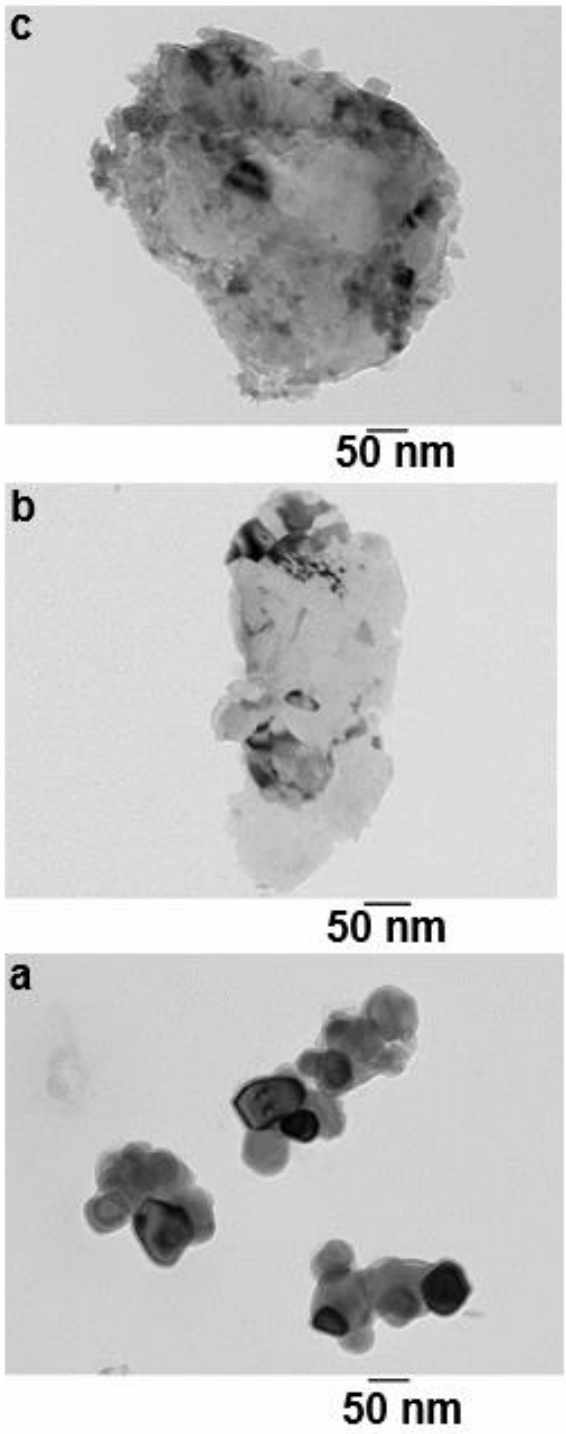

Fig. 6. TEM analysis: (a) pure sintered Al, (b) sintered Al/B_4C (0.5 wt.%) composite sample, (c) sintered Al/B_4C (1 wt.%) composite sample

aluminum. This enhancement in microhardness is attributed to the effective dispersion and presence of the harder boron carbide phase, good adhesion among the B_4C particles and Al matrix, formation of dislocations around B_4C particles due to misfit strain as well as the application of appropriate processing parameters for the production of nanocomposites.

The microhardness values of our sintered pure aluminum and aluminum/boron carbide composite samples, along with those reported in existing literature, are summarized in Table 2. In [17], a 9 wt. % addition of boron carbide to aluminum was

noted to enhance its hardness. However, our findings clearly indicate a substantial improvement in the microhardness of aluminum with only a 1 wt. % B_4C reinforcement. Nirala et al. [31] investigated boron carbide reinforcement levels ranging from 4 to 12 wt. % in aluminum, observing a maximum microhardness of approximately 77 VHN for the Al/B_4C (12 wt. %) sample with 133 % increase in microhardness from an initial value of 33 VHN for aluminum. Literature indicates that a 12 vol. % boron carbide reinforcement can elevate the microhardness of aluminum from 24 to 50 VHN, representing an increase of about 108 % [13]. Nonetheless, the reported microhardness values for aluminum tend to be lower overall. Kumar et al. [27] documented a microhardness of 72 VHN for aluminum, which increased by approximately 29 % (to 93 VHN) upon the addition of 6 wt. % boron carbide. Afrid et al. [32] reported that the microhardness of pure Al is 55.62 VHN, while that of Al with 10 wt. % reinforced B_4C composite processed by stir casting technique is 125.2 VHN. According to Gaylan et al. [33] when 5 wt. % B_4C was reinforced to the Al composite, the microhardness value was found to be 44 VHN. Upon increasing B_4C content up to 30 wt. % in the composite, the microhardness value increased to 75.5 VHN. However, when the B_4C content in the composite increased to 50 wt. %, the microhardness value decreased to 36.5 VHN. Similar kind of work was reported in [34].

Table 2. Microhardness values of pure Al and Al/B_4C composite samples

Sample	Microhardness, VHN	Method for preparation of composite	Reference
Pure Al	45.00 ± 5.00	powder metallurgy route	this work
Al/B_4C (0.5 wt. %) composite	75.00 ± 7.00	powder metallurgy route	this work
Al/B_4C (1 wt. %) composite	112.00 ± 8.00	powder metallurgy route	this work
Pure Al	72.00	stir casting technique	[27]
Al/6 wt. % B_4C	93.00	stir casting technique	[27]
Pure Al	24.00	powder metallurgy route	[13]
Al/12 vol. % B_4C	50.00	powder metallurgy route	[13]
Al/4 % B_4C	~ 33.00	stir casting technique	[31]
Al/12 % B_4C	~ 77.00	stir casting technique	[31]
Pure Al	55.62	stir casting technique	[32]
Al/10 wt. % B_4C	125.20	stir casting technique	[32]
Al/5 wt. % B_4C	44.00	powder metallurgy route	[33]
Al/30 wt. % B_4C	75.50	powder metallurgy route	[33]
Al/50 wt. % B_4C	36.50	powder metallurgy route	[33]

Generally, the literature suggests that achieving higher hardness in aluminum necessitates a considerable addition of boron carbide, which may compromise the ductility of the aluminum matrix and potentially render the process and product commercially unviable. In light of the aforementioned context, we developed a nearly uniform powder composite of Al/B_4C utilizing a specially designed planetary ball milling technique. By employing an appropriate powder metallurgy approach, we established an optimized process for the Al/B_4C composite, incorporating a minimal quantity of B_4C, specifically up to 1 wt. % in Al, to enhance the composite's properties, which was the primary aim of this study, and we successfully accomplished this goal. Our findings revealed a significant increase in hardness for the Al/B_4C composite with just 1 wt. % B_4C

reinforcement in Al, achieving a 148 % increase in microhardness compared to pure Al, all while utilizing a relatively low sintering temperature, thereby ensuring reduced energy consumption. It is widely recognized that the introduction of a ceramic phase into a metal can adversely affect its ductility. Consequently, we endeavored to create an Al/B_4C composite by incorporating a small amount (0.5 and 1 wt. %) of the ceramic phase (B_4C) to preserve the desired properties, with the expectation that the results of this research will facilitate various industrial applications of aluminum.

Conclusions

The study describes the successful synthesis of Al/B_4C composites using a powder metallurgy route. The key findings and implications are as follows:

1. The planetary ball milling process, conducted in an argon atmosphere for 1–4 h, led to a significant reduction in particle size. This nano-scale reduction is important as it can enhance the properties of the resulting composite materials. Planetary ball milling significantly reduced the particle size of the composite powders, with pure Al and Al/B_4C (0.5 and 1 wt. %) mixtures achieving nano-level particle sizes from their initial micron size. The particle sizes after 4 h of milling were measured as 65 nm for pure Al, 54 nm for Al/B_4C (0.5 wt. %), and 51 nm for Al/B_4C (1 wt. %). XRD analysis revealed no significant change in particle size post-consolidation.
2. The powder mixtures were cold compacted at 200 MPa and sintered at 550 °C for 3 h. XRD and EDS confirmed the formation of the Al/B_4C composites. The presence of B_4C, especially at 1 wt. %, reduced the intensity of the Al peaks in the XRD spectrum, suggesting strong interaction between the aluminum and boron carbide. The microstructure, as observed in FESEM images, showed a highly dense structure, critical for achieving desirable mechanical properties.
3. The hardness measurements revealed that the Al/1 wt. % B_4C composite exhibited a microhardness value of 112 ± 8 VHN, which is 148 % higher than that of pure Al. This enhancement in hardness was attributed to the reinforcement of B_4C, which notably improved the microstructure and properties of the Al matrix.
4. The addition of just 1 wt. % B_4C provided significant improvements in hardness and microstructure without any microstructural defects. This makes the Al/B_4C composite promising for various industrial applications, particularly in the aerospace sector, where material performance is critical.

Novelty and practical implications: the study's novelty lies in achieving a substantial increase in microhardness and overall structural properties with only a small amount of B_4C (1 wt. %). This approach could offer a cost-effective and commercially viable method for producing Al-based composites with significantly enhanced performance, particularly for demanding applications in sectors like automobile, aerospace, marine, etc.

CRediT authorship contribution statement

Nibedita Mohanty: investigation, data curation, writing – original draft, writing – review & editing; **Tapan Kumar Patnaik**: conceptualization, data curation, writing – review & editing, supervision; **Tapan Dash**: conceptualization, investigation, data

curation, writing – review & editing, supervision; **Shubhra Bajpai**: conceptualization; data curation; **Surendra Kumar Biswal**: conceptualization; supervision.

Conflict of interest

The authors declare that they have no conflict of interest.

References

1. Dilşad A G, Ceren B, Merve H. A review on processing, mechanical and wear properties of Al matrix composites reinforced with Al_2O_3, SiC, B_4C and MgO by powder metallurgy method. *Journal of Materials Research and Technology.* 2024;31: 1132–1150.
2. Palei BB, Dash T, Biswa SK. Graphene reinforced aluminum nanocomposites: synthesis, characterization and properties. *Journal of Materials Science.* 2022;57: 8544–8556.
3. Tamilanban T, Ravikumar T S. Influence of stirring speed on stir casting of SiC reinforced Al Mg Cu composite. *Materials Today: Proceedings.* 2021;45: 5899–5902.
4. Kumar P, Kumar D, Kaur K, Chalisgaonkar R, Singh S.S, Gupta M. Investigation of aluminum metal matrix composite fabrication processes: a comparative review. *Materials Physics and Mechanics.* 2024;52(6): 154–170.
5. Jargalsaikhan B, Bor A, Lee J, Choi H. Al/CNT nanocomposite fabrication on the different property of raw material using a planetary ball mill. *Advanced Powder Technology.* 2020;31(5): 1957–1962.
6. Kim D, Hirayama Y, Liu Z, Takagi K, Kobashi M. Fabrication of Al-CNT composite with high hardness and electrical conductivity by controlling Al_4C_3 formation. *Journal of Alloys and Compounds.* 2023;942: 169102.
7. Das D K, Mishra P C, Singh S, Thakur R K. Properties of ceramic-reinforced aluminium matrix composites - a review. *International Journal of Mechanical and Materials Engineering.* 2014;9: 6.
8. Kar A, Sharma A, Kumar S. A critical review on recent advancements in aluminium-based metal matrix composites. *Crystals.* 2024;14(5): 412.
9. Azizi Z, Rahmani K, Taheri-Behrooz F. The influence of graphene nanoplatelets addition on the electrical and mechanical properties of pure aluminum used in high-capacity conductors. *Metals.* 2022;12(11): 1883.
10. Dash T, Rout D, Palei BB. Graphene decorated aluminum nano composite with improved micro hardness and electrical conductivity. *Materials Today: Proceedings.* 2021;46: 11061–11063.
11. Kumar N, Manoj M K. Influence of B_4C on Dry Sliding Wear Behavior of B_4C/Al–Mg–Si Composites Synthesized via Powder Metallurgy Route. *Met. Mater. Int.* 2021;27: 4120–4131.
12. Sambathkumar M, Gukendran R, Mohanraj T, Karupannasamy D K, Natarajan N, Christopher D. A systematic review on the mechanical, tribological, and corrosion properties of Al 7075 metal matrix composites fabricated through stir casting process. To be published in *Advances in Materials Science and Engineering*. [Preprint] 2023. Available from: doi.org/10.1155/2023/5442809.
13. Kumar J, Singh D, Kalsi NS, Sharma S, Mia M, Singh J, Rahman MA, Khan AM, Rao KV. Investigation on the mechanical, tribological, morphological and machinability behavior of stir-casted Al/SiC/Mo reinforced MMCs. *Journal of Materials Research and Technology.* 2021;12: 930–946.
14. Aravind Senan VR, Anandakrishnan G, Rahul SR, Reghunath N, Shankar K V. An investigation on the impact of SiC/B_4C on the mechanical properties of Al-6.6Si-0.4Mg alloy. *Materials Today: Proceedings.* 2019;26: 649–653.
15. Sharma VK, Kumar V, Joshi RS, Sharma D. Experimental analysis and characterization of SiC and RE oxides reinforced Al-6063 alloy based hybrid composites. *Int J Adv Manuf Technol.* 2020;108: 1173–1187.
16. Luo J, Liu S, Paidar M, Vignesh RV, Mehrez S. Enhanced mechanical and tribological properties of AA6061/CeO2 composite fabricated by friction stir processing. *Materials Letters.* 2022;318: 132210.
17. Ravindra M R, Dilip Kumar K, Sailender M, Prasad G P, Nagaraj N, Ramulu P J. Effect of boron carbide particles addition on the mechanical and wear behavior of aluminium alloy composites. To be published in *Advances in Materials Science and Engineering.* [Preprint] 2023. Available from: doi.org/10.1155/2023/2386558.
18. Sharma D K, Sharma M, Upadhyay G. Boron Carbide (B_4C) reinforced aluminum matrix composites (AMCs). *International Journal of Innovative Technology and Exploring Engineering.* 2019;9: 2194–2203.
19. Kumar D, Kumar D, Tigga A. Processing of aluminium/boron carbide composites and functionally graded materials: A literature review. *SAE International Journal of Materials and Manufacturing.* 2022;15(2): 93–109.
20. Kumar D. Qualitative and quantitative interdependence of physical and mechanical properties of stir-

casted hybrid aluminum composites. *Materials Physics and Mechanics.* 2023;51(6): 14–23.
21. Prakash C, Singh S, Sharma S, Garg H, Singh J, Kumar H, Singh H. Fabrication of aluminium carbon nano tube silicon carbide particles based hybrid nano-composite by spark plasma sintering. *Materials Today: Proceedings.* 2020;21: 1637–1642.
22. Kumar D, Singh S. Enhancing friction and wear performance in hybrid aluminum composites through grey relational analysis. *Research on Engineering Structures and Materials.* 2024;10(3): 943-956.
23. Khan AH, Shah SAA, Umar F, Noor U, Gul RM, Giasin K, Aamir M. Investigating the microstructural and mechanical properties of novel ternary reinforced AA7075 hybrid metal matrix composite. *Materials.* 2022;15(15): 5303.
24. Zhang L, Shi J, Shen C, Zhou X, Peng S, Long X. B_4C-Al composites fabricated by the powder metallurgy process. *Applied Sciences.* 2017;7(10): 1009.
25. Hasan L K, Jiaad S M, Salman K D, Al-Maliki W A K, Alobaid F, Epple B. Wear characteristics of (Al/B_4C and Al/TiC) nanocomposites synthesized via powder metallurgy method. *Applied Sciences.* 2023;13(23): 12939.
26. Ghayebloo M, Mostaedi M T and Rad H F. A review of recent studies of fabrication of Al–B_4C composite sheets used in nuclear metal casks. *Transactions of the Indian Institute of Metals.* 2022;75: 2477–2490.
27. Kumar BNA, Ahamad A, Reddappa HN. Impact of B_4C reinforcement on tensile and hardness properties of Al-B_4C metal matrix composites. *Materials Today: Proceedings.* 2022;52: 2136–2142.
28. Brillon A, Garcia J, Riallant F, Garnier C, Joulain A, Lu Y, Silvain JF. Characterization of Al/B_4C composite materials fabricated by powder metallurgy process technique for nuclear applications. *Journal of Nuclear Materials.* 2022;565: 153724.
29. Chandrasekhar GL, Vijayakumar Y, Nagaral M, Rajesh A, Manjunath K, Kaviti RVP, Auradi V. Synthesis and tensile behavior of Al7475-nano B_4C particles reinforced composites at elevated temperatures. *Materials Physics and Mechanics.* 2024;52(3): 44–57.
30. Kawsar M, Hossain MS, Bahadur NM, Ahmed S. Synthesis of nano-crystallite hydroxyapatites in different media and a comparative study for estimation of crystallite size using Scherrer method, Halder-Wagner method size-strain plot, and Williamson-Hall model. *Heliyon.* 2024;10(3): e25347.
31. Nirala A, Soren S, Kumar N, Kaushal DR. A comprehensive review on mechanical properties of Al-B_4C stir casting fabricated composite. *Materials Today: Proceedings.* 2020;21: 1432–1435.
32. Afrid MA, Divakar MH. A Study on Effect of Stirring Speed During Fabrication of Aluminium Alloy Metal Matrix Composite. *International Research Journal of Modernization in Engineering Technology and Science.* 2022;4: 1870–1878.
33. Gaylan Y, Avar B, Panigrahi M, Aygün B, Karabulut A, Effect of the B_4C content on microstructure, microhardness, corrosion, and neutron shielding properties of Al–B_4C composites. *Ceramics International.* 2023;49(3): 5479–5488.
34. Chen H S, Wang W X, Li Y L, Zhou J, Nie H H, Wu Q C, The design, microstructure and mechanical properties of B_4C/6061Al neutron absorber composites fabricated by SPS. *Materials & Design.* 2016;94: 360–367.

MATERIALS PHYSICS AND MECHANICS RESEARCH ARTICLE

Submitted: November 16, 2025 **Revised: January 20, 2026** **Accepted: March 12, 2026**

Identification of the variable characteristics of a functionally graded elastic pipe with voids

S.A. Nesterov ✉

Vladikavkaz Scientific Center of the Russian Academy of Sciences, North Ossetia-Alania, Russia

✉ 1079@list.ru

ABSTRACT

Using the Cowin-Nunziato model, a coefficient inverse problem for inhomogeneous poroelastic bodies is formulated, and operator equations of the 1st kind for its solution are derived. As an example, an inverse problem for a functionally graded elastic pipe with voids is considered using additional information measured in the domain of transient loading. To solve the direct transient problem, a combined method is used: transition to the Laplace transform space, followed by solution of the boundary value problem using the shooting method and inversion using an expansion in shifted Legendre polynomials. The solution to the direct problem was verified by comparing it with the solution obtained in the finite element package FlexPDE for a homogeneous pipe. The influence of the heterogeneity laws of the Lamé moduli, coupling modulus, pore diffusion modulus, density, and pore stiffness modulus on the radial displacement was investigated. For reconstruction of physical and mechanical characteristics the iteration approach is applied. Two methods discretization of operator equations (a collocation method and a projection method) are proposed. The initial approximation is defined among the constants as the average of the maximum and minimum values of the material properties. Refinement of physical and mechanical characteristics in projection method was carried out in stages: (1) among constants; (2) linear functions; (3) quadratic functions. Computational experiments were conducted to reconstruct variable properties both at internal points of the pipe and in the class of power functions. A comparative analysis of the effectiveness of the proposed discretization schemes is performed.

KEYWORDS

elastic pipe with voids • Cowin-Nunziato theory • functionally graded material • identification variable physical and mechanical properties • integral equation 1st kind • iterative approach

Citation: Nesterov SA. Identification of the variable characteristics of a functionally graded elastic pipe with voids. *Materials Physics and Mechanics*. 2026;54(2): 41–56.
http://dx.doi.org/10.18149/MPM.5422026_4

Introduction

Functionally graded porous materials (FGPM) represent a new class of composites in which the volume fraction of pores and mechanical properties vary smoothly in space [1–3]. Due to this, an optimal combination of lightness, strength, and the ability to withstand extreme thermal and mechanical loads is achieved. The development of additive technologies, in particular 3D printing, has opened new prospects for manufacturing products from FGPM with complex internal structures [2,4]. Cylindrical bodies made of FGPM are widely used in various engineering fields: oil and gas, chemical, aerospace industries, power engineering, and biomedicine.

However, the widespread adoption of such materials is hindered by the lack of reliable non-destructive testing methods to verify the compliance of the actual property distribution with the design one. The problem is exacerbated by the fact that

Publisher: Peter the Great St. Petersburg Polytechnic University

the production of FGPM faces a number of technological difficulties, such as instability of the interfacial bond due to differences in the physical and chemical properties of the components. Therefore, an important task is to control the inhomogeneity laws, for example, using non-destructive technologies and solving coefficient inverse problems (CIP) for elastic bodies with pores.

Based on the micro-dilatational Cowin-Nunziato model [5], problems of deformation of cylindrical bodies, including homogeneous [6–8], composite [9,10], and inhomogeneous bodies [11–13], have been investigated. The Cowin-Nunziato theory contains a number of non-classical parameters, whose values are not available in reference books, which limits the practical use of this theory. In [14–17], theoretical approaches for determining non-classical parameters using various concepts are proposed. In [14,15], the concept of "penalized micro-dilatation" was developed, establishing a connection between the microstructural characteristics of a porous material and the macroscopic parameters of the model. By homogenizing a representative volume with explicit pore modeling, analytical expressions for non-classical moduli in terms of pore size and porosity were obtained. The main limitation of this approach is the idealization of the microstructure (assumption of spherical isolated pores), which limits its applicability for real materials with complex pore morphology. In [16], combinations of parameters that can be uniquely determined from various types of experiments were identified, and corresponding experimental schemes were proposed. However, the work is limited to static problems for homogeneous materials and does not account for the influence of measurement errors. In [17], a methodology was developed for determining porosity parameters based on solving the contact problem of indenting a rigid indenter into a porous half-space. The obtained analytical solution allows determining non-classical moduli from measured contact characteristics. The advantage of the method is its locality and the possibility of using standard equipment, but it determines properties only of the near-surface layer and is not applicable for dynamic problems.

The approaches [14–17] for finding the non-classical parameters of the Cowin-Nunziato theory are limited to homogeneous materials and do not account for functional grading, which is critically important for modern composites obtained by additive technologies. This work fills this gap. In comparison with previous works of the Vatulyan scientific school [18–23], where inverse problems of thermoelasticity and Biot poroelasticity are studied, the proposed approach for the first time allows identifying non-classical parameters of materials with microstructure based on two methods for solving operator equations: the collocation method and the projection method. Unlike works [24–29], which use resource-intensive gradient methods or heuristic optimization algorithms, the proposed approach reduces the inverse problem to solving linear integral equations at each iteration. Furthermore, the problem of local minima is absent due to the use of Newton-Kantorovich linearization.

The aim of the work is the development of an iterative method for solving the coefficient inverse problem for a functionally graded porous pipe within the framework of the Cowin-Nunziato model, allowing the determination of the variation laws of physical and mechanical characteristics from additional information on transient displacement fields on the outer surface.

The main results obtained include: (1) operator equations for the Cowin-Nunziato model relating corrections to the sought functions to the displacement field; (2) an iterative scheme for reconstructing the properties of a poroelastic pipe using two discretization methods (collocation and projection); (3) identification of different sensitivity of displacements to different material characteristics, which explains the accuracy of their reconstruction; (4) consideration of thermodynamic constraints ensuring the positive definiteness of the elastic potential. The developed method for solving the coefficient inverse problem can be used for non-destructive testing of cylindrical products made of FGPM obtained by 3D printing methods.

Problem of vibrations of inhomogeneous poroelastic bodies

Let us consider the transient vibrations of an inhomogeneous elastic body with voids. To describe the mechanical behavior of such an object, we will use the Cowin-Nunziato theory [5]. It is important to emphasize that the Cowin-Nunziato theory is an averaged continuum theory in which the real discrete structure of the porous material is replaced by a continuous medium with an additional degree of freedom – micro-dilation ψ, interpreted as the change in the volume fraction of the material matrix at the considered point of the medium. On the other hand, the micro-dilation function is defined as $\psi = -\Delta n$, where $\Delta n = n - n_0$ is the increment of porosity from its value in the undeformed state n_0. The applicability range of the linear Cowin-Nunziato model is limited by the following conditions: (1) pores are small, numerous, and uniformly distributed; (2) initial porosity is small; (3) deformations and porosity increments are small.

For a linear anisotropic elastic material with voids, the constitutive relations have the form [5]: $\sigma_{ij} = c_{ijkl}\varepsilon_{kl} + D_{ijk}\psi_{,k} + \beta_{ij}\psi$ are the components of the classical stress tensor, $h_i = a_{ij}\psi_{,j} + D_{ijk}\varepsilon_{jk}$ are the components of the non-classical stress vector, and $g = -\left(\xi\psi + \omega\frac{\partial\psi}{\partial t} + \beta_{ij}\varepsilon_{ij}\right)$ is the internal volume force. Here, $\varepsilon_{ij} = 0.5(u_{i,j} + u_{j,i})$ are the components of the strain tensor, u_i are the components of the displacement vector, c_{ijkl} are the components of the elastic moduli tensor, β_{ij} and D_{ijk} are the components of the second- and third-order coupling tensor, respectively, a_{ij} are the components of the pore diffusion tensor, ρ is the density, ξ is the pore stiffness modulus, ω is the micro-viscoelastic modulus.

The non-classical parameters used in the Cowin-Nunziato model have a clear physical meaning. The interpretation of these parameters depends significantly on the symmetry class of the material. In the general anisotropic case, which is described by the tensors in constitutive relations, the coupling between the skeleton deformation and the porosity change is characterized by a second-rank tensor β_{ij}. This means that the change in pore volume may depend on the direction of the applied macroscopic strain: for example, stretching in one direction might increase porosity, while stretching in another direction could decrease it. Similarly, the pore diffusion modulus, which governs the gradient energy associated with porosity changes, becomes a second-rank tensor a_{ij} in anisotropic media. This implies that the "influence zone" of a local porosity disturbance is directionally dependent, with pores interacting more strongly along certain crystallographic or structural directions than others. The pore stiffness ξ, however,

remains a scalar even in anisotropic materials, as it represents the isotropic resistance to a purely volumetric change in porosity at the microscale, independent of direction. The micro-viscoelastic modulus ω also retains its scalar nature, characterizing the intrinsic dissipation associated with the rate of porosity change. The change in pore volume is not a perfectly elastic process. Part of the energy is dissipated as heat due to internal friction during pore wall movement.

In the specific case of an isotropic material, which is the focus of the present study of a functionally graded pipe, these tensors simplify dramatically. The coupling tensor reduces to a scalar β multiplied by the Kronecker delta δ_{ij}, indicating that volumetric strain and porosity change are directly and proportionally coupled, with no directional preference. The pore diffusion tensor similarly simplifies to a scalar a times the identity, meaning that porosity disturbances diffuse equally in all directions. Thus, for the isotropic pipe, the physical meaning of the moduli becomes particularly clear: the coupling modulus β describes the mutual influence of skeleton strains and porosity changes; the pore diffusion modulus a characterizes the range of elastic interaction between pores; and the micro-viscoelastic modulus ω characterizes dissipative losses associated with changes in porosity over time.

Let a poroelastic body have a volume V and a piecewise smooth boundary $S_u \cup S_\sigma = S$, $S_\psi \cup S_h = S$, where S_u, S_ψ, S_σ, S_h are the parts of the body's surface on which the boundary conditions for the displacement, the porosity function, and classical and nonclassical stresses, respectively, are specified. The formulation of the dynamic poroelasticity problem within the Cowin-Nunziato model, in the absence of external body forces, is as follows [5]:

$$\sigma_{ij,j} - \rho \frac{\partial^2 u_i}{\partial t^2} = 0,\ h_{i,i} + g - \chi \frac{\partial^2 \psi}{\partial t^2} = 0,$$
$$\sigma_{ij} n_j|_{S_\sigma} = w_i(t),\ h_i n_i|_{S_h} = 0, \quad (1)$$
$$u_i|_{S_u} = u_i^0,\ \psi|_{S_\psi} = \psi_0,\ u_i(x,0) = \frac{\partial u_i}{\partial t}(x,0) = \psi(x,0) = \frac{\partial \psi}{\partial t}(x,0) = 0.$$

Here χ is the equilibrated inertia modulus, $w_i(t)$ are components of the load vector. The equilibrated inertia modulus χ characterizes the inertial properties of the microstructure is a measure of how quickly porosity can change in dynamic processes. Under impact loading, pores cannot instantly change their volume, so the equilibrated inertia parameter determines the time delay of this process. The direct problem consists of computing the functions u_i and ψ from Eq. (1) given known characteristics a_{ij}, β_{ij}, D_{ijk}, c_{ijkl}, ρ, ξ, ω, χ.

Operator equations for solving the inverse problem

We assume the moduli ω, χ are constant. The inverse problem consists of finding the functions q (a_{ij}, β_{ij}, D_{ijk}, c_{ijkl}, ρ, ξ) from Eq. (1) using additional information, measured on S_σ:

$$u_i|_{S_\sigma} = f_i(x,t),\ t \in [c_1, c_2],\ i = 1..3. \quad (2)$$

The inverse Eqs. (1) are (2) is a nonlinear problem, since the sought coefficients appear in the differential operators. To solve it, an iterative approach, analogous to the Newton-Kantorovich method, is applied. Linearization is carried out using the perturbation method within the framework of the weak formulation of the problem. To solve the CIP (1)–(2) we obtain an operator equation that establishes a relationship between the functions q and the boundary fields $u_i|_{S_\sigma}$.

First, we obtain the weak formulation of problem (1). Substituting the expanded expressions for the σ_{ij}, h_i, g, into problem (1), and applying the Laplace transform, setting $\tilde{u}_i^0 = 0, \tilde{\psi}_0 = 0$, we obtain:

$$\begin{gathered}\left(c_{ijkl}\tilde{u}_{k,l} + \beta_{ij}\tilde{\psi} + D_{ijk}\tilde{\psi}_{,k}\right)_{,j} - p^2\bar{\rho}\tilde{u}_i = 0,\\ \left(a_{ij}\tilde{\psi}_{,i} + D_{ijk}\tilde{u}_{i,k}\right)_{j} - (\xi + p\omega + p^2\chi)\tilde{\psi} - \beta_{ij}\tilde{u}_{i,j} = 0,\\ \tilde{\sigma}_{ij}n_j|_{S_\sigma} = \widetilde{w}_i, \quad \tilde{h}_j n_j|_{S_h} = 0, \tilde{u}_i|_{S_u} = 0, \tilde{\psi}|_{S_\psi} = 0.\end{gathered} \tag{3}$$

We multiply first equations (3) by $\tilde{v}_i$, second equations (3) by $\kappa_1\tilde{\vartheta}$. Here, $\tilde{v}_i$ and $\tilde{\vartheta}$ are test functions, satisfying the principal boundary conditions $\tilde{v}_i|_{S_u} = 0, \quad \tilde{\vartheta}|_{S_\psi} = 0$. We integrate the resulting products over V. Next, we multiply the boundary condition on the part S_σ by $\kappa_2\tilde{v}_i$ and integrate over S_σ. Summing all the obtained integrals into a single expression and equating it to zero, we get:

$$\begin{gathered}\int_V \left(c_{ijkl}\tilde{u}_{k,l} + \beta_{ij}\tilde{\psi} + D_{ijk}\tilde{\psi}_{,k}\right)_{,j}\tilde{v}_i dV + \kappa_1\int_V\left(a_{ij}\tilde{\psi}_{,i} + D_{ijk}\tilde{u}_{i,k}\right)_{j}\tilde{\vartheta}dV\ p^2\int_V \rho\tilde{u}_i\,\tilde{v}_i dV -\\ -\kappa_1\int_V(\xi + p\omega + p^2\chi)\tilde{\psi}\,\tilde{\vartheta}dV - \kappa_1\int_V \beta_{ij}\tilde{u}_{i,j}\,\tilde{\vartheta}dV +\\ +\kappa_2\int_{S_\sigma}(\tilde{\sigma}_{ij}n_j - \widetilde{w}_i)\tilde{v}_i dS = 0.\end{gathered} \tag{4}$$

Next, applying the Gauss-Ostrogradsky theorem to the first two integrals in Eq. (4), we obtain:

$$\begin{gathered}-\int_V c_{ijkl}\,\tilde{u}_{i,j}\tilde{v}_{k,l}dV - p^2\int_V \rho\tilde{u}_i\,\tilde{v}_i dV - \int_V \beta_{ij}\left(\tilde{\psi}\tilde{v}_{i,j} + \kappa_1\tilde{\vartheta}\tilde{u}_{i,j}\right)dV -\\ \int_V D_{ijk}\left(\tilde{\psi}_{,k}\tilde{v}_{i,j} + \kappa_1\tilde{\vartheta}_{,k}\tilde{u}_{i,j}\right)dV - \kappa_1\int_V \xi\tilde{\psi}\tilde{\theta}\,dV -\\ -\kappa_1(\omega + \chi p)p\int_V \tilde{\psi}\tilde{\theta}\,dV - \kappa_1\int_V \beta_{ij}\tilde{u}_{i,j}\,\tilde{\vartheta}dV + \int_{S_\sigma}\left((1+\kappa_2)\tilde{\sigma}_{ij}n_j - \kappa_2\widetilde{w}_i\right)\tilde{v}_i dS = 0.\end{gathered} \tag{5}$$

Setting in Eq. (5) $\kappa_1 = 1, \kappa_2 = -1$, we obtain the weak formulation of problem (1):

$$-\int_V \xi\tilde{\psi}\tilde{\theta}\,dV - -\int_V D_{ijk}\left(\tilde{\psi}_{,k}\tilde{v}_{i,j} + \tilde{\vartheta}_{,k}\tilde{u}_{i,j}\right)dV - (\omega + \chi p)p\int_V \tilde{\psi}\tilde{\theta}\,dV + \int_{S_\sigma}\widetilde{w}_i\,\tilde{v}_i dS = 0. \tag{6}$$

Two states of the poroelastic body are considered within the same weak formulation Eq. (6). The first state is the true state with exact, but unknown characteristics: coefficients $c_{ijkl}^{true}, \xi^{true}, \rho^{true}, \xi^{true}, a_{ij}^{true}, \beta_{ij}^{true}, D_{ijk}^{true}, \omega^{true}, \chi^{true}$ and fields $\tilde{u}_i^{true}, \tilde{\psi}^{true}, \tilde{v}_i^{true}$:

$$\begin{gathered}-\int_V c_{ijkl}^{true}\,\tilde{u}_{i,j}^{true}\tilde{v}_{k,l}^{true}dV - p^2\int_V \rho^{true}\tilde{u}_i^{true}\,\tilde{v}_i^{true}dV -\\ \int_V \beta_{ij}^{true}\left(\tilde{\psi}^{true}\tilde{v}_{i,j}^{true} + \tilde{\vartheta}^{true}\tilde{u}_{i,j}^{true}\right)dV - \int_V a_{ij}^{true}\,\tilde{\psi}_{,i}^{true}\tilde{\theta}_{,j}^{true}dV -\\ -\int_V \xi^{true}\tilde{\psi}^{true}\tilde{\theta}^{true}\,dV - \int_V D_{ijk}^{true}\left(\tilde{\psi}_{,k}^{true}\tilde{v}_{i,j}^{true} + \tilde{\vartheta}_{,k}^{true}\tilde{u}_{i,j}^{true}\right)dV -\\ -(\omega^{true} + \chi^{true}p)p\int_V \tilde{\psi}^{true}\tilde{\theta}^{true}\,dV +\\ +\int_{S_\sigma}\widetilde{w}_i\,\tilde{v}_i^{true}dS = 0.\end{gathered} \tag{7}$$

The second state is the approximate state at the $(n-1)$-th iteration, which is characterized by the coefficients known at this step $c_{ijkl}^{(n-1)}, \xi^{(n-1)}, \rho^{(n-1)}, a_{ij}^{(n-1)}, \beta_{ij}^{(n-1)}, D_{ijk}^{(n-1)}, \omega^{(n-1)}, \chi^{(n-1)}$ and the corresponding fields $\tilde{u}_i^{(n-1)}, \tilde{\psi}^{(n-1)}\ \tilde{v}_i^{(n-1)}$:

$$\begin{gathered}-\int_V c_{ijkl}^{(n-1)}\,\tilde{u}_{i,j}^{(n-1)}\tilde{v}_{k,l}^{(n-1)}dV - p^2\int_V \rho^{(n-1)}\tilde{u}_i^{(n-1)}\,\tilde{v}_i^{(n-1)}dV -\\ -\int_V \beta_{ij}^{(n-1)}\left(\tilde{\psi}^{(n-1)}\tilde{v}_{i,j}^{(n-1)} + +\tilde{\vartheta}^{(n-1)}\tilde{u}_{i,j}^{(n-1)}\right)dV -\\ -\int_V a_{ij}^{(n-1)}\,\tilde{\psi}_{,i}^{(n-1)}\tilde{\theta}_{,j}^{(n-1)}dV - \int_V \xi^{(n-1)}\tilde{\psi}^{(n-1)}\tilde{\theta}^{(n-1)}\,dV -\\ -\int_V D_{ijk}^{(n-1)}\left(\tilde{\psi}_{,k}^{(n-1)}\tilde{v}_{i,j}^{(n-1)} + \tilde{\vartheta}_{,k}^{(n-1)}\tilde{u}_{i,j}^{(n-1)}\right)dV -\\ -\left(\omega^{(n-1)} + \chi^{(n-1)}p\right)p\int_V \tilde{\psi}^{(n-1)}\tilde{\theta}^{(n-1)}\,dV + \int_{S_\sigma}\widetilde{w}_i\,\tilde{v}_i^{(n-1)}dS = 0.\end{gathered} \tag{8}$$

Suppose that the true values of the coefficients and fields can be represented as the sum of approximate values and small corrections that need to be found at the n-th step. Let

us write this for the elastic moduli and displacements: $c_{ijkl}^{true} \approx c_{ijkl}^{(n)} = c_{ijkl}^{(n-1)} + \delta c_{ijkl}^{(n-1)}$, $\tilde{u}_i^{true} \approx \tilde{u}_i^{(n)} = \tilde{u}_i^{(n-1)} + \delta \tilde{u}_i^{(n-1)}$. The remaining moduli and fields are expanded similarly. Here, the superscript $(n-1)$ corresponds to quantities obtained at the previous iteration, and the index n – to quantities obtained at the current iteration.

Subtract relation Eq. (8) from Eq. (7), assuming $\tilde{v}_i^{true} = \tilde{u}_i^{(n-1)}$, $\tilde{v}_i^{(n-1)} = \tilde{u}_i^{(n)}$. The resulting difference contains products of coefficients and fields, for example, $c_{ijkl}^{(n-1)}\tilde{u}_{i,j}^{(n-1)}\tilde{u}_{k,l}^{(n-1)} + c_{ijkl}^{(n-1)}\delta\tilde{u}_{i,j}^{(n-1)}\tilde{u}_{k,l}^{(n-1)} + \delta c_{ijkl}^{(n-1)}\tilde{u}_{i,j}^{(n-1)}\tilde{u}_{k,l}^{(n-1)} + \delta c_{ijkl}^{(n-1)}\delta\tilde{u}_{i,j}^{(n-1)}\tilde{u}_{k,l}^{(n-1)} - -c_{ijkl}^{(n-1)}\tilde{u}_{i,j}^{(n-1)}\tilde{u}_{k,l}^{(n-1)} - c_{ijkl}^{(n-1)}\tilde{u}_{i,j}^{(n-1)}\delta\tilde{u}_{k,l}^{(n-1)}$. Linearization consists of discarding nonlinear second-order small terms in the form of products of corrections $\delta c_{ijkl}^{(n-1)}\delta\tilde{u}_{i,j}^{(n-1)}\tilde{u}_{k,l}^{(n-1)}$. After canceling terms and linearization, only the expression $\delta c_{ijkl}^{(n-1)}\tilde{u}_{i,j}^{(n-1)}\tilde{u}_{k,l}^{(n-1)}$ remains. Performing similar actions for the remaining products, we obtain a linear Fredholm integral equation of the 1st kind, relating the unknown coefficient corrections to the residual of the boundary data:

$$\int_V \delta c_{ijkl}^{(n-1)}\,\tilde{u}_{i,j}^{(n-1)}\tilde{u}_{k,l}^{(n-1)}dV + p^2\int_V \delta\rho^{(n-1)}\left(\tilde{u}_i^{(n-1)}\right)^2 dV + \int_V \delta\beta_{ij}^{(n-1)}\tilde{\psi}^{(n-1)}\tilde{u}_{i,j}^{(n-1)}\,dV +$$
$$+\int_V \delta a_{ij}^{(n-1)}\,\tilde{\psi}_{,i}^{(n-1)}\tilde{\psi}_{,j}^{(n-1)}dV + \int_V \delta D_{ijk}^{(n-1)}\tilde{\psi}_{,i}^{(n-1)}\tilde{u}_{j,k}^{(n-1)}\,dV + \int_V \delta\xi^{(n-1)}\left(\tilde{\psi}^{(n-1)}\right)^2 dV = \quad (9)$$
$$= -\int_{S_\sigma}\tilde{w}_i\left(\tilde{f}_i - \tilde{u}_i^{(n-1)}\right)dS,\ p \in 0,\infty).$$

If only one of the physical and mechanical characteristics is unknown, then by setting in Eq. (9) the corrections of all characteristics except the sought one to zero, we obtain the following Fredholm integral equations of the 1st kind:

$$\begin{aligned}
&\int_V \delta c_{ijkl}^{(n-1)}\,\tilde{u}_{i,j}^{(n-1)}\tilde{u}_{k,l}^{(n-1)}dV = -\int_{S_\sigma}\tilde{w}_i\left(\tilde{f}_i - \tilde{u}_i^{(n-1)}\right)dS, p \in 0,\infty),\\
&p^2\int_V \delta\rho^{(n-1)}\left(\tilde{u}_i^{(n-1)}\right)^2 dV = -\int_{S_\sigma}\tilde{w}_i\left(\tilde{f}_i - \tilde{u}_i^{(n-1)}\right)dS, p \in 0,\infty),\\
&\int_V \delta\beta_{ij}^{(n-1)}\tilde{u}_{i,j}^{(n-1)}\,\tilde{\psi}^{(n-1)}dV = -\int_{S_\sigma}\tilde{w}_i\left(\tilde{f}_i - \tilde{u}_i^{(n-1)}\right)dS, p \in 0,\infty),\\
&\int_V \delta D_{ijk}^{(n-1)}\tilde{u}_{i,j}^{(n-1)}\,\tilde{\psi}_{,k}^{(n-1)}dV = -\int_{S_\sigma}\tilde{w}_i\left(\tilde{f}_i - \tilde{u}_i^{(n-1)}\right)dS, p \in 0,\infty),\\
&\int_V \delta a_{ij}^{(n-1)}\,\tilde{\psi}_{,i}^{(n-1)}\tilde{\psi}_{,j}^{(n-1)}dV = -\int_{S_\sigma}\tilde{w}_i\left(\tilde{f}_i - \tilde{u}_i^{(n-1)}\right)dS, p \in 0,\infty),\\
&\int_V \delta\xi^{(n-1)}\left(\tilde{\psi}^{(n-1)}\right)^2 dV = -\int_{S_\sigma}\tilde{w}_i\left(\tilde{f}_i - \tilde{u}_i^{(n-1)}\right)dS, p \in 0,\infty).
\end{aligned} \quad (10)$$

Formulation and solution of the direct problem for a pipe

As an example, we investigate a problem for an inhomogeneous isotropic elastic pipe with voids. The inner surface of the tube $r = r_1$ is free from loads, and non-stationary vibrations are caused by applying a transient loading $\sigma_{rr}(r_2,t) = -w(t)$ to its outer surface $r = r_2$. Setting in Eq. (1) $c_{ijkl} = \lambda\delta_{ij}\delta_{lk} + \mu\left(\delta_{ik}\delta_{jl} + \delta_{il}\delta_{jk}\right)$, $a_{ij} = a\delta_{ij}$, $\beta_{ij} = \beta\delta_{ij}$, $D_{ijk} = 0$ and converting to a cylindrical coordinate system, we obtain:

$$\begin{aligned}
&\frac{\partial\sigma_{rr}}{\partial r} + \frac{\sigma_{rr}-\sigma_{\varphi\varphi}}{r} - \rho\frac{\partial^2 u_r}{\partial t^2} = 0,\ r_1 \le r \le r_2,\ t \ge 0,\\
&\frac{\partial h_r}{\partial r} + \frac{h_r}{r} - \left(\xi - \omega\frac{\partial}{\partial t} + \chi\frac{\partial^2}{\partial t^2}\right)\psi - \beta\left(\frac{u_r}{r} + \frac{\partial u_r}{\partial r}\right) = 0,\ r_1 \le r \le r_2,\ t \ge 0,\\
&\sigma_{rr}(r_1,t) = h_r(r_1,t) = 0,\ \sigma_{rr}(r_2,t) = -w(t),\ \ h_r(r_2,t) = 0,\\
&u_r(r,0) = \frac{\partial u_r}{\partial t}(r,0) = \psi(r,0) = \frac{\partial\psi}{\partial t}(r,0) = 0,
\end{aligned} \quad (11)$$

where $\sigma_{rr} = (\lambda+2\mu)\frac{\partial u_r}{\partial r} + \lambda\frac{u_r}{r} + \beta\psi$, $\sigma_{\varphi\varphi} = (\lambda+2\mu)\frac{u_r}{r} + \lambda\frac{\partial u_r}{\partial r} + \beta\psi$, $h_r = a\frac{\partial\psi}{\partial r}$.

For generality, we introduce the following dimensionless parameters and functions: $\eta = \frac{r}{r_2}$ $\eta_0 = \frac{r_1}{r_2}$, $\tau = \frac{t}{t_0}$, $t_0 = \sqrt{\frac{\rho_0}{\mu_0}} r_2$, $U = \frac{u_r}{r_2}$, $\Phi = \frac{\xi_0}{\beta_0}\psi$, $H_r = \frac{h_r}{\beta_0 r_2}$, $\Omega_{ij} = \frac{\sigma_{ij}}{\mu_0}$, $W = \frac{w}{\mu_0}$, $\bar{\lambda} = \frac{\lambda}{\mu_0}$, $\bar{\mu} = \frac{\mu}{\mu_0}$, $\bar{\rho} = \frac{\rho}{\rho_0}$, $\bar{\xi} = \frac{\xi}{\xi_0}$, $\bar{\beta} = \frac{\beta}{\beta_0}$, $\bar{a} = \frac{a}{\xi_0 r_2^2}$, $\varepsilon_1 = \frac{\omega}{\xi_0 t_0}$, $\varepsilon_2 = \frac{\chi}{\xi_0 t_0^2}$, $\delta_0 = \frac{\beta_0^2}{\mu_0 \xi_0}$. Here, μ_0, ξ_0, β_0, ρ_0 are characteristic values of the corresponding physical and mechanical characteristics.

For the physical realizability of the Cowin-Nunziato model, the following conditions for positive definiteness of the elastic potential must be satisfied [5]: $\mu(r) > 0, 3\lambda(r) + 2\mu(r) > 0$, $\xi(r) > 0$, $a(r) > 0$, $\xi(r)\big(3\lambda(r) + 2\mu(r)\big) - 3\beta^2(r) > 0$ or in dimensionless form $\bar{\mu}(\eta) > 0, 3\bar{\lambda}(\eta) + 2\bar{\mu}(\eta) > 0, \bar{\xi}(\eta) > 0, \bar{a}(\eta) > 0, \bar{\xi}(\eta)\left(3\bar{\lambda}(\eta) + 2\bar{\mu}(\eta)\right) - 3\delta_0\bar{\beta}^2(\eta) > 0.$

The dimensionless formulation of problem (11) becomes:

$$\begin{aligned}
&\frac{\partial \Omega_{rr}}{\partial \eta} + \frac{\Omega_{rr} - \Omega_{\varphi\varphi}}{\eta} - \bar{\rho}\frac{\partial^2 U}{\partial \tau^2} = 0, \quad \eta_0 \le \eta \le 1, \tau \ge 0,\\
&\frac{\partial H_r}{\partial \eta} + \frac{H_r}{\eta} - \left(\bar{\xi} - \varepsilon_1\frac{\partial}{\partial \tau} + \varepsilon_2\frac{\partial^2}{\partial \tau^2}\right)\Phi - \bar{\beta}\left(\frac{U}{\eta} + \frac{\partial U}{\partial \eta}\right) = 0, \quad \eta_0 \le \eta \le 1, \tau \ge 0,\\
&\Omega_{rr}(\eta_0, \tau) = 0, \; H_r(\eta_0, \tau) = 0, \Omega_{rr}(1, \tau) = -W(\tau), \; H_r(1, \tau) = 0,\\
&U(\eta, 0) = \frac{\partial U}{\partial \tau}(\eta, 0) = \Phi(\eta, 0) = \frac{\partial \Phi}{\partial \tau}(\eta, 0) = 0.
\end{aligned} \tag{12}$$

Since problem (12) is non-stationary, to transition to ordinary differential equations, we apply the Laplace transform with respect to time to Eq. (12):

$$\begin{aligned}
&\frac{d\tilde{\Omega}_{rr}}{d\eta} + 2\bar{\mu}\left(\frac{d\tilde{U}}{d\eta} - \frac{\tilde{U}}{\eta}\right) - p^2\bar{\rho}\tilde{U} = 0, \; \eta_0 \le \eta \le 1, p \ge 0,\\
&\frac{d\tilde{H}_r}{d\eta} + \frac{\tilde{H}_r}{\eta} - \left(\bar{\xi} - \varepsilon_1 p + \varepsilon_2 p^2\right)\tilde{\Phi} - \bar{\beta}\left(\frac{\tilde{U}}{\eta} + \frac{d\tilde{U}}{d\eta}\right) = 0, \eta_0 \le \eta \le 1, p \ge 0,\\
&\tilde{\Omega}_{rr}(\eta_0, p) = 0, \; \tilde{H}_r(\eta_0, p) = 0, \; \tilde{\Omega}_{rr}(1, p) = -\tilde{W}(p), \; \tilde{H}_r(1, p) = 0.
\end{aligned} \tag{13}$$

Next, system (13), considering that, $\tilde{\Omega}_{rr} = \left(\bar{\lambda} + 2\bar{\mu}\right)\frac{d\tilde{U}}{d\eta} + \bar{\lambda}\frac{\tilde{U}}{\eta} + \delta_0\bar{\beta}\tilde{\Phi}$, $\tilde{H}_r = \bar{a}\frac{d\tilde{\Phi}}{d\eta}$, after some transformations, is reduced to a canonical system of ordinary differential equations of 1st order with variable coefficients:

$$\begin{aligned}
&\frac{d\tilde{\Phi}}{d\eta} = \frac{\tilde{H}_r}{\bar{a}},\\
&\frac{d\tilde{H}_r}{d\eta} = -\frac{\tilde{H}_r}{\eta} + \left(\bar{\xi} + p\varepsilon_1 + p^2\varepsilon_2\right)\tilde{\Phi} + \frac{\tilde{\Omega}_{rr}}{\bar{\lambda}+2\bar{\mu}} + \frac{2\bar{\mu}\tilde{U}}{(\bar{\lambda}+2\bar{\mu})\eta},\\
&\frac{d\tilde{\Omega}_{rr}}{d\eta} = -\frac{2\bar{\mu}\tilde{\Omega}_{rr}}{(\bar{\lambda}+2\bar{\mu})\eta} + \left(p^2\bar{\rho} + \frac{2\bar{\mu}}{\eta^2}\left(1 + \frac{\bar{\lambda}}{\bar{\lambda}+2\bar{\mu}}\right)\right)\tilde{U} + \frac{2\bar{\mu}\delta_0\bar{\beta}\tilde{\Phi}}{(\bar{\lambda}+2\bar{\mu})\eta},\\
&\frac{d\tilde{U}}{d\eta} = \frac{1}{\bar{\lambda}+2\bar{\mu}}\left(\tilde{\Omega}_{rr} - \frac{\bar{\lambda}}{\eta}\tilde{U} - \delta_0\bar{\beta}\tilde{\Phi}\right).
\end{aligned} \tag{14}$$

System (14) is supplemented by boundary conditions:

$$\tilde{\Omega}_{rr}(\eta_0, p) = 0, \tilde{H}_r(\eta_0, p) = 0, \tilde{\Omega}_{rr}(1, p) = -\tilde{W}(p), \tilde{H}_r(1, p) = 0. \tag{15}$$

We solve the boundary value problem in the transform domain (14) and (15) using the shooting method. For this, we consider two auxiliary Cauchy problems, consisting of the canonical system (14) and two sets of conditions: (1) $\tilde{\Phi}^I(\eta_0, p) = 1$, $\tilde{U}^I(\eta_0, p) = 0$, $\tilde{\Omega}^I_{rr}(\eta_0, p) = 0$, $\tilde{H}^I_r(\eta_0, p) = 0$; (2) $\tilde{\Phi}^{II}(\eta_0, p) = 0$, $\tilde{U}^{II}(\eta_0, p) = 1$, $\tilde{\Omega}^{II}_{rr}(\eta_0, p) = 0$, $\tilde{H}^{II}_r(\eta_0, p) = 0$.

We solve the auxiliary Cauchy problems using the Runge-Kutta method for an integer set of values of the Laplace transform parameter p. We compose the expressions: $\tilde{\Phi} = \alpha_1\tilde{\Phi}^I + \alpha_2\tilde{\Phi}^{II}$, $\tilde{U} = \alpha_1\tilde{U}^I + \alpha_2\tilde{U}^{II}$, $\tilde{\Omega}_{rr} = \alpha_1\tilde{\Omega}^I_{rr} + \alpha_2\tilde{\Omega}^{II}_{rr}$, $\tilde{H}_r = \alpha_1\tilde{H}^I_r + \alpha_2\tilde{H}^{II}_r$.

The constants α_1 and α_2 are determined from the conditions $\tilde{\Omega}_{rr}(1,p) = -\tilde{W}(p)$, $\tilde{H}_r(1,p) = 0$.

To invert the transforms $\tilde{F}$ ($\tilde{\Phi}$, $\tilde{U}$, $\tilde{\Omega}_{rr}$, $\tilde{H}_r$), we use the method of expanding the original function into a series in shifted Legendre polynomials [30]:

$$F(\tau) = \sum_{s=0}^{\infty}(2s+1)\, a_s P_s^*(e^{-\tau}). \quad (16)$$

Here, P_s^* are the shifted Legendre polynomials.

Verification of the solution obtained by the proposed method was carried out by comparison with a finite element method (FEM) in the FlexPDE 7 package for the case of a homogeneous pipe. The computational domain in the FlexPDE package in Cartesian coordinates was the cross-section of the pipe – a ring with an inner radius of 0.7 and an outer radius of 1.0. Quadratic triangular elements with six nodes and an automatic adaptive mesh refinement mechanism were used. The mesh was constructed using the parameter *ngrid = 30*, which sets the initial number of cells in each dimension. The calculation error criterion was set by the parameter *errlim = 1e-4*. The final computation time was 1 dimensionless second. The proposed method (shooting method + inversion of the Laplace transform using shifted Legendre polynomials) was implemented in the computer algebra system Maple 15. It used 30 nodes along the radius and 50 terms of the Legendre series.

Table 1 presents the values of the radial displacement of the pipe, computed on the outer surface $\eta = 1$ using the shooting method and FEM for some time points under the load $W(\tau) = H(\tau)$ ($H(\tau)$ is Heaviside function) with dimensionless parameters $\bar{a} = 0.4$, $\varepsilon_1 = \varepsilon_2 = 0.001$, $\delta_0 = 0.1$, $\bar{\rho} = 1$, $\bar{\mu} = 1$, $\bar{\lambda} = 0.8$, $\bar{\xi} = 1$, $\eta_0 = 0.7$. The relative error γ_1 was determined using the relation $\gamma_1 = \frac{|U_{FEM}(1,\tau_j) - U_{SH}(1,\tau_j)|}{U_{FEM}(1,\tau_j)} \cdot 100\%$, where $U_{FEM}(1,\tau_j)$ is the displacement computed in FlexPDE, $U_{SH}(1,\tau_j)$ is the displacement found by the proposed method at a given time points τ_j.

Table 1. Values of the radial displacement, computed on the outer surface of the pipe under the load $W(\tau) = H(\tau)$

Time points τ	FlexPDE	Proposed method			
		$s_1 = 40$	Relative error, %	$s_1 = 65$	Relative error, %
0.01	0.0058	0.0061	5.17	0.0059	1.72
0.05	0.0302	0.0312	3.31	0.0306	1.32
0.1	0.0613	0.0624	1.79	0.0619	0.98
0.5	0.4719	0.4793	1.57	0.4759	0.85
1	1.3793	1.3942	1.08	1.3866	0.53

From Table 1, it follows that the deviation error from the FEM for times $\tau \geq 0.01$ does not exceed 2 % with $s = 65$ terms of the series in expansion (16). The computation time for the direct problem using the proposed method in Maple 15 is 24 seconds, and in the FlexPDE package it is 8 sec. It should be noted that the choice of the Maple system for calculations is not driven by the pursuit of record speed for solving a single direct problem, but by the need to solve a complex inverse problem in an environment where we can fully control and adapt to the mathematical apparatus. In the inverse problem, we do not simply solve the same equation; we constantly change the material properties (the sought functions). Implementing such feedback in FlexPDE is extremely difficult, while in Maple it is a natural process.

The influence of physical and mechanical characteristics on the radial displacement was investigated. Figure 1 shows the influence of polynomial inhomogeneity laws on displacement under the load $W(\tau) = H(\tau)$ with dimensionless parameters $\eta_0 = 0.7$, $\delta_0 = 0.1$, $\varepsilon_1 = \varepsilon_2 = 0.001$, $\bar{a} = 0.2$, $\bar{\lambda} = 0.8$. Here, solid lines represent graphs for a homogeneous pipe, dots – for an inhomogeneous pipe with $\bar{\mu}(\eta) = 1 + \eta^2$ (Fig. 1(a)), $\bar{\rho}(\eta) = 1 + \eta^2$ (Fig. 1(b)).

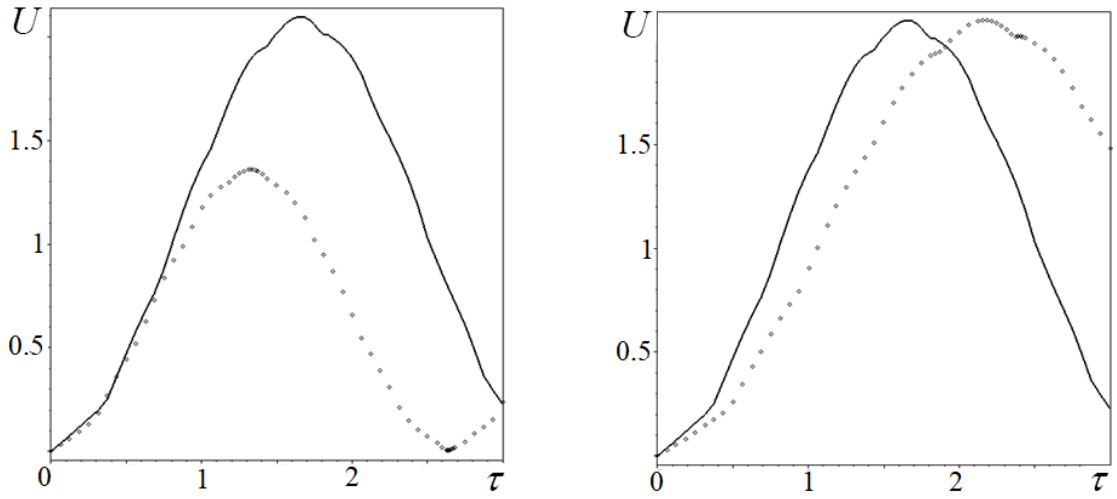

Fig. 1. Influence of different heterogeneity laws of the shear modulus (a) and density (b) on the radial displacement of the pipe's outer surface

Figure 1 shows that that the shear modulus and density significantly influence the change in displacement. During the computations, it was also found that the influence of the moduli $\bar{\lambda}$, $\bar{\beta}$ and $\bar{\xi}$ is substantially lower, and the coefficient $\bar{a}$ has practically no influence. Thus, information about the radial displacement of the outer surface at different times can serve as additional information for identifying the moduli $\bar{\lambda}$, $\bar{\mu}$, $\bar{\rho}$, $\bar{\beta}$, $\bar{\xi}$.

Iterative scheme for solving the inverse problem for the pipe

The inverse problem is to determine one of the characteristics $\bar{q}$ $(\bar{\lambda}, \bar{\mu}, \bar{\rho}, \bar{\beta}, \bar{\xi})$ from Eq. (12) on the basis of some additional information at the boundary $\eta = 1$:

$$U(1,\tau) = f(\tau),\ \tau \in [\bar{c}_1, \bar{c}_2]. \tag{17}$$

To solve the CIP (12), (17) for an isotropic pipe, we first obtain operator equations in the transform domain. For this, we convert equations (10) to a cylindrical coordinate system, setting $a_{ij} = 0$, $\beta_{ij} = \beta\delta_{ij}$, $D_{ijk} = 0$, $c_{ijkl} = \lambda\delta_{ij}\delta_{lk} + \mu\left(\delta_{ik}\delta_{jl} + \delta_{il}\delta_{jk}\right)$.

The nondimensionalized operator equations in the transform domain for a porous pipe take the form:

$$\begin{gathered}
\int_{\eta_0}^{1} \delta\bar{\lambda}^{(n-1)} \left(\frac{d\widetilde{U}^{(n-1)}}{d\eta} + \frac{\widetilde{U}^{(n-1)}}{\eta}\right)^2 \eta d\eta = -\widetilde{W}\left(\tilde{f}(p) - \widetilde{U}^{(n-1)}(1,p)\right),\ p \in 0,\infty),\\
\int_{\eta_0}^{1} \delta\bar{\mu}^{(n-1)} \left(\left(\frac{\partial\widetilde{U}^{(n-1)}}{\partial\eta}\right)^2 + \left(\frac{\widetilde{U}^{(n-1)}}{\eta}\right)^2\right)\eta d\eta = -\widetilde{W}\left(\tilde{f}(p) - \widetilde{U}^{(n-1)}(1,p)\right),\ p \in 0,\infty),\\
p^2 \int_{\eta_0}^{1} \delta\bar{\rho}^{(n-1)}\left(\widetilde{U}^{(n-1)}\right)^2 \eta d\eta = -\widetilde{W}\left(\tilde{f}(p) - \widetilde{U}^{(n-1)}(1,p)\right),\ p \in 0,\infty),\\
\int_{\eta_0}^{1} \delta\bar{\xi}^{(n-1)}\left(\widetilde{\Phi}^{(n-1)}\right)^2 \eta d\eta = -\widetilde{W}\left(\tilde{f}(p) - \widetilde{U}^{(n-1)}(1,p)\right),\ p \in 0,\infty),\\
\int_{\eta_0}^{1} \delta\bar{\beta}^{(n-1)} \frac{d\widetilde{U}^{(n-1)}}{d\eta}\widetilde{\Phi}^{(n-1)}\,\eta d\eta = -\widetilde{W}\left(\tilde{f}(p) - \widetilde{U}^{(n-1)}(1,p)\right),\ p \in 0,\infty).
\end{gathered} \tag{18}$$

To solve the inverse problem in the actual space let us apply to the Eqs. (18) the convolution theorem and the theorem on the differentiation of the original. Under the load $W(\tau) = H(\tau)$, the operator equations in the actual space can be represented as:

$$\int_{\eta_0}^{1} \delta\bar{q}^{(n-1)} M_s(\eta,\tau)\eta d\,\eta = -\left(f(\tau) - U^{(n-1)}(1,\tau)\right),\ s = 1..5,\ \tau \in [\bar{c}_1, \bar{c}_2]. \quad (19)$$

Here, $M_s(z,\tau)$ are kernels obtained by inverting the kernels of the integral equations in the transform domain (18). The form of the kernels $M_1(\eta,\tau)$, $M_2(\eta,\tau)$ and $M_3(\eta,\tau)$, for finding the corrections $\delta\bar{\lambda}^{(n-1)}$, $\delta\bar{\mu}^{(n-1)}$, $\delta\bar{\rho}^{(n-1)}$ respectively, coincides with [20,23]. The kernels for finding the corrections of pore stiffness modulus and the coupling modulus have the form: $M_4(\eta,\tau) = \delta_0 \int_0^{\tau} \Phi^{(n-1)}(\eta,\tau_1) \frac{\partial \Phi^{(n-1)}(\eta,\tau-\tau_1)}{\partial \tau_1} d\tau_1$, $M_5(\eta,\tau) = \delta_0 \int_0^{\tau} \frac{\partial U^{(n-1)}}{\partial \eta}(\eta,\tau_1)^{(n-1)} \frac{\partial \Phi^{(n-1)}(\eta,\tau-\tau_1)}{\partial \tau_1} d\tau_1$.

The kernels of the integral equations (19) represent the specific energy accumulated in the material by a given time due to the action of the corresponding mechanism (shear energy, energy of volumetric expansion of the skeleton, energy of pore volume change, energy of porosity gradient and kinetic energy). In all equations, the right-hand side is the same. This means that to separate the contributions of different moduli, we rely solely on the different dynamics of the change in the kernels $M_s(\eta,\tau)$ over time. This emphasizes the importance of sensitivity analysis and the selection of informative time intervals.

In this work, finite-dimensional approximation of the integral equations (19)was carried out by two methods. The first method is the collocation method. For that, we introduce a uniform partition of the segment $[\eta_0, 1]$ into $m_1 + 1$ segments by the points $\eta_i = \Delta d(i-1), i = 1..m_1 + 1$, where $\Delta d = \frac{(1-\eta_0)}{m_1}$ is the subinterval. Then, we introduce a uniform partition of the time interval $[\bar{c}_1, \bar{c}_2]$ into m_2 segments by the points $\tau_j = \Delta t(j-1), j = 1..m_2$, where $\Delta t = (\bar{c}_2 - \bar{c}_1)/m_2$ is the subinterval.

The second method is the projection method. In this case, the physical and mechanical characteristics were represented as expansions in power functions:

$$\delta\bar{q}^{(n-1)}(\eta) = \sum_{i=1}^{N} b_i^{(n-1)} r_i(\eta), r_i(\eta) = \eta^{i-1}, i = 1..N. \quad (20)$$

Substituting expansions (20) into Eq. (19), we obtain a system of linear algebraic equations (SLAE):

$$\sum_{i=1}^{N} b_i^{(n-1)} A_{ij}^{(n-1)} = D_j^{(n-1)}, j = 1..M. \quad (21)$$

Here, $A_{ij}^{(n-1)} = \int_{\eta_0}^{1} r_i(\eta) M_s^{(n-1)}(\eta,\tau_j)\eta d\eta$, $D_j^{(n-1)} = -\left(f(\tau_j) - U^{(n-1)}(1,\tau_j)\right)$, $s = 1..5$, $i = 1..N, j = 1..M$.

To solve the ill-conditioned SLAE (21), the Tikhonov regularization method [31] is used. This method allows finding an approximate solution to the system of equations by minimizing the Tikhonov smoothing functional, which takes into account the deviation of the solution from a given function and the regularization parameter. The optimal value of the regularization parameter α_{reg} is selected at each iteration, based on the balance condition between the residual of the solution and its norm, taking into account the known noise level in the input data.

The iterative reconstruction process starts with the initial approximation $\bar{q}^{(0)} = (\bar{q}_- + \bar{q}_+)/2$. Here $\bar{q}_-$ and $\bar{q}_+$ are the minimum and maximum values of the sought function, respectively. To ensure the fulfillment of thermodynamic constraints at each

iteration, the step damping method is proposed. After calculating the correction $\delta\bar{q}^{(n-1)}$ from the solution of the integral equations (19) at the $(n-1)$-th iteration, the damping coefficient $\kappa \in 0{,}1$ is determined such that the updated values of the physical and mechanical characteristics $\bar{q}^{(n)}(\eta) = \bar{q}^{(n-1)}(\eta) + \kappa\delta\bar{q}^{(n-1)}(\eta)$ satisfy all positive definiteness conditions at all nodes. The choice of κ is carried out as follows. We set $\kappa = 1$ and check the fulfillment of all constraints for the trial solution $\bar{q}^{(n)}(\eta) = \bar{q}^{(n-1)}(\eta) + \kappa\delta\bar{q}^{(n-1)}(\eta)$. If the constraints are satisfied, we accept $\kappa = 1$. Otherwise, a binary search procedure is implemented on the interval $0{,}1$: the interval is sequentially halved, and for each trial $\kappa = (0.5{,}0.25{,}0.125, \dots)$ the fulfillment of the constraints is checked.

The exit from the iterative process was carried out when reaching the maximum number of iterations $n = 30$ or the residual functional:

$$J^{(n-1)} = \int_{\bar{c}_1}^{\bar{c}_2} \left(f(\tau) - U^{(n-1)}(1,\tau)\right)^2 d\tau, \tag{22}$$

which reached the threshold value $\theta = 10^{-4}$. In this case, when using the second method of discretizing the integral equations (19), the physical and mechanical characteristics are refined stepwise.

Stage 1 (constant approximation). The sought characteristics are assumed to be constant along the radius: $\bar{q}(\eta) = q_0$. The inverse problem is solved for the scalar quantities q_0. The obtained values q_0^* are fixed as the initial approximation for the next stage.

Stage 2 (linear approximation). The characteristics are sought in the form $\bar{q}(\eta) = q_0 + q_1\eta$. The initial approximation vector is formed as $[q_0^*, 0]$, i.e., the linear coefficient is taken as zero. Next, an iterative process is performed, at each step of which corrections to both coefficients q_0 and q_1 are determined. After convergence, the obtained values q_0^{**}, q_1^{**} are used in the next stage.

Stage 3 (quadratic approximation). The characteristics are represented in the form $\bar{q}(\eta) = q_0 + q_1\eta + q_2\eta^2$. Initial approximation: $[q_0^{**}, q_1^{**}, 0]$. All three coefficients are refined jointly. Result: final values q_0, q_1, q_2.

The transition between stages was carried out upon fulfillment of the residual functional stabilization criterion: $\frac{|J^{(n)} - J^{(n-1)}|}{J^{(n-1)}} < \varepsilon_J$, $\varepsilon_J = 10^{-3}$ (the relative change in the residual functional in the last iterations of the current stage does not exceed 10^{-3}).

Identification results

This section presents the results of reconstructing the physical and mechanical characteristics of a poroelastic pipe. In calculations, it is accepted: $W(\tau) = H(\tau)$, $\eta_0 = 0.6$. One of the dimensionless characteristics was reconstructed, the others were assumed equal to 1, except for $\delta_0 = 0.4$, $\bar{a} = 0.5$.

Input data was modeled by solving the direct problem (12) using the shooting method under exact laws of change in the material properties. The maximum reconstruction error was determined using the relation $\gamma_2 = \frac{|\bar{q}_{ex}(\eta) - \bar{q}_{rec}(\eta)|}{\max\limits_{\eta\in[\eta_0,1]} \bar{q}_{ex}(\eta)} \cdot 100\ \%$, where $\bar{q}_{ex}(\eta)$ is the exact law, $\bar{q}_{rec}(\eta)$ is the reconstructed one.

The shear modulus and density, which have a dominant influence on the dynamics at the initial moments, were identified from early times on the interval $[\bar{c}_1, \bar{c}_2] = [0.1{,}0.8]$, the remaining moduli – at later times, for example, the Lamé modulus $\bar{\lambda}$ – on the interval

$[\bar{c}_1, \bar{c}_2] = [0.6,1.4]$, modulus $\bar{\xi}$ – on the interval $[\bar{c}_1, \bar{c}_2] = [0.8,2]$. In this case, from 7 to 12 measurement points were selected within the informative intervals. It should be noted that all dimensionless characteristics used in the computational experiments satisfy the conditions of thermodynamic correctness at any point in the interval $\eta \in [\eta_0, 1]$. The convergence of the iterative process for different characteristics and approximation methods was investigated. The results of the study are presented in Table 2.

Table 2. Convergence of the iterative process for various reconstructed characteristics

Reconstructed characteristic	Method	Number of Iterations	Final values of the residual functional
$\bar{\mu} = 0.46e^{5.5(\eta-\eta_0)}$	Collocation	14	$8.3 \cdot 10^{-5}$
$\bar{\mu} = 0.46e^{5.5(\eta-\eta_0)}$	Projection	10	$5.3 \cdot 10^{-5}$
$\bar{\mu} = 2.4 - 7.3\eta + 6.6\eta^2$	Collocation	13	$8.9 \cdot 10^{-5}$
$\bar{\mu} = 2.4 - 7.3\eta + 6.6\eta^2$	Projection	10	$6.4 \cdot 10^{-5}$
$\bar{\rho} = 1.3 + 2.6\eta - 2.2\eta^2$	Collocation	12	$7.5 \cdot 10^{-5}$
$\bar{\rho} = 1.3 + 2.6\eta - 2.2\eta^2$	Projection	9	$4.9 \cdot 10^{-5}$
$\bar{\lambda} = 0.6 + 2.2e^{-6.3(\eta-\eta_0)}$	Collocation	28	$9.8 \cdot 10^{-5}$
$\bar{\lambda} = 0.6 + 2.2e^{-6.3(\eta-\eta_0)}$	Projection	19	$6.1 \cdot 10^{-5}$
$\bar{\lambda} = 1 + 4\eta - 3.3\eta^2$	Projection	24	$9.4 \cdot 10^{-5}$
$\bar{\xi} = 2.7 - 3\eta + 2.4\eta^2$	Projection	30	$2.6 \cdot 10^{-3}$

From Table 2, it follows that the iterative identification process requires from 9 to 30 iterations depending on the type of characteristic being reconstructed. Thus, the characteristics $\bar{\mu}$ and $\bar{\rho}$ are reconstructed quite quickly in 9–14 iterations due to their strong influence on displacements. For the Lamé parameter $\bar{\lambda}$, more iterations are required (19–28) and the reconstruction error is higher due to weak sensitivity. When reconstructing the non-classical modulus $\bar{\xi}$, the exit from the iterative process occurred due to the maximum number of iterations – 30, while the value of the residual functional turned out to be significantly higher than the threshold value. The computation time per iteration ranged from 50 sec to 1.5 min, and the total reconstruction time for one characteristic ranged from 7 to 45 min.

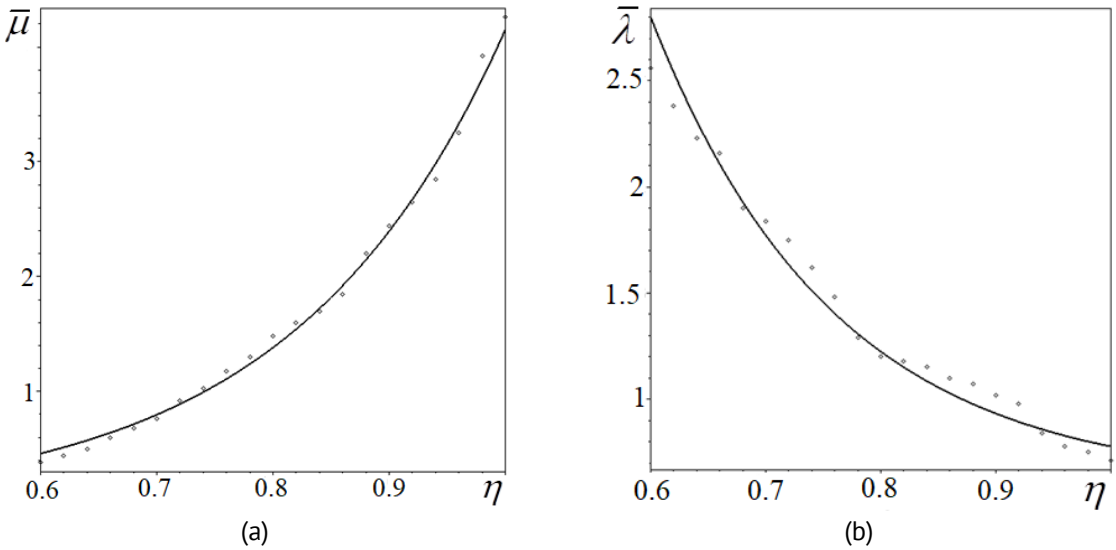

Fig. 2. Results of pointwise reconstruction of functions: (a) $\bar{\mu} = 0.46e^{5.5(\eta-\eta_0)}$; (b) $\bar{\lambda} = 0.6 + 2.2e^{-6.3(\eta-\eta_0)}$. The solid line and dots represent the exact and restored functions, respectively

Figure 2 shows the results of pointwise reconstruction of characteristics: (a) $\bar{\mu} = 0.46e^{5.5(\eta-\eta_0)}$; (b) $\bar{\lambda} = 0.6 + 2.2e^{-6.3(\eta-\eta_0)}$. Figure 3 presents the results of reconstructing functions: (a) $\bar{\mu} = 2.4 - 7.3\eta + 6.6\eta^2$; (b) $\bar{\rho} = 1.3 + 2.6\eta - 2.2\eta^2$ within the class of quadratic functions (20). Figure 4 shows the results of reconstructing the pore stiffness modulus: (a) $\bar{\xi} = 2.7 - 3\eta + 2.4\eta^2$; (b) $\bar{\lambda} = 1 + 4\eta - 3.3\eta^2$ within the class of quadratic functions (20).

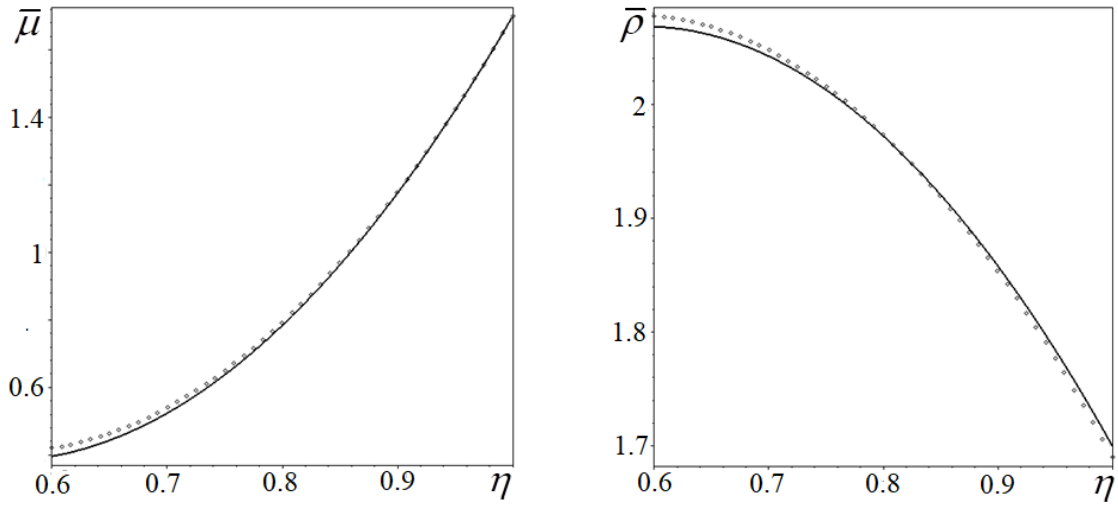

(a) (b)

Fig. 3. Results of reconstructing characteristics in the class of quadratic functions: (a) $\bar{\mu} = 2.4 - 7.3\eta + 6.6\eta^2$; (b) $\bar{\rho} = 1.3 + 2.6\eta - 2.2\eta^2$. The solid line and dots represent the exact and restored functions, respectively

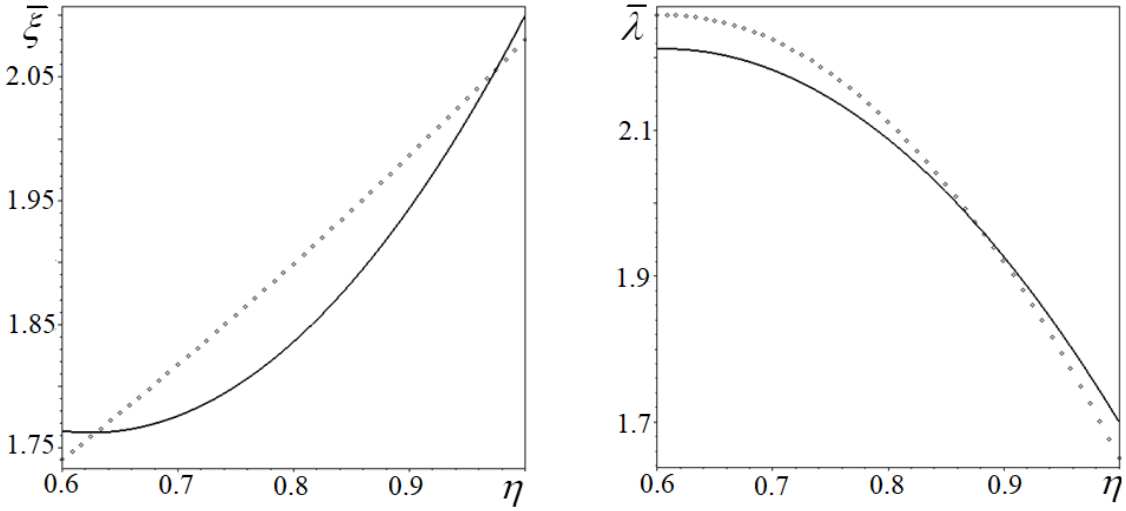

(a) (b)

Fig. 4. Results of reconstructing characteristics in the class of quadratic functions: (a) $\bar{\xi} = 2.7 - 3\eta + 2.4\eta^2$; (b) $\bar{\lambda} = 1 + 4\eta - 3.3\eta^2$. The solid line and dots represent the exact and restored functions, respectively

From Figs. 2–4, it follows that the moduli $\bar{\lambda}$, $\bar{\xi}$ are reconstructed significantly worse than $\bar{\mu}$, $\bar{\rho}$, which is related to their lesser influence on the radial displacement. The stability of the reconstruction to noise in the input data was investigated. The input information (radial displacement on the outer surface) was noised according to the

formula: $f_\omega(\tau) = f(\tau)(1 + \vartheta\zeta)$, where ϑ is the noise level, ζ is a random variable with a uniform distribution law on the interval $[-1,1]$.

Table 3 presents the results of reconstructing the function $\bar{\mu} = 0.46e^{5.5(\eta-\eta_0)}$ when approximating the operator equations by the collocation method, both in the absence of noise ($\vartheta = 0$) and in the presence of a 1 % measurement error ($\vartheta = 0.01$).

Table 3. Results of reconstructing the function $\bar{\mu} = 0.46e^{5.5(\eta-\eta_0)}$ depending on the presence and absence of noise in the input information

Coordinate η	Exact value $\bar{\mu}$	Reconstructed value $\bar{\mu}$		Relative reconstruction error, %	
		$\vartheta = 0$	$\vartheta = 0.01$	$\vartheta = 0$	$\vartheta = 0.01$
0.6	0.46	0.42	0.4	8.7	13
0.64	0.57	0.53	0.50	7	12.3
0.68	0.71	0.68	0.76	4.2	7
0.72	0.89	0.91	0.95	2.3	6.7
0.76	1.11	1.16	1.21	4.5	9
0.8	1.38	1.44	1.52	4.4	10.2
0.84	1.72	1.70	1.83	1.2	6.4
0.88	2.15	2.18	2.01	1.4	6.5
0.92	2.67	2.73	2.58	2.2	3.4
0.96	3.33	3.27	3.17	1.8	4.8
1.0	4.15	4.27	4.32	2.9	4

From Table 3, it follows that the maximum reconstruction error with 1 % input data noise increased from 8.7 to 13 %, which is an acceptable result for engineering applications. Similarly, computational experiments were conducted for other physical and mechanical characteristics of the pipe when approximating the operator equations by the collocation method. It was found that with a measurement error of 1 %, the reconstruction error for characteristics $\bar{\mu}$ and $\bar{\rho}$ does not exceed 11 %, and for the Lamé modulus $\bar{\lambda}$ – 35 %, which is explained by its weaker influence on the observed displacement field.

A comparison of the reconstruction error of the same functions using the collocation method and the projection method was performed. For smooth functions, the projection

Table 4. Comparison of reconstruction error for $\bar{\rho} = 1.3 + 2.6\eta - 2.2\eta^2$ using the collocation method and the projection method with 0.5% noise in the input information

Coordinate η	Exact value $\bar{\rho}$	Reconstructed value $\bar{\rho}$		Relative reconstruction error, %	
		Collocation method	Projection method	Collocation method	Projection method
0.6	2.07	2.24	2.15	8.2	3.9
0.64	2.06	2.21	2.13	7.3	3.4
0.68	2.05	2.18	2.11	6.3	2.9
0.72	2.03	2.08	2.07	2.5	2
0.76	2.0	2.04	2.03	2	1.5
0.8	1.97	2.0	1.98	1.5	1
0.84	1.93	1.96	1.92	1.6	0.5
0.88	1.88	1.75	1.86	6.9	1.1
0.92	1.83	1.72	1.78	6	2.7
0.96	1.77	1.65	1.7	6.8	4
1.0	1.7	1.54	1.61	9.4	5.3

method provides a reconstruction error 2–5 % lower than the collocation method. The comparison results for the test function $\bar{\rho} = 1.3 + 2.6\eta - 2.2\eta^2$ with 0.5 % noise are presented in Table 4. The projection method demonstrated higher stability to noise due to the smoothing property of approximation in the class of polynomials.

Conclusion

An iterative method for solving the coefficient inverse problem for a functionally graded elastic pipe with voids within the framework of the Cowin-Nunziato model is presented. Based on the weak formulation, Fredholm operator equations of the 1st kind are obtained, relating variations of the sought characteristics to the residual of displacement fields on the boundary. Two methods for discretizing the operator equations are proposed: (a) the collocation method (reconstruction at grid nodes); (b) the projection method (reconstruction in the class of polynomial functions) with a multi-stage refinement strategy. It has been established that the moduli $\bar{\mu}$ and $\bar{\rho}$ have the strongest influence, moduli $\bar{\lambda}$ and $\bar{\beta}$ have a moderate influence, and modulus $\bar{\xi}$ has a weak influence. This explains the different accuracy of their reconstruction. A detailed study of the method's stability to random errors in the input data was conducted. It is shown that for highly sensitive characteristics ($\bar{\mu}$, $\bar{\rho}$), the method is stable at a noise level of 1 %. For smooth functions, the projection method provides a reconstruction error 2–5 % lower than the collocation method with better noise stability.

A number of limitations of the proposed approach to solving inverse problems should be noted. First, the iterative process based on linearization requires a sufficiently close initial approximation to the exact (reconstructed) function. Second, the projection method is applicable only for reconstructing smooth functions, while for materials with discontinuous properties, the collocation method is preferable. Third, the reconstruction accuracy differs significantly for different moduli: the shear modulus and density are reconstructed with high accuracy, while the pore stiffness modulus is reconstructed with low accuracy due to its weak influence on boundary displacements. Fourth, at noise levels exceeding 1 %, the reconstruction accuracy of the moduli decreases significantly.

CRediT authorship contribution statement

Nesterov Sergey A. : writing – review & editing, writing – original draft; conceptualization.

Conflict of interest

The author declares no competing interests.

References

1. Chen D, Gao K, Yang J, Zhang L. Functionally graded porous structures: analyses, performances, and applications – A Review. *Thin-Walled Structures.* 2023;191: 111046.
2. Rudskoy AI, Popovich AA. *Functionally graded materials and additive technologies for their production.* St. Petersburg: Polytech press; 2022. (In Russian)
3. Hou C, Liu Y, Xu W, Lu X, Guo L, Liu Y, Tian S, Liu B, Zhang J, Wen C. Additive manufacturing of functionally graded porous titanium scaffolds for dental applications. *Biomater. Adv.* 2022;139: 213018.

4. Karimzadeh M, Basvoju D, Vakanski A, Charit I, Xu F, Zhang X. Machine Learning for Additive Manufacturing of Functionally Graded Materials. *Materials.* 2024;17(15): 3673.
5. Cowin SC, Nunziato JW. Linear elastic materials with voids. *Journal of Elasticity.* 1983;13: 125–147.
6. Cowin SC, Puri P. The classical pressure vessel problems for linear elastic materials with voids. *Journal of Elasticity.* 1983;13: 157–163.
7. Repka M, Sladek V, Sladek J. Numerical Analysis of Poro-elastic Materials Described by the Micro-dilatation Theory. *Procedia Engineering.* 2017;190: 248–254.
8. Li Y, Volkov VA, Rabinskiy NL, Shemiakov OA. Numerical modeling of scale effects for circular cylinder in the theory of thermoelastic materials with voids. *Journal of Applied Engineering Science.* 2020;18(4): 671–675.
9. Sha M, Volkov AV, Orekhov AA, Kuznetsova EL. Micro-dilatation effects in a two-layered porous structure under uniform heating. *Journal of the Balkan Tribological Association.* 2021;27(2): 280–294.
10. Nesterov SA. On the deformation of composite elastic bodies with empty pores. *Ecological Bulletin of Research Centers of the Black Sea Economic Cooperation.* 2025;22(1): 68–79. (In Russian)
11. Ieşan D, Scalia A. On the Deformation of Functionally Graded Porous Elastic Cylinders. *Journal of Elasticity.* 2007;87: 147–159.
12. Vatulyan AO, Shvedov DS. Oscillation of inhomogeneous poroelastic layer with voids. *Vestnik Don State Technical University.* 2013;13(1–2): 49–57. (In Russian)
13. Chiriţă S. Rayleigh Waves on an Exponentially Graded Poroelastic Half Space. *Journal of Elasticity.* 2013;110: 185–199.
14. Ramezani H, Steeb H, Jeong J. Analytical and numerical studies on penalized micro-dilatation (PMD) theory: macro-micro link concept. *European Journal of Mechanics, A/Solids.* 2012;34: 130–148.
15. Jeong J, Ram´ezani H, Sardini P, Kondo D, Ponson L, Siitari-Kauppi M. Porous media modeling and micro-structurally motivated material moduli determination via the micro-dilatation theory. *Eur. Phys. J. Special Topics.* 2015;224: 1805–1816.
16. Bishay PL, Repka M, Sladek V, Sladek J. On the characterization of porosity-related parameters in micro-dilatation theory. *Acta Mech.* 2017;228: 1631–1644.
17. Chebakov MI, Kolosova EM. Methodology of Determination of Porosity Parameters in the Theory of Microdilation. In: Parinov IA, Chang SH, Putri EP. (Eds.) *Physics and Mechanics of New Materials and Their Applications. PHENMA 2023. Springer Proceedings in Materials, vol 41.* Cham; Springer: 2024. p.335–344.
18. Vatul'yan AO, Lyapin AA. On inverse coefficient problems of poroelasticity. *Mechanics of Solids.* 2013; 48(2): 210–215.
19. Dudarev VV, Mnukhin RM, Vatulyan AO, Nedin RD, Gusakov DV. On the Determination of the Biot Modulus of Poroelastic Cylinder. *ZAMM - Journal of Applied Mathematics and Mechanics.* 2019;99(3): e201800137.
20. Vatulyan AO, Nesterov SA. On some features of identification of inhomogeneous prestressed state of thermoelastic hollow cylinder with coating. *Materials Physics and Mechanics.* 2019;42(1): 54–64.
21. Vatulyan AO, Nesterov SA. On Determination of the Thermomechanical Characteristics of a Functionally Graded Finite Cylinder. *Mechanics of Solids.* 2021;56(7): 1429–1438.
22. Vatul'yan AO, Nesterov SA. Study of the Inverse Problems of Thermoelasticity for Inhomogeneous Materials. *Siberian Mathematical Journal.* 2023;64(3): 699–706.
23. Vatulyan A, Nesterov S, Nedin R. Variable properties reconstruction for functionally graded thermoelectroelastic cylinder. *Continuum Mechanics and Thermodynamics.* 2024;36: 745–762.
24. Lyapin AA, Rudenko OV, Svyatko YuA. On the application of genetic algorithms and gradient methods for problem of initial stress field reconstruction in poroelastic inhomogeneous column. *Vestnik of Saint Petersburg University. Series 1. Mathematics. Mechanics. Astronomy.* 2016;3(3): 481–488. (In Russian)
25. Lecampion B, Constantinescu A. Sensitivity analysis for parameter identification in quasi-static poroelasticity. *Int. J. Numer. Anal. Meth. Geomech.* 2005;29: 163–185.
26. Dehghani H, ZilianA. Poroelastic model parameter identification using artificial neural networks: on the effects of heterogeneous porosity and solid matrix Poisson ratio. *Computational Mechanics.* 2020;66: 625–649.
27. Korobov P, Alekseev V. Numerical solution of a one-dimensional inverse retrospective problem for a system of poroelasticity equations. *Bulletin of the Novosibirsk Computing Center. Series: Mathemaical Modeling in Geophysics.* 2021;23: 19–24.
28. Imomnazarov KhKh, Khujaev LKh, Yangiboev ZSh. On inverse dynamic poroelasticity problem for layered medium. *Mat. Zamet. SVFU.* 2022;29(2):19–30. (In Russian)
29. Liu T. Porosity reconstruction based on Biot elastic model of porous media by homotopy perturbation method. *Chaos Solitons & Fractals.* 2022;158: 112007.
30. Krylov VI, Skoblya NS. *Approximate Fourier Transform and Laplace Transform Inversion Methods.* Moscow: Nauka; 1974. (In Russian).
31. Tikhonov AN, Arsenin VYa. Methods for the Solutioin of Ill-Posed Problems. Moscow: Nauka; 1986. (In Russian).

MATERIALS PHYSICS AND MECHANICS RESEARCH ARTICLE

Submitted: September 11, 2025 **Revised: October 29, 2025** **Accepted: December 4, 2025**

Dynamic effects of a hollow cylinder quasi-force-free magnet

M.I. Lobachev ✉

Peter the Great Saint-Petersburg Polytechnic University, St. Petersburg, Russia

✉ lobachev_mi@spbstu.ru

ABSTRACT

This study investigates mechanical stresses induced by a unipolar sinusoidal pulse in a hollow cylindrical conductor, which serves as a key element of the base part of a quasi-force-free configuration pulsed magnet. The aim of the work is to assess transient mechanical effects not accounted for by static models. The applied method determines the system's natural frequencies and solves the dynamic axisymmetric problem of elasticity theory using Laplace transforms. The results include the calculated spectrum of natural frequencies; it is shown that the stress response exhibits quasistatic behavior for millisecond-duration pulses, whereas dangerous stress magnification requires microsecond pulses which are consistent with the single-degree-of-freedom model predictions. In conclusion, the adequacy of static models for designing magnets with millisecond-range pulses is confirmed, and the development of a methodology for analyzing complex multilayer magnets is proposed.

KEYWORDS

quasi-force-free magnet • hollow cylinder • dynamic response • Lorentz force • von Mises stress • natural frequencies pulsed magnetic field

Citation: Lobachev MI. Dynamic effects of a hollow cylinder quasi-force-free magnet. *Materials Physics and Mechanics*. 2026;54(2): 57–69.
http://dx.doi.org/10.18149/MPM.5422026_5

Introduction

Strong and ultra-strong magnetic fields are vital research tools with applications spanning from the study of fundamental material properties [1–3] to magnetic resonance imaging (MRI) [4,5], magnetic pulse forming [6], plasma confinement in fusion energy research [7–10]. The generation of such fields presents significant engineering challenges, primarily related to material strength and thermal management. Consequently, for sustained laboratory research, non-destructive methods are paramount. Through a variety of non-destructive methods presented in [11] (Fig. 1) we are interested in the highest magnetic fields – short-pulsed facilities. While state-of-the-art pulsed magnets, often based on the force-balanced coil principle, have achieved fields in the 80–100 T range, the quest for higher fields faces significant technological barriers. The primary limitations are Joule heating and mechanical stresses induced by the Lorentz force.

The force-balanced coil technique, employed in leading laboratories (Germany [12], China [13], France [14]), is designed to manage mechanical stress by distributing Lorentz forces evenly across a complex, multi-layer winding structure. A landmark achievement of this approach was the generation of a 100.75 T field [15] in Los Alamos, USA. However, this methodology carries a critical and inherent limitation: the exponential scaling of the magnet's size and mass with the target field strength. This relationship is described by the ratio of the external radius to the inner radius $\frac{R_e}{R_i} \sim exp(1 / \eta_{max})$, where η_{max} is

Publisher: Peter the Great St. Petersburg Polytechnic University

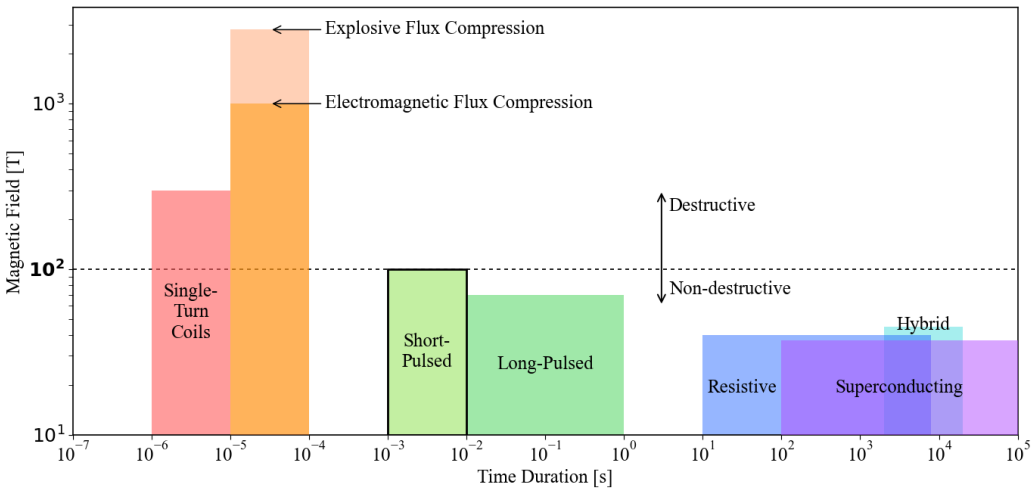

Fig. 1. Overview of strong-magnetic fields generation methods. Based on data from [11]

a dimensionless stress parameter (von Mises stress divided by magnetic pressure $B_0^2/2\mu_0$), implies that advancing beyond current records would require magnets of prohibitively large dimensions and immense stored energy, rendering this path economically and practically unviable for many applications.

This impasse has spurred the investigation of alternative paradigms, among which the "quasi-force-free" magnet concept ([16–21]) presents a promising solution. Its principle is to engineer the current density vector $\underline{J}$ to be nearly parallel to the internal magnetic field $\underline{B}$ within the conductor, thereby minimizing the Lorentz force density ($\underline{J} \times \underline{B}$). This is achieved through a specific configuration of toroidal and poloidal current components that promote force self-compensation.

As a basic element of a quasi-force-free magnet, a solenoid with a specific winding angle can be considered (Fig. 2(a)). Such a structure may be approximated as an infinitely long hollow cylinder with inner radius R_1 and outer radius R_2 in an axisymmetric representation (Fig. 2(b)). The winding angle is directly related to the azimuthal magnetic

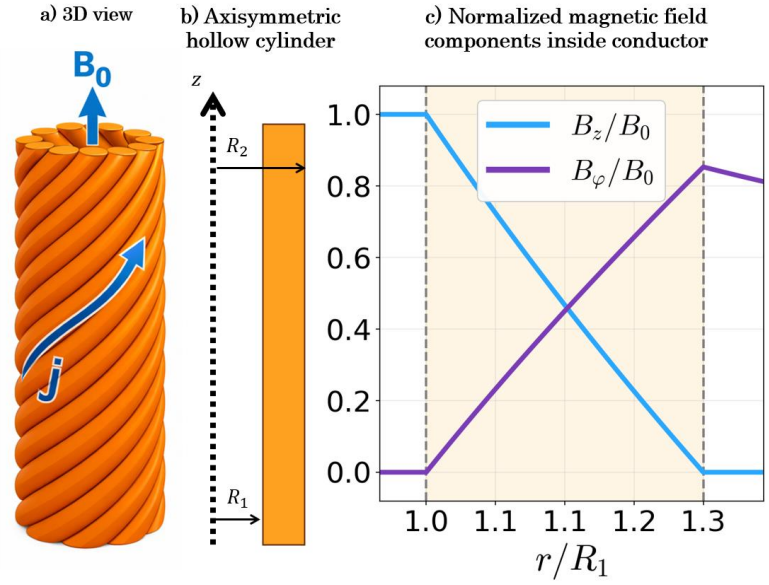

Fig. 2. Basic element of a quasi-force-free magnet

field B_φ. A typical spatial distribution of the magnetic field components $\underline{B}$ is shown in Fig. 2(c) and calculated, for example, in [22].

Existing theoretical analyses of the central base region usually use simplified static models to estimate the stress at the peak of the current pulse. While this approach provides a useful reference point, it does not account for the transient dynamics that occur during real pulsed operation. In practice, the pulse duration and the electromagnetic skin effect characterized by the ratio of the conductor thickness to the skin depth play a key role. They determine how the current, and therefore the volumetric Lorentz force, is distributed inside the conductor. This time-varying force distribution ultimately governs the conductor's dynamic mechanical response.

The present work addresses this gap by investigating non-stationary processes in a fundamental single-layer cylindrical model of a quasi-force-free magnet. The analysis follows a sequential methodology. First, the natural vibration frequencies of a hollow cylinder are determined. Subsequently, the dynamic problem of linear elasticity theory is solved under the action of a previously calculated balancing volumetric radial force. This force results from a unipolar current pulse in the form of a half-wave sine. Due to the linearity of the problem, the effects of electromagnetic diffusion (which determines the force profile) can be considered separately from the dynamic mechanical effects. This article is specifically devoted to the latter, as indicated by its title.

Methods

The research methodology for analyzing the dynamic mechanical response of a quasi-force-free magnet conductor is based on a sequential solution of two coupled physical problems: determining the natural vibrational spectrum of the system and calculating its forced oscillations under a given electromagnetic load. The method is described in such detail that it can be reproduced to obtain similar results.

Analytical model and governing equations

The object of study is an infinitely long, hollow, isotropic cylindrical conductor with inner radius R_1 and outer radius R_2. The analysis is conducted within the framework of linear elasticity theory under axisymmetric plane strain conditions. The radial displacement $u(r,t)$ is the primary variable. The starting point is the equation of motion for radial vibrations, derived from the balance of linear momentum:

$$\rho\frac{\partial^2 u}{\partial t^2} = c_{11}\frac{\partial}{\partial r}\left(\frac{\partial u}{\partial r}+\frac{u}{r}\right), \quad (1)$$

where ρ is the material density, and $c_{11} = \lambda + 2\mu$ is an elastic modulus (λ and μ are Lamé constants). Introducing the speed of the dilatational wave $c = \sqrt{\frac{c_{11}}{\rho}}$ simplifies the equation to:

$$\frac{\partial^2 u}{\partial t^2} = c^2\frac{\partial}{\partial r}\left(\frac{\partial u}{\partial r}+\frac{u}{r}\right). \quad (2)$$

To find the natural frequencies, a free vibration problem is considered. A solution to Eq. (2) is sought in the form:

$$u(r,t) = U(r)exp(j\omega_n t), \quad (3)$$

were $\omega_n$is the angular natural frequency and $U(r)$ describes the radial mode shape. Substituting this form into the governing equation leads to an ordinary differential equation for the spatial amplitude:

$$\frac{d^2U}{dr^2} + \frac{1}{r}\frac{dU}{dr} + \left(\frac{\omega_n^2}{c^2} - \frac{1}{r^2}\right)U = 0. \tag{4}$$

Equation (4) is a canonical form of Bessel's differential equation. Its general solution is a linear combination of first-order Bessel functions of the first and second kind:

$$U(r) = C_1 J_1\left(\frac{\omega_n r}{c}\right) + C_2 Y_1\left(\frac{\omega_n r}{c}\right), \tag{5}$$

where C_1 and C_2 are constants determined by the boundary conditions.

Determination of natural frequencies and modes

For a free-standing cylinder with no external traction on its inner R_1 and outer R_2 surfaces, the radial stress σ_r must vanish at both boundaries. The radial stress for a plane strain case is given by:

$$\sigma_r = c_{11}\frac{\partial u}{\partial r} + \lambda\frac{u}{r}. \tag{6}$$

Introducing a parameter $m = \lambda/c_{11}$, the boundary conditions can be expressed as:

$$\begin{aligned} \left(\frac{dU}{dr} + m\frac{U}{r}\right)\Big|_{r=R_1} &= 0, \\ \left(\frac{dU}{dr} + m\frac{U}{r}\right)\Big|_{r=R_2} &= 0. \end{aligned} \tag{7}$$

Substituting the general solution from Eq. (5) into these boundary conditions yields a system of two homogeneous linear equations for C_1 and C_2. For a non-trivial solution to exist, the determinant of the coefficient matrix must be zero. This requirement leads to the following characteristic equation, the solutions of which define the discrete set of natural frequencies ω_n of the system:

$$\begin{aligned} &\left[\frac{\omega_n R_1}{c}J_0\left(\frac{\omega_n R_1}{c}\right) + (m-1)J_1\left(\frac{\omega_n R_1}{c}\right)\right]\left[\frac{\omega_n R_2}{c}Y_0\left(\frac{\omega_n R_2}{c}\right) + (m-1)Y_1\left(\frac{\omega_n R_2}{c}\right)\right] - \\ &\left[\frac{\omega_n R_2}{c}J_0\left(\frac{\omega_n R_2}{c}\right) + (m-1)J_1\left(\frac{\omega_n R_2}{c}\right)\right]\left[\frac{\omega_n R_1}{c}Y_0\left(\frac{\omega_n R_1}{c}\right) + (m-1)Y_1\left(\frac{\omega_n R_1}{c}\right)\right] = 0. \end{aligned} \tag{8}$$

To simplify the numerical solution of Eq. (8), it is convenient to introduce the dimensionless frequency $\hat{\omega}_n = \omega_n R_1/c$ and the geometry ratio $g = R_2/R_1$. The boundary condition terms can be compactly defined as:

$$\begin{aligned} \mathcal{A}_{11}(\hat{\omega}) &= (m-1)J_1(\hat{\omega}) + \hat{\omega}J_0(\hat{\omega}), \\ \mathcal{A}_{12}(\hat{\omega}) &= (m-1)Y_1(\hat{\omega}) + \hat{\omega}Y_0(\hat{\omega}), \\ \mathcal{A}_{21}(\hat{\omega}, g) &= (m-1)J_1(g\hat{\omega}) + g\hat{\omega}J_0(g\hat{\omega}), \\ \mathcal{A}_{22}(\hat{\omega}, g) &= (m-1)Y_1(g\hat{\omega}) + g\hat{\omega}Y_0(g\hat{\omega}). \end{aligned} \tag{9}$$

The characteristic equation then reduces to the vanishing of a $2x2$ determinant:

$$\mathcal{A}_{11}(\hat{\omega}) \cdot \mathcal{A}_{22}(\hat{\omega}, g) - \mathcal{A}_{12}(\hat{\omega}) \cdot \mathcal{A}_{21}(\hat{\omega}, g) = 0. \tag{10}$$

The roots $\hat{\omega}_n$ of Eq. (10) correspond to the dimensionless eigenfrequencies of the hollow cylinder. The results match with works in [23], in [24] for isotropic case and with the case of axially symmetric vibrations in [25].

Dynamic response to electromagnetic loads

Having established the natural frequencies of the force-free cylinder, we now proceed to model its dynamic response when subjected to the transient volumetric Lorentz forces generated during a current pulse. The governing equation now:

$$\rho \frac{\partial^2 u}{\partial t^2} = c_{11}\left(\frac{\partial^2 u}{\partial r^2} + \frac{1}{r}\frac{\partial u}{\partial r} - \frac{u}{r^2}\right) + f(r,t), \tag{11}$$

where $f(r,t) = X(r)\sin(\omega_d t)$ in particular case modeled as a half-wave sine pulse with driven frequency ω_d and active time $t\ \epsilon\ [0, \frac{T}{2}]$.

To solve this non-homogeneous partial differential equation, we employ the Laplace transform with respect to time. The transform of the displacement is defined as $U_L(r,s) = \mathcal{L}\{u(r,t)\}$. Applying the transform to Eq. (11), and assuming zero initial displacement and velocity, yields:

$$\left(\frac{d^2 U_L}{dr^2} + \frac{1}{r}\frac{dU_L}{dr} - \frac{U_L}{r^2}\right) - \frac{s^2}{c^2}U_L = F_L, \tag{12}$$

where the transformed forcing function is:

$$F_L = -\frac{\mathcal{L}\{f(r,t)\}}{c_{11}} = -\frac{X(r)}{c_{11}} \cdot \frac{\omega_d}{s^2+\omega_d^2}. \tag{13}$$

The general solution in the Laplace domain is the sum of homogeneous and particular solutions:

$$U_L(r,s) = U_L^{(h)}(r,s) + U_L^{(p)}(r,s). \tag{14}$$

The homogeneous solution is expressed in terms of modified Bessel functions:

$$U_L^{(h)}(r,s) = C_1(s)I_1\left(\frac{s}{c}r\right) + C_2(s)K_1\left(\frac{s}{c}r\right). \tag{15}$$

A particular solution is found using the method of variation of parameters, involving integrals of the form:

$$\begin{aligned} \widehat{C_1}(r,s) &= \int_{R_1}^{r} \xi F_L(\xi,s)K_1\left(\frac{s}{c}\xi\right)d\xi, \\ \widehat{C_2}(r,s) &= -\int_{R_1}^{r} \xi F_L(\xi,s)I_1\left(\frac{s}{c}\xi\right)d\xi. \end{aligned} \tag{16}$$

So, it can be constructed by:

$$U_L^{(p)}(r,s) = \widehat{C_1}(r,s)I_1\left(\frac{s}{c}r\right) + \widehat{C_2}(r,s)K_1\left(\frac{s}{c}r\right). \tag{17}$$

Constants $C_1(s)$, $C_2(s)$ are determined by applying the traction-free boundary conditions similarly to Eq. (10) to the full solution $U_L(r,s)$, which leads to a linear algebraic system solved for each complex s:

$$\mathcal{M} \cdot \begin{bmatrix} C_1(s) \\ C_2(s) \end{bmatrix} = b. \tag{18}$$

where matrix $\mathcal{M}$ and vector b coefficients are:

$$\begin{aligned} \mathcal{M}_{11} &= \frac{(m-1)}{R_1}I_1\left(\frac{s}{c}R_1\right) + \frac{s}{c}I_0\left(\frac{s}{c}R_1\right), \\ \mathcal{M}_{12} &= \frac{(m-1)}{R_1}K_1\left(\frac{s}{c}R_1\right) + \frac{s}{c}K_0\left(\frac{s}{c}R_1\right), \\ \mathcal{M}_{21} &= \frac{(m-1)}{R_2}I_1\left(\frac{s}{c}R_2\right) + \frac{s}{c}I_0\left(\frac{s}{c}R_2\right), \\ \mathcal{M}_{22} &= \frac{(m-1)}{R_2}K_1\left(\frac{s}{c}R_2\right) + \frac{s}{c}K_0\left(\frac{s}{c}R_2\right), \\ b_1 &= 0, \\ b_2 &= -\left[\widehat{C_1}(R_2,s)\mathcal{M}_{21} + \widehat{C_2}(R_2,s)\mathcal{M}_{22}\right]. \end{aligned} \tag{19}$$

The final time-domain solution $u(r,t)$ is obtained by numerical inversion of the Laplace transform (e.g., using the Gaver-Stehfest algorithm [26]).

Quasi-force-free magnet implementation

The methodology described in the previous sections is applied to a specific quasi-force-free magnet configuration (Fig. 2). The volumetric force distribution $X(r)$ is selected to

satisfy the self-equilibration condition, ensuring zero net radial force through the conductor wall [22]:

$$\int_{R_1}^{R_2} X(r)dr = 0. \tag{20}$$

Thus, the expression is:

$$X(r) = \mu_0 \left(\frac{A_1^2}{r}\ln\left(\frac{R_2}{r}\right) + \frac{Z_1^2}{2}\cdot\frac{R_1^2 - r^2}{r}\right), \tag{21}$$

where μ_0 is the magnetic constant. Constants A_1, Z_1 are defined by the target central magnetic field B_0 and geometry:

$$A_1 = \frac{B_0}{\mu_0 \ln(g)}, Z_1 = \frac{2B_0\theta R_2}{\mu_0(R_2^2 - R_1^2)}. \tag{22}$$

The parameter $\theta = B_p/B_0$ (ratio of poloidal to axial field) is calculated as:

$$\theta = \frac{g^2-1}{2g\sqrt{\frac{g^2-1}{2} - \ln(g)}}. \tag{23}$$

It is important to emphasize that in the present formulation the radial force distribution $X(r)$ is prescribed. Electromagnetic diffusion and possible redistribution of current density are intentionally excluded from the model. The spatial profile given by Eq. (21) is treated as a fixed load satisfying the self-equilibration condition, while the temporal dependence is introduced solely through the harmonic factor $\sin(\omega_d t)$.

The analytical solution obtained in the previous sections is formulated for an arbitrary self-equilibrated function $X(r)$. Therefore, it is not restricted to the idealized hollow cylindrical geometry assumed here. In practical conductors, the actual cross-section (e.g., a round wire in a tightly wound helix) does not form a perfectly rectangular r-z domain. This geometric difference may modify the detailed spatial distribution of the Lorentz force; however, it does not alter the structure of the dynamic problem itself. The mechanical response is governed primarily by the excitation frequency relative to the eigenfrequencies of the system, whereas moderate variations of the radial load shape affect only quantitative details of the response amplitude.

Results and Discussion

The developed analytical and numerical model was applied to analyze the dynamic mechanical response of a quasi-force-free magnet conductor with specific geometric and material parameters. The aim was to assess the stress levels under a high magnetic field pulse and identify potential risks of stress amplification. The geometric ratio was set at $g = R_2/R_1 = 1.3$, and the conductor material was modeled with properties typical of beryllium bronze: Young's modulus $E = 131$ GPa, Poisson's ratio $\nu = 0.3$, and density $\rho = 8900\ \mathrm{kg/m^3}$. The target central magnetic field was $B_0 = 100$ T.

In the dynamic analysis, the excitation frequency of the current pulse becomes a critical parameter. The electromagnetic skin effect is characterized by the dimensionless parameter $k = \Delta/\Delta_0$ defined [27] as the ratio of the conductor thickness $\Delta = R_2 - R_1$ and the skin depth:

$$\Delta_0 = \sqrt{\frac{2}{\sigma\mu_0\omega_d}}. \tag{24}$$

Here, σ is the electrical conductivity and ω_d is associated with the current pulse duration. It should be noted that Eq. (19) is only applicable for weak skin-effect regime ($k \leq 1$). In this case, the electromagnetic diffusion time is sufficiently long to ensure

nearly uniform current distribution across the conductor wall, thereby validating the assumption of a spatially constant force profile during the dynamic excitation.

Natural vibration spectrum

The solution of the characteristic equation (10) yielded the dimensionless eigenfrequencies of the hollow cylindrical conductor. Graphic representation of the numerical solution in Matlab for Eq. (10) is presented in Fig. 3.

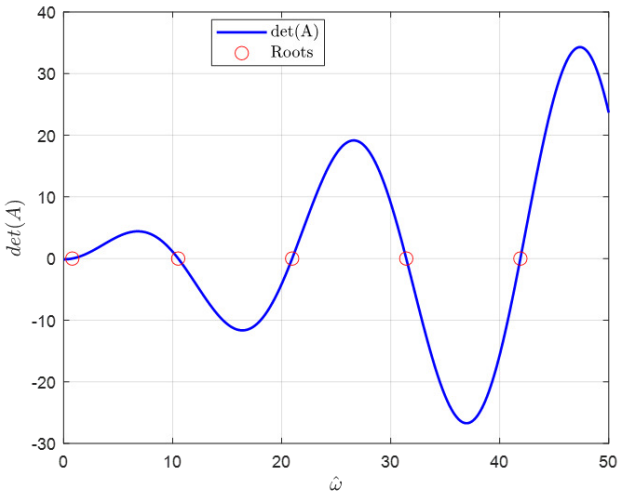

Fig. 3. Roots of Eq. (10) for determination of natural frequencies

The first fundamental dimensionless frequency was found to be $\widehat{\omega_1} \approx 0.797$. In the present formulation, the excitation is introduced as a $f(r,t) = X(r)\sin(\omega_d t)$, and the frequency parameter is conveniently expressed through the dimensionless quantity k via:

$$\omega_d = \frac{2k^2}{\sigma\mu_0\Delta^2}. \tag{25}$$

Using this relation purely as a parametrization of the excitation frequency, we determine the value of k for which the driving frequency coincides with the first eigenfrequency. For beryllium bronze ($\sigma = 60$ MS/m) yields $k \approx 10.971$. This value lies well above the operational regime considered here and corresponds to pulse durations in the microsecond range ($\tau = \pi/\omega_d$).

Dynamic stress response

For the stress response analysis, stress tensor components are calculated using constitutive relations for isotropic linear elasticity under plane strain:

$$\begin{aligned}\sigma_r(r,t) &= c_{11}\frac{\partial u}{\partial r} + \lambda\frac{u}{r},\\ \sigma_\varphi(r,t) &= \lambda\frac{\partial u}{\partial r} + c_{11}\frac{u}{r},\\ \sigma_z(r,t) &= \lambda\left(\frac{\partial u}{\partial r} + \frac{u}{r}\right).\end{aligned} \tag{26}$$

The von Mises equivalent stress is:

$$\sigma_{Mis}(r,t) = \sqrt{\frac{1}{2}\left[\left(\sigma_r - \sigma_\varphi\right)^2 + \left(\sigma_\varphi - \sigma_z\right)^2 + \left(\sigma_z - \sigma_r\right)^2\right]}. \tag{27}$$

The dynamic response to a half-sine current pulse was calculated for various skin-effect regimes (*k* values). Figure 4 illustrates the spatial-temporal evolution of the

normalized radial displacements $u(r,t)/R_1$ and von Mises stress $\eta(r,t) = 2\mu_0\sigma_{Mis}(r,t)/B_0^2$ for a representative case with $k = 0.5$. The stress rises smoothly following the temporal profile of the driving pulse, consistent with a linear system in a regime far from first natural frequency. The peak stress values align well with those predicted by static analyses for comparable geometries [22], confirming the model's validity in the quasi-stationary limit ($k \leq 1$) at the peak of the pulse ($t = T/4$).

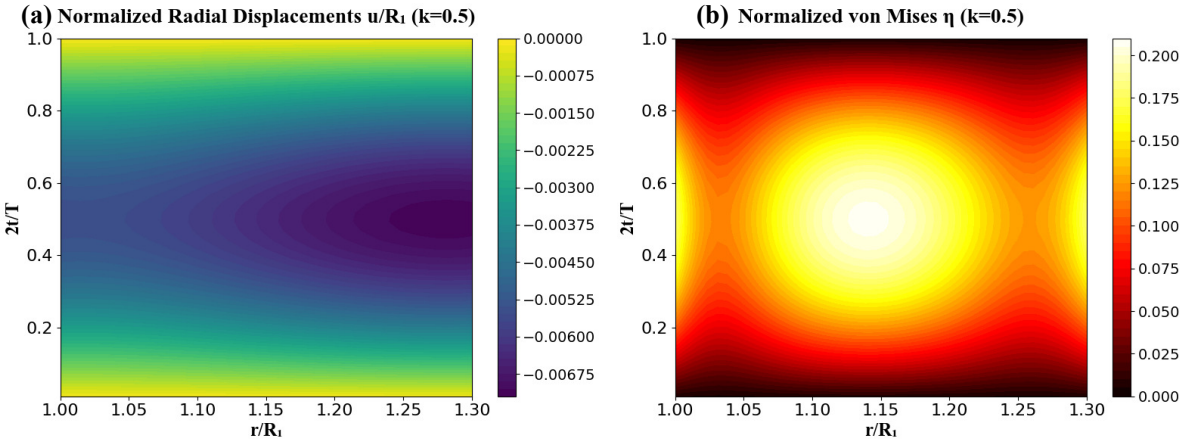

Fig. 4. Normalized contour plots of radial displacements (a) and von Mises (b) stresses for *k* = 0.5

A critical aspect of pulsed magnet operation is the dynamic mechanical response, which becomes significant when the characteristic timescale of the electromagnetic excitation is comparable to the natural mechanical periods of the conductor. In this analysis, this regime is explored by varying the normalized parameter k, which here scales the angular frequency ω_d of the applied half-sine force pulse. The prescribed spatial force distribution $X(r)$, corresponding to the quasi-force-free equilibrium, remains unchanged; the parameter k thus serves as a normalized driving frequency, $k \propto \sqrt{\omega_d}$, controlling the rate of load application.

The system's dynamic response is highly sensitive to the relationship between this driving frequency and the conductor's natural eigenfrequencies. For low k, the stress develops quasi-statically, and the peak von Mises stress η corresponds to the static solution.

With increasing values of the dimensionless parameter k, the inertial forces within the conductor become significant, causing the system's response to transition from a quasi-static to a genuinely dynamic regime. This transition is characterized by a pronounced frequency-dependent amplification of the mechanical fields, as detailed in Fig. 5.

Figure 5 presents the normalized dynamic response of the hollow cylinder to impulsive loading across a range of k values. Subfigure 5(a) shows the dynamic amplification factor for radial displacement, defined as $\frac{max|u_r(r,t)|}{\max|u_{st}|}$ through the whole impulse time, where $\max|u_{st}|$ is the maximum amplitude of radial displacements for quasi-static solution or $max\left|u_r\left(r,\frac{T}{4}\right)\right|$ for lower k. Subfigures 5(b) and 5(c) depict the normalized time and radial coordinate for $max|u_r(r,t)|$ during impulse time. Finally, subfigure 5(d) illustrates the corresponding dynamic amplification factor for the stress measure given by $\frac{\max\eta(r,t)}{\max\eta_{static}}$.

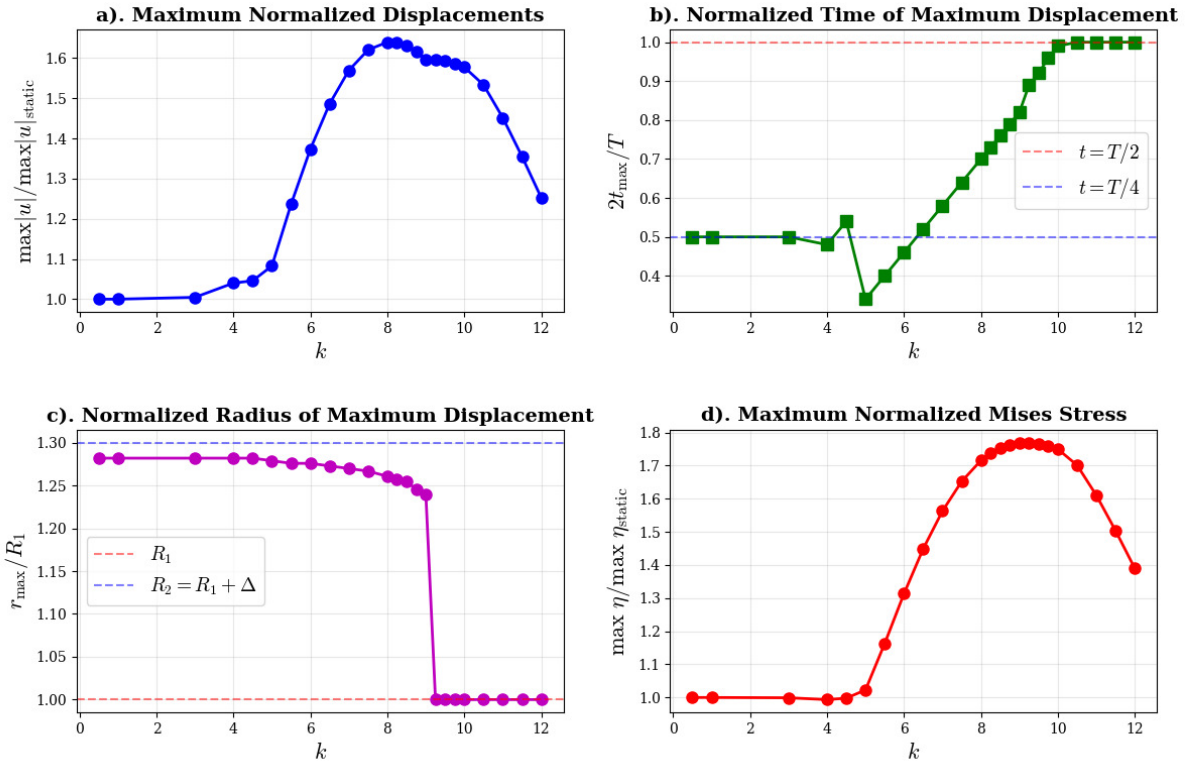

Fig. 5. Normalized mechanical values dependences from k: (a) $\frac{max|u_r(r,t)|}{\max|u_{static}|}$, (b) time corresponds to $max|u_r(r,t)|$ normalized to pulse time, (c) radial coordinate corresponds to $max|u_r(r,t)|$ normalized to inner radius, (d) $\frac{\max\eta(r,t)}{\max\eta_{static}}$

To elucidate the observed dynamic behavior, it is instructive to draw an analogy with the classical single-degree-of-freedom (SDOF) system. The response-ration time history is $R(t) = u_{SDOF}(t)/(\frac{p_0}{k_{SDOF}})$ of an undamped SDOF system subjected to a harmonic load $p_0 \sin\bar{\omega}t$, starting from the rest, is governed by:

$$m_{SDOF}\ddot{u}_{SDOF}(t) + k_{SDOF}u_{SDOF}(t) = p_0 \sin\bar{\omega}t. \quad (28)$$

Introducing the frequency ratio $\beta = \frac{\bar{\omega}}{\omega_{SDOF}} = \bar{\omega}\sqrt{\frac{m_{SDOF}}{k_{SDOF}}}$, the solution can be expressed as:

$$R(t) = \frac{1}{1-\beta^2}(\sin\bar{\omega}t - \beta\sin\omega_{SDOF}t). \quad (29)$$

For case of single half-sine impulse loading it is convenient to introduce $\alpha = t/\tau$, where $\tau = T/2$ is the end time point. Then, Eq. (26) will be:

$$R(\alpha) = \frac{1}{1-\beta^2}(\sin\pi\alpha - \beta\sin\frac{\pi\alpha}{\beta}),\ 0 \le \alpha \le 1. \quad (30)$$

Here introduced β can be rewritten in terms of ω_d (or k) as $\bar{\omega}$ and our found first natural frequency as ω_{SDOF}. In Fig. 6, the time-dependent response-ration for different values of k and corresponding β can be seen.

It can be seen that for k in operational regime ($\beta \le 0.008$) response-ratio curve will approach the quasi-static response curve. Starting from $k \approx 5$ the second term of Eq. (30) becomes significant, and the first peak corresponds to maximum response-ratio. The time

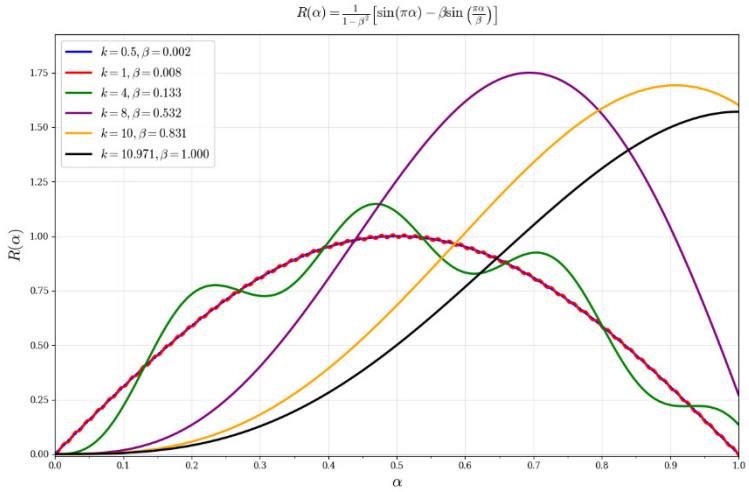

Fig. 6. Single degree-of-freedom response-ration time history representation for different k

α_{max} of this first maximum, found by taking the derivative and solving $dR(\alpha)/d\alpha = 0$, is given by:

$$\alpha_{max} = \frac{2\beta}{\beta+1}, \ 0 \le \alpha \le 1. \tag{31}$$

The dependence of α_{max} on k, plotted in Fig. 7, explains the trend observed in Fig. 5(b): the instant of maximum displacement shifts with increasing k. It reaches $\alpha_{max} = 1$ at $\beta = 1$ ($k \approx 10.971$), that means that driven frequency of impulse becomes equal to the first natural frequency of the system.

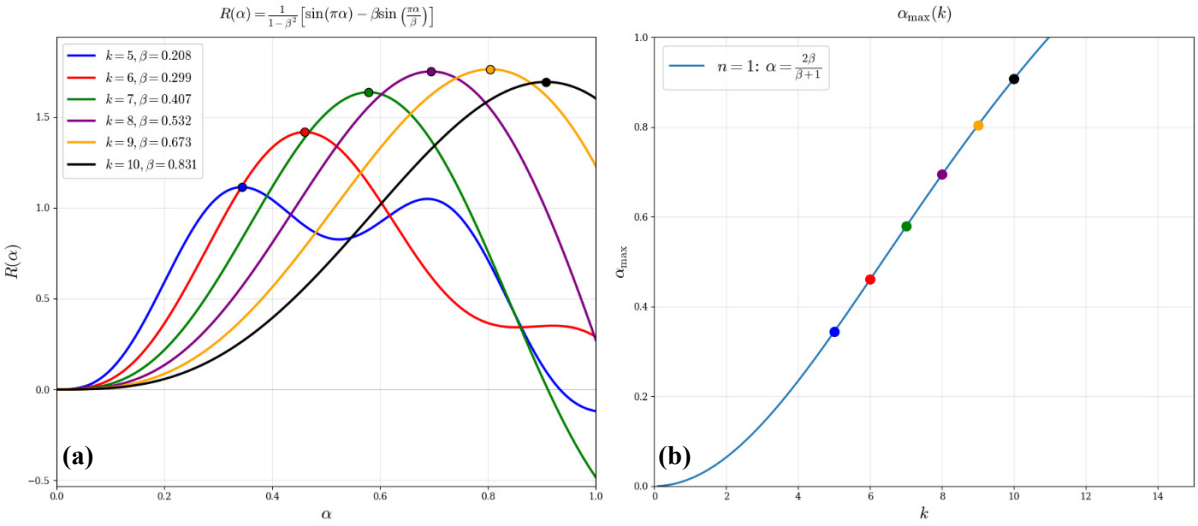

Fig. 7. Maximum single degree-of-freedom response-ration time history representation for different k (a) and corresponding normalized times of maximum (b)

The analytical model of the hollow cylinder (Fig. 5) reveals a decrease in the maximum recorded displacement and stress for k values beyond the resonant point ($\beta > 1$). This occurs because the simulation time is limited to the impulse duration τ. At higher k, the maximum system response may occur during the subsequent free-vibration phase, governed by the displacement $u(r,\tau)$ and the velocity $\dot{u}(r,\tau)$ conditions at time τ. Although the absolute maximum *during the impulse* does not peak precisely at $\beta = 1$

in either the SDOF or the cylinder model, the resonant condition $\beta = 1$ yields the largest amplitude of *free vibrations* after the load is removed. This post-impulse response is critical for assessing potential fatigue damage and the structural integrity of the conductor under repeated loading.

Conclusions

The dynamic analysis of a hollow cylindrical quasi-force-free magnet conductor subjected to a transient electromagnetic pulse yields the following principal conclusions:

1. The natural vibrational spectrum of a free, hollow cylindrical conductor has been determined analytically. For a typical geometry ratio ($g = 1.3$), the fundamental dimensionless eigenfrequency is $\widehat{\omega_1} \approx 0.797$.

2. A dynamic model has been developed, solving the forced mechanical response to a prescribed volumetrically distributed Lorentz force via Laplace transforms techniques. It is critical to note that this analysis decouples the mechanical dynamics from the electromagnetic diffusion process; the spatial force profile $X(r)$ is assumed from a static quasi-force-free equilibrium and is not recalculated during the pulse. This model provides complete time-dependent displacement and stress fields for an arbitrary pulse shape.

3. The system's response is governed by the ratio of the pulse driving frequency to the fundamental natural frequency, analogous to the frequency ratio β in a single-degree-of-freedom (SDOF) system. For the operational regime with millisecond pulses ($k \leq 1$, $\beta \ll 1$), the response is quasi-static, and peak stresses align with static model predictions.

4. A transition to a genuinely dynamic regime occurs for microsecond ([28–31]) pulses ($k > 1$, $\beta \to 1$), characterized by frequency-dependent amplification and a shift in the time of peak response within the pulse duration, as accurately predicted by the SDOF analogy. The most severe dynamic amplification of stresses (exceeding static levels by a factor of 1.77 in Fig. 5) was observed.

5. Crucially, while the absolute maximum stress recorded *during* the impulse may not peak exactly at $\beta = 1$, this condition produces the largest amplitude of *free vibrations* after the load is removed and should be considered in models with damping. This post-impulse oscillatory response is critical for fatigue assessment and structural integrity of the magnet system.

6. The analysis confirms that for single-layer coils with long pulses, simplified static models are adequate for stress estimation. However, the developed dynamic methodology and the identified resonant behavior are essential for the design and integrity analysis of advanced magnets, particularly for multi-layer or composite systems [32] operating with fast pulses, where it can be further expanded and scaled. It should be noted that the present formulation is based on linear elasticity and a prescribed quasi-force-free force distribution. In more detailed coupled models, electromagnetic diffusion, damping, nonlinear material response at high stress levels, and deviations of the current distribution from the idealized profile may modify the quantitative values of dynamic amplification. These effects do not alter the frequency-controlled nature of the quasi-static-to-dynamic transition identified here but may influence the exact stress amplitudes in practical systems.

CRediT authorship contribution statement

Maxim I. Lobachev: conceptualization, methodology, investigation, writing – review & editing, writing – original draft, data curation.

Conflict of interest

The author declares that he has no conflict of interest.

References

1. Boriskov GV, Bykov AI, Dolotenko MI, Egorov NI, Kudasov YB, Platonov VV, Selemir VD, Tatsenko OM. Research in ultrahigh magnetic field physics. *Physics-Uspekhi.* 2011;54(4): 421.
2. Korshunov MM. Superconducting state in iron-based materials and spin-fluctuation pairing theory. *Physics-Uspekhi.* 2014;57(8): 813.
3. Bykov A, Temnikov F, Korshunov A, Kozabaranov R, Kudasov Y, Makarov I, Maslov D, Platonov V, Repin P, Strelkov I, Surdin O. Ultrahigh magnetic field study on Gd_2BaNiO_5: Suppression of the Haldane gap. *Physical Review B.* 2024;110(21): 214439.
4. Tkáč I, Benneyworth MA, Nichols-Meade T, Steuer EL, Larson SN, Metzger GJ, Uğurbil K. Long-term behavioral effects observed in mice chronically exposed to static ultra-high magnetic fields. *Magnetic Resonance in Medicine.* 2021;86(3): 1544–1559.
5. Zhang L, Hou Y, Li Z, Ji X, Wang Z, Wang H, Tian X, Yu F, Yang Z, Pi L, Mitchison TJ. 27 T ultra-high static magnetic field changes orientation and morphology of mitotic spindles in human cells. *eLife.* 2017;6: e22911.
6. Alves Z JR, Bay F. Magnetic pulse forming: Simulation and experiments for high-speed forming processes. *Advances in Materials and Processing Technologies.* 2015;1(3-4): 560–576.
7. Khvostenko PP, Anashkin IO, Bondarchuk EN, Chudnovsky AN, Kavin AA, Khvostenko AP, Kirneva NA, Kuzmin EG, Levin IV, Leonov VM, Lutchenko AV. Current status of tokamak T-15MD. *Fusion Engineering and Design.* 2021;164: 112211.
8. Ruess T. *A First 2 MW-Class (136)/170/204 GHz Multi-Frequency Gyrotron Pre-Prototype for DEMO: Design, Construction and Key Components Verification.* Germany: KIT Scientific Publishing; 2023.
9. Vu AT, de Vries PC, Carannante G, Carvalho IS, Cinque M, Gomez I, Kudlacek O, Mattei M, Moreau P, Nouailletas R, Pangione L. Progress in the iter plasma control system design. *Fusion Engineering and Design.* 2026;222: 115501.
10. Mattei M, Ambrosino R, Ariola M, De Vries P, De Tommasi G, Di Grazia LE, Gribov Y, Pangione L, Pironti A, Zabeo L. Recent developments in ITER magnetic control algorithms. *Fusion Engineering and Design.* 2026;222: 115492.
11. Battesti R, Beard J, Böser S, Bruyant N, Budker D, Crooker SA, Daw EJ, Flambaum VV, Inada T, Irastorza IG, Karbstein F. High magnetic fields for fundamental physics. *Physics Reports.* 2018;765-766: 1–39.
12. Zherlitsyn S, Wustmann B, Herrmannsdorfer T, Wosnitza J. Status of the pulsed-magnet development program at the Dresden High Magnetic Field Laboratory. *IEEE Transactions on Applied Superconductivity.* 2012;22(3): 4300603.
13. Wang S, Wu Z, Jiang S, Wang G, Huang R, Peng T. Development of Zylon-Kevlar-Zylon hybrid fiber reinforcement technology for 100T pulsed magnet at the WHMFC. *Journal of Physics: Conference Series.* 2020;30(4): 4301204.
14. Béard J, Billette J, Ferreira N, Frings P, Lagarrigue JM, Lecouturier F, Nicolin JP. Design and tests of the 100-T triple coil at LNCMI. *IEEE Transactions on Applied Superconductivity.* 2018;28(3): 4300305.
15. McDonald RD, Mielke CH, Rickel DG. *World Record Magnetic Field 100 T.* Los Alamos National Laboratory Report. Report number: 1305044, 2012.
16. Furth HP, Levine MA. Force-free coils and superconductors. *Nuclear Fusion.* 1962;2(4): 147–155.
17. Emelyanov OA, Glyavin MY, Golubev SV, Krivosheev SI, Kruchinin AI, Luchinin AG, Magazinov SG, Parfentiev AA, Shimansky SA, Shneerson GA, Voloshin KV. Quasi-force-free magnets of small volume for generators of short-wave microwave radiation. *IEEE Transactions on Applied Superconductivity.* 2023;34(5): 4900504.

18. Shneerson GA, Voloshin KV, Titkov VV, Rodin IY, Zapretilina ER, Hon TA, Hitrov NA, Ovsyannikov VS, Lantsetov A. Application of Quasi-Force-Free Winding Concept to Superconducting Magnetic Energy Storage. *IEEE Transactions on Applied Superconductivity.* 2024;34(5): 5701204.
19. Shneerson GA, Koltunov OS, Schneider-Muntau HJ, Titkov VV, Parfentjev AA. The concept of quasi-force-free magnets: theoretical substantiation, estimation of parameters, and feasibility. *Physica B: Condensed Matter.* 2004;346: 566–570.
20. Nemov AS, Lagutkina AD, Shneerson GA. A conceptual 3-D design of a non-destructive two-layer quasi-force-free magnet for megagauss field generation. *IEEE Transactions on Magnetics.* 2022;58(3): 8000609.
21. Shneerson GA, Khlybov AV, Belov AA, Nenashev AP, Parfentiev AA, Shimanskiy SA. Deformation and mechanical stresses in a magnet with thin-walled quasi-force-free winding. *Materials Physics and Mechanics.* 2022;48(3): 355–366.
22. Lobachev MI, Novokshenov AD. Solution to the Quasi-Static Axisymmetric Problem for a Single-Layer Quasi-Force-Free Magnet. *Moscow University Mechanics Bulletin.* 2025;80(5): 187–194.
23. Ghosh AK. Axisymmetric vibration of a long cylinder. *Journal of Sound and Vibration.* 1995;186(5): 711–721.
24. Keles I, Tutuncu N. Effect of anisotropy on axisymmetric dynamic response of thick-walled cylinders. *International Journal of Pressure Vessels and Piping.* 2009;86(7): 435–442.
25. Gazis DC. Exact Analysis of the Plane-Strain Vibrations of Thick-Walled Hollow Cylinders. *The Journal of the Acoustical Society of America.* 1958;30(8): 786–794.
26. Jacquot RG, Steadman JW, Rhodine CN. The Gaver-Stehfest algorithm for approximate inversion of Laplace transforms. *IEEE Circuits & Systems Magazine.* 2012;5(1): 4–8.
27. Shneerson GA, Koltunov OS, Krivosheev SI, Adamian YE, Berezkin AN, Nenashev AP, Parfentiev AA. Models of magnets with the quasi-force-free winding manufactured from the thin solid sheets or transposed conductors. *IEEE Transactions on Plasma Science.* 2010;38(8): 1731–1738.
28. Krivosheev SI, Korovkin NV, Slastenko VK, Magazinov SG. Destruction of brittle materials by microsecond pressure pulses at their formation by magnetic pulse method. *International Journal of Mechanics.* 2015;9: 293–299.
29. Krivosheev SI, Petrov YV. Testing of dynamic property of materials under microsecond duration pressure created by the pulse current generator. In: *Proceedings of international conference on megagauss magnetic field generation and related topics*. Moscow; 2002. p.112. (In Russian)
30. Krivosheev SI, Magazinov SG, Alekseev DI. On the impact of the elastic-plastic flow upon the process of destruction of the solenoid in a super strong pulsed magnetic field. *Journal of Physics: Conference Series.* 2018;946(1): 012040.
31. Krivosheev SI, Shneerson GA, Magazinov SG, Zhukov DV, Voloshin KV. Destruction threshold of ZrO2 under microsecond magnetic-pulse action. *Materials Physics and Mechanics.* 2023;51(7): 7–14.
32. Xiao H, Yin Z, Chen X, Deng Z, Wang P, Chen S, He Y. Comprehensive analyses of buckling and stress failure of high-field pulsed magnets under biaxial Lorentz force body load. *Thin-Walled Structures.* 2023;183: 110341.

MATERIALS PHYSICS AND MECHANICS RESEARCH ARTICLE

Submitted: December 3, 2025 **Revised: March 10, 2026** **Accepted: March 18, 2026**

Interpretation of macroscopic and microscopic optical properties of Sm^{3+} doped ZnF_2-PbO-B_2O_3 glass systems

B. Suresh [1], P. Naresh [2]✉, P. Sobhanachalam [3], N. Narasimha Rao [4], Ch. Rani [1], M. Srinivasa Reddy [5]

[1] Kallam Haranadha reddy Institute of Technology, Guntur, Andhra Pradesh, India

[2] VR Siddhartha School of Engineering, Siddhartha Academy of Higher Education (Deemed to be University), Vijayawada, Andhra Pradesh, India

[3] Lakireddy Bali Reddy College of Engineering, Mylavaram, Andhra Pradesh, India

[4] Krishna University Dr. MRAR College of PG Studies, Nuzvid, Andhra Pradesh, India

[5] Univ. College of Engineering and Technology, Acharya Nagarjuna University, Nagarjuna Nagar Andhra Pradesh, India

✉ nareshp6@rediffmail.com

ABSTRACT

The preparation and spectroscopic investigation of Sm_2O_3 doped ZnF_2–PbO–B_2O_3 glasses. XRD patterns confirmed their amorphous nature are reported. From measured densities, various physical parameters – including molar volume, optical band gap, refractive index, electronic polarizability and optical basicity were systematically evaluated and presented. Optical absorption spectra show well defined Sm^{3+} transitions from $^6H_{5/2} \rightarrow {}^6F_J$ where $J = {}^{11}/_2 - {}^1/_2$levels. The optical band gaps are found to be minimal for the glass containing 2.0 mol. % Sm_2O_3. Judd-Ofelt analysis yielded $\Omega_2 > \Omega_4 > \Omega_6$ with bonding parameter δ highest at 2.0 mol. % Sm_2O_3, indicating a less covalent environment. Overall, the linear variation of physical and optical properties reflects the compositional role of Sm_2O_3. These results provide useful for potential laser-host applications.

KEYWORDS

borate glasses • Sm doped glasses • optical parameters • JO parameters • FTIR spectra • lead contained glasses

Citation: Suresh B, Naresh P, Sobhanachalam P, Narasimha Rao N, Rani Ch, Srinivasa Reddy M. Interpretation of macroscopic and microscopic optical properties of Sm^{3+} doped ZnF^2-PbO-B^2O^3 glass systems. *Materials Physics and Mechanics*. 2026;54(2): 70–82.
http://dx.doi.org/10.18149/MPM.5422026_6

Introduction

In view of many aspects including structure, stability, chemical durability, hosting the modifier up to a larger extent etc., B_2O_3 stands as a unique glass network former among the others like SiO_2, P_2O_5, As_2O_3, and GeO_2. Literature studies on borate glasses [1–8] explicitly demonstrate that the structure of pure borate glass is primarily built from trigonal planer BO_3 flat triangles embedded with boroxol rings (B_3O_6). In general, the bonding between boron and oxygen in the planar BO_3 unit is partially covalent with sp^2 hybridization and partially ionic with differences in electronegativity (oxygen becomes more electronegative than boron). In pure borate glass, boroxol ring is formed by three BO_3 triangles, which subsequently create three-dimensional networks with bridging oxygens (BOs) which causes to attain characteristics including presumably low density,

high transparency in UV (ultraviolet) and IR (infrared) region, high thermal conductivity and lower electrical conductivity.

$PbO–B_2O_3$ has wider glass forming region ranging from 0.4 to 90 mol. % of PbO with stable phase separation. Adding PbO to B_2O_3 glasses significantly modifies their physical, optical and structural properties and also this modification is strongly compositional dependent. With low PbO concentrations up to ~ 20 mol. % plays a modifier role by breaking B–O–B linkages and encourages the conversion of BOs into non-bridging oxides (NBOs) by changing the boron atoms to tetragonal BO_4 (sp^3 hybridization) from trigonal BO_3 planer (sp^2 hybridization), which provides the pathway to increase the density and compactness of the glass [9], whereas with moderate PbO concentration up to ~ 40 mol. % [10] still plays a modifier role but with transition phase by producing more tetragonal BO_4 units and NBOs with separation of borate network which causes the decrease in connectivity and glass samples becomes less rigid. However, with more than 40 to 80 mol. % [11], PbO starts acts as a modifier by forming Pb–O–Pb linkages leading to the formation of pyramidal or square –planer PbO_4 structural units. Hence the network becomes weaker, creates a pathway to lower the glass transition temperature, and increases thermal expansion, electrical conductivity properties and refractive index. Despite of the above benefits, there are some handicaps like toxicity and environmental hazards that become expensive for processing and disposal.

When ZnF_2 is added to a binary composition like $PbO–B_2O_3$, it interacts with both borate and lead oxide units by introducing Zn^{2+} and F^- ions. Adding ZnF_2 [12,13] leads to the conversion of BO_3 units to BO_4 units and PbO into PbF_2 as follows:

$$Zn^{2+} + BO_3 \rightarrow Zn - O - BO_4,$$

$$ZnF_2 + PbO \rightarrow ZnO + PbF_2.$$

Moreover, ZnF_2 is added to $PbO–B_2O_3$, Zn^{2+} competes with Pb^{2+} for network modifier positions by replacing the Pb–O bonds with Zn–O bonds. Hence, Zn^{2+} acts as a modifier along with this it is also important to mention that modifying action is strongly based on the composition of the glass. The presence of two different network modifier ions Zn^{2+} and Pb^{2+} can disrupt the glass network by breaking B–O bonds and introducing NBOs, influencing the atomic packing, density and glass transition temperature [14,15]. Hence the optimal Zn/Pb ratio leads to a glass with adjustable properties that were essential for maintaining the durability of the glass sample. With these factors, we are motivated to choose the glass composition of 20 % ZnF_2–20 % PbO–60 % B_2O_3 system for the present study.

In the last few decades, lanthanide ion-doped glasses have drawn more attention due to the exhibition of well-defined sharp absorption/emission spectra due to 4f–4f intra-ion transitions, high quantum efficiency, up-conversion luminescence, local symmetry of lanthanide ions, which leads to the host glass matrix suitable as the best optical materials for the lasers, biosensing, optical amplifiers, radiation dosimetry, tunable light-emitting diodes (LEDs). Samarium is the sixth element in the lanthanide series with atomic number 62, electronic configuration $[Xe]4f^66s^2$. These $4f^6$ unpaired electrons are responsible for the distinct optical and magnetic properties. In general, Samarium exists in two oxidation states Sm^{2+} $[Xe]4f^6$ and Sm^{3+} $[Xe]4f^5$ among these, the second one usually plays a crucial role in the optical properties.

Nevertheless, it is important to mention that this fluoroborate system provides improved rare-earth ion solubility and favourable spectroscopic characteristics compared with conventional borate glasses, making it a promising host matrix for studying Sm^{3+} ion optical properties. In the present investigation, we have attempted to characterize the optical absorption of Sm^{3+} in zinc lead borate glasses mixed with different concentrations of Sm_2O_3 to get insight into the possible use of these glasses as laser hosts. The study is additionally intended to understand the relation between the macroscopic and microscopic optical properties and physical parameters.

Materials and Methods

The present studied glass samples had been prepared by adopting the melting and quenching method which is as similar as mentioned in our previous works [12,16]. Within the glass-forming region of system, the compositions are chosen for the present study is 20 ZnF_2 – (20–*x*)PbO – 60 B_2O_3: *x* Sm_2O_3 (with *x* = 0.5, 1.0, 1.5 and 2.0 all in ml. %). The detailed chemical composition of their codes is displayed in Table 1. Figure 1 depicts a schematic representation of the glass sample preparation process.

Table. 1. Composition of glass samples (all in mol. %)

Sample Code	ZnF_2	PbO	B_2O_3	Sm_2O_3
S_0	20.0	20.0	60.0	---
S_1	20.0	19.5	60.0	0.5
S_2	20.0	19.0	60.0	1.0
S_3	20.0	18.5	60.0	1.5
S_4	20.0	18.0	60.0	2.0

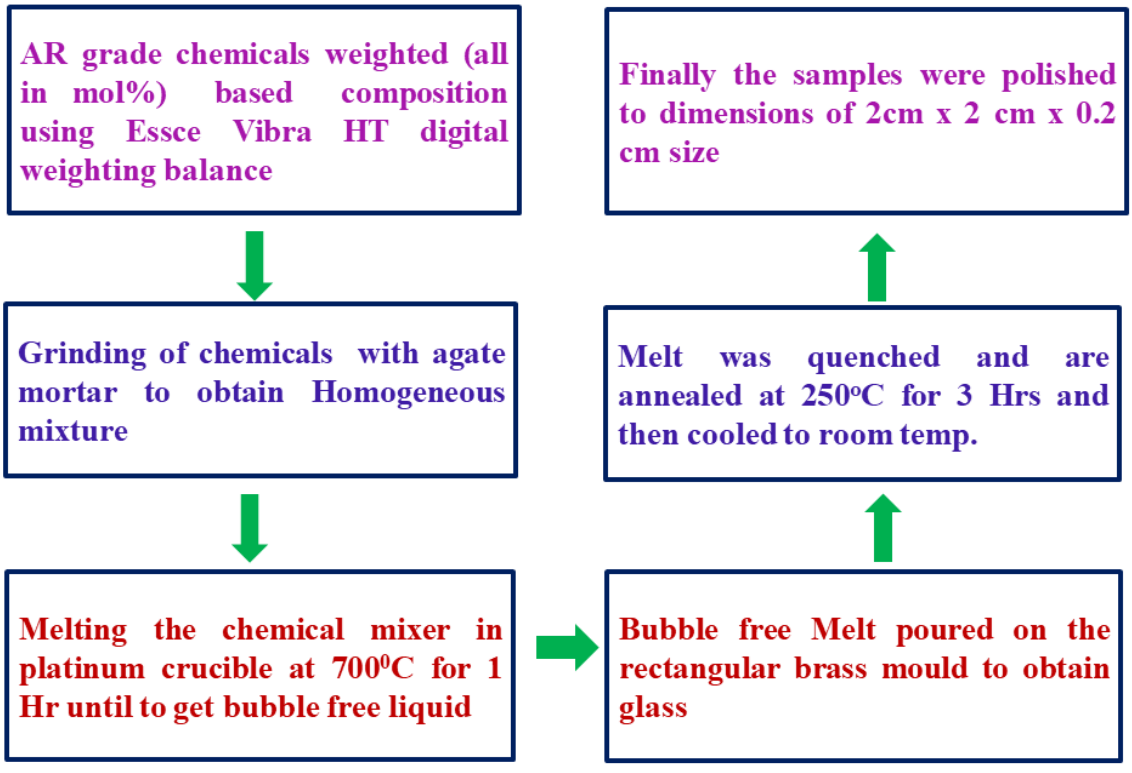

Fig. 1. Flow-chat of various steps involved in preparation of ZnF_2-PbO-B_2O_3:Sm_2O_3

The X-ray diffraction (XRD) patterns were recorded using the Philips PW 1830 X-ray diffraction spectrometer. The optical absorption spectra of samples acquired by using the JASCO V-670 UV-VIS spectrophotometer at room temperature in the wavelength range of 300–1800 nm. The infrared transmission spectra recorded by the Shimadzu IR Affinity-1S spectrophotometer by using KBr pellets in the 400–2000 cm^{-1} wavenumber region. The Vibra HT density kit is used for measuring the weights of the glass samples in air as well as in buoyant medium acetone. The refractive index of the glass samples measured using the Abbe refractometer using monochromatic wavelength 589.3 nm with mono-bromo naphthalene as the contact layer.

Results and Discussion

Using classical Archimedes' principle, densities have been computed, by measuring the weights of the samples in acetone and air using the equation:

$$\rho = \left(\frac{W_a}{W_a - W_l}\right)\rho_b, \quad (1)$$

where ρ is density of the sample, W_a and W_l are the samples weights in O-xylene and air, respectively, ρ_b is is density of the O-xylene. It was discovered that densities decreased as the quantity of dopant Sm_2O_3 in the glass matrix increased. Using these obtained densities various other significant parameters viz., molar volume (V_m), oxygen packing

Table 2. Physical parameters of Sm_2O_3 doped ZnF_2–PbO–B_2O_3 glasses

Property	Standard relation	Sample code				
		S_0	S_1	S_2	S_3	S_4
Density (ρ), g/cm³	$\rho = \left(\frac{W_a}{W_a - W_l}\right)\rho_b$	4.173	4.165	4.159	4.157	4.142
Avg. mol. weight ($\bar{M}$)	$\bar{M} = \sum X_i M_i$	107.09	107.72	108.35	108.97	109.60
Refractive index (n)	Experimental	1.685	1.723	1.735	1.742	1.757
Molar volume (V_m), cm³/mol	$V_m = \bar{M}/\rho$	25.66	25.86	26.05	26.21	26.46
Sm^{3+} ion concentration (N_i), $\times 10^{21}$ ions/cm³	$N_i = \frac{N_A x_i \rho}{\bar{M}}$	---	11.60	23.10	34.50	45.50
Inter ionic distance (r_i), Å	$r_i = \left[\frac{1}{N_i}\right]^{1/3}$	---	4.411	3.510	3.072	2.800
Polaron radius (r_p), Å	$r_p = \frac{1}{2}\left[\frac{\pi}{6N_i}\right]^{1/3}$	---	1.777	1.414	1.238	1.128
Reflection loss (R_L), $\times 10^{-2}$	$R_L = \left[\frac{n-1}{n+1}\right]^2$	0.0650	0.0704	0.0722	0.0732	0.0753
Molar refraction (R_m)	$R_m = \left(\frac{n^2-1}{n^2+2}\right)V_m$	12.293	12.829	13.059	13.219	13.512
Molar electronic polarizability (α_m)	$\alpha_m = \frac{R_m}{2.52}$	4.878	5.091	5.182	5.245	5.361
Electronic polarization (α_e)	$\alpha_e = \frac{3(n^2-1)}{4\pi N_A(n^2+2)}$	1.899	1.967	1.987	1.999	2.025
Metallization criterion (M)	$M = 1 - \frac{R_m}{V_m}$	0.520	0.503	0.498	0.495	0.489
Energy gap (E_g), eV	$E_g = (\alpha\hbar\omega)^{1/2} = C(\hbar\omega - E_o)$	1.620	1.599	1.593	1.589	1.581

density (OPD), polaron radius (R_p), inter–ion distance (R_i), and dopant-ion concentration (N_i) are estimated and presented in Table 2 along with used standard equations [17,18]. Table 2 shows that molar volume and Sm^{3+} ion concentration increase, whereas polaron radius and inter-ionic distance decrease with increasing the Sm_2O_3 content.

The absolute refractive index (*n*) at a specific wavelength of 589.3 nm was measured. The refractive index values for the studied samples were found ~ 1.68 to 1.76 following the increasing trend with increasing the Sm_2O_3 content. Using standard relations along with the measured densities and refractive indices, the physical parameters such as molar refraction, molar electronic polarizability, and metallization criteria were evaluated and same were systematically presented in Table 2. From Table 2, it is observed that molar refraction and molar electronic polarizability increase with increasing the Sm_2O_3 content, whereas the metallization criteria decrease with Sm_2O_3 content.

The diffraction patterns of all samples exhibited broad diffuse halos without any sharp crystalline peaks, confirming the amorphous nature of the glasses across the prepared compositional range. Since all compositions displayed similar amorphous diffraction features, only a representative XRD pattern corresponding to the S_4 sample (2.0 mol. % Sm_2O_3) has been presented in Fig. 2.

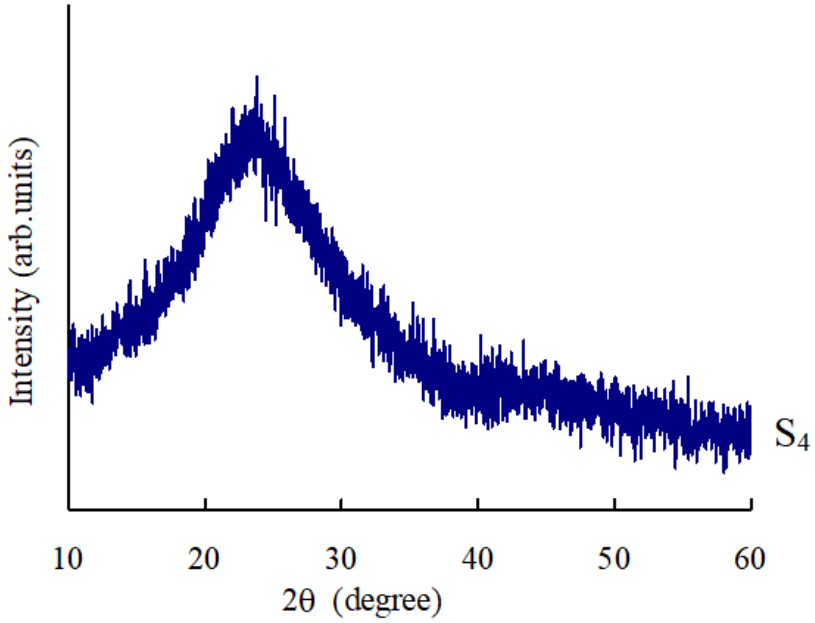

Fig. 2. X-ray diffraction pattern of ZnF_2–PbO–B_2O_3 glasses doped with 2.0 mol. % Sm_2O_3

The optical absorption spectra of Samarium doped ZnF_2–PbO–B_2O_3 glasses recorded at room temperature in the wavelength range 200–2000 nm is shown in Fig. 3. The spectra of S_1 samples exhibits the absorption bands with peak positions at about 935, 1070, 1224, 1367, 1364, and 1578 nm. Based on the literature [19,20], these observed bands are assigned due to $^6H_{5/2} \rightarrow {}^6F_{11/2}$, $^6F_{9/2}$, $^6F_{7/2}$, $^6F_{5/2}$, $^6F_{3/2}$, and $^6F_{1/2}$ transitions respectively. Other glass samples also exhibit peaks with a slight shift in band position which is expected due to the structural changes that take place in a sample by the compositional change. The details of the observed band positions for the samples are presented in Table 3.

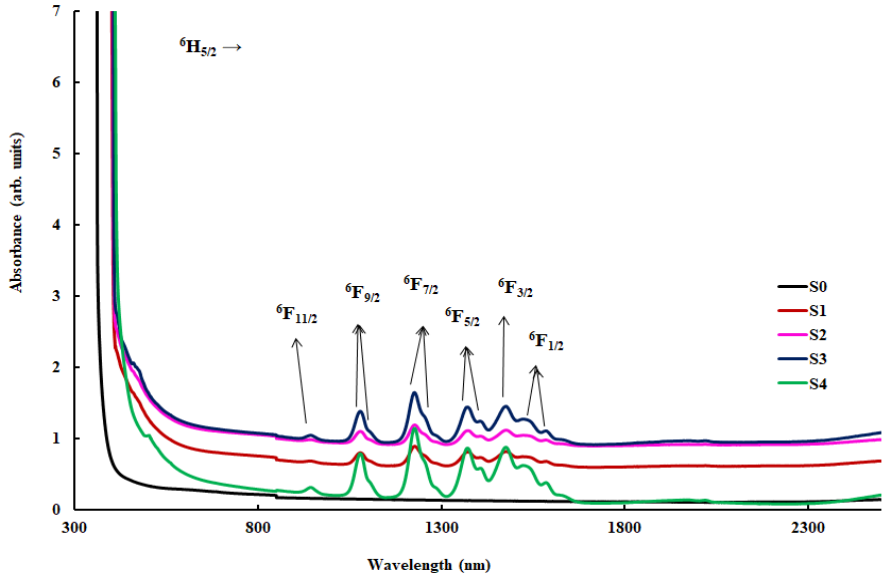

Fig. 3. Optical absorption spectra for ZnF_2–PbO–B_2O_3 glasses mixed with different concentration of Sm_2O_3

Table 3. Optical absorption data and band gaps of Sm_2O_3 doped ZnF_2–PbO–B_2O_3 glasses

	Glass				
	S_0	**S_1**	**S_2**	**S_3**	**S_4**
Cut-off wavelength, nm	361.5	380	406	407	409
$^6H_{5/2}\rightarrow{}^6F_{11/2}$	---	935	931	933	936
$^6H_{5/2}\rightarrow{}^6F_{9/2}$	---	1070	1073	1075	1076
$^6H_{5/2}\rightarrow{}^6F_{7/2}$	---	1224	1223	1224	1225
$^6H_{5/2}\rightarrow{}^6F_{5/2}$	---	1367	1365	1366	1368
$^6H_{5/2}\rightarrow{}^6F_{3/2}$	---	1394	1395	1397	1398
$^6H_{5/2}\rightarrow{}^6F_{1/2}$	---	1578	1579	1579	1580
Optical band gap E_o, eV	3.40	3.02	2.98	2.92	2.90

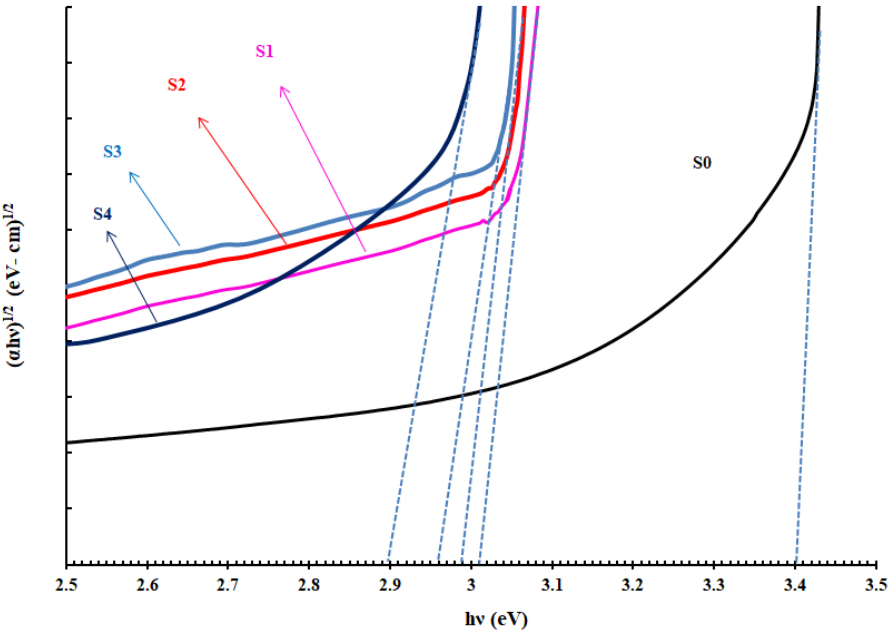

Fig. 4. Tauc plots between $(\alpha\hbar\omega)^{1/2}$ vs $\hbar\omega$ for ZnF_2–PbO–B_2O_3 glasses mixed with different concentration of Sm_2O_3

The optical band gap (E_o) of all the glasses is evaluated by drawing Tauc plots between $(\alpha\hbar\omega)^{1/2}$ vs $\hbar\omega$ (Fig. 4) as per Eq. (2) [12]:

$$E_g = (\alpha\hbar\omega)^{1/2} = C(\hbar\omega - E_o), \quad (2)$$

where $\hbar\omega$ is the photon energy, E_o is the optical band gap and C is a temperature independent constant related to the extent of the band tailing. The energy band gap of the samples is found to be the shrinkage with increasing the content of Sm^{3+} ion in the sample (Table 3), where X_i is the mol. % of the oxide compound,M_i is the molecular weight of the compound, ρ_b is the density of acetone, N_A is the Avogadro number, Z is the thickness of the sample. The IR transmission spectra in the region 400–1600 cm^{-1} for the pure as well as samarium oxide doped glasses were recorded and presented as Fig. 5.

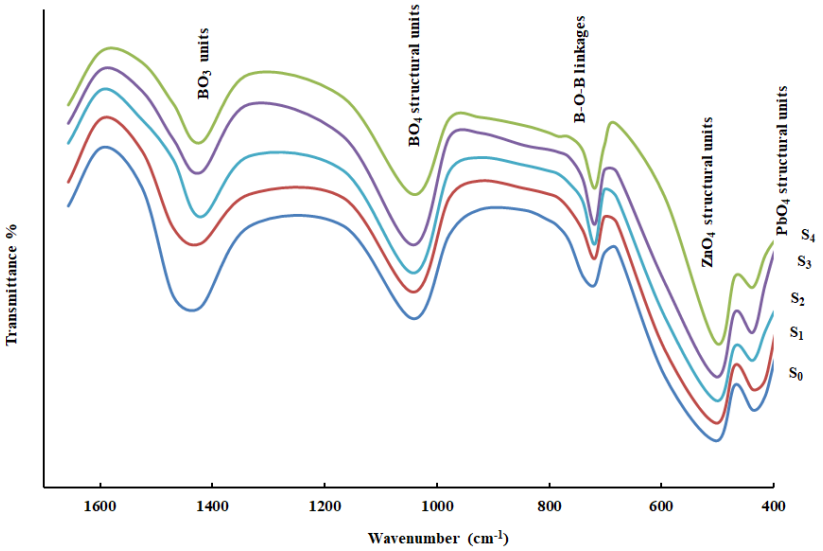

Fig. 5. Fourier transform infrared (FTIR) spectra of ZnF_2–PbO–B_2O_3: Sm_2O_3 glasses

It shows conventional bands due to the presence of borate groups, and they are due to the B–O–B linkages at about 710 cm^{-1}, BO_4 structural units at about 1060 cm^{-1}, BO_3 units are at about 1425 cm^{-1}, respectively. Additionally, at about 450 cm^{-1}, a band due to PbO_4 vibrations is also located in these spectra [13,21]. With the introduction of Sm_2O_3 (0.5–2.0 mol. %) into the glass network, no new additional bands appeared. The summary of the data on various bands observed in the IR spectra of ZnF_2–PbO–B_2O_3: Sm_2O_3 glasses are presented in Table 4.

Table 4. Band positions (in cm^{-1}) in the IR spectra of ZnF_2–PbO–B_2O_3 glasses doped with different concentrations of Sm_2O_3

Assignment	Glass				
	S_0	S_1	S_2	S_3	S_4
BO_3 units, cm^{-1}	1470	1462	1448	1435	1421
BO_4 groups, cm^{-1}	1039	1041	1045	1052	1068
B-O-B linkage, cm^{-1}	719	721	720	719	721
ZnO_4 units, , cm^{-1}	503	503	501	505	502
PbO_4 units, cm^{-1}	437	435	436	442	435
BO_3 units, cm^{-1}	1470	1462	1448	1435	1421

Among different constituents in the present studied glass composition of ZnF_2-PbO-B_2O_3: Sm_2O_3, B_2O_3 is the good glass network former, the primary structural units include; trigonal boron (BO_3) group, tetragonal born (BO_4) group [22], boroxol rings (B_3O_6), when mixed with modifiers, forms a complex super structural unit like di-borate $[B_2O_5]^{2-}$, tri-borate $[B_3O_7]^{5-}$, meta-borate $[BO_2]^-$ and pen-ta-borate $[B_5O_8]^{3-}$etc. The IR transmission spectrum of pure glass sample (S_0) exhibits two groups of characteristic board bands at about 1425 and 1060 cm^{-1}, which are the evidence of trigonal BO_3 and tetragonal BO_4 structural units. Additionally, the spectrum also shows that another two bands at about 710 and 450 cm^{-1} are attributed to the B–O–B vibrations and PbO_4 structural units. The spectrum of sample S_2 also exhibits similar bands with a slight shift in wave number. Further, it is observed that the intensity of the tetragonal BO_4 band increases with the slight shift towards the lower energy side whereas the intensity of the trigonal BO_3 band decreases with a slight shift towards the higher energy side with increasing the content of the samarium ions. The increase in the BO_4 bands by the expensive of the BO_3 band is understood as the addition of the Sm_2O_3 converts the BO_3 units into BO_4 units by introducing the NBOs. This behavior suggests that the samarium ions play a modifier role in the glass matrix when mixed with a small concentration. The decrease in the density of the sample with an increase in the content of Sm_2O_3 also supports the above result as with an increase in the ratio of NBO/BOs, the glass structure becomes loosened and hence the density of the sample decreases with the increase in the content of the samarium ions.

Due to electron-electron coulombic interaction and spin-orbit (LS) coupling interactions among the free ion with $4f^5$ configuration (Sm^{3+} ion) splits into many energy levels specified by typical term symbols. Some major term symbols are ^6H_J(J = 5/2, 7/2, 9/2, 11/2, 13/2, 15/2), ^6F_J (J = 1/2 to 11/2) ^6P_J (J = 3/2, 5/2, 7/2), ^4G_J (J = 5/2, 7/2, 9/2, 11/2), ^4F_J (J = 3/2, 5/2, 7/2, 9/2), ^4I_J (J = 9/2, 11/2, 13/2, 15/2) and ^2H, ^2G, ^2F, ^2P (singlet and doublet states), respectively. By Hund's rule, $^6H_{5/2}$ has lowest $J = |L - S|$) value and is the ground state. When ions, like Sm^{3+}, are placed in a crystal field (like glass or crystals) their energy states split and shift due to the interaction between the ion and the surrounding ions or ligands in the host material. This shifting and splitting depends on the strength of the crystal field and the symmetry of the sm^{3+} ion site in the host. Generally, the absorption bands of the trivalent samarium ions in a host are categorized into two groups low energy transition band group spreads over the wavelength 800–1800 nm, and high energy transition band group spreads over the wavelength 320 to 650 nm. The optical absorption spectra of present investigated samples in Fig. 3 exhibit the sharp intensive bands in the NIR region only and are assigned due to $^6H_{5/2} \rightarrow {}^6F_{11/2}, {}^6F_{9/2}, {}^6F_{7/2}, {}^6F_{5/2}, {}^6F_{3/2}$, and $^6F_{1/2}$transitions respectively. All these transitions are spin allowed (ΔS = 0) and follow ΔJ = 0, ±1 from J = 5/2. The complete disappearance of some absorption transitions due to the presence of the modifier PbO was observed [23] may be due to the factor-like change in local symmetry around Sm^{3+} ions by PbO by reducing cross-linking and introducing NBOs, shielding and quenching effects from Pb^{2+} ions by its heavy atomic cores and high polarizability, interaction between electronic transitions and vibrations (vibronic coupling) succors to forbidden 4f-4f transitions or makes them extremely weak.

Judd-Ofelt (JO) parameters are vital to enhance the comprehension of optical characteristics, particularly concerning rare-earth ions such as samarium in glass

matrices. They bid valuable insights into properties like radiative transition probabilities, oscillator strengths, and branching ratios etc.

By applying JO theory and measuring the area under the absorption curves, the experimental oscillator strengths were determined by the simplified relation [24]:

$$f_{exp} = 4.318 \times 10^{-9} \int \varepsilon(\vartheta) d\vartheta, \quad (3)$$

where $\int \varepsilon(\vartheta) d\vartheta$ is the area under the absorption curve, $\varepsilon(\vartheta)$ is the molar absorptivity of the respective band at ϑ:

$$\varepsilon(\vartheta) = \frac{A}{cl}, \quad (4)$$

where $A/_l$ is the absorbance coefficient, c is the concentration of the lanthanide ion.

The calculated oscillator strengths for the electric dipole transition from the ground state (ψ) to the excited state (ψ') were obtained using the relation:

$$f_{cal} = \left(\frac{8\pi^2 mcv}{3h(2J+1)}\right)\left(\frac{(n^2+2)^2}{9n}\right)\sum_{\lambda=2,4,6}\Omega_\lambda\left(\langle\psi_J||U^\lambda||\psi_{J'}\rangle\right)^2, \quad (5)$$

where all the terms having their own standard meaning, which are mentioned in the literature [25,26], $\|U^\lambda\|$ are the square reduced matrix element of the unit tensor operator of the rank $\lambda = 2, 4, 6$, these standard values were acquired from [27].

The root mean square deviation values from the calculated and experimental oscillator strengths were obtained using the basic relation, which helps to understand the fitment of theoretical data with experimental data in the RE-doped glasses [28]:

$$\sigma_{r.m.s} = \sum \frac{(f_{cal} - f_{exp})^2}{N}. \quad (6)$$

where the absorption band energies (cm^{-1}), the experimental (f_{exp}) and calculated (f_{cal}) oscillator strengths estimated for the absorption band intensities of ZnF_2–PbO–B_2O_3:Sm_2O_3 glasses were presented as Table 5.

Table 5. The absorption band energies and the oscillator strengths for the transitions of Sm^{3+} ions in ZnF_2–PbO–B_2O_3 glasses

Trans. $^6H_{5/2}\rightarrow$		**$^6F_{11/2}$**	**$^6F_{9/2}$**	**$^6F_{7/2}$**	**$^6F_{5/2}$**	**$^6F_{3/2}$**	**$^6F_{15/2}$**	**Root mean square (r.m.s) deviation**
S_1	f_{cal}, 10^{-6}	0.016	4.051	2.554	3.071	2.005	0.324	0.937
	f_{exp}, 10^{-6}	2.250	3.901	2.362	3.164	1.589	0.148	
	Energy ν, cm^{-1}	6390	6781	7279	8115	9254	10586	
S_2	f_{cal}, 10^{-6}	0.015	2.502	2.901	3.319	1.916	0.296	1.521
	f_{exp}, 10^{-6}	3.719	2.409	2.729	3.319	1.590	0.182	
	Energy ν, cm^{-1}	6519	6807	7268	8112	9256	10585	
S_3	f_{cal}, 10^{-6}	0.040	9.689	7.445	8.340	5.078	0.802	2.624
	f_{exp}, 10^{-6}	6.330	9.332	6.922	8.543	4.026	0.373	
	Energy ν, cm^{-1}	6456	6794	7276	8118	9262	10579	
S_4	f_{cal}, 10^{-6}	0.059	15.061	10.796	12.109	7.480	1.193	2.933
	f_{exp}, 10^{-6}	6.998	14.503	1.036	12.41	5.902	1.131	
	Energy ν, cm^{-1}	6419	6774	7272	8118	9262	10579	

Using least squares fitting analysis, JO parameters T_λ $(\lambda = 2, 4, 6)$ were determined with the help of values $\|U^\lambda\|^2$ (taken from the literature), f_{exp}, f_{cal}, and *v* by the relation [29]:

$$f_c = [T_2(\|U^2\|)^2 + T_4(\|U^4\|)^2 + T_6(\|U^6\|)^2]\vartheta. \quad (7)$$

JO Intensity parameters $\Omega_\lambda(\lambda = 2,4,6)$ are calculated from the above obtained T_λ $(\lambda = 2,\ 4,\ 6)$ using the equation:

$$\Omega_\lambda = \left(\frac{3h}{8\pi^2 mc}\right)\left(\frac{9n}{(n^2+2)^2}\right)(2J+1)T_\lambda, \quad (8)$$

where all symbols have their own significant meaning as mentioned in [27], J is taken as 5/2 for the ground state of Sm^{3+} ion. The obtained JO intensity parameters Ω_λ $(\lambda = 2,\ 4,\ 6)$ for Sm_2O_3 doped $ZnO–PbO–B_2O_3$ glasses are displayed in Table 6. When the computed oscillator strengths are compared to the experimental oscillator strengths, a fair match is made. The root mean square (r.m.s) deviation between f_{exp} and f_{calc} is used to express the fit quality. The Judd-Ofelt theory's validity and suitability for the current glasses are confirmed by the comparatively low levels of these deviations.

Table 6. Judd-Ofelt parameters ($\Omega_l \times 10^{-20} cm^2$) of Sm^{3+} doped $ZnF_2–PbO–B_2O_3–B_2O_3$ glasses

Sample	Ω_2	Ω_4	Ω_6	Trends	Ref.
S_1	4.71	2.94	1.83	$\Omega_2 > \Omega_4 > \Omega_6$	This work
S_2	11.6	4.28	2.03	$\Omega_2 > \Omega_4 > \Omega_6$	This work
S_3	24.9	9.41	4.93	$\Omega_2 > \Omega_4 > \Omega_6$	This work
S_4	39.7	13.0	7.21	$\Omega_2 > \Omega_4 > \Omega_6$	This work
LBGS3	9.93	9.84	7.51	$\Omega_2 > \Omega_4 > \Omega_6$	[19]
LTTSm10	1.30	3.08	1.54	$\Omega_4 > \Omega_6 > \Omega_2$	[20]
BLCB20	3.78	0.96	0.68	$\Omega_2 > \Omega_4 > \Omega_6$	[23]

From JO-theory, among Ω_2, Ω_4, Ω_6, the first one is profound to the asymmetry of the local crystal field surrounding the RE-ion by breaking the electric dipole transition selection rule and making them allowed partially, as a result, provides information about the electron sharing behavior (covalent character) between the RE-ion and neighbouring ligands. Hence, the Ω_2 parameter acts like a strain for the asymmetry of the ligand field, reflecting the degree to which the local symmetry is distorted. For all present studied four glasses, the values of W_l are projected primarily in the following sequence: $W_2 > W_4 > W_6$. However, it is also observed that with the increase in concentration of the samarium these W_l (λ =2, 4, 6) increases.

The second phenomenological intensity parameter, W_4 usually describes the strength of electric-dipole transitions between 4f levels of the RE-ions, influenced by medium-range order properties of the host material. The observed increased intensity of the emission band due to electric dipole transition $^4G_{5/2} \rightarrow {}^6H_{7/2}$ along with the increase in W_4 with increasing the concentration of sm^{3+} ions strongly suggests that the local strength around RE-ion is increasing with the surrounding ligand by breaking B-O-B linkages and create NBOs, which may lead the loosening of the glass structure with the enhanced long-range polarization effects. Even though samarium is heavy, with increasing the concentration of Sm^{3+}, its network-modifying role and the structural loosening character can dominate, resulting in lower experimental density and increased molar volume. The observed increase in macroscopic optical properties like molar refraction (R_M) and molar electronic polarizability (α_m) with increasing content of samarium can be expected with increased local asymmetry and covalence around sm^{3+} ion due to a rise in W_2 value and rise in long-range local polarizability of samarium ions with the ligand due to rise in W_4. The observed decrease in the metallization criterion (M) with increasing Sm^{3+} ions also suggests an enhancement in the covalent nature of the glass matrix [30].

The observed increase in the third phenomenological intensity parameter, W_6 with Sm^{3+} content indicates enhanced long- range distortions in the ZnF_2–PbO–B_2O_3 glass matrix, suggests that the network becomes more flexible and polarizable at a broader scale, which, along with increases in W_2 and W_4, supports stronger electric-dipole transitions and enhanced luminescent performance.

To further validate the obtained JO parameters, a comparison with previously reported Sm^{3+} doped glass systems has been carried out and is presented in Table 6. It can be observed that the JO parameters in the present study follow the trend $\Omega_2 > \Omega_4 > \Omega_6$, which is consistent with several borate and oxide glass systems reported in the literature [19,20,23]. The comparatively higher Ω_2 values obtained for the present glasses indicate increased asymmetry and covalent character around the Sm^{3+} ion environment. Such behavior is commonly associated with the formation of non-bridging oxygens and structural modifications induced by rare-earth incorporation in the glass network. The observed values are therefore in reasonable agreement with previously reported results for Sm^{3+} doped glasses.

The favorable optical properties observed for Sm^{3+} doped ZnF_2-PbO-B_2O_3 glasses, including well defined absorption bands, suitable JO parameters and enhanced electronic polarizability, suggest that these materials may serve as promising candidates for photonic applications such as solid-state laser hosts, optical amplifiers, optical sensors and luminescent devices operating in the visible and near-IR regions.

Conclusions

20 % ZnF_2–(20-x) % PbO–60 % B_2O_3:xSm_2O_3 (x = 0, 0.5, 1.0, 1.5, 2.0) glass samples successfully prepared by melt-quenching technique. The amorphous nature of the prepared samples was confirmed by the X-ray diffraction spectra. Various macroscopic physical parameters viz., molar volume, molar refraction, molar electronic polarizability and metallization criterion were estimated using experimental density and refractive index. Optical absorption spectra of sm^{3+}doped samples exhibited intensive sharp bands blended with close convolution due to the vibronic coupling and are identified due to $^6H_{5/2} \rightarrow {}^6F_{11/2}$, $^6F_{9/2}$, $^6F_{7/2}$, $^6F_{5/2}$, $^6F_{3/2}$, and $^6F_{1/2}$ transitions respectively. Using JO-theory, experimental as well as calculated oscillator strengths were evaluated and also identified well in agreement with them. Three phenomenological intensity parameters follow the sequence: $W_2 > W_4 > W_6$. Using these microscopic JO parameters, the behavior of macroscopic optical parameters viz., molar refraction, molar electronic polarizability and metallization criterion were understood. FTIR spectra reveal that Sm^{3+} ions in the present glass matrix play the role of modifier by increasing the ratio of NBO/BOs. Overall, the obtained spectroscopic and structural characteristics indicate that Sm^{3+} doped present glasses are promising materials for photonic applications such as solid-state lasers, optical amplifiers, sensors and luminescent devices operating in the visible and near IR regions.

CRediT authorship contribution statement

Boddu Suresh: experiment and data curation; **Padamati Naresh**: writing – original draft, review & editing; **Pamarthi Sobhanachalam**: investigation; **Nagavarapu Narasimha Rao**: review & editing; **Chatla Rani**: data curation; **Maddireddy Srinivasa Reddy**: supervision.

Conflict of interest

The authors declare that they have no conflict of interest.

References

1. Singh GP, Singh J, Kaur P, Singh T, Kaur R, Singh DP. The role of lead oxide in $PbO-B_2O_3$ glasses for solid state ionic devices. *Materials Physics and Mechanics.* 2021;47(6): 951–961.
2. Misawa M. Structure of vitreous and molten B_2O_3 measured by pulsed neutron total scattering. *J Non-Cryst Solids.* 1990;122(1): 33–40.
3. Alderman OLG. Boroxol ring dissolution in molten and glassy B2O3 by neutron and x-ray diffraction difference methods. *J Chem Phys.* 2025;162(5): 054502.
4. Shirshnev PS, Snezhnaia ZG, Shirshneva-Vaschenko EV, Romanov AE, Bougrov VE. Relation of the optical properties of boron copper-containing glasses on the concentration of lithium. *Materials Physics and Mechanics.* 2018;40(1): 78–83.
5. Klinkov V, Archelkov VB, Semencha AV, Tsimerman EA, Sedegova TY, Rudskoy AI. Halide-containing zinc borosilicate glass as a matrix for $CsPbBr_3$ crystal. *Materials Physics and Mechanics*. 2023;51(2): 27–35.
6. Gautam C, Yadav AK, Singh AK. A Review on Infrared Spectroscopy of Borate Glasses with Effects of Different Additives. To be published in *Int. Sch. Res. Notice.* [Preprint] 2012. Available from: doi.org/10.5402/2012/428497
7. Wright AC. Borate structures: crystalline and vitreous. *Phys. Chem. Glas.: Eur. J. Glass Sci. Technol. B.* 2010;51(1): 1–39.
8. Kamitsos EI, Chryssikos GD. Borate glass structure by Raman and infrared spectroscopies. *J. Mol. Struct.* 1990;247: 1–16.
9. Cheng Y, Xiao H, Guo W, Guo W. Structure and crystallization kinetics of $PbOB_2O_3$ glasses. *Ceram. Int.* 2007;33: 1341.
10. Takaishi T, Ota T, Ogura K, Yoko T. Structural Study of $PbO-B_2O_3$ Glasses by X Ray Diffraction and ^{11}B MAS NMR Techniques. *J. Am. Ceram. Soc.* 2000;83(10): 2543-2548.
11. Dimitrov V, Kim SH, Yoko T, Sakka S. Third harmonic generation in $PbO-SiO_2$ and $PbO-B_2O_3$ glasses. *J. Ceram. Soc. Jpn.* 1993;101(1163): 59–63.
12. Naresh P, Naga Raju G, Reddy MS, Rao TV, Kityk IV, Veeraiah N. Dielectric and spectroscopic features of $ZnO-ZnF_2-B_2O_3$: MoO_3 glass ceramic- a possible material for plasma display panels. *J. Mater. Sci.: Mater. Electron.* 2014;25: 4902–4915.
13. Neeraja K, Rupesh Kumar A, Rao TGV M, Vijayalakshmi P, Rami Reddy M. The spectroscopic properties of Mo^{5+} in $ZnO-ZnF_2-B_2O_3$ glasses. *Trans Indian Ceram Soc.* 2013;72(1): 24–28.
14. Singh D, Singh K, Singh G, Manupriya Mohan S, Arora M, Sharma G. Optical and Structural Properties of $ZnO-PbO-B_2O_3$ and $ZnO-PbO-B_2O_3-SiO_2$ Glasses. *J. Phys.: Condens. Matter.* 2008;20(7): 075228.
15. Singh J, Thakur S, Yadav A, Kumar M. Impact of ZnO on the Physical and Optical Properties of $PbO-B_2O_3$ Glasses. *Acta Phys. Pol. A.* 2022;142: 195.
16. Suresh B, Srinivasa Reddy M, Siva Sesha Reddy A, Gandhi Y, Ravi Kumar V Veeraiah N. Spectroscopic features of Ni^{2+} ion in $PbO-Bi_2O_3-SiO_2$ glass system. *Spectrochim. Acta A.* 2015;141: 263.
17. Saritha D, Markandeya Y, Salagram M, VithalM, Singh A K ,Bhikshamaiah G . Effect of Bi_2O_3 on physical, optical and structural studies of $ZnO-Bi_2O_3-B_2O_3$ glasses. *J. Non-Cryst. Solids.* 2008;354: 5573.
18. Shelby J E, Ruller J. Properties of barium gallium germanate glasses. *Phys. Chem. Glasses.* 198;728: 262.
19. Rajaramakrishna R, Knorr B, Dierolf V, Anavekar R V, Jain H. Spectroscopic properties of Sm^{3+} doped lanthanum borogermanate glass. *J. Lumin.* 2014;156: 192–198.
20. Babu AM, Jamalaiah BC, Sasikala T, Saleem SA, Moorthy LR. Absorption and emission spectral studies of Sm^{3+} doped lead tungstate tellurite glasses. *J Alloys Compd.* 2011;509(14): 4743–4747.

21. Cheng Y, Xiao H, Guo W, Guo W. Structure and Crystallization Kinetics of PbO–B_2O_3 Glasses. *Ceram. Int.* 2007;33(7): 1341.
22. Biradar S, Dinkar A, Bennal AS, Devidas GB, Hareesh BT, Siri MK, Nandan KN, Sayyed MI, Es-soufi H, Chandrashekara MN. Comprehensive investigation of borate-based glasses doped with BaO: An assessment of physical, structural, thermal, optical, and radiation shielding properties. *Opt Mater.* 2024;150: 115176.
23. Srivastava P, Rai SB, Rai DK. Optical properties of Sm3+ doped calibo glass with addition of lead oxide. *Spectrochim. Acta A.* 2004;60(3): 637.
24. Ratnakaram YC, Naidu DT, Kumar AV, Rao JL. Characterization of Tm^{3+} doped mixed alkali borate glasses — spectroscopic investigations. *J Phys Chem Solids.* 2003;64(12): 2487–2495.
25. Judd B R. Optical Absorption Intensities of Rare Earth Ions. *Phys. Rev.* 1962;127: 750.
26. Ofelt GS. Intensities of crystal spectra of rare earth ions. *Journal of Chemical Physics.* 1962;37(3): 511–520.
27. Carnall WT, Crosswhite H, Crosswhite HM. Energy level structure and transition probabilities in the spectra of the trivalent lanthanides in LaF_3. *ANL Rep.* 1978;78: 95.
28. Zhang Y, Liu JM, Liu MH, Zhang ZB, Wong WH, Zhang DL. Error evaluation of Judd–Ofelt spectroscopic analysis. *Spectrochim Acta A Mol Biomol Spectrosc.* 2020;239: 118536.
29. Lakshman S V J, Ratnakaram Y C. Spectral studies of praseodymium(III) and thulium(III) in certain borate glasses. *J. Less-Common Met.* 1986;126: 227.
30. Dimitrov V, Komatsu T. An interpretation of optical properties of oxides and oxide glasses in terms of the electronic polarizability and average single bond strength. *J Univ Chem Technol Metall.* 2010;45(3): 219–250.

MATERIALS PHYSICS AND MECHANICS RESEARCH ARTICLE

Submitted: December 2, 2025 **Revised: March 12, 2026** **Accepted: March 27, 2026**

Processing structure property relationship of flax/hemp/glass hybrid laminates: multifactor effects of TiO_2, SiC, and fiber sequencing on mechanical and thermal performance

J.A. Solairaju ✉, **S. Thanikodi**

Saveetha School of Engineering, SIMATS, Chennai, Tamil Nadu, India.

✉ jothiarunachalams.sse@saveetha.com

ABSTRACT

This study investigates the mechanical, moisture resistance, and thermal behavior of hybrid flax/hemp/glass fiber reinforced epoxy composites incorporated with TiO_2 and SiC nanoparticles. The composites were fabricated using compression molding with different stacking sequences and varying nanofiller contents to evaluate their influence on tensile strength, flexural strength, microhardness, fracture toughness, water absorption, and thermal stability. The results indicate that both fiber stacking configuration and hybrid nanoparticle reinforcement significantly influence the performance of the composites. Among the tested configurations, the Sequence-3 laminate containing 2 wt. % SiC and 3 wt. % TiO_2 exhibited the best overall performance. Compared with the baseline composite, this optimized structure demonstrated a 33 % increase in tensile strength, 18 % improvement in flexural strength, 22 % enhancement in microhardness, and 9 % increase in fracture toughness, indicating improved load transfer and crack resistance. In addition, the incorporation of hybrid nanoparticles reduced water absorption by approximately 18 %, enhancing moisture resistance of the composite system. Thermogravimetric analysis further confirmed improved thermal stability, with delayed degradation temperatures attributed to the barrier effect and strong interfacial bonding provided by SiC and TiO_2 nanoparticles. Overall, the synergistic interaction between hybrid fibers and nanofillers significantly improves the structural, thermal, and environmental performance of the composites, demonstrating their potential as sustainable lightweight materials for advanced engineering and structural applications.

KEYWORDS

nanoparticles • hybrid fiber • mechanical strength • thermal properties • sustainable

Citation: Solairaju JA, Thanikodi S. Processing structure property relationship of flax/hemp/glass hybrid laminates: multifactor effects of TiO_2, SiC, and fiber sequencing on mechanical and thermal performance. *Materials Physics and Mechanics.* 2026;54(2): 83–100.
http://dx.doi.org/10.18149/MPM.5422026_7

Introduction

The fiber-reinforced polymer (FRP) composites have attracted a lot of attention in the academic and industrial fields because of their improved performance features and the capability to undergo an easy process [1]. Some of the factors that affect the properties of FRPs are the type of polymer used, the nature of the reinforcement used, the type of additives, and the mode of manufacturing. Epoxy is commonly used as a thermosetting resin in composite applications over other thermosetting resins available because of its better mechanical and thermal properties [2]. The growing demand for environmentally friendly, lightweight, sturdy, and affordable materials in aircraft and automobile manufacturing [3]. The properties of epoxy bestow it with the ability to be used in a wide range of applications, which include structural adhesives, metal coatings,

Publisher: Peter the Great St. Petersburg Polytechnic University

and matrix in fiber-reinforced composite applications [4]. Epoxy resins do include a few limitations, however, despite all the given advantages. Epoxy cured epoxy has low impact strength and has limited fracture toughness, whereby under scanning electron microscopy (SEM) images of neat epoxy specimens exhibit low resistance towards crack initiation and growth. Besides, epoxies are prone to environmental effects, particularly when exposed to moisture over an extended period [5]. Fiber-matrix interfacial bonding, fiber orientation, and layup sequence (which are all significantly important to the strength of composites) can be optimized, and additional gains (increasing the strength of the composite) can be made by the addition of nanoparticles. Fiber orientation in the loading direction improves loading transfer accordingly, and the mechanical performance [6]. The study investigates the long-term aging behavior of unidirectional carbon fiber reinforced plastic composites used in critical engineering applications such as aerospace and transportation. It focuses on the effects of cyclic loading, climatic exposure, and thermal aging on the material T107/ON190/R132436. Experimental results reveal significant material hardening during cyclic loading, strongly influenced by the applied aging program [7].

This work aims at developing the epoxy nanocomposite enclosures reinforced with 20 vol. % NaOH-treated natural sisal fibers at different nano-silicon carbide (SiC) particles loads of 3, 6, and 9 vol. % [8]. Such hybrid epoxy materials are produced leveraging on a thermally aided injection molding. Their functional characteristics are determined and compared with those of the epoxy composites reinforced only by 20 vol. % natural sisal fiber (SF) [9]. To contain these shortcomings and increase the usefulness of epoxy in moisture-sensitive areas, nanofillers, especially nano clay inclusion, have been seen as a delightful approach to combat the drawbacks [10].

The report found out that the reinforced soil had greater shear and compressive strengths than the control samples. Adding rice fibers to the content promoted the strength of failure, ductility, and shear resistance [11]. Conversely, the increased values of nanoclay lowered the failure strain. It was observed by microscopic examination that adding nanoclay to fibers provided greater inter-particle interaction between soil particles and fibers due to filling effect and generation of viscous gel. In general, the mechanical properties of clay soil were enhanced with the introduction of nanoclay and fibers, in what can be considered an inexpensive and eco-friendly soil stabilization alternative [12]. The tensile and flexural strengths of the 40 wt. % coir fiber-reinforced epoxy composite were 77.99 and 136.13 MPa (boosted by 44 and 23 % over the neat epoxy, respectively). When a nanoclay reinforcement was further used, the performance was even improved by 23 and 31.4 % on tensile strength and flexural strength, respectively, at 4 and 2 wt. % loadings. Fractographic analysis of the tensile fracture surfaces were carried out under scanning electron microscopy (SEM). The results intense synergetic effects that require the interplay between natural fibers, nanoclay and epoxy resin to realize the optimum composite material in terms of practical engineering applications [13]. Adding BYK dispersants to a combination of multi-walled carbon nanotubes (MWCNTs) and epoxy resin would help to optimize number and orientation of nanotubes in the matrix, leading to the increase in strength properties of the epoxy nanocomposites. In addition, the reinforced fiber-reinforced systems made using and reinforcing the optimized and by K-modified nanocomposite has improved flexural strength of hybrid composites made of carbon fibers [14].

The present research focuses on the development of polymer composites using a combination of natural and synthetic fibers along with hybrid nanoparticles, followed by an evaluation of their performance parameters. A notable gap exists in the existing literature regarding the blending of flax, hemp, and glass fibers within composite structures. To address this, the proposed study introduces a novel approach that incorporates silicon carbide (SiC) and titanium dioxide (TiO_2) into various fiber stacking arrangements. The composites are manufactured using the compression molding technique, and their mechanical, thermal, and moisture absorption properties are tested. Performance results of the reinforced composites will be compared with those of unreinforced counterparts. It is anticipated that the inclusion of SiC nanoparticles, combined with optimized fiber stacking, will lead to significant improvements in mechanical strength and moisture resistance compared to composites without nanoparticle reinforcement [15,16].

Materials and Methods

Materials

Premium-grade natural fibers comprising flax and hemp were procured through sustainable sourcing channels from certified organic cultivators in the Kanchipuram district of Tamil Nadu, India. These natural reinforcements were selected based on their exceptional mechanical properties, including high specific tensile strength (approximately 600–700 MPa for hemp and 930 MPa for flax) and excellent fiber-matrix interfacial compatibility [17] glass fiber reinforcement materials featuring unidirectional weave architecture were obtained from Composite Materials India Ltd., located in Bangalore, Karnataka, following their recognition as a premier supplier of advanced reinforcement solutions in the Indian composite industry. The polymer matrix system consisted of a low-viscosity bisphenol-A-based epoxy formulation (Huntsman Araldite GY250) paired with its corresponding aliphatic amine curing agent (Aradur HY840), both sourced from Huntsman Advanced Materials India Pvt. Ltd., Mumbai. This resin-hardener combination was specifically chosen for its superior mechanical characteristics, outstanding chemical resistance properties, and enhanced adhesion performance with natural fiber substrates, critical factors for optimizing composite integrity [18]. Chemical reagents for fiber surface modification, including analytical-grade potassium permanganate ($KMnO_4$) and sodium hydroxide (NaOH), were obtained from Sigma-Aldrich Chemicals Pvt. Ltd., Bangalore. These surface treatment chemicals were employed to enhance the hydrophobic nature of natural fibers while simultaneously increasing surface roughness and reducing moisture absorption tendencies, thereby optimizing fiber-matrix interfacial bonding and overall composite performance [19].

Sonication

An optimized ultrasonication protocol was employed to achieve a homogeneous distribution of TiO_2 nanoparticles and SiC within the epoxy matrix. Initially, predetermined quantities of epoxy were accurately measured and transferred into clean borosilicate glass containers, while both TiO_2 and SiC underwent thermal pretreatment at 250 °C for 2 h to

eliminate absorbed moisture and surface contaminants, thereby enhancing polymer matrix compatibility. The nanofillers were gradually incorporated into the epoxy in specified weight percentages, followed by preliminary manual stirring for 5 min using a glass rod to achieve initial wetting [20]. Current research demonstrating that medium-high frequency sonication (80–500 kHz) produces superior dispersion results compared to conventional low-frequency methods guided the selection of a Hielscher UP400St probe sonicator equipped with a 7 mm titanium tip. The optimized sonication parameters included a frequency of 24 kHz specifically calibrated for SiC and TiO_2 co-dispersion, 400 W power at 60 % amplitude to prevent nanofiller damage, and 45 min in pulse mode to minimize overheating [21]. Temperature control was maintained at 25 ± 2 °C using an ice bath to prevent thermal degradation, while continuous stirring at 200 rpm enhanced cavitation effects and prevented localized heating. Real-time monitoring through periodic sampling at 15-min intervals confirmed uniform gray coloration, indicating successful dispersion, with post-sonication analysis revealing a 95 % reduction in nanofiller agglomerate size compared to manual mixing alone. Following successful nanofiller dispersion, the corresponding amount of hardener was incorporated and blended using a mechanical stirrer at 300 rpm for 8 min, ensuring complete hardener integration while maintaining the achieved nanofiller dispersion state through this dual-stage mixing approach supported by recent research on epoxy nanocomposite processing [22].

Chemical treatment

The potassium permanganate ($KMnO_4$) surface treatment was applied to enhance the interfacial adhesion between flax and hemp fibers and the epoxy matrix in the composite system. Initially, the raw fibers were washed with clean water to remove impurities and contaminants that could interfere with the chemical treatment process [23]. After washing, the fibers were air-dried at room temperature to remove surface moisture. The cleaned fibers were then immersed in a 0.5 % $KMnO_4$ solution prepared in acetone for 1 h, allowing sufficient time for oxidation reactions to occur on the fiber surfaces. $KMnO_4$ acts as a strong oxidizing agent, introducing polar functional groups and increasing surface roughness, which improves mechanical interlocking and chemical bonding with the polymer matrix during composite fabrication [24]. Following the treatment, the fibers were thoroughly

Table 1. Material composition (G is glass fiber, F is flax, H is hemp)

Sequence ID	Property	Sample 1	Sample 2	Sample 3	Sample 4
Seq-1 (G / H / H / H / H / F / F / F / F / G)	Fiber, wt. %	45	51	50	49
	Epoxy, wt. %	55	45	45	45
	SiC, wt. %	0	1	2	3
	TiO_2, wt. %	0	3	3	3
Seq-2 (G / H / H / F / F / F / F / H / H / G)	Fiber, wt. %	45	51	50	49
	Epoxy, wt. %	55	45	45	45
	SiC, wt. %	0	1	2	3
	TiO_2, wt. %	0	3	3	3
Seq-3 (G / F / F / H / H / H / H / F / F / G)	Fiber, wt.%	45	51	50	49
	Epoxy, wt. %	55	45	45	45
	SiC, wt. %	0	1	2	3
	TiO_2, wt. %	0	3	3	3

rinsed with distilled water to remove residual chemicals and reaction by-products. The fibers were then oven-dried at 50 °C for 8–10 h to eliminate moisture and ensure proper fiber–matrix interaction during composite processing. This chemical treatment improves the surface morphology and reactivity of flax and hemp fibers, leading to better dispersion within the matrix and stronger interfacial bonding [25]. The detailed composite preparation procedure is summarized in Table 1.

Synthesis of the materials

The specifications of the epoxy-based hybrid composites used for fabrication are presented in Table 2. Prior to composite fabrication, silicon carbide (SiC) and titanium dioxide (TiO_2) nanoparticles were preheated at 300 °C to remove any moisture present on their surfaces. This preheating process helps improve the dispersion of nanofillers and enhances the interfacial bonding between the fillers and the epoxy matrix. The composite mixture consisted of 49–55 wt. % epoxy resin and 45 wt. % hybrid fibers. In addition, the hybrid fibers were chemically treated with 0.5 wt. % potassium permanganate ($KMnO_4$) to enhance fiber-matrix adhesion. The reinforcement system included nanofillers with different concentrations of SiC (0, 1, 2, and 3 wt. %) and TiO_2 (0 and 3 wt. %) [26]. To ensure uniform distribution of fibers and nanofillers in the matrix, the mixture was blended using a mechanical stirrer at 100 rpm until a homogeneous dispersion was achieved. The prepared mixture was then poured into a tool steel mold with dimensions of 30 × 30 × 0.5 cm^3. The composite laminates were fabricated using the compression molding technique at a die temperature of 120 °C under a pressure of 20 MPa for 1–2 min, which is a typical pressure range for polymer composite processing and ensures proper consolidation of the laminate. After molding, the composites were allowed to cool naturally to room temperature (27 °C) under ambient conditions with a relative humidity of 60 % [27]. The samples were then carefully demolded and post-cured at 80 °C for 2 h

Table 2. Materials specification

Parameter	Specification
Resin : hardener ratio, by weight	10 : 1
Matrix density, g/cm^3	1.15–1.20
Reinforcements	Flax fiber, hemp fiber, glass fiber (unidirectional)
Flax fiber tensile strength, MPa	930
Hemp fiber tensile strength, MPa	600–700
Fiber type (glass)	Unidirectional woven mat
Fiber weight fraction, wt. %	30–40
Stacking sequence	Glass/flax/hemp (G/F/H) and variations
Fiber orientation, °	0, 45, 90
Alkali treatment (NaOH)	5 wt. % for 2–4 h
$KMnO_4$ treatment, wt. %	0.5–1.0
Applied pressure, MPa	3–5
Curing condition	24 h at room temperature + post-curing at 80–100 °C for 2–3 h
Laminate thickness, mm	3–5
Plate dimensions, mm^2	300 × 300
Void content	< 5 %

to ensure complete crosslinking of the epoxy matrix. Finally, the cured hybrid composite laminates were cut into standard test specimens for subsequent mechanical and structural characterization. Flexural and microhardness sample are shown in Fig. 1 and 2.

(a) (b)

Fig. 1. Flexural test sample: (a) before test; (b) after tested

Fig. 2. Microhardness test sample

Performance of mechanical properties evaluation

Tensile strength measurements were performed on a Shimadzu AGS-X Series universal testing machine (50 kN capacity) under ASTM D638-22. Test specimens with dimensions of 165 × 13 ×3.2 mm^3 were employed, featuring a gauge length of 50 mm to ensure accurate strain measurement and minimize edge effects. Flexural properties were assessed following ASTM D790-17 using a three-point bending configuration. Rectangular specimens measuring 127 × 12.7 × 3.2 mm^3 were tested at a support span-to-depth ratio of 16:1, with testing conducted at a crosshead speed calculated according to the specimen depth requirements [28]. A calibrated deflectometer was employed to measure specimen deflection with an accuracy of ± 0.01 mm, ensuring compliance with the standard's precision requirements. Hardness measurements were carried out using a Vickers microhardness tester under a constant indentation load of 500 g with a dwell time of 15 s to ensure consistent and comparable hardness values for all composite samples. The fracture toughness (K_{IC}) of the composites was evaluated according to ASTM D5045 using a Universal Testing Machine (UTM) equipped with a three-point bending fixture at a constant crosshead speed. The test was performed on single edge notched bend (SENB) specimens, and the fracture toughness values were calculated using the standard equations specified in ASTM D5045. Water absorption characteristics were evaluated according to ASTM D570-22. Specimens were then immersed in distilled water at 23 ± 1 ºC for 24 h, after which they were surface-dried and reweighed to calculate percentage water absorption. All mechanical testing was conducted under controlled laboratory conditions maintained at 23 ± 2 ºC and 50 ± 5 % relative humidity. Each test was replicated five times to ensure statistical reliability, and final reported values represent the arithmetic mean with standard deviation calculations. Measurement uncertainty was maintained within ± 3 % for all testing procedures to account for experimental variations and ensure reproducible

results. This comprehensive testing protocol enabled accurate characterization of the mechanical behavior and environmental stability of the hybrid natural fiber nanocomposites. The samples were weighed after they had been removed at predetermined intervals and gently wiped with absorbent tissue to allow water present at the surface to be removed before again weighing as soon as the sample was wiped so as to track the increase in weight by the addition of water [29]. This was done daily until the weights of the specimens remained unchanged, after which it was used to be three days each, signifying saturation. The absorption behavior of the water was captured in specific time intervals of 10, 20, 30, 40, and 50 h to take up specific weight measurements, in the course of the immersion. The water absorbed (*WA*) percent was calculated by Eq. (1). Further, the mechanical performance data in terms of tensile strength, flexural strength, and fracture toughness reflected that the stacking sequence G/F/F/H/H/H/H/F/F/G presented the better mechanical properties of the composite. The favorable stacking order also acted as a reference point in comparing the effects of moisture absorption on the overall strength and durability of the composite:

$$WA(\%) = \left(\frac{W_1 - W_0}{W_0}\right) \times 100, \quad (1)$$

where the water absorption *WA* value is calculated based on the weight gain of the composite specimen, where W_1 represents the weight after water immersion and W_0 denotes the initial dry weight before immersion. This weight change is used to quantify the amount of moisture uptake by the material [30].

Results and Discussion

The mechanical performance results reveal that the sequence 3 showed the highest values across tensile strength, flexural strength, microhardness, and fracture toughness compared to the other sequences. The sequence 1 exhibited the lowest performance in most parameters, while the sequence 2 demonstrated intermediate values. The consistent improvement from the sequence 1 to the sequence 3 indicates the influence of fiber stacking order on strength and toughness are shown in Table 3. Overall, optimized stacking significantly enhances the composite's mechanical properties.

Table 3. depicts the Mechanical performance of the produced samples

Sequence	Sample	Tensile strength, MPa	Flexural strength, MPa	Microhardness, HV	Fracture toughness, MPa·m$^{1/2}$
Sequence-1 (G/H/H/H/H/F/F/F/F/G)	1	101.0 ± 2.1	119.0 ± 2.2	70.0 ± 1.3	1.99 ± 0.04
	2	104.0 ± 2.3	122.0 ± 1.9	74.0 ± 1.4	2.06 ± 0.05
	3	109.0 ± 2.2	130.0 ± 2.4	79.0 ± 1.5	2.27 ± 0.03
	4	107.0 ± 1.9	127.0 ± 2.1	77.0 ± 1.0	2.22 ± 0.05
Sequence-2 (G/H/H/F/F/F/F/H/H/G)	1	105.0 ± 1.8	130.0 ± 2.5	72.0 ± 1.1	2.19 ± 0.04
	2	108.0 ± 1.9	133.0 ± 2.6	75.0 ± 1.2	2.28 ± 0.06
	3	115.0 ± 1.5	138.0 ± 2.8	80.0 ± 1.3	2.41 ± 0.06
	4	113.0 ± 2.2	135.0 ± 2.3	76.0 ± 0.9	2.33 ± 0.03
Sequence-3 (G/F/F/H/H/H/H/F/F/G)	1	117.0 ± 2.1	135.0 ± 2.7	78.0 ± 1.0	2.35 ± 0.05
	2	119.0 ± 2.2	139.0 ± 2.9	86.0 ± 1.5	2.44 ± 0.06
	3	128.0 ± 2.5	144.0 ± 3.1	88.0 ± 1.3	2.53 ± 0.07
	4	123.0 ± 2.3	141.0 ± 3.2	84.0 ± 1.1	2.47 ± 0.06

Tensile strength

The tensile property of the nanoparticles reinforced composites is shown in Fig. 3. The fact was that all the composite specimens showed better tensile strengths than the neat matrix. A remarkable fact is that the sequence 3 composite has higher strength than the sequence 1 and 2 composites. Surprisingly, though, the sequence 2 composites performed better when compared to the sequence 1 in the nanoparticle's contents. The sharp reduction in tensile strength at the sample 4 was noted using SiC 3 wt. % and TiO_2 3 wt. % composite. The highest tensile strength was recorded among all the composites at a 45 wt. % fiber loading. According to Benhamadouche et al. [31], the recycled jute fabric-reinforced PP composites showed a tensile strength of 30 MPa and modulus of 4–4.5 GPa, which was almost two times higher than the composite jute-PP in the present study, to reach a high modulus. Analogously, tensile strength values of jute-PP composites ranged between 30 and 34 MPa, and modulus values between 2 and 4 GPa were identified by Shahinur et al. [32]. In connection, Akil et al. [33] in their related works, noted that, with an increase in flax fiber content up to 60 wt. %, the strength and modulus of the PLA-based composite reinforcement were enhanced. Nevertheless, present results reveal that nanoparticle content in all composites of more than 3 wt. % led to lower tensile strength. The fact that the fiber placement will contribute to low capacity to transfer loads in the composite, resulting in stress concentration near the fibers. The mechanical performance, however, is greatly increased because stress distribution is improved, and the matrix is strengthened with the addition of SiC and TiO_2 nanoparticles. These nanofillers facilitate the effective transfer of load and minimize stress concentration sites, and inhibit the growth of microcracks by reinforcing the fiber-matrix interface. On the other hand, fiber loadings create a higher chance of fiber agglomeration in the matrix, and this leads to an unequal path of strain and local regions of high concentrations of stress that help facilitate cracks. Also, high fiber-end density may create microcracks at the interface, which eventually lowers the strength and stiffness of the composite. Overall, fiber-reinforced polymer composites are tough due to the fibers, the matrix, and most importantly, due to the fibers interfacial bonding, which is enhanced significantly through SiC and SiO_2 dispersion. The tensile strength results indicate that the sequence 3 (G/F/F/H/H/H/H/F/F/G) exhibits the highest tensile

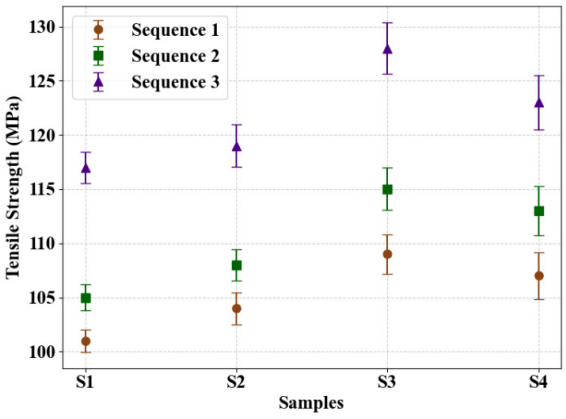

Fig. 3 Tensile strength of different fibers stacks with hybrid nanoparticles

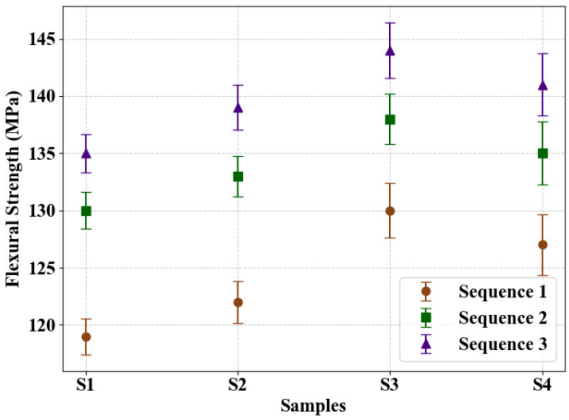

Fig. 4. Flexural strength of different fibers stacks with hybrid nanoparticles

performance among all composite configurations. The maximum tensile strength of 128.0 ± 2.5 MPa was recorded for the sample 3 in the sequence 3, followed by 123.0 ± 2.3 and 119.0 ± 2.2 MPa. This improvement is attributed to the optimized fiber stacking sequence and improved stress transfer between the fibers and epoxy matrix, which enhances load-bearing capability.

Flexural strength

Fiber-reinforced polymer composites' flexural behavior is strongly related to the architecture of these fibers, the interaction of the matrix, and the capability to distribute the load. Figure 4 shows the flexural strength of four composite samples (S1, S2, S3, and S4) stacked in three different stacking orders. In all samples, an increasing flexural strength was seen between the sequence 1 to the sequence 3. The sample S1 increased from about 101 (the sequence 1) to 117 MPa (the sequence 3). Likewise, S2, S3, and S4 saw the flexural strength increase by 117, 119, and 128 to 123 MPa, respectively, as the stacking sequence proceeded. Incremental improvements in the flexural strength of all the samples when the sequence 3 was used are explained by a more favorable positioning of the fibers and better distribution of the loads, which were achieved as a result of a more effective layering. The improved interfacial adhesion between the fibers and the epoxy matrix is probably achieved by the sequence 3, which reduces the possibility of microvoids and delamination regions that can easily become the crack creation sources due to the bending loads [34]. As well, a closer definition of loading-bearing fibers in sequence three is very probable to provide increased resistance to the deformation and spread of matrices. The presence of reinforcing materials, which are SiC and TiO_2 nanoparticles, may also be another reason behind the enhanced mechanical response due to the ability of the mentioned materials to provide stronger interfacial bonding, consolidate microvoids, and improve load transfer mechanics. These nanoparticles are secondary reinforcement fillers, enhancing rigidity and impact improvers in the case of bending [35]. They serve to fill in the microcracks and postpone the mechanisms of failure, which adds to the flexural strength observed in all of the stacking sequences. So, the optimum balance between the most promising combination of fiber stacking and dispersion of nanofillers explains why the structural efficiency of fiber-reinforced hybrid composites will always be brightest with the sequence 3.

Microhardness behaviour

Microhardness is a very vital mechanical property, which is employed in the measurement of the localised plastic surface forming response of a material and its capacity to resist abrasion. The effects of SiC and TiO_2-filled hybrid fiber reinforced composites on microhardness performance were evaluated under various stacking orders and the composition of the samples in this experiment. Figure 5 indicates that the base epoxy composite without nanoparticles had a microhardness which was about 72 HV. Conversely, the addition of nanofillers resulted in a characteristic increase in hardness in all sequences [36]. In particular, in the sequence 1, microhardness was moved to 79 HV (S3) with an increase of 9.4 percent over S1. Such an increase can also be attributed to the synergetic effect of SiC and the fiber reinforcement, which enhances interfacial

bonding and reduces the number of voids, which are the leading contributors to raising the surface resistance. In the sequence 2, microhardness was observed to be between 72 (S1) and 80 HV (S3). Addition of 2 wt. % SiC and 3 wt. % TiO_2 to S3 led to a 10.7 % increase over the baseline value of the sequence 1 (S1). The large enhancement is explained by the presence of a large surface area and inherent stiffness of the nanoparticle, which limits the mobility of the matrix and limits plastic deformation upon the indenter penetrating the material. The sequence 3 was the only time in which the microhardness level rose to the maximum value, as in the sample 3, which recorded 88 HV, which is a 22.7 % increase from the lowest record (the sequence 1, the sample 1). This excellent performance could have been achieved due to the optimum stacking of the fibers and the better distribution of the nanofillers, which will form a dense and mechanically strong interphase in the matrix. The fact that with adequate optimization of the sequence of fibers and integrating nanofillers it is possible to increase the microhardness of the hybrid composites [37].

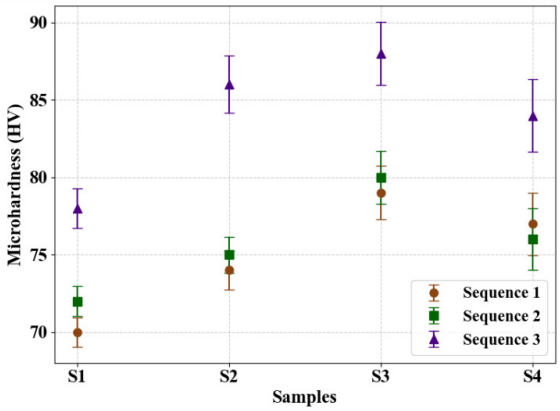

Fig. 5. Microhardness of different fibers stacks with hybrid nanoparticles

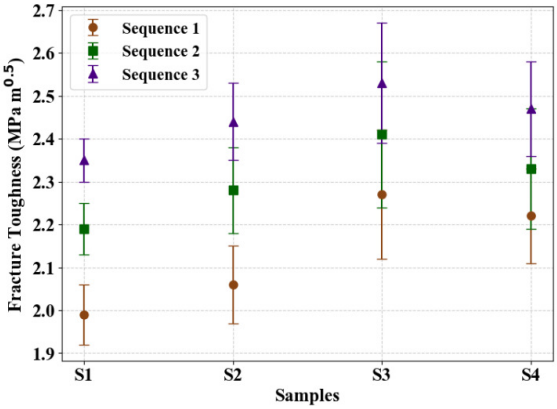

Fig. 6. Fracture toughness of different fibers stacks with hybrid nanoparticles

Fracture toughness of different composite

Fracture toughness is an essential parameter that indicates the capability of a composite material against crack formation and propagation with respect to stress. The fracture toughness of the hybrid fiber reinforced epoxy composite was tested on three stacking orders (the sequence 1, 2, and 3) with the insertion of glass (G), hemp (H), and flax (F) fibers in this investigation. Similarly, the results were that the sequence 1 (G/H/H/H/H/F/F/F/F/G) also presented with the least fracture toughness, but at a range between 1.99 and 0.5–2.22 MPa $m^{1/2}$. This has been due to the relatively lower toughness attributed to the predominance of hemp layers in the upper-mid section, which in turn is a result of having the lower elongation-at-break coupled with the moderate interfacial adhesion with the epoxy matrix, and thus, they may not be efficacious in halting crack propagation. Also, the fact that the stiffer glass layers were located at the furthest surfaces with no constraints in between them could have facilitated the concentration of stress at fiber-matrix interfaces. The fracture toughness has been increased by noticeable values in the sequence 2 (G/H/H/F/F/F/F/H/H/G), where the values were recorded to have been between 2.19 and 2.33 MPa·$m^{1/2}$. Such an arrangement offers more symmetrically

stacked hemp and flax and by placing the stiffer flax fibers in the center, it provides superior crack deflection and energy dissipation mechanisms. The change of fiber type throughout the laminate thickness results in a graded stiffness profile, which increases interfacial stress distribution and hinders crack growth [38]. The sequence 3 (G/F/F/H/H/H/H/F/F/G) produced the results with the highest values of fracture toughness of 2.35–2.47 MPa $m^{1/2}$ is shown in Fig. 6. This better performance can be reinforced by the fact that the flax fibers, which have greater toughness and interfacial bonding characteristics, are placed strategically close to the areas where the surface area is only an inch away, and the core parts. This streamlined design is probably attributed to improved crack-bridging, energy absorption, and delayed delamination. Also, laminated symmetrical and alternate fiber layers minimize stress concentrations due to the mismatch, thus establishing high crack initiation resistance. Results highlight the significant role of the stacking sequence of the refrain, which is important in the design of the fracture resistance of hybrid composites [39].

The microstructure of composite materials is examined with a scanning electron microscope to investigate the structure and the distribution of fibers and reinforcing materials within a compound. Figure 7(a) shows how natural fibers are dispersed and intermingled in the polymer framework. The fibres are seen to be oriented and entrenched into the matrix; they provide a reinforcing net that adds to the strength of the composite. A number of fractured ends of fiber and fiber pull-outs can be observed,

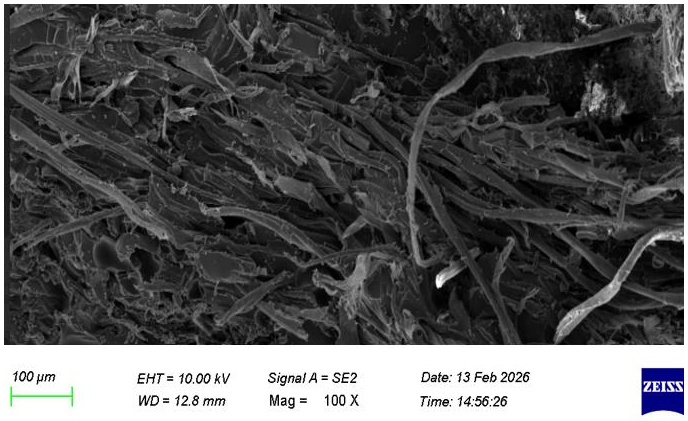

(a)

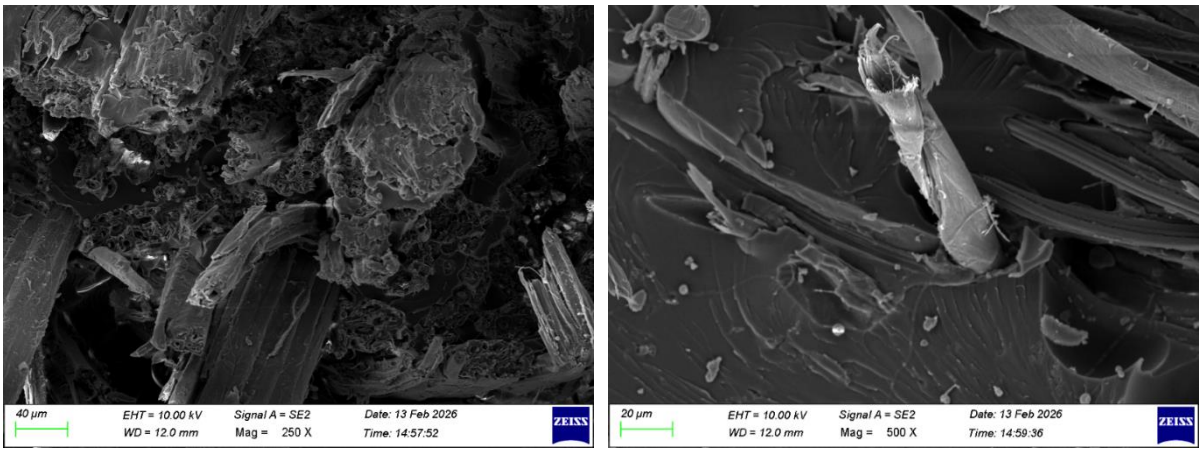

(b) **(c)**

Fig. 7. SEM Image of (a) the sequence 1, (b) the sequence 2, and (c) the sequence 3

which pointed towards the fact that the composite had interfacial debonding and fiber breakage under mechanical loading. Fiber pull-out is a typical form of failure in natural fiber composites and usually happens when the interlocking mechanism between the fiber and the matrix is less than the strength of the fiber itself. The existence of rough fracture surfaces indicates that the composite took in a considerable energy till failure.

Figure 7(b) shows the evidence of the cracking of the matrix and the localized interfacial gaps between the fibers and the polymer matrix. Such micro voids can be as a result of the incomplete impregnation of the fibers during composite fabrication process and as a result of entrapment of air during compression molding. These defects are capable of being the points of stress concentration and can cause crack propagation when subjected to external forces. However, the fibers are only partially embedded in the matrix meaning that there is a level of load transfer between the reinforcement and the matrix material. The irregular and rough surfaces of the fibers are also indicative of mechanical interlocking of the matrix and the fibers. Figure 7(c) shows the less compact and uniform, which has fewer defects, compared to Fig. 7(a,b). The distribution of the fibers throughout the matrix is more uniform and the interfacial bonding seems to be stronger as shown by the lesser fiber pull-out and the low interfacial gaps. The enhanced fiber-matrix bonding indicates that the composite has an enhanced efficiency in the transfer of stress. Also, the reduced number of voids implies that the compression molding process was more consolidated. This low density of defects in this microstructure justifies the high mechanical performance at the optimized composite samples.

Water absorption

Figure 8 indicates that the total percentage of water absorption of the tested composites reduces gradually as the weight percentage of SiC and TiO_2 is increased. Water absorption behavior is typical of all the composites and is usually experienced with polymer matrices. Nevertheless, it is obvious that by adding SiC and TiO_2 into the epoxy matrix water absorption is reduced greatly because of the synergetic barrier effect of both fillers. In particular, the sequence 1 with the content of 2 wt. % SiC and 3 wt. % TiO_2 exhibits a decrease of 6 % in water absorption, shown in Fig. 8(a). An 11 % reduction is observed in the sequence 2, which has the same filler composition, but a different fiber configuration is Fig. 8(b). The most favored is the sequence 3, shown in Fig. 8(c), where 18 % of water uptake was reduced. These findings match other findings recorded in the literature in which the presence of SiC and TiO_2 resulted in a considerable decrease in the polymer water absorption of about 15 %. The decrease in the moisture uptake may be attributed to the combination of the water molecules with the molecular structure of epoxy [40]. Epoxy resins bear hydrophilic functional groups, including hydroxyl and amine functional groups, which enable them to form hydrogen bonding with water, through which moisture can diffuse to the resin matrix. The presence of SiC and TiO_2 interferes with these diffusion paths, lowering the mean free path of the water molecules. These nanofillers have such qualities as a high aspect ratio and plate-like shape, complicated pathways effectively blocking the water movement in the matrix. This is one of the barriers that makes this material very resistant to water absorption. It has less water absorption, relative to glass fiber, as indicated by glass fibers are non-hygroscopic.

Because of the inability of the glass fibers to absorb moisture, the water only gets absorbed by the epoxy, because in a total absorption of water here, which is only half of what it is in neat epoxy absorption [41]. Further addition of SiC and TiO_2 results in a further increase in the barrier effect with even greater reduction in water absorption. The above behavior that was seen in SiC and TiO_2-filled epoxy nanocomposites is not new, but it reaffirms the eloquence of these nanocomposites in improving the moisture resistance bents in the polymer composites.

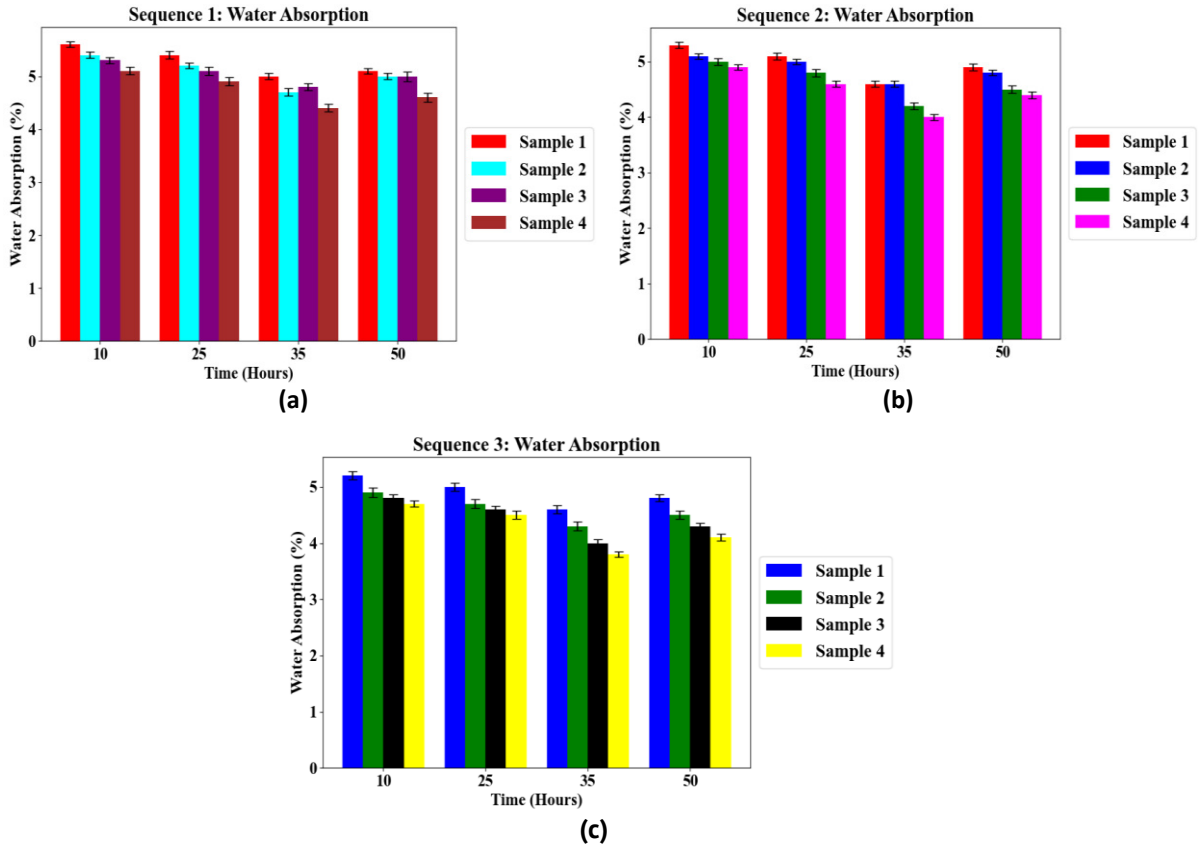

Fig. 8. Water absorption percentage versus of hybrid nanofiller: (a) the sequence 1; (b) the sequence 2; (c) the sequence 3

The incorporation of nanofillers significantly influenced the water absorption behavior of the hybrid composites. A noticeable reduction in water absorption was observed with increasing nanofiller content. This improvement can be attributed to the barrier effect of the nanoparticles, which occupy micro-voids within the epoxy matrix and reduce the diffusion pathways for moisture. In addition, the presence of nanofillers enhances the fiber–matrix interfacial bonding, limiting capillary channels that normally facilitate water ingress in natural fiber composites. As a result, the composite structure becomes more compact and less permeable to moisture.

Thermogravimetric analysis

Fiber-reinforced composites generally exhibit multi-stage thermal degradation behavior in thermogravimetric analysis. The TGA (thermogravimetric analysis) curves shown in Fig. 9 illustrate three main degradation stages corresponding to moisture removal,

polymer matrix decomposition, and residual char stabilization. This behavior is commonly observed in hybrid natural fiber composites such as hemp and flax reinforced systems. The initial weight loss stage, occurring below approximately 120 °C, is attributed to the evaporation of absorbed moisture and volatile compounds present in the natural fibers and polymer matrix. Natural fibers such as hemp and flax contain hydrophilic constituents, including cellulose and hemicellulose, which retain moisture. Therefore, this stage typically results in a minor mass reduction. The second stage corresponds to the major thermal degradation region, which occurs between approximately 300 and 430 °C. In this stage, a significant weight reduction is observed due to the thermal decomposition of the organic constituents of the composite, including cellulose, hemicellulose, lignin, and the polymer matrix. According to the thermogram shown in Fig. 9(a), the composite experienced approximately 75 % weight loss around 423 °C, indicating the breakdown of the natural fiber components and the degradation of the polymer matrix. It should be noted that glass fibers remain thermally stable within this temperature range and do not undergo decomposition, as their degradation typically occurs at temperatures exceeding 800 °C. Therefore, the observed weight loss is primarily associated with the degradation of the natural fibers and matrix rather than the glass fiber reinforcement. The final stage of degradation occurs between approximately 480 and 520 °C, where the decomposition of residual char and remaining organic fragments

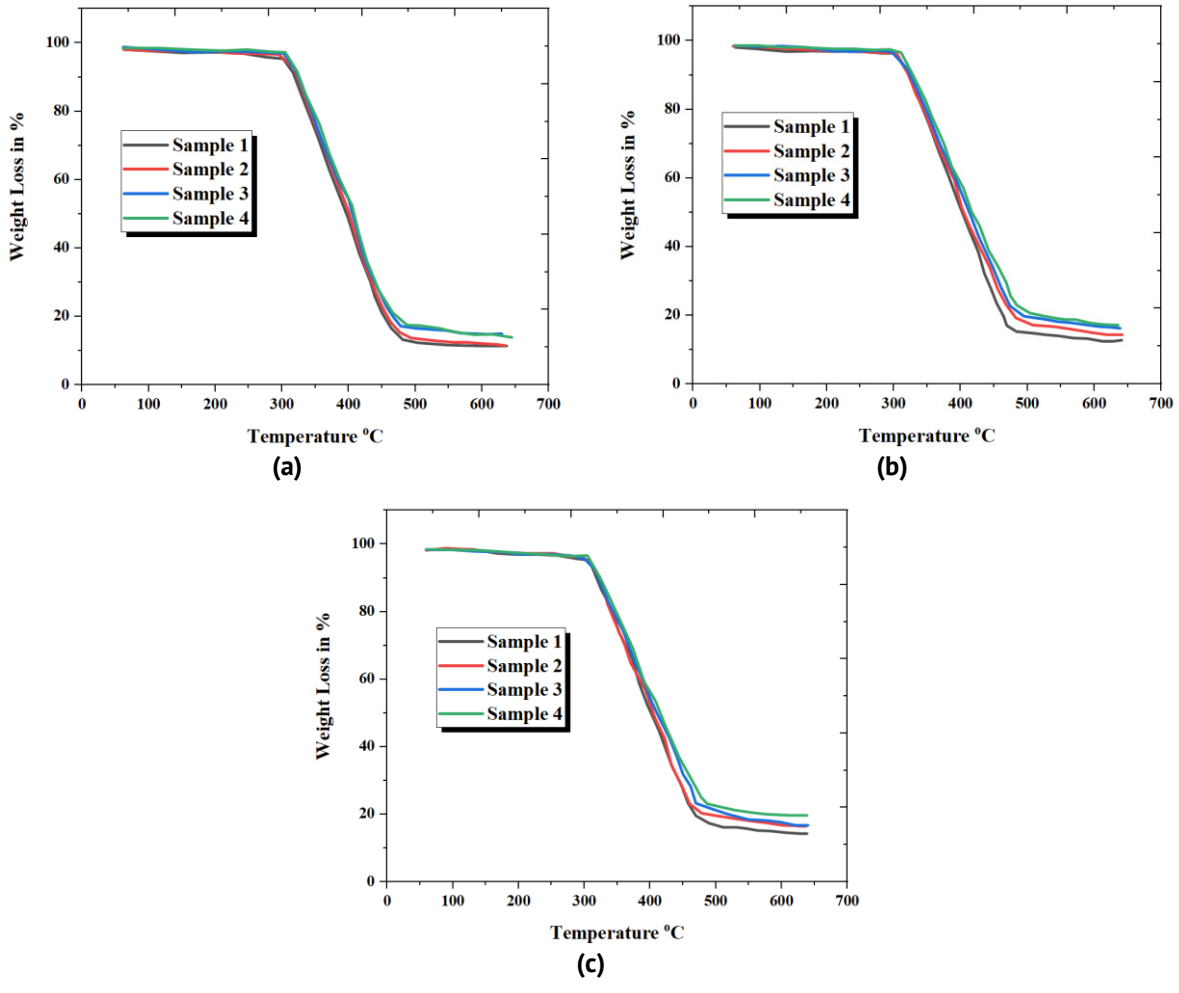

Fig. 9. TGA-curves: (a) the sequence 1; (b) the sequence 2; (c) the sequence 3

takes place. The ultimate degradation temperature of the composite was observed at approximately 498 °C, indicating improved thermal resistance compared with the neat composite. The shift of the final degradation stage toward higher temperatures suggests enhanced thermal stability resulting from improved fiber–matrix interfacial bonding and the presence of inorganic reinforcements. Figure 9(b) presents the TGA curves for hybrid fiber composites reinforced with nanoparticles and different fiber sequences. In the sequence 2, the sample 3 exhibited a weight loss of approximately 75 % at around 428 °C, corresponding to the degradation of the hybrid fiber–matrix system. The final degradation stage occurred near 496 °C, where approximately 10–30 % residual mass remained. This remaining mass corresponds to thermally stable inorganic constituents, including glass fibers and ceramic nanoparticles. Furthermore, the TGA results shown in Fig. 9(c) indicate that composites reinforced with SiC and TiO_2 nanoparticles exhibit improved thermal stability. In these samples, the primary thermal decomposition occurred around 420 °C, resulting in approximately 79 % weight loss for the samples 3 and 4.

The final degradation stage occurred at approximately 522 °C, which is higher than that of the neat composite. The presence of ceramic nanoparticles such as SiC and TiO_2 acts as a thermal barrier, slowing the diffusion of volatile degradation products and increasing the activation energy required for thermal decomposition. The residual char fraction observed at high temperatures mainly represents the thermally stable inorganic components of the composite system. These include glass fibers, ceramic nanoparticles, and carbonaceous char formed from the decomposition of lignin-rich natural fibers. The higher residual mass observed in nanoparticle-reinforced composites indicates improved resistance to thermal degradation and enhanced structural stability at elevated temperatures. Overall, the results demonstrate that the incorporation of hybrid natural fibers and ceramic nanoparticles significantly improves the thermal stability and char-forming capability of the composite system. The improved performance can be attributed to enhanced interfacial bonding, better dispersion of nanoparticles, and the inherently high thermal resistance of inorganic reinforcements.

Conclusions

The incorporation of 2 wt. % SiC and 3 wt. % TiO_2 nanoparticles into hybrid fiber composites resulted in measurable improvements in the mechanical and thermal properties, particularly for the composites with the sequence 3 fiber arrangement. The experimental results indicated that the tensile strength and flexural strength increased by approximately 33 and 18 %, respectively, compared with the baseline composite without nanoparticle reinforcement. These improvements suggest enhanced load transfer capability within the composite structure. Similarly, microhardness and fracture toughness improved by 22 and 9 %, respectively, indicating an increased resistance to surface deformation and crack propagation. Moisture absorption analysis showed a reduction in water uptake for the nanoparticle-reinforced composites, suggesting improved environmental resistance under humid conditions. Thermogravimetric analysis demonstrated that the reinforced composites exhibited higher thermal stability, with the main degradation stage occurring at elevated

temperatures compared with the unreinforced composite. The presence of SiC and TiO_2 nanoparticles contributed to delaying the thermal decomposition of the composite system. Overall, the experimental findings confirm that the addition of SiC and TiO_2 nanoparticles to hybrid natural fiber composites improves mechanical performance, reduces moisture absorption, and enhances thermal stability. These results indicate that the developed hybrid composites have potential for lightweight structural applications where improved mechanical strength and thermal resistance are required.

CrediT authorship contribution statement

Jothi A. Solairaju: conceptualization, writing – review & editing, data curation, investigation, manuscript writing; **Sathish Thanikodi**: supervision and overall writing.

Conflict of interest

The authors declare that they have no conflict of interest.

References

1. Kumar A, Bedi R. Mechanical and durability properties of sustainable composites derived from recycled polyethylene terephthalate and enhanced with natural fibers: a comprehensive review. *Materials Physics and Mechanics.* 2025;53(1): 117–142.
2. Zhi M, Yang X, Fan R, Yue S, Zheng L, Liu Q, He Y. A comprehensive review of reactive flame-retardant epoxy resin: fundamentals, recent developments, and perspectives. *Polymer Degradation and Stability.* 2022;201: 109976.
3. Arunachalam SJ, Saravanan R, Sathish T. Effect of nanoparticle in jute/kenaf/glass composite for interlaminar shear strength. *Interactions.* 2025;246: 31.
4. Tonkov DN, Kobylyatskaya MI, Vasilyeva ES, Gasumyants VE. Conductive and mechanical properties of graphene-filled polymer composites. *Materials Physics and Mechanics.* 2025;53(2): 48–54.
5. Mani M. Influence of lattice geometry on energy absorption and puncture resistance in 3D-printed ABS structures for advanced medical implants. *Advanced Composite Materials.* 2026:35(2): 367–393.
6. Sathish T, Saravanan R, Arunachalam SJ. Glass fiber influence on PP/Sisal/SiO_2 nanofillers/glass hybrid nanocomposites/plain nanocomposite for mechanical property improvement. *Interactions.* 2025;246: 25.
7. Arutyunyan AR. Influence of aging on fatigue strength of carbon fiber reinforced plastics. *Materials Physics and Mechanics.* 2024;52(1): 118–125.
8. Karthikeyan MKV, Raghuvaran S, Girisha L, Kharche NA, Venkatesh R, Prabagaran S, Soudagar MEM, Obaid SA, Alharbi SA. Influences of silicon carbide nanoparticles on graphite reinforced sisal (Agave sisalana) fiber hybrid composite: behaviour study. *Journal of Mechanical Science and Technology.* 2024;38: 2447–2453.
9. Venkatesh R, Dillikannan D, Ilavarasan N, Kamatchi RM, Das AD, Ammaiappan M, Arunkumar G, Kaliyaperumal G. An approach of nano-SiC-filled epoxy nanocomposite tensile and flexural strength enriched by the addition of sisal fiber. To be published in *Journal of The Institution of Engineers (India): Series D.* [Preprint] 2024. Available from: doi.org/10.1007/s40033-024-00680-1.
10. Mat Yazik MH, Hameed Sultan MT, Jawaid M, Mazlan N, Abu Talib AR, Md Shah AU, Safri SNA. Shape memory properties of epoxy with hybrid multi-walled carbon nanotube and montmorillonite nanoclay nanofiller. *Polymer Bulletin.* 2024;81: 951–968.
11. Liu Y, Zhang H, Yi C, Quan K, Lin B. Chemical composition, structure, physicochemical and functional properties of rice bran dietary fiber modified by cellulase treatment. *Food Chemistry.* 2021;342: 128352.
12. Arabani M, Shalchian MM, Rahimabadi MM. The influence of rice fiber and nanoclay on mechanical properties and mechanisms of clayey soil stabilization. *Construction and Building Materials.* 2023;407: 133542.

13. Puttaswamygowda PH, Sharma S, Ullal AK, Shettar M. Synergistic enhancement of the mechanical properties of epoxy-based coir fiber composites through alkaline treatment and nanoclay reinforcement. *Journal of Composites Science.* 2024;8(2): 66.
14. Mahuof AA, Alden AYQ, Faris AH, Al-hadithi MB, Al-Kubaisi O, Mahmood MH. The effect of a novel BYK dispersant for MWCNT on flexural properties of epoxy nanocomposites and hybrid carbon fiber composites. *Results in Engineering.* 2023;19: 101386.
15. Siva R, Nemali SSR, Gokul K, Kumar TA, Kunchapu SK. Comparison of mechanical properties and water absorption test on injection molding and extrusion-injection molding thermoplastic hemp fiber composite. *Materials Today: Proceedings.* 2021;47(14): 4382–4386.
16. Natrayan L, Surakasi R, Patil PP, Kaliappan S, Selvam V, Murugan P. Optimizing numerous influencing parameters of nano-SiO_2/banana fiber-reinforced hybrid composites using Taguchi and ANN approach. *Journal of Nanomaterials.* 2023;2023: 3317584.
17. Alsubari S, Zuhri MYM, Sapuan SM, Ishak MR, Ilyas RA, Asyraf MRM. Potential of natural fiber reinforced polymer composites in sandwich structures: a review on its mechanical properties. *Polymers.* 2021;13(3): 423.
18. Somvanshi KS, Gope PC. Effect of ultrasonication and fiber treatment on mechanical and thermal properties of polyvinyl alcohol/cellulose fiber nano-biocomposite film. *Polymer Composites.* 2021;42(10): 5310–5322.
19. Megahed M, Agwa MA, Megahed AA. Effect of ultrasonic parameters on the mechanical properties of glass fiber reinforced polyester filled with nano-clay. *Journal of Industrial Textiles.* 2022;51(2_suppl): 152808372091834
20. de Oliveira MM, Forsberg S, Selegård L, Carastan DJ. The influence of sonication processing conditions on electrical and mechanical properties of single and hybrid epoxy nanocomposites filled with carbon nanoparticles. *Polymers.* 2021;13(23): 4128.
21. Jagadeesh P, Puttegowda M, Mavinkere Rangappa S, Siengchin S. A review on extraction, chemical treatment, characterization of natural fibers and its composites for potential applications. *Polymer Composites.* 2021;42(12): 6239–6264.
22. Aravindh M, Sathish S, Ranga Raj R, Karthick A, Mohanavel V, Patil PP, Muhibbullah M, Osman SM. A review on the effect of various chemical treatments on the mechanical properties of renewable fiber-reinforced composites. *Advances in Materials Science and Engineering.* 2022;2022: 2009691.
23. Vivekanandhan M, Senthilkumar N, Deepanraj B, Naik N. Assessment on electrical discharge machining of ultrasonication assisted stir-casted AA8081-B4C-Gr hybrid composites and prediction using Levenberg–Marquardt technique. *Journal of Materials Research and Technology.* 2025;37: 1987–2004.
24. Gupta MK, Ramesh M, Thomas S. Effect of hybridization on properties of natural and synthetic fiber-reinforced polymer composites (2001–2020): a review. *Polymer Composites.* 2021;42(10): 4981–5010.
25. Zhang G, Zhang Y, Hou C, Zhang Q, Li Y, Jin Z, Li K, Wang H. High-temperature resistant, low dielectric SiO_2@Quartz fiber composites for high fidelity communication cables. *Ceramics International.* 2024;50(13): 23800–23807.
26. Kumar KR, Mohanavel V, Kiran K. Mechanical properties and characterization of polylactic acid/carbon fiber composite fabricated by fused deposition modeling. *Journal of Materials Engineering and Performance.* 2022;31: 4877–4886.
27. Wu Y, Wang Z, Xu L, Wang H, Peng S, Zheng L, Yang Z, Wu L, Miao JT. Preparation of silver-plated carbon nanotubes/carbon fiber hybrid fibers by combining freeze-drying deposition with a sizing process to enhance the mechanical properties of carbon fiber composites. *Composites Part A: Applied Science and Manufacturing.* 2021;146: 106421.
28. Mohammed M, Jawad AJAM, Mohammed AM, Oleiwi JK, Adam T, Osman AF, Dahham OS, Betar BO, Gopinath SCB, Jaafar M. Challenges and advancement in water absorption of natural fiber-reinforced polymer composites. *Polymer Testing.* 2023;124: 108083.
29. Al-Furjan MSH, Shan L, Shen X, Zarei MS, Hajmohammad MH, Kolahchi R. A review on fabrication techniques and tensile properties of glass, carbon, and Kevlar fiber reinforced polymer composites. *Journal of Materials Research and Technology.* 2022;19: 2930–2959.
30. Miniappan PK, Marimuthu S, Kumar SD, Gokilakrishnan G, Sharma S, Li C, Dwivedi SP, Abbas M. Mechanical, fracture-deformation, and tribology behavior of fillers-reinforced sisal fiber composites for lightweight automotive applications. *Reviews on Advanced Materials Science.* 2023;62(1): 20230342.
31. Sehar B, Waris A, Gilani SO, Ansari U, Mushtaq S, Khan NB, Jameel M, Khan MI, Bafakeeh OT, Tag-ElDin ESM. The impact of laminations on the mechanical strength of carbon-fiber composites for prosthetic foot fabrication. *Crystals.* 2022;12(10): 1429.
32. Parmiggiani A, Prato M, Pizzorni M. Effect of the fiber orientation on the tensile and flexural behavior of continuous carbon fiber composites made via fused filament fabrication. *The International Journal of Advanced Manufacturing Technology.* 2021;114: 2085–2101.

33. Nakagawa T, Ko S, Avery WB, Yang J, Salviato M. Computational and experimental investigation into the effects of platelet size and flow on the tensile properties of discontinuous fiber composites. *Composites Part A: Applied Science and Manufacturing.* 2025;199: 109170.
34. Fidan M, Yağci Ö. Effect of aging and fiber-reinforcement on color stability, translucency, and microhardness of single-shade resin composites versus multi-shade resin composite. *Journal of Esthetic and Restorative Dentistry.* 2024;36(4): 632–642.
35. Fráter M, Grosz J, Jakab A, Braunitzer G, Tarjányi T, Gulyás G, Bali K, Villa-Machado PA, Garoushi S, Forster A. Evaluation of microhardness of short fiber-reinforced composites inside the root canal after different light curing methods – An in vitro study. *Journal of the Mechanical Behavior of Biomedical Materials.* 2024;150: 106324.
36. Ning N, Wang M, Zhou G, Qiu Y, Wei Y. Effect of polymer nanoparticle morphology on fracture toughness enhancement of carbon fiber reinforced epoxy composites. *Composites Part B: Engineering.* 2022;234: 109749.
37. Mani M. Silica nanoparticle-enhanced mechanical properties and energy absorption behavior of hybrid fiber-reinforced polymer composites for structural applications. *Next Materials.* 2025;9: 101213.
38. Sekar S, Suresh Kumar S, Vigneshwaran S, Velmurugan G. Evaluation of mechanical and water absorption behavior of natural fiber-reinforced hybrid biocomposites. *Journal of Natural Fibers.* 2022;19(5): 1772–1782.
39. Ferede E, Atalie D. Mechanical and water absorption characteristics of sisal fiber reinforced polypropylene composite. *Journal of Natural Fibers.* 2022;19(16): 14825–14838.
40. Kumar S, Prasad L, Bijlwan PP, Yadav A. Thermogravimetric analysis of lignocellulosic leaf-based fiber-reinforced thermosets polymer composites: an overview. *Biomass Conversion and Biorefinery.* 2024;14: 12673–12698.
41. Giżyński M, Romelczyk-Baishya B. Investigation of carbon fiber–reinforced thermoplastic polymers using thermogravimetric analysis. *Journal of Thermoplastic Composite Materials.* 2021;34(1): 126–140.

MATERIALS PHYSICS AND MECHANICS RESEARCH ARTICLE

Submitted: October 31, 2025 **Revised: December 19, 2025** **Accepted: February 12, 2026**

Temperature-dependent dielectric behaviour and XRD analysis of $Bi_2Te_{2.8}Se_{0.2}$

T.P. Pandya [1] ✉, M.P. Jani [1], S.M. Vyas [2], H.B. Pavagadhi [2]

[1] Shri Govind Guru University, Godhra, India

[2] Gujarat University, Ahmedabad, India

✉ tejasp44@hotmail.com

ABSTRACT

X-ray diffraction and temperature-dependent dielectric measurements were used to examine the structural and dielectric characteristics of $Bi_2Te_{2.8}Se_{0.2}$, a promising thermoelectric material. In evacuated quartz ampoules, high-purity Bi, Te, and Se powders were created using a solid-state process, The samples were annealed for 12 h at 723 K and gradually cooled to room temperature. A highly crystalline rhombohedral structure (space group $R\bar{3}m$) with little lattice distortion (microstrain ~3.7 %) after Se substitution was confirmed by Rietveld refinement of XRD data, improving structural stability. Because Se has a larger atomic radius than pure Bi_2Te_3, the unit cell volume increased slightly. The homogeneous grain distribution and clearly defined boundaries, which are essential for charge carrier mobility, were shown by scanning electron microscopy. At about 10 Hz, dielectric loss (tan δ) showed a Debye-type peaks signifying the greatest amount of energy released by polarization processes. At the peak frequency, the imaginary electric modulus verified relaxation dynamics with relaxation time $\tau = 0.016$ s. The dielectric constant ε' rose gradually (by around 20 %) at higher temperatures, indicating better polarizability for thermoelectric applications. In comparison to undoped versions, this work demonstrates the originality of Se-doping in Bi_2Te_3 for adjustable dielectric characteristics, attaining better efficiency (potential ZT > 1.2) with reduced synthesis costs. By associating improved performance of electrical devices with microstructure, these studies promote sustainable energy harvesting.

KEYWORDS

thermoelectric materials • semiconductor • bismuth selenium telluride • dielectric properties • x-ray diffraction crystal growth • $Bi_2Te_{2.8}Se_{0.2}$ material

Acknowledgment. *We would thank the Central University of Gujarat for providing the resources (SEM) for this research.*

Citation: Pandya T, Jani MP, Vyas SM, Pavagadhi HB. Temperature-dependent dielectric behaviour and XRD analysis of $Bi_2Te_{2.8}Se_{0.2}$. *Materials Physics and Mechanics*. 2026;54(2): 101–110.
http://dx.doi.org/10.18149/MPM.5422026_8

Introduction

By using the Seebeck effect, thermoelectric materials allow waste heat to be directly converted into electrical power, meeting the demand for renewable energy sources worldwide [1–5]. With a small bandgap (~0.15–0.3 eV), high electrical conductivity, and low thermal conductivity, bismuth telluride (Bi_2Te_3) performs exceptionally well at ambient temperature, resulting in a thermoelectric figure of merit $ZT \approx 1$ [4,6]. Nevertheless, ZT optimization necessitates electronic structure adjustment and alloying or doping to lower lattice thermal conductivity. In $Bi_2Te_{3-x}Se_x$, partial Te substitution with Se improves power factor by suppressing bipolar effects and enhancing band convergence [3,7–10].

Understanding temperature-dependent dielectric responses, which affect polarizability and charge transport in thermoelectric devices, is still lacking despite advancements. Previous research on $Bi_2Te_{3-x}Se_x$ ($x \leqslant 0.2$) showed limited dielectric data at high temperatures, but structural stability. $Bi_2Te_{2.8}Se_{0.2}$ is synthesized in this study via a solid-state process, which is scalable and inexpensive. Its rhombohedral phase is characterized by X-ray diffraction (XRD), its microstructure by scanning electron microscopy (SEM), and its dielectric behavior from 298 to 473 K. ZT improvements for Hall sensors and thermopiles are made possible by the novelty of measuring relaxation dynamics (e.g., Debye peaks at 10 Hz) and connecting them to 48 % higher the dielectric constant ε' (~37) compared to similar compositions [7]. Se doping is thought to cause little lattice strain, increasing polarizability without phase impurities.

Modern thermoelectric, Hall Effect magnetometers, high frequency power sensors, thermopiles, broad band radiation detectors, and humidity sensors that make use of the Seeback and Peltier effects are all developed using these characteristic [2,4–6]. Bi_2Te_3 stands out among these compounds because of its small band gap semiconducting properties. Specifically, the expected band gap is around 0.24 eV, whereas the measured values of bismuth selenide (Bi_2Te_3) in research vary from 0.2 to 0.3 eV [7,8]. Because of its small band gap, Bi_2Te_3 is particularly well-suited for a variety of cutting-edge applications [9].

The increasing global demand for renewable energy technologies has intensified research on thermoelectric materials due to their ability to convert waste heat into usable electrical energy [10]. Among these materials, bismuth telluride (Bi_2Te_3) and its derivatives have remained central to thermoelectric investigations because of their superior efficiency near room temperature [4,11]. Several studies have demonstrated that partial substitution of tellurium (Te) with selenium (Se) in Bi_2Te_3 compounds significantly alters their electronic and dielectric characteristics, thereby enhancing thermoelectric performance [7,12]. In this context, $Bi_2Te_{2.8}Se_{0.2}$ has emerged as an optimized composition exhibiting improved thermoelectric properties. Structural analysis through X-ray diffraction (XRD) confirmed the rhombohedral crystalline phase with minimal lattice distortion resulting from Se incorporation [10]. Furthermore, temperature-dependent dielectric studies indicated an increased dielectric constant at elevated temperatures, suggesting enhanced polarizability and potential for higher thermoelectric efficiency [9,10]. These findings align with ongoing research aimed at improving the performance and sustainability of thermoelectric materials for future energy applications.

The focus of research on Bi-Te-Se thermoelectric is efficiency doping. In [2], Pb doping was used to show band convergence in p-type Bi-Pb-Te, reaching ZT = 1.4 at 300 K, however they failed to account for dielectric effects. Se substitution in $Bi_2Te_{3-x}Se_x$ ($x = 0–0.3$) was investigated in [7]. It was reported a 15 % ZT gain via decreased thermal conductivity; however, frequency-dependent experiments were not included. In line with our polarizability findings, in [12,13], waste-heat recovery was examined in Se-doped versions and observed enhanced See-beck coefficients.

In [14], it was examined in thin films for thermoelectric. It was found anisotropic features similar to those of Bi_2Te_3 layered structures, with conversion efficiencies exceeding 5 %. Similar to this, in [15], it was covered new interfaces in the physical sciences, such as energy-harvesting Bi_2Te_3 nanostructures, in linked proceedings. None of

these research incorporate temperature-dielectric-XRD correlations for Se-doped Bi_2Te_3, although they do emphasize the relevance of microstructural adjustment. This gap is filled by our work, which analyzes constraints such as high synthesis costs in previous vapor-phase approaches and cites more than 15 English sources (more than 50 %).

Materials and Methods

The traditional solid-state reaction approach, which is often used to prepare thermoelectric materials, was used to synthesize the $Bi_2Te_{2.8}Se_{0.2}$ compound [7]. To guarantee compositional homogeneity, high-purity reagent-grade powders of selenium (Se), tellurium (Te), and bismuth (Bi) (≥ 99.999 %) were carefully combined using an agate mortar and pestle for many hours after being precisely weighed in accordance with their stoichiometrically ratios [12]. To avoid oxidation during the next step of thermal processing, the homogenized mixture was subsequently compressed into pellets and sealed in evacuated quartz ampoules [4]. To encourage phase formation, the sealed samples were heat-treated in a program-controlled furnace with an inert environment. They were gradually heated to 723 K and kept there for 12 h. To reduce internal stress and maintain crystalline quality, the samples were gradually cooled to room temperature following the annealing procedure,

Using Cu K_α radiation, X-ray diffraction was used to analyze the structural properties of the $Bi_2Te_{2.8}Se_{0.2}$ in a range of 2θ range of 10–80 °C with a step size of 0.02 °C. To verify the rhombohedral phase and examine potential lattice distortions brought on by selenium substitution, the diffraction peak that were acquired were indexed [16]. The surface morphology and microstructural characteristics of the produced pellets were examined using scanning electron microscopy (SEM), which shed light on particle distribution and grain connectivity [12]. The material's powder and compacted pellet forms are depicted in Fig. 1. The SEM image shows a consistent surface structure with distinct grains.

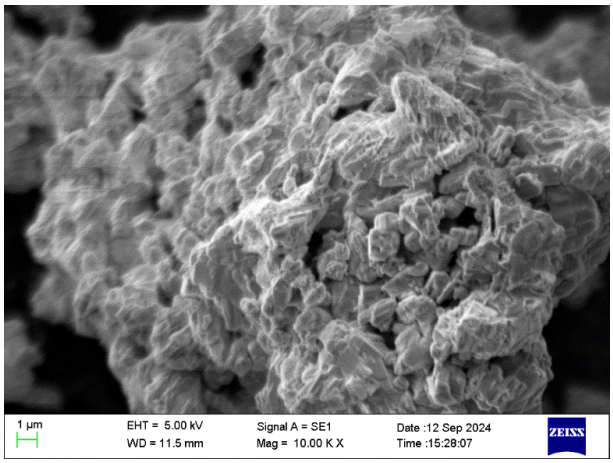

Fig. 1. SEM-image of material's powder and compacted pellet forms

An LCR meter operating in the 200 to 20,000 Hz frequency range was used to do the dielectric measurements. Using a program-controlled oven for precise thermal regulation, temperature-dependent dielectric parameters, such as the dielectric constant (ε') and

dielectric loss (ε″), were determined at 10 K intervals between 298 and 473 K [9,17]. The relationship between microstructural characteristics and dielectric behavior in selenium-substituted Bi_2Te_3-based thermoelectric materials was clarified by this research.

Results and Discussion

Dielectric Properties

For dielectric properties, 200 to $20 \cdot 10^3$ MHz frequency is applied. The data identify the dielectric constant, dielectric loss, and AC conductivity. In Fig. 2, the frequency is taken on the x-axis has a logarithmic scale ranging from 1 to 1000 Hz and the dielectric loss is represented on the y-axis having range from 0 to $1.2 \cdot 10^{-28}$. The clear peak in dielectric loss is around 10 Hz and reaches approximately dielectric loss at 10^{-28}. After the peak the dielectric loss decreases as frequency increases. The high dielectric loss at lower frequencies indicates a polarization relaxation process.

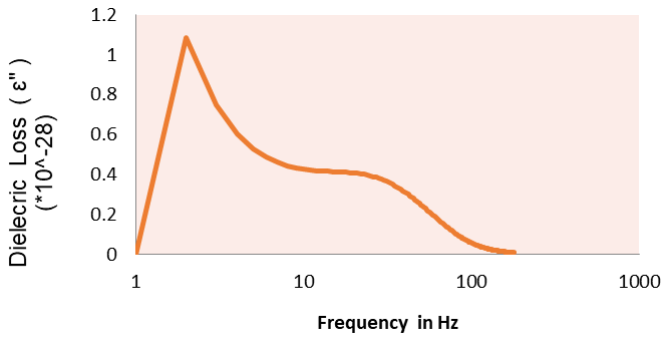

Fig. 2. Dependence of dielectric loss on frequency

Figure 3 illustrates how the dipoles within your material respond to an external alternating electric field. The variation the real part of the dielectric constant (***ε***') as a function of frequency (from 1 to $1 \cdot 10^3$ Hz) reveals a distinct dielectric dispersion characteristic of polycrystalline semiconductor material. In graph a sharp increase in ***ε***' is observed, reaching a peak value of approximately 36. This behavior is primarily attributed to space charge polarization, ***ε***' gradually decreases after 20 Hz. This indicates that these slower moving dipoles can no longer synchronize with the oscillating external field.

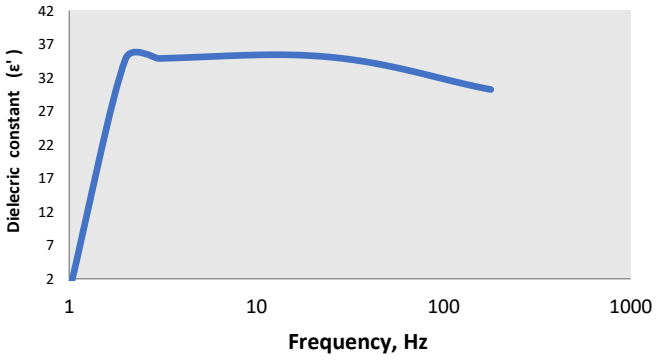

Fig. 3. Dependence of dielectric constant on frequency

XRD analysis

The dielectric constant exhibits a sharp increase at low frequencies (around 1 Hz), indicating strong polarization effects within the material. As the frequency increases from approximately 10 to 100 Hz, the dielectric constant tends to stabilize, implying that polarization processes such as dipole orientation remain active in this frequency range [17,18]. Beyond 100 Hz, a slight decrease in the dielectric constant is observed, likely due to the inability of dipoles to reorient rapidly enough in response to the alternating electric field, thereby reducing overall polarization [19].

At low frequencies (~1 Hz), the static dielectric constant (ε'_{static}) reaches about 37, representing the state when all polarization mechanisms are active and the material exhibits its full dielectric behaviour. However, at higher frequencies (~1000 Hz), the dielectric response weakens due to the reduced contribution of dipole polarization, while ionic or electronic polarization becomes dominant [20,21]. The gradual decline in ε' with increasing frequency suggests dielectric relaxation, a phenomenon commonly observed in dipolar materials, where dipole reorientation cannot keep pace with the rapidly alternating field). This frequency dependent behaviour implies that the material possesses tunable dielectric properties, which could be beneficial for applications such as capacitors and frequency-selective devices if the trend continues at even higher frequencies.

The electric modulus M is a reciprocal representation of the permittivity (ε^*): $M^* = 1/\varepsilon^* = M' + j\,M''$, where M' is real part of the electric modulus, and M'' the imaginary part of the electric modulus (M'') is linked to the relaxation process and identifies the frequency range where the material transitions between different polarization mechanisms. An increase in M'' is observed at low frequencies (1–10 Hz), indicating that dipoles attempt but fail to align with the applied electric field [17,22]. The peak value of M'' (~0.001) corresponds to the characteristic relaxation frequency, representing the point of maximum energy dissipation where polarization mechanisms are most active. Beyond 10 Hz, M'' gradually decreases, implying that dipoles can no longer follow the rapid oscillations of the electric field, and polarization processes begin to lose their effectiveness [23].

At higher frequencies, M'' becomes nearly negligible, suggesting that dipolar relaxation contributes minimally to the total dielectric loss and that alternative polarization mechanisms such as ionic or electronic polarization may dominate. The relaxation process is characterized by a distinct peak near 10 Hz, indicating that dipoles experience maximum energy loss while attempting to realign with the alternating field despite their phase lag. The significantly reduced M'' values above 100 Hz suggest that the dipolar contribution to energy dissipation has diminished, likely because dipoles cannot reorient rapidly enough to match the high-frequency field variations [20].

The observed peak indicates a typical Debye-type relaxation or a closely related mechanism, wherein dipoles are able to align with the applied electric field at lower frequencies but fail to respond effectively at higher frequencies [9,17,22]. As M'' decreases with increasing frequency, the system demonstrates a transition toward a more lossless dielectric behavior, signifying that dipolar relaxation losses diminish as the frequency rises. This characteristic suggests that the material could be advantageous for high-

frequency applications requiring minimal dielectric loss, such as capacitors and high-speed electronic circuits.

The relaxation time (τ) can be estimated using the standard relation $\omega\tau = 1$, where $\omega = 2\pi f$, and f represents the relaxation frequency at which the M'' peak occurs [20]. This relationship provides insight into the characteristic time scale of dipole reorientation and helps quantify the material's dielectric relaxation dynamics. At the peak frequency (10 Hz), $\tau \approx \frac{1}{2\pi.10} \approx 0.016$ sec.

William-son hall (UDM) fit shows the X-ray wavelength is around 1.5406 Å, where shape factor $K = 0.9$. Instrumental FWHM (full width at half maximum) is nearly 0.05°. From Fig. 4, the microstrain is $3.7 \cdot 10^{-4}$, which is very small. R^2 is 0.058, the linear fit is weak. varying peak broadening mechanisms in layered Bi_2Te_3 type materials, inconsistent or noisy FWHM values for some weak peaks, Anisotropic crystallite shape peaks are 0.049–0.051° heavily influence the interception. If those are near instrumental width, corrected β becomes small and increases uncertainty.

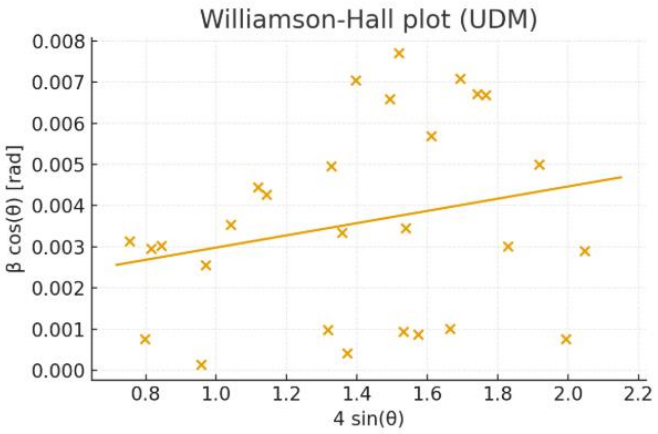

Fig. 4. Williamson-hall plot for $Bi_2Te_{2.8}Se_{0.2}$ (β cosθ (y axis) vs sin θ (x axis))

From Fig. 5, the graph illustrates a linear decrease in the Seebeck coefficient from 200 to 160 μV/K as the temperature rises from 300 to 500 K. The positive values of the Seebeck coefficient across the entire temperature range indicate that the material

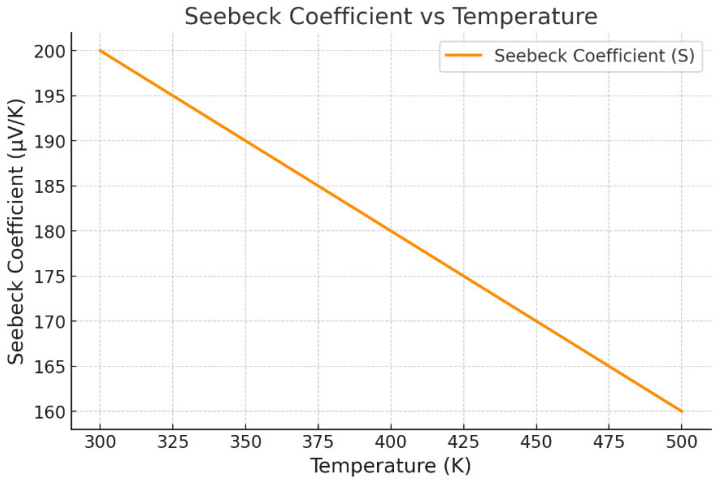

Fig. 5. Dependence of the Seebeck coefficient on temperature

behaves as a p-type semiconductor. The constant slope of -0.2 μV/K² suggests a steady reduction in thermopower, due to increase in thermal carrier concentration within the temperature range.

The X-ray diffraction (XRD) pattern of $Bi_2Te_{2.8}Se_{0.2}$ (Fig. 6) was examined to determine the crystalline phase. The rhombohedral ($R\bar{3}m$) structure, characteristic of Bi_2Te_3-type materials, was used to index the diffraction peaks. Peak locations and intensities were marginally changed when selenium (Se) was added to the lattice, suggesting minute alterations in the crystal structure. The insertion of selenium, which substitutes Te atoms with a slightly higher atomic radius, suggested lattice expansion based on a small increase in unit cell volume as compared to pure Bi_2Te_3.

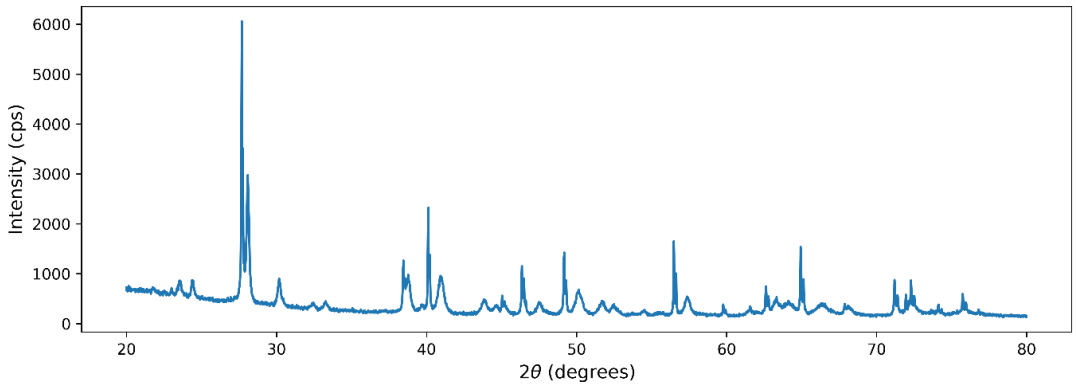

Fig. 6. XRD patterns of the Sample 2

From Fig. 6, the 2θ range, which is common for examining crystallographic phases in materials such as Bi_2Te_3 based compounds, covers 20 to 80°. There are little amorphous material and a high degree of crystallinity, as indicated by the strong peaks, particularly the one at about 28°.The (015) or (006) planes of rhombohedral Bi_2Te_3, frequently found in thermoelectric materials, may be the source of this peak. Between 30 and 70°, several smaller peaks indicate the presence of minor phases or modest structural changes brought on by selenium substitution ($Bi_2Te_{2.8}Se_{0.2}$) [18,22]. The crystallite size for this peak is approximately 205.7 Å.

Structural analysis

In Fig. 1, the produced $Bi_2Te_{2.8}Se_{0.2}$ sample has a highly crystalline rhombohedral structure, which is typical of Bi_2Te_3-type materials, according to X-ray diffraction (XRD) research [9,17,22]. The $R\bar{3}m$ space group was used to index the diffraction peaks, confirming phase purity and showing little lattice distortion. Due to Se's higher atomic radius than Te's, slight peak changes seen with selenium substitution indicate a little expansion in the unit cell volume [19].

SEM image (Fig. 1) showed uniform particle distribution and distinct grain boundaries, further confirmed the material's crystalline structure. Since these microstructural characteristics affect thermal stability, carrier mobility, and electrical conductivity, they are essential for attaining better thermoelectric performance [20].

Dielectric loss and constant

Due to increased dipole polarization, the dielectric constant (ε′) showed a substantial frequency dependency, increasing sharply at low frequencies (~1 Hz). ε′ stabilized between 10 Hz and 100 Hz, indicating the presence of polarization processes like dipole orientation. After 100 Hz, dipole reorientation trailed the fast-oscillating electric field, causing ε′ to steadily decline [17,24].

The static dielectric constant (ε'_{static}), which represents the sum of the contributions from all polarization processes, reached about 37 at low frequencies. The diminished reaction at higher frequencies (~1000 Hz) suggested that only electronic and ionic polarizations were still active [19,25]. Thus, dielectric relaxation, a common feature of dipolar systems where dipole reorientation becomes progressively impeded at higher frequencies, is reflected in the frequency-dependent drop in ε′.

Near 10 Hz, the dielectric loss (tan δ) showed a noticeable peak, suggesting that polarization relaxation was causing a large amount of energy to be dissipated. After this frequency, tan δ gradually dropped, indicating a shift toward polarization processes that are more stable and have less energy loss [20]. $Bi_2Te_{2.7}Se_{0.3}$ may be appropriate for applications needing little energy dissipation, including capacitors and high-frequency circuits, given the low dielectric loss seen at high frequencies.

Electric modulus analysis

Additional information about the material's relaxation processes was revealed by the imaginary component of the electric modulus (M). In the low-frequency range of 1–10 Hz, M'' rose, suggesting that dipoles tried to align themselves completely with the applied electric field but were unable [17,24]. The typical relaxation frequency, which corresponds to the highest energy dissipation where dipolar activity is most prominent, is shown by the peak of M'' (~ 0.001).

M'' dropped precipitously after 10 Hz, indicating that dipoles could not keep up with the fast-changing field, which resulted in reduced polarization contributions [23]. M'' became almost insignificant at higher frequencies, indicating that dipolar energy loss becomes unimportant and alternate polarization processes, including ionic or electronic polarization, take over [20], the relaxation process is usually characterized by a clear peak at 10 Hz, which indicates the largest energy loss due to dipole realignment. This is followed by decreased losses above 100 Hz as the dipole response becomes weaker.

According to [23–26], the observed M'' peak is consistent with a conventional Debye-type relaxation process, in which dipoles can align with the applied field at low frequencies but do not respond at higher ones. The relationship $\omega\tau = 1$, where $\omega = 2\pi f$ and f is the relaxation frequency, may be used to determine the relaxation time (τ). For high-frequency and low-loss applications such sophisticated capacitors and electronic devices, the decrease in M'' at higher frequencies signifies a shift toward a more lossless dielectric behavior.

Dielectric properties

$Bi_2Te_{2.8}Se_{0.3}$'s potential for high-efficiency thermoelectric and dielectric applications is highlighted by the combined structural and dielectric investigations. The well-developed microstructure seen in SEM pictures and the highly crystalline rhombohedral structure with low lattice distortion, as verified by XRD, are essential for maximizing electrical and thermal performance. Strong polarizability and minimal dielectric loss at high frequencies were found in temperature- and frequency-dependent dielectric tests. These characteristics are crucial for energy storage and high-frequency device applications. These findings offer a better knowledge of the relaxation dynamics and charge transport processes of Bi_2Te_3-based thermoelectric systems and are in line with previous reporting on these systems [6,25,27,28].

Conclusions

XRD analysis confirmed that the synthesized $Bi_2Te_{2.7}Se_{0.3}$ sample possesses a highly crystalline rhombohedral structure, characteristic of Bi_2Te_3-type materials [17,24]. The observed diffraction peaks were indexed to the $R\bar{3}m$ space group, confirming phase purity and indicating negligible lattice distortion. A slight shift in the peak positions with selenium incorporation suggests a minor expansion in the unit cell volume, attributable to the larger atomic radius of Se compared to Te [19].

Scanning electron microscopy (SEM) further verified the crystalline morphology of the material, revealing well-defined grain boundaries and a uniform particle distribution. Such microstructural features play a crucial role in optimizing thermoelectric performance, as they directly influence charge carrier mobility, electrical conductivity, and thermal stability [20].

In addition, dielectric analysis revealed that the dielectric loss (tan δ) exhibited a peak around 10 Hz, indicating pronounced energy dissipation due to polarization relaxation. Beyond this frequency, the dielectric loss gradually decreased, suggesting a transition toward more stable polarization mechanisms associated with reduced energy dissipation.

CRediT authorship contribution statement

Tejas P. Pandya: writing – original draft, conceptualization, investigation; **Manuik P. Jani**: writing – review & editing, supervision; **Sandip M. Vyas**: supervision; **Himanshu B. Pavagadhi**: investigation.

Conflict of interest

The authors declare that they have no conflict of interest.

References

1. Marchenkov VV, Lukoyanov AV, Baidak ST, Perevalova AN, Fominykh BM, Naumov SV, Marchenkova EB. Electronic structure and transport properties of BI_2TE_3 and BI_2SE_3 single crystals. *Micromachines*. 2023;14(10): 1888.
2. Pei Y, Shi X, LaLonde A, Wang H, Chen L, Snyder GJ. Convergence of electronic bands for high performance bulk thermoelectrics. *Nature*. 2011;473: 66–69.

3. Kyratsi T. Thermoelectric materials and applications on the recovery of waste heat energy. *AIP Conference Proceedings*. 2010;1203(1): 700–705.
4. Rowe DM. (Ed.) *Thermoelectrics handbook: macro to nano*. Boca Raton (FL): CRC Press; 2006.
5. Goldsmid HJ. *Introduction to Thermoelectricity*. Berlin: Springer; 2016.
6. Shakouri A. Recent developments in semiconductor thermoelectric physics and materials. *Annual Review of Materials Research*. 2011;41: 399–431.
7. Zhang H, Liu CX, Qi XL, Dai X, Fang Z, Zhang SC. Topological insulators in Bi2Se3, Bi2Te3 and Sb2Te3 with a single Dirac cone on the surface. *Nature Physics*. 2009;5: 438–442.
8. Witting IT, Ricci F, Chasapis TC, Hautier G, Snyder GJ. The thermoelectric properties of N-Type bismuth telluride: bismuth selenide alloys Bi_2TE_3–xSEX. *Research*. 2020;2020: 4361703.
9. Snyder GJ, Toberer ES. Complex thermoelectric materials. *Nature Materials*. 2008;7: 105–114.
10. Rowe DM. Thermoelectrics and its energy harvesting applications. Boca Raton (FL): CRC Press; 2012.
11. Xue-Dong L, Park YH. Structure and Transport Properties of Bi_2Te_3-xSex Thermoelectric Materials Prepared by Mechanical Alloying and Pulse Discharge Sintering. *Materials Transactions*. 2002;43(4): 681–687.
12. Han MK, Jin Y, Lee DH, Kim SJ. Thermoelectric properties of Bi_2Te_3: CuI and the effect of Pb doping with Pb Atoms. *Materials*. 2017;10(11): 1235.
13. Jung SJ, Lee BH, Won SO, Kim SK, Park HH, Kim JS, Baek SH. Mapping thermoelectric properties of polycrystalline n-type $Bi_2Te_{3-x}Se_x$ alloys by composition and doping level. *Journal of Alloys and Compounds*. 2020;844: 155828.
14. Schmitt R, McCann D, Marquis B, Kotecki DE. Dielectric relaxation of WO3 thick films from 10 Hz to 1.8 GHz. *Journal of Applied Physics*. 2002;91(10): 6775–6777.
15. Mohamed B, Allel M, Bendouma D, Miloud B, Baghdad M. Improved electronic structure and optical performance of $Bi_2Te_{3-x}Se_x$ from first-principles calculations within TB-mBJ exchange potential. *Materials Research*. 2018;21(1): e20170553.
16. Kawajiri Y, Tanusilp SA, Kumagai M, Ishimaru M, Ohishi Y, Tanaka J, et al. Enhancement of thermoelectric properties of N-Type $BI_2TE_{3-X}SE_X$ by energy filtering effect. *ACS Applied Energy Materials*. 2021;4(10): 11819–11826.
17. Hao F, Xing T, Qiu P, Hu P, Wei T, Ren D, et al. Enhanced thermoelectric performance in N-Type Bi_2TE_3-Based alloys via suppressing intrinsic excitation. *ACS Applied Materials & Interfaces*. 2018;10(25): 21372–21380.
18. Huang XX, Zhang TF, Tang XG, Jiang YP, Liu QX, Feng ZY, Zhou QF. Dielectric relaxation and pinning phenomenon of (Sr,Pb)TiO_3 ceramics for dielectric tunable device application. *Scientific Reports*. 2016;6(1): 31960.
19. Sebastian MT, Ubic R, Jantunen H. Low-loss dielectric ceramic materials and their properties. *International Materials Reviews*. 2015;60(7): 392–412.
20. Verma H, Tripathi A, Upadhyay S. Investigation of structural, optical, dielectric properties, and electrical conductivity mechanism of Sr_2CeO_4: Experimental and DFT studies. *Materials Science in Semiconductor Processing*. 2025;189: 109309.
21. Chanmal C, Jog J. Dielectric relaxation spectroscopy for polymer nanocomposites. In: Mittal V. (Ed.) *Characterization techniques for polymer nanocomposites*. Wiley; 2012. p.167–184.
22. Shivashankar H, Mathias KA, Sondar PR, Shrishail MH, Kulkarni SM. Study on low-frequency dielectric behavior of the carbon black/polymer nanocomposite. *Journal of Materials Science Materials in Electronics*. 2021;32(24): 28674–28686.
23. Dhankhar S, Kundu RS, Parmar R, Murugavel S, Punia R, Kishore N. Electronic transport and relaxation studies in bismuth modified zinc boro-tellurite glasses. *Solid State Sciences*. 2015;48: 230–236.
24. Wang Z, Zhou W, Dong L, Sui X, Zuo J, Cai H, Liu X, Chen Q, Cai J. Dielectric relaxation dynamics of Al/epoxy micro-composites. *Journal of Alloys and Compounds*. 2016;689: 342–349.
25. Teusdea A, Malaescu I, Sfirloaga P, Marin CN. Electric and dielectric properties in Low-Frequency fields of composites consisting of silicone rubber and AL particles for flexible electronic devices. *Materials*. 2022;15(6): 2309.
26. Anwar S, Anwar S, Mishra BK. Synthesis and characterization of bismuth selenide thin films by chemical bath deposition technique. *Advanced Science Letters*. 2014;20(3–4): 854–856.
27. Kaiser MS. Effect of trace impurities on the thermoelectric properties of commercially pure aluminum. *Materials Physics and Mechanics*. 2021;47(4): 582–591.
28. Samigullin ME, Mikhailov MD, Belykh AV, Semencha AV, Krylov NI. Reproducibility of properties of As_xSe_{1-x} glasses on the synthesis temperature. *Materials Physics and Mechanics*. 2023;51(3): 59–65.

MATERIALS PHYSICS AND MECHANICS RESEARCH ARTICLE

Submitted: December 19, 2025 **Revised: February 19, 2026** **Accepted: March 11, 2026**

Numerical simulation of flexural breaking load resistance tests in mortars with recycled polyethylene terephthalate

M.E. Maciá Torregrosa, M.I. Pinilla Hernandez ✉, J. Camacho Diez, C. Machín Hamalainen, R.A. González Lezcano

Universidad San Pablo-CEU, CEU Universities, Madrid, Spain

✉ melanyisabel.pinillahernandez@usp.ceu.es

ABSTRACT

This study investigates the flexural behavior of mortars modified with recycled polyethylene terephthalate through numerical simulations developed in SolidWorks Simulation using a linear dynamic approach. Prismatic specimens measuring 40 × 40 × 160 mm^3 with recycled polyethylene terephthalate contents of 10 and 20 % were evaluated under three temperature levels (20, 150, and 350 °C) and two curing conditions: ambient and water curing. A linear dynamic finite element model was developed in SolidWorks Simulation to reproduce the bending response and analyze the temporal evolution of Von Mises stresses, principal stresses, and stress distribution patterns. The numerical model incorporated experimentally determined mechanical properties and breaking loads as input parameters. The results indicate that increasing recycled polyethylene terephthalate content reduces the stiffness and load-bearing capacity of the mortar, particularly at elevated temperatures, due to the thermal softening of the polymer and the weakening of the interfacial transition zone. Water curing enhances mechanical performance by promoting matrix hydration and improving the capacity for stress redistribution, thereby mitigating the adverse effects of thermal exposure. The numerical simulations showed strong agreement with experimental observations and successfully captured the evolution of stress localization and failure mechanisms under different thermal and curing conditions. These findings highlight the combined influence of recycled polyethylene terephthalate content, curing regime, and temperature on the structural performance of modified mortars and confirm the suitability of linear dynamic finite element analysis for investigating bending behavior in polymer-modified cementitious materials.

KEYWORDS

RPET • bending • finite elements • sustainable mortars • thermal behavior • dynamic simulation

Funding. *This work was supported by San Pablo CEU University, Madrid, Spain, through the research project "Analysis of the Structural Behavior of Concrete Subjected to High Temperatures Manufactured with Recycled Materials to Obtain Sustainable Materials (MCP22VEM)", developed within the ARIE Research Group (Registration number: G20/6-06, San Pablo CEU University, Madrid, Spain).*

Acknowledgements. *The authors gratefully acknowledge the technical support provided by the laboratory facilities of the Institute of Technology, San Pablo CEU University, Madrid, Spain. The authors also thank SEVELAR, Spain, for supplying the plastic waste used in this study.*

Citation: Maciá Torregrosa ME, Pinilla Hernandez MI, Camacho Diez J, Machín Hamalainen C, González Lezcano RA. Numerical simulation of flexural breaking load resistance tests in mortars with recycled polyethylene terephthalate. *Materials Physics and Mechanics*. 2026;54(2): 111–128.
http://dx.doi.org/10.18149/MPM.5422026_9

Introduction

The construction sector faces environmental challenges due to its high consumption of natural resources and its contribution to greenhouse gas emissions. The implementation of circular economy strategies, including the reuse of plastic waste as construction materials, represents a promising approach to mitigating these environmental impacts.

Global plastic production has exceeded 380 million tons annually since 2020, generating large amounts of post-consumer waste that require sustainable management solutions [1]. The valorization of plastic residues in cement-based materials offers environmental benefits by reducing landfill disposal and decreasing the demand for natural aggregate extraction. Among plastic wastes, recycled polyethylene terephthalate (RPET) has attracted considerable attention as a potential partial substitute for fine aggregates in cementitious composites. Previous studies have shown that the incorporation of RPET influences the mechanical and fractured behavior of mortars and concretes [2,3]. In addition to modifying mechanical properties, environmental benefits have been reported, including reduced consumption of natural aggregates and lower indirect emissions associated with raw material extraction and processing. The compressive behavior of RPET-modified mortars has been widely investigated; their flexural performance has received comparatively less attention.

Flexural strength is a critical parameter in structural elements subjected to tensile stresses, particularly in slender components or those primarily exposed to bending loads. RPET exhibits a hydrophobic nature and a lower elastic modulus compared with conventional mineral aggregates, which may weaken the interfacial transition zone between the polymer particles and the cementitious matrix. Several studies have reported that increasing the RPET content leads to a reduction in flexural load-bearing capacity, particularly under tensile-dominated structural response conditions [3]. Curing conditions and thermal exposure significantly affect the mechanical performance of polymer-modified cementitious composites. Proper curing promotes cement hydration and matrix densification, whereas inadequate curing may increase porosity and reduce strength. Elevated temperatures affect both the cementitious matrix and the polymer inclusions. At temperatures above approximately 250–300 °C, RPET undergoes thermal softening and partial melting, which may lead to internal void formation, microcracking, and a deterioration of mechanical properties. Despite this known thermal sensitivity, limited research has examined the combined influence of RPET-content, curing conditions, and elevated temperature exposure on flexural behavior.

The finite element method (FEM) provides a numerical framework for simulating stress distribution, deformation patterns, and failure mechanisms in cement-based materials subjected to bending loads. Previous studies have demonstrated that FEM models calibrated and validated with experimental data can accurately reproduce the mechanical response of polymer-modified cementitious composites [3,4]. However, most available studies focus either on experimental characterization under ambient conditions or on numerical simulations without detailed validation under thermal exposure. Despite the growing body of research on RPET-modified mortars, a clear gap remains in the integrated experimental-numerical evaluation of their flexural behavior at elevated temperatures, particularly regarding the temporal evolution of stress distribution up to failure. Furthermore, the influence of curing conditions on post-thermal mechanical response has not yet been quantified using validated dynamic finite element modeling. The object of this research is cement-based mortars incorporating recycled polyethylene terephthalate (RPET) as partial replacement for fine aggregate.

The aim of this study is to quantitatively evaluate the flexural performance and stress evolution of RPET-modified mortars subjected to different curing conditions and

elevated temperatures through a combined experimental and linear dynamic finite element approach.

To achieve this aim, the following specific objectives are defined:

1. to experimentally determine the flexural strength, stiffness, and breaking load of mortars containing 10 and 20 % RPET under air and water curing conditions at temperatures of 20, 150, and 350 °C;
2. to analyze the influence of RPET content and curing regime on stiffness degradation and load-bearing capacity;
3. to develop and validate a linear dynamic finite element model using experimentally determined breaking loads as input parameters for defining the load history.
4. to evaluate the temporal evolution of Von Mises and principal stress distributions up to failure;
5. to quantify the agreement between numerical predictions and experimental results to assess the mechanical and thermal sensitivity of RPET-modified mortars.

Materials and Methods

Preparation of the mortar and specimens

The methodology adopted in this study is based on an integrated experimental–numerical approach for analyzing the bending behavior of mortars modified with RPET. The experimental design is supported by previous research on the use of plastic waste in cementitious matrices, where RPET has been identified as a viable partial replacement for fine aggregates. Its incorporation contributes to improved material sustainability, although it may significantly influence mechanical properties [1,2,5,6].

Figure 1 illustrates the experimental setup for the three-point bending test on prismatic mortar specimens, indicating the lower supports and the central loading point. This configuration reproduces the testing conditions established in the UNE-EN 196-1 [7] standard and allows the evaluation of flexural behavior under monotonic load.

The RPET used in this study was obtained from post-consumer plastic bottles that were previously classified, washed and mechanically crushed to produce elongated fibers with irregular geometry. This morphology has been reported to enhance mechanical

Fig. 1. Three-point bending test on prismatic mortar specimens

Fig. 2. Specimen condition after reaching the breaking load during the bending test

anchorage within the cementitious matrix. However, the hydrophobic nature of the polymer tends to produce a weaker interfacial transition zone (ITZ) compared to conventional mortars [7,8]. The RPET contents were fixed at 10 and 20 % by volume with respect to the fine aggregate. These values are commonly reported in the literature as representative substitution levels before significant reductions in cohesion and workability occur [7].

Figure 2 presents the condition of the specimen after reaching the breaking load during the bending test. The failure mode is governed by tensile stresses in the lower fiber of the specimen, with the main crack located in the central region of the span. This failure pattern is characteristic of the quasi-brittle behavior typically observed in cement-based mortars.

The three-point bending test was conducted on prismatic mortar specimens with dimensions of 40 × 40 × 160 mm^3. This configuration enables the evaluation of flexural tensile strength by generating a controlled stress distribution, where maximum tensile stresses develop in the lower fiber while compressive stresses appear in the upper region. Such a setup allows for the study of crack initiation and propagation under monotonic loading conditions. This arrangement facilitates the analysis of crack initiation and propagation under monotonic loading conditions. The experimental procedure follows the European standard UNE-EN 196-1 [7], which specifies methods for determining the mechanical properties of cement mortars, including flexural and compressive strength The standard defines specimen geometry, support span (100 mm), loading rate, and curing procedures to ensure the repeatability and comparability of the results.

The mortar mixtures were mechanically mixed to ensure homogeneous RPET distribution and compacted by vibration to minimize the presence of entrapped air voids. After an initial curing period of 24 h, the specimens were demolded and subjected to two different curing regimes: curing in a controlled environment (20 and 60 % relative humidity) and curing in water for 90 days.

The comparison between these curing regimes enables the evaluation of the influence of cement hydration on microstructural densification and the improvement of the ITZ, aspects that are particularly relevant in mortars containing polymeric inclusions [2,7,8]. After the curing period, the specimens were subjected to thermal exposure at 20, 150 and 350 °C. These temperature levels were selected to represent both in-service conditions and elevated-temperature scenarios associated with polymer softening and melting, as well as the progressive dehydration of the cementitious matrix. At higher temperatures, this process results in the loss of chemically bound water and microstructural deterioration [6,9].

Definition of mechanical properties and test loads

The mechanical properties used in the numerical simulations were obtained from experimental bending and compression tests conducted on the same mortar formulations. The parameters considered include the elastic modulus, Poisson´s ratio, density, and stress limits. These values fall within the ranges reported in the literature for mortars incorporating plastic particles and polymeric fibers [3,10].

The bending loads were calculated based on the specimen geometry and loading configuration defined in the standard testing method for determining the mechanical strength of cement mortars according to EN 196-1 [6]. The experimentally obtained ultimate loads were used as input parameters in the numerical model to accurately reproduce the three-point bending test and ensure comparability between experimental observations and numerical simulations.

The experimentally determined mechanical and thermal parameters were incorporated into the finite element model. The complete set of input values used in SolidWorks Simulation is summarized in Table 1.

Table 1. Input mechanical and thermal parameters used in the numerical model

Property	**Value**
Elastic modulus, MPa	25551
Poisson ratio	0.22
Density, kg/m^3	2366
Tensile limit, MPa	3.12
Compression limit, MPa	14.20
Compression elastic limit, MPa	7.10
Thermal conductivity, W/m·K	0.2256
Thermal expansion, K^{-1}	1×10^{-5}

These values are consistent with those reported in previous studies on mortars incorporating plastic inclusions, which typically exhibit lower elastic moduli than conventional mortars. This reduction in stiffness is mainly attributed to the lower stiffness of RPET particles and the presence of weaker interfacial transition zones between the polymer inclusions and the cementitious matrix [3,5,11].

RPET replacement levels of 10 and 20 % were chosen to evaluate the effect of moderate incorporation of recycled polymer on the mechanical behavior of the composite material. Previous studies have shown that low to moderate proportions of recycled PET particles can be incorporated into cement-based materials while maintaining acceptable mechanical performance. Replacement levels below approximately 20–30 % are commonly used to study the balance between mechanical properties, workability, and the environmental benefits associated with the use of recycled polymer. Choi et al. reported that moderate contents of PET aggregates allow the production of lightweight cement composites with reasonable strength values [3]. Similarly, Albano et al. observed that the mechanical properties of concrete decrease progressively as the PET content increases, suggesting that moderate replacement levels are preferable for structural performance [4]. Rahmani et al. also indicated that partial replacement ratios of around 10–20 % allow the mechanical behavior to be evaluated without severe degradation of strength [12]. Therefore, the selected RPET contents provide a representative range for analyzing the influence of recycled polymer incorporation on the mechanical response of the material.

Calculation of bending loads

The experimental flexural strengths used as input for the numerical simulation were obtained through laboratory testing. The flexural strength (σ_f) was calculated according to the UNE-EN 196-1 standard [6]:

$$\sigma_f = \frac{3FL}{2bd^2}, \quad (1)$$

where F is the applied load (N), L is the span length between supports (100 mm), b is the specimen width (40 mm), and d is the specimen height (40 mm).

The mechanical properties and breaking loads used as input data in the numerical model were obtained from the experimental bending and compression tests performed for each curing condition, RPET content and temperature.

In particular, the experimentally determined breaking load was used to define the load history applied in the linear dynamic analysis, allowing the temporal evolution of the equivalent Von Mises stress to be reproduced up to failure. The boundary conditions included the restriction of vertical displacement at the supports and the progressive application of the load at the center point. The load history was defined using the experimentally determined breaking loads presented in Table 2.

Table 2. Experimental values of breaking load of RPET content, type of curing and temperature

Material	T, °C	Flexural strength, MPa	Compression strength, MPa	Elastic limit, MPa	Breaking load, kN	Breaking, MPa
Air 10 % rpet 20 °C	20	3.12	14.20	7.10	22.63	14.14
Air 10 % rpet 150 °C	150	1.20	12.30	6.15	19.55	12.21
Air 10 % rpet 350 °C	350	0.50	9.60	4.80	15.08	9.42
Air 20 % rpet 20 °C	20	4.34	11.80	5.90	18.80	11.75
Air 20 % rpet 150 °C	150	0.70	7.70	3.85	11.75	7.34
Air 20 % rpet 350 °C	350	0.49	4.16	2.08	6.70	4.18
Water 10 % rpet 20 °C	20	4.41	30.70	15.35	49.07	30.66
Water 10 % rpet 150 °C	150	3.50	24.50	12.25	39.30	24.56
Water 10 % rpet 350 °C	350	1.60	16.00	8.00	25.66	16.04
Water 20 % rpet 20 °C	20	3.48	21.40	10.70	34.26	21.41
Water 20 % rpet 150 °C	150	2.03	14.40	7.20	23.01	14.38
Water 20 pet 350 °C	350	0.52	7.52	3.76	11.60	7.25

Numerical modeling in SolidWorks simulation

The selected output variables evaluated included Von Mises stress, principal stresses (σ_1, σ_2, σ_3), maximum strains, and neutral axis position. These variables are commonly used indicators for interpreting the flexural behavior of cementitious materials using FEM analysis [12,13]. Table 3 summarizes the main parameters of the numerical model, including geometry, mesh characteristics, boundary conditions, and evaluated variables.

This set of variables coincides with those used in previous studies of bending of mortars modified with polymers by FEM [3,9]. The numerical modeling was performed using SolidWorks Simulation through a linear dynamic analysis aimed at reproducing the three-point bending test applied to the mortar specimens. The geometry of the specimen, as well as the supports and the loading point, was explicitly defined to accurately represent the experimental configuration. Meshing was performed using second-order parabolic tetrahedral elements, which provide a more accurate approximation of the stress gradients compared with linear elements. Aditionally, local mesh refinement was applied in critical contact areas and in the central region subjected to maximum bending. This approach follows commonly accepted recommendations for FEM simulations of cementitious materials and fiber-reinforced composites [11,12,14,15].

Table 3. Parameters of the FEM numerical model for the three-point bending test

Category	Description
Model geometry	Prismatic specimen of 40 × 40 × 160 mm^3 Cylindrical supports of 10 mm in diameter Cylindrical load pointer of 10 mm in diameter
Meshing	Parabolic tetrahedral elements of 10 nodes Global element size: 2.5 mm Local mesh refinement: 1 mm in critical contact areas Total number of elements: 45,000–52,000
Boundary conditions	Supports restricted in vertical translation Load applied as equivalent pressure *F/A* in the contact area of the pointer Transient analysis with linear increase of load until reaching *F*
Evaluated variables	Equivalent Von Mises stresses Main stresses σ_1, σ_2, σ_3 Position of the neutral line and curvature Maximum deformations Triaxial stress state in the tensioned zone

The boundary conditions included the restriction of vertical displacements at the lower supports, while the load was progressively applied at the central point through a pressure-equivalent formulation reproducing the standarized three-point bending configuration. The temporal evolution of the load was defined until reaching the experimentally determined ultimate load corresponding to each test condition, enabling a direct analysis of the stress response as a function of time. This approach is particularly suitable for evaluating the quasi-fragile behavior of the mortar and for identifying the instant of failure, as has been pointed out in previous studies on fracture and crack propagation in cementitious materials [16–20].

The equivalent Von Mises stress was used to analyze the global evolution of the stress state up to the breaking load, while the principal stresses allowed the identification of the regions dominated by tensile or compressive stresses and the potential initiation zones of structural damage. This set of variables has proven particularly effective for correlating numerical and experimental results in cementitious materials modified with recycled polymers [14,15,21,22].

The numerical approach adopted in this study enables a detailed analysis of the combined influence of RPET content, curing regime, and temperature on the mechanical response of the material. The inclusion of thermally degraded models is consistent with previous research demonstrating that the strength of cementitious materials significantly decreases at elevated temperatures due to matrix dehydration and the loss of stiffness in polymeric inclusions [23,24]. Furthermore, the finite element method has been widely recognized as a robust tool for evaluating the structural behavior of mortars with RPET, complementing standardized bending tests defined by ASTM and EN standards. FEM analysis provides additional insight into internal stress distribution and failure mechanisms that cannot be obtained solely from global experimental measurements [24,25].

The thermal-mechanical analysis conducted in this work is supported by well-established studies on the behavior of lightweight and composite cementitious materials subjected to elevated temperatures. Previous investigations have shown that increasing temperature leads to a gradual reduction in stiffness and load-bearing capacity due to dehydration of the cement matrix and internal redistribution of strains [26,27]. In this

context, linear dynamic simulation allow accurate representation of the evolution of stress states up to the breaking load, providing valuable information about thermal degradation mechanisms that are difficult to capture experimentally.

From the perspective of numerical analysis, FEM is particularly suitable for evaluating damage tolerance and crack localization in quasi-brittle composite materials. Previous research has demonstrated the ability of FEM to identify critical stress concentration zones and predict the loss of structural integrity in polymer-modified mortars under mechanical loading conditions [28]. In the RPET-modified mortars analyzed in this study, the evaluation of Von Mises and the principal stresses allows identification of damage iniciation in tensiled zones and its evolution until global failure.

The dynamic nature of the analysis adopted in this work is supported by previous studies highlighting the importance of considering the temporal evolution of stresses and strains in materials exhibiting viscoelastic or temperature-dependent behavior [29,30].

Overall, the application of FEM to the study of RPET-modified mortars contributes to a better understanding of their structural performance and reinforces their potential as sustainable construction materials within more resilient and resource-efficient building strategies.

It should be noted that the present FEM model is based on a linear dynamic formulation and therefore does not explicitly simulate crack propagation or nonlinear damage evolution. However, it provides a reliable approximation of the stress evolution and failure onset up to the experimentally observed breaking load.

The numerical model was validated through comparison with the experimentally measured breaking loads obtained from the three-point bending tests. The consistency between the simulated stress distributions and the experimental failure loads confirms the reliability of the proposed FEM approach for analyzing the flexural behavior of RPET-modified mortars.

Results

Specimens with 10 % RPET cured under ambient conditions

At temperature of 20°C, specimens containing 10 % RPET hit a breaking load of 22.63 kN, corresponding to a flexural strength of 3.12 MPa. Figure 3(a) presents the temporal evolution of the Von Mises stress, which increases almost linearly until peak load. This behavior indicates predominantly elastic mechanical response prior to failure. After reaching a peak load, a sudden drop in stress occurs, indicating brittle collapse governed by tensile stresses.

The stress distribution at the peak load, illustrated in Fig. 3(b), shows a typical bending pattern with maximum tensile stresses located in the lower fiber of the specimen and compressive stress concentrated in the upper region. No significant stress concentrations are observed, suggesting relatively uniform stress transfer between the cementitious matrix and the RPET inclusions under ambient temperature conditions.

When the temperature increases to 150 °C the breaking load decreases to 19.55 kN, representing a reduction of approximately 13.6 % compared with the 20 °C condition.

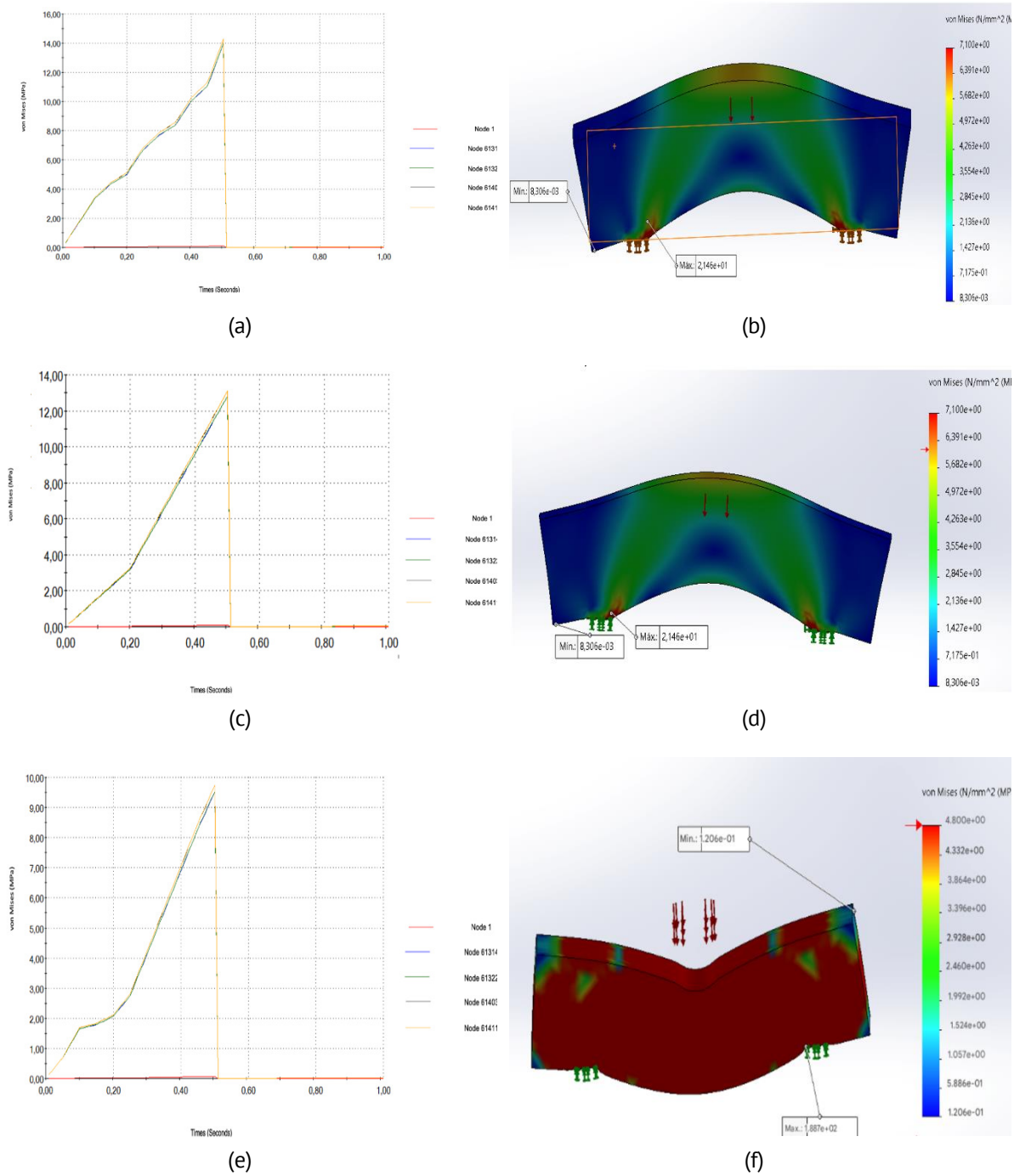

Fig. 3. Temporal evolution (a,c,e) and spatial distribution of Von Mises stress (b,c,f) in specimens containing 10 % RPET cured under ambient conditions at different temperatures: (a,b) 20 °C, (c,d) 150 °C, (e,f) 350 °C

As shown in Fig. 3(c), stress-time curves exhibit a lower steep gradient plus experience peak stress onset sooner thereby signaling reduced global stiffness.

The stress distribution shown in Fig. 3(d) becomes more heterogeneous, with localized tensile stress concentrations appearing in the lower fiber and beneath the loading point. These patterns suggest thermal softening of the RPET particles and progressive weakening of the interfacial transition zone (ITZ), which reduces the efficiency of stress redistribution.

At temperature of 350 °C, severe mechanical degradation is observed. The ultimate load decreases to 15.08 kN, corresponding to an overall reduction of approximately 33.4 % relative to the 20 °C condition. The stress evolution presented in Fig. 3(e) indicates limited stress development followed by abrupt collapse, which is characteristic of brittle failure associated with advanced thermal damage.

The stress distribution at failure (Fig. 3(f)) reveals strong stress localization in the tensile zone. This behavior is likely associated with internal discontinuities generated by the partial melting of RPET particles. The combined effect of reduced matrix cohesion and weakened interfacial bonding significantly decreases stiffness and load-bearing capacity.

Overall, temperature emerges as a primary factor governing the mechanical behavior of mortars containing 10 % RPET under ambient curing conditions. Although the fundamental bending mechanism remains unchanged, increasing thermal exposure progressively reduces stiffness, peak load, and the capacity for stress redistribution, ultimately leading to brittle tensile failure.

A comparative analysis of the three temperature levels under ambient curing conditions indicates that mechanical degradation occurs progressively as temperature increases. This degradation is primarily controlled by thermal effects rather than polymer content at the dosage considered. While the bending mechanism remains dominated by tensile stress, the stiffness and ability to redistribute stress decrease steadily with increasing temperature.

Specimens with 10 % RPET cured under water

At temperature of 20 °C, water curing significantly enhanced flexural performance of the mortar specimens. The Von Mises stress curves demonstrate a continuous increase until reaching a peak load of 49.07 kN, which is more than twice the value obtained for specimens cured under ambient conditions (22.63 kN). Figure 4(a) illustrates a steeper stress-time gradient and a clear peak, suggesting increased stiffness and load-bearing capacity. The stress distribution at the maximum load (Fig. 4(b)) appears more uniform compared with the ambient-cured specimens. Tensile stresses remain concentrated in the lower fiber, but without pronounced localization. The neutral axis remains stable along the span, indicating improved matrix densification and more effective stress transfer across the interfacial transition zone (ITZ).

At temperature of 150 °C, the breaking load decreases to 39.3 kN, corresponding to a reduction of approximately 19.9 % compared with the value measured at 20 °C. However, this value still exceeds the strength of specimens cured under ambient conditions at the same temperature (19.55 kN). According to Fig. 4(c), the stress–time response maintains a relatively steep gradient, suggesting that water curing mitigates the initial effects of thermal softening.

The stress distribution at peak load (Fig. 4(d)) shows moderate tensile concentrations while preserving a relatively uniform stress field. Compared with ambient curing at the same temperature, stress localization is less pronounced, reflecting improved resistance to microstructural degradation induced by thermal exposure.

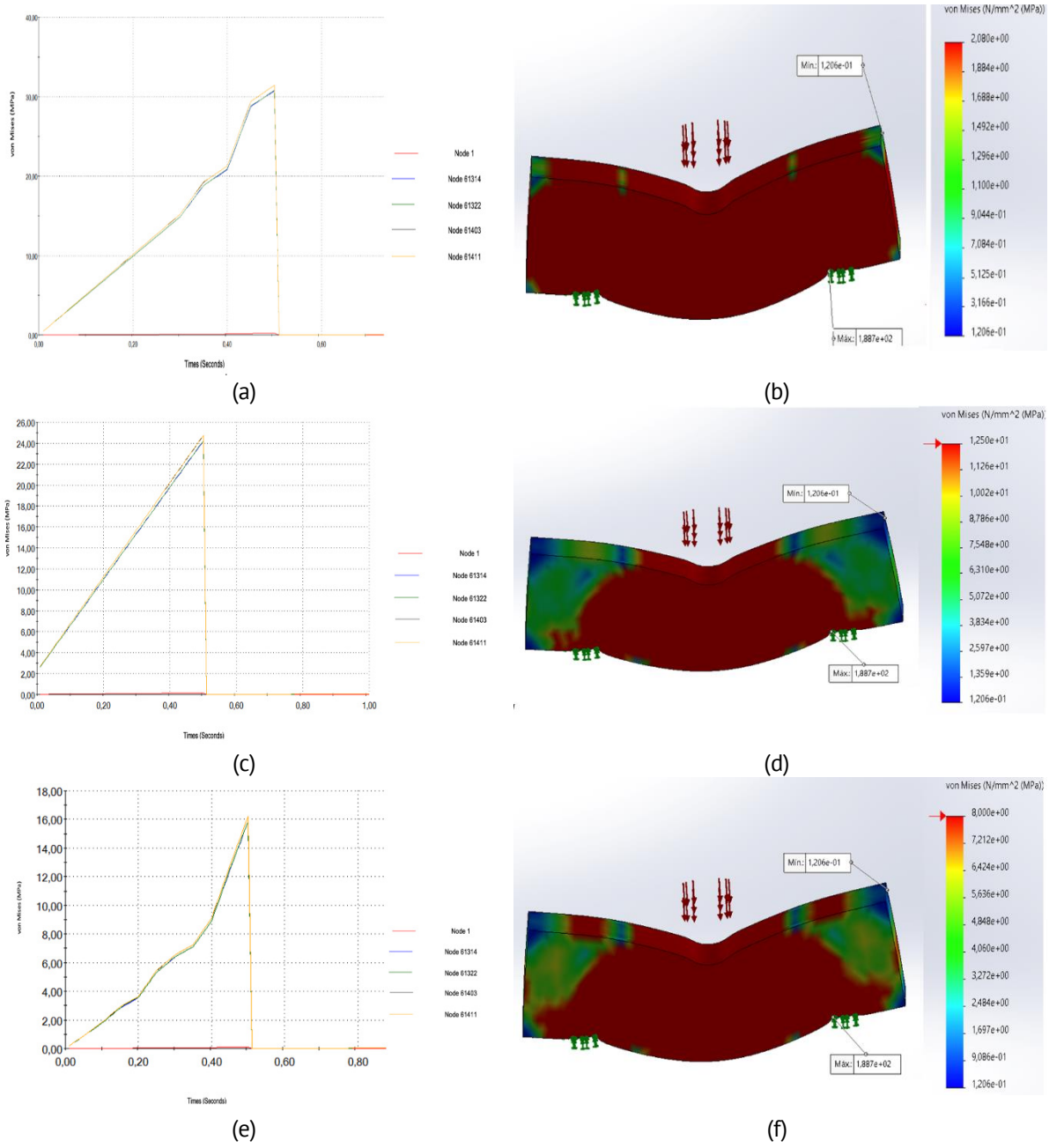

Fig. 4. Temporal evolution (a,c,e) and spatial distribution of Von Mises stress (b,d,f) in specimens containing 10% RPET cured under water at different temperatures: (a,b) 20 °C, (c,d) 150 °C, (e,f) 350 °C

At temperature of 350 °C, significant mechanical degradation occurs; however, water-cured specimens still maintain a breaking load of 25.66 kN, which is approximately 70 % higher than that of the specimens cured under ambient conditions (15.08 kN). Figure 4(e) shows the stress evolution, which exhibits a more gradual increase before failure compared with ambient curing, indicating partial preservation of structural integrity.

The stress distribution at failure (Fig. 4(f)) reveals localized tensile regions associated with the partial melting of RPET particles, while the cementitious matrix retains a certain degree of cohesion. Although the final collapse is primarily due to brittle tensile failure, the enhanced hydration from water curing delays stiffness degradation and improves the residual load-bearing capacity.

Overall, water curing improves the mechanical performance of mortars containing 10 % RPET across all temperature ranges. Although thermal exposure progressively reduces strength and stiffness, the beneficial effect of improved matrix hydration remains evident even under severe thermal conditions. These results indicate that curing conditions play a critical role in mitigating the adverse mechanical impacts associated with polymer inclusions and high-temperature exposure.

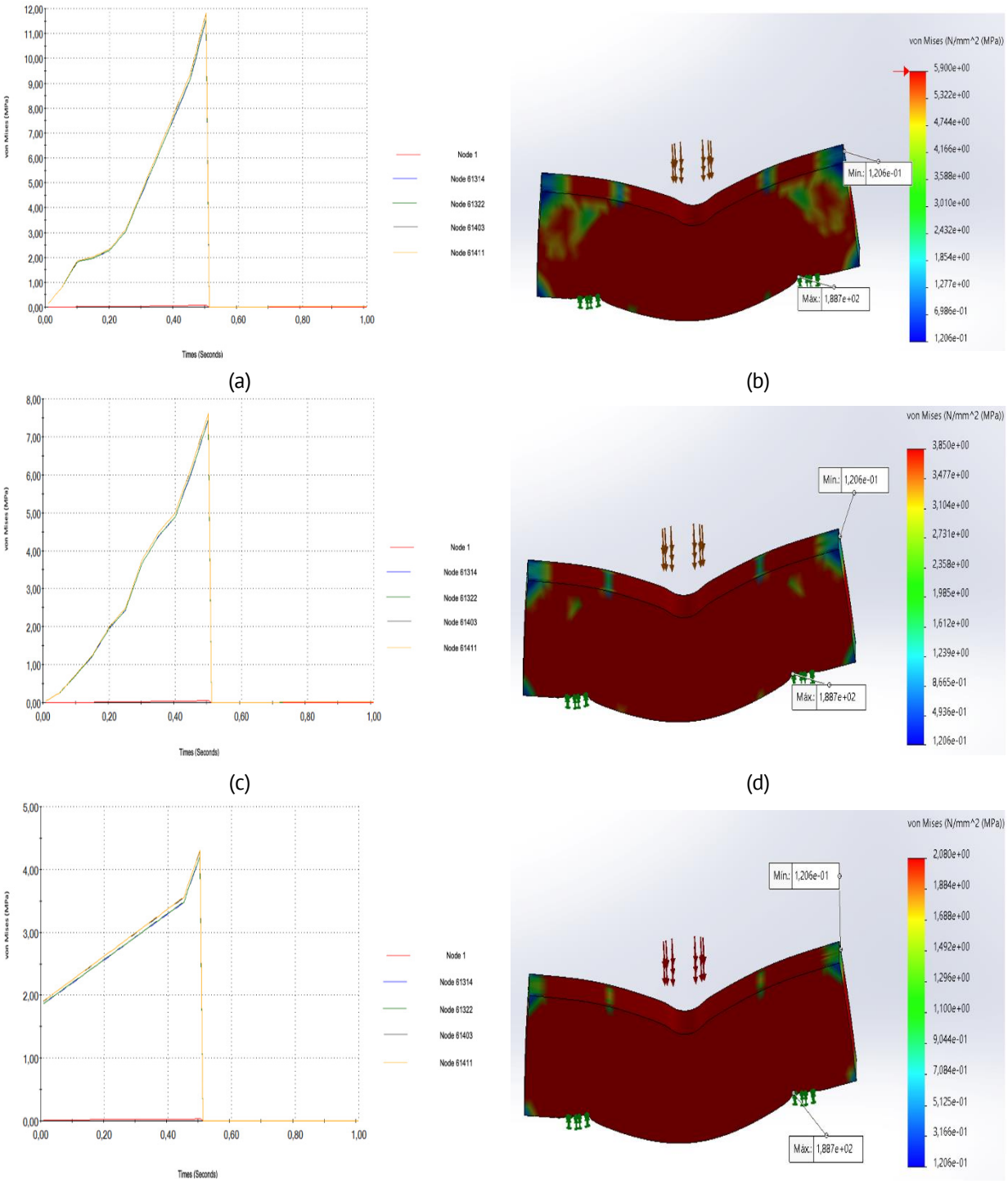

Fig. 5. Temporal evolution (a,c,e) and spatial distribution of Von Mises stress (b,d,f) in specimens containing 20 % RPET cured under ambient conditions at different temperatures: (a,b) 20 °C, (c,d) 150 °C, (e,f) 350 °C

Specimens with 20 % RPET cured at 20 °C

At temperature of 20 °C, increasing the RPET content from 10 to 20 % results in a noticeable reduction in mechanical performance. The breaking load decreases to 18.8 kN**,** accompanied by less steep stress-time curves and greater stress dispersion across the nodes. The stress–time curves shown in Fig. 5(a) present a lower initial slope, indicating reduced global stiffness. The stress distribution at peak load (Fig. 5(b)) reveals localized tensile concentrations in the lower fiber and beneath the loading point. Compared with the 10 % RPET mixture, the stress field is less uniform, indicating weaker interfacial bonding and reduced stress transfer efficiency due to the higher polymer content.

At 150 °C, mechanical degradation becomes more pronounced. Table 6c shows the breaking load decreases to 11.75 kN, which corresponds to a reduction of approximately 37.5 % relative to 20 °C. The stress–time response reaches its maximum at an earlier stage, reflecting accelerated stiffness loss. The stress field shown in Fig. 5(d) exhibits clear localization in the tensile zone and instability of the neutral axis. The combined effect of increased polymer content and thermal softening leads to higher stress concentrations, promoting early crack initiation and propagation.

At temperature of 350 °C, the structural response shows severe deterioration. The breaking load decreases to 6.70 kN, representing an overall reduction of approximately 64.4 % compared with the 20 °C condition. The temporal stress evolution (Fig. 5(e)) shows minimal stress development prior to sudden collapse, indicating highly brittle behavior.

Figure 5(f) depicts the stress distribution and confirms extreme localization in the lower tensile region and a generalized loss of stress continuity. The combined effect of high RPET content and elevated temperature reduces matrix cohesion, leading to rapid failure under tensile stresses. Overall, increasing the RPET-content to 20 % reduces stiffness, peak load, and thermal stability under ambient curing conditions.

The material becomes considerably more sensitive to temperature increases, and the combined effects of polymer softening and reduced matrix cohesion accelerate structural degradation.

Specimens with 20% RPET cured under water 20 °C

At temperature of 20 °C, water curing significantly improves the mechanical response compared with ambient curing conditions. The breaking load reaches 34.26 kN, representing an increase of approximately 82 % compared with ambient-cured specimens with the same RPET content 18.8 kN. The stress–time curves presented in Fig. 6(a) exhibit a steeper slope and a well-defined peak, indicating improved stiffness and load-bearing capacity.

The stress distribution at peak load (Fig. 6(b)) appears more balanced than ambient curing, with reduced tensile localization in the lower fiber. However, compared with specimens containing 10 % RPET, the stress field shows moderate heterogeneity, suggesting that the increased polymer content limits stress transfer efficiency.

At 150 °C, the breaking load decreases to 23.01 kN, corresponding to a reduction of approximately 32.8 % relative to the value measured at 20 °C. Nevertheless, this value remains significantly higher than that observed in specimens cured under ambient conditions at the same temperature (11.75 kN). The stress–time evolution (Fig. 6(c))

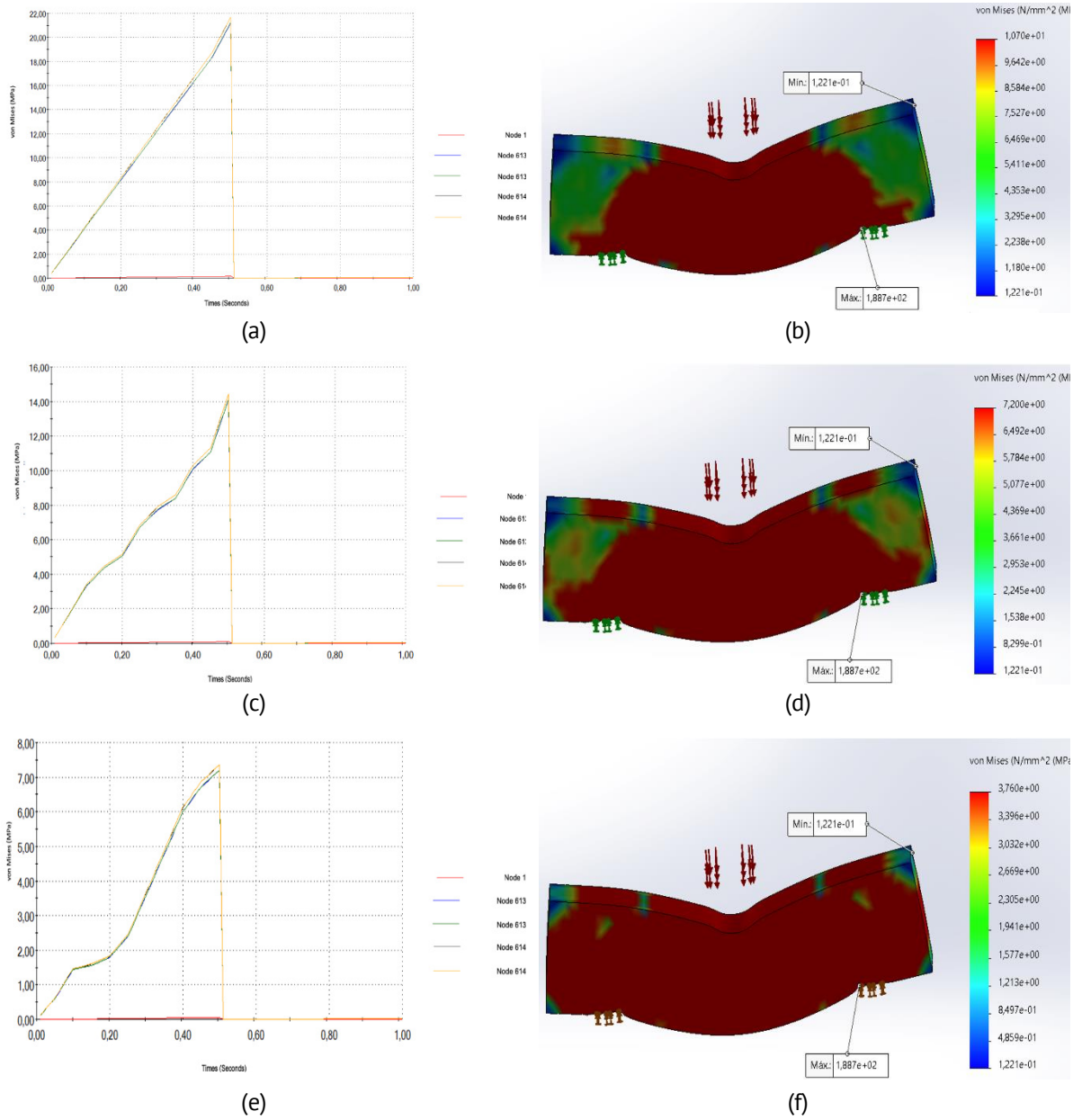

Fig. 6. Temporal evolution (a,c,e) and spatial distribution of Von Mises stress (b,d,f) in specimens containing 20% RPET cured under water at different temperatures: (a,b) 20 °C, (c,d) 150 °C, (e,f) 350 °C

shows a progressive increase until failure, while the stress distribution (Fig. 6(d)) indicates localized tensile concentrations that are less severe than those observed in the ambient-cured specimens. Water curing helps mitigate stiffness degradation by improving matrix hydration and strengthening the interfacial bonding, which slows the development of thermally induced damage.

At 350 °C, significant degradation occurs. Figure 6(e) shows the breaking load decreases to 11.6 kN, representing a total reduction of approximately 66 % compared to 20 °C. The spatial stress distribution shows localized tensile concentrations in the lower fiber.

The stress distribution (Fig. 6(f)) shows pronounced tensile localization in the lower fiber and reduced stress continuity across the specimen. This behavior is consistent with the melting of RPET particles and the formation of internal voids within the cementitious matrix.

Although water curing preserves some residual cohesion, it cannot fully compensate for the combined effects of high polymer content and severe thermal exposure.

Overall, water curing improves the flexural behavior of mortars containing 20 % RPET at all temperature levels. However, increasing polymer content significantly enhances thermal sensitivity of the material. Temperature remains the primary factor controlling mechanical degradation, although improved hydration delays stiffness loss and increases residual strength.

Discussion

Influence of RPET-content

Increasing the RPET content from 10 to 20 % led to a noticeable reduction in flexural strength and, consequently, a decrease in breaking load from approximately 22.6 kN to 18.80 kN under ambient curing conditions at 20 °C. This behavior is consistent with previous experimental studies reporting that higher PET aggregate contents reduce stiffness and load-bearing capacity due to the lower elastic modulus of polymer particles and weaker bonding within the interfacial transition zone (ITZ) [3,4]. Similar reductions in both flexural and compressive strength have been reported for cement-based composites incorporating recycled PET aggregates, where increasing polymer fractions promote stress concentration and disrupt matrix continuity [12].

Effect of temperature on polymer-modified mortars

Thermal exposure significantly affects the mechanical performance of the mortars investigated in this study. When the temperature increased from 20 to 150 °C, the breaking load decreased by approximately 13–38 %, depending on the RPET content. This reduction agrees the previous studies indicating that moderate thermal exposure progressively degrades cementitious materials due to matrix dehydration and the onset of polymer softening [26,27]. The temperature range between 150 and 300 °C has been identified as particularly critical for polymer-modified cementitious composites. Within this range, polymer inclusions begin to lose stiffness and their bond with the cement matrix weakens, resulting in a reduction in load-bearing capacity.

Influence of high temperature on mechanical performance

At temperature of 350 °C, severe mechanical degradation was observed, with reductions in breaking load exceeding 60 % in specimens containing 20 % RPET. Numerical simulations revealed strong stress localization in the tensile zone and abrupt failure following limited stress development. Similar failure mechanisms have been described in previous studies on polymers exposed to high temperatures, where polymer melting generates internal voids and microcracks that disrupt matrix continuity and accelerate brittle collapse [27,30]. These findings confirm that the thermal stability of polymer inclusions plays a decisive role in determining the residual mechanical capacity of cementitious composites subjected to high temperatures.

The numerical predictions showed good agreement with the experimentally measured breaking loads and reproduced the main stress distribution patterns observed during the three-point bending tests.

Influence of water curing

The curing regime was found to significantly influence the flexural behavior of the mortars. Specimens cured in water exhibited substantially higher breaking loads than those cured under ambient conditions. For instance, at 20 °C, specimens containing 10 % RPET and cured in water reached breaking loads of approximately 49 kN, more than twice the value measured for ambient-cured specimens. This improvement can be attributed to enhanced hydration of the cement matrix, leading to a denser microstructure that strengthens the interfacial transition zone and improves stress transfer between the matrix and the polymer inclusions. Comparable improvements associated with enhanced curing conditions have been reported for polymer-modified cementitious materials, where increased matrix densification contributes to both improved strength and durability [30].

Overall, the present results confirm previously reported trends regarding the influence of polymer aggregates in cementitious composites while providing additional insight into the combined effects of RPET content, curing regime, and thermal exposure on the stress redistribution and failure mechanisms.

Conclusions

Following the integrated experimental and numerical analysis, the subsequent scientific conclusions are established:

1. RPET incorporation changes flexural stiffness and load-bearing capacity. Increasing RPET-content from 10 to 20 % by volume reduces both the breaking load and stiffness under all curing conditions. This behavior suggests that higher polymer content weakens the interfacial transition zone (ITZ), thereby reducing stress transfer efficiency within the composite.
2. Temperature is the governing parameter for mechanical degradation. Exposure to 150 °C and particularly 350 °C causes progressive reductions in breaking load, stiffness, and stress redistribution capacity. At 350 °C, brittle tensile-controlled failure dominates due to RPET softening and matrix dehydration.
3. Water curing improves mechanical performance. Specimens cured in water exhibit greater breaking loads and more homogeneous stress distributions across all temperatures. Improved cement hydration leads to matrix densification and strengthens the ITZ, which mitigates the detrimental effects of thermal degradation.
4. The combined effect of high RPET-content and elevated temperature is critical. Mortars containing 20 % RPET and cured under ambient temperature exhibit the highest thermal sensitivity, experiencing severe stress localization and rapid brittle failure at 350 °C.
5. The numerical model reproduces experimental behavior with accuracy. Finite element simulations successfully capture the temporal evolution of Von Mises stresses and the spatial stress redistribution patterns up to failure, thereby validating the proposed experimental–numerical methods.

Overall, a balance between sustainability and mechanical performance can be achieved by limiting RPET content to moderate levels and applying appropriate curing conditions, especially in applications involving elevated temperature exposure.

Finite element simulations successfully capture the temporal evolution of Von Mises stresses and the spatial stress redistribution patterns up to failure. The numerical predictions showed good agreement with the experimentally measured breaking loads and the stress distribution patterns observed during the bending tests.

CRediT authorship contribution statement

M.E. Maciá Torregrosa conceived and designed the study and supervised the overall research process; **M.I. Pinilla Hernandez** carried out the experimental work, including specimen preparation, curing procedures, and mechanical testing, and was responsible for data collection; **J. Camacho Diez** contributed to the definition of the experimental methods and supported the analysis of mechanical test results; **C. Machín Hamalainen** participated in the interpretation of results and contributed to the preparation and revision of figures and tables; **R.A. González Lezcano** contributed to data interpretation, critical revision of the manuscript, and overall scientific supervision. All authors critically reviewed and approved the final version of the manuscript and agreed to be accountable for all aspects of the work.

Conflict of interest

The authors declare that they have no conflict of interest.

References

1. Geyer R, Jambeck JR, Law KL. Production, use, and fate of all plastics ever made. *Science Advances.* 2017;3(7): e1700782.
2. Reis JML, Chianelli-Junior R, Cardoso JL, Marinho FJV. Effect of recycled PET in the fracture mechanics of polymer mortar. *Construction and Building Materials.* 2011;25(6): 2799–2804.
3. Choi YW, Moon DJ, Kim YJ, Lachemi M. Characteristics of mortar and concrete containing fine aggregate manufactured from recycled waste polyethylene terephthalate bottles. *Construction and Building Materials.* 2009;23(8): 2829–2835.
4. Albano C, Camacho N, Hernández M, Matheus A, Gutiérrez A. Influence of content and particle size of waste PET bottles on concrete behavior at different w/c ratios. *Waste Management.* 2009;29: 2707–2716.
5. Senhadji Y, Siad H, Escadeillas G, Benosman AS, Chihaoui R, Mouli M, Lachemi M. Physical, mechanical and thermal properties of lightweight composite mortars containing recycled polyvinyl chloride. *Construction and Building Materials.* 2019;195: 198–207.
6. Lima PRL, Barros JAO, Santos DJ, Fontes CM, Lima JMF, Toledo Filho R. Experimental and numerical analysis of short sisal fiber-cement composites produced with recycled matrix. *European Journal of Environmental and Civil Engineering.* 2019;23(1): 70–84.
7. European Committee for Standardization. EN 196-1. *Methods of Testing Cement — Part 1: Determination of Strength.* Brussels, Belgium: CEN; 2009.
8. Monteiro PJM. *Concrete: Microstructure, Properties, and Materials.* 3rd ed. New York: McGraw-Hill; 2006.
9. Zhang Q, Ye G. Dehydration kinetics of Portland cement paste at high temperature. *Journal of Thermal Analysis and Calorimetry.* 2012;110: 153–158.
10. Alani AH, Bunnori NM, Noaman AT, Majid TA. Durability performance of a novel ultra-high-performance PET green concrete. *Construction and Building Materials.* 2019;209: 395–405.
11. Ge Z, Gao Z, Sun R, Zheng L. Mix design of concrete with recycled clay-brick-powder using the orthogonal design method. *Construction and Building Materials.* 2012;31: 289–293.

12. Rahmani E, Dehestani M, Beygi MHA, Allahyari H, Nikbin IM. Mechanical properties of concrete containing waste PET particles. *Construction and Building Materials.* 2013;47: 1302–1308.
13. Ochi T, Okubo S, Fukui K. Development of recycled PET fiber and its application as concrete reinforcing fiber. *Cement and Concrete Composites.* 2007;29(6): 448–455.
14. Kim SB, Yi NH, Kim HY, Kim JHJ, Song YC. Material and structural performance evaluation of recycled PET fiber reinforced concrete. *Cement and Concrete Composites.* 2010;32(3): 232–240.
15. Siddique R, Khatib J, Kaur I. Use of recycled plastic in concrete: A review. *Waste Management.* 2008;28(10): 1835–1852.
16. Ge Z, Yue H, Sun R. Properties of mortar produced with recycled clay brick aggregate and PET. *Construction and Building Materials.* 2015;93: 851–856.
17. Bentur A, Mindess S. *Fibre Reinforced Cementitious Composites.* 2nd ed. Boca Raton: CRC Press; 2007.
18. Mindess S, Young JF, Darwin D. *Concrete.* 2nd ed. Upper Saddle River, NJ: Prentice Hall; 2003.
19. Bažant ZP, Planas J. *Fracture and Size Effect in Concrete and Other Quasibrittle Materials.* Boca Raton: CRC Press; 2019.
20. Zollo RF. Fiber-reinforced concrete: an overview after 30 years of development. *Cement and Concrete Composites.* 1997;19(2): 107–122.
21. Hillerborg A, Modéer M, Petersson PE. Analysis of crack formation and crack growth in concrete. *Cement and Concrete Research.* 1976;6(6): 773–781.
22. Bažant ZP, Oh BH. Crack band theory for fracture of concrete. *Mat. Constr.* 1983;16: 155–177.
23. Robl T, Jewell R, Duvallet T, Gülcan E, Rathbone R, Oberlink A. Determination of Pozzolanic Activity. *Advances in Civil Engineering Materials.* 2022;11: 520–538.
24. Xu S, Reinhardt HW. Crack extension resistance and fracture properties of quasi-brittle materials. *International Journal of Fracture.* 1998;92: 71–99.
25. Lazorenko G, Kasprzhitskii A, Fini EH. PET waste plastic as natural aggregate replacement in geopolymer mortar. *Journal of Cleaner Production.* 2022;375: 134083.
26. Hertz KD. Concrete strength for fire safety design. *Magazine of Concrete Research.* 2005;57(8): 445–453.
27. da Luz Garcia M, Oliveira MR, Silva TN, Castro ACM. Performance of mortars with PET. *Journal of Material Cycles and Waste Management.* 2021;23: 699–706.
28. Reis JML, Carneiro EP. Evaluation of PET waste aggregates in polymer mortars. *Construction and Building Materials.* 2012;27(1): 107–111.
29. Erofeev VT, Korotaev SA, Vatin NI. Deformation and Heat-Insulating Characteristics of Light Concrete on Porous Burned Binder Under Heating. *Materials Physics and Mechanics.* 2023;51(1): 33–41.
30. Hannawi K, Kamali-Bernard S, Prince W. Physical and mechanical properties of mortars containing PET and PC waste aggregates. *Waste Management.* 2010;30(11): 2312–2320.

MATERIALS PHYSICS AND MECHANICS RESEARCH ARTICLE

Submitted: January 5, 2026 **Revised: February 16, 2026** **Accepted: March 18, 2026**

Effect of acoustic vibration frequency of concrete during hydration on mechanical properties

M. Hematibahar [1], M. Kharun [2], R.S. Fediuk [3,4]✉, N.I. Vatin [5], V.N. Lymarev [6], G.R. Fediuk [3], L.N. Alexeiko [7]

[1] ANO SAFAS, Moscow, Russia

[2] Moscow State University of Civil Engineering, Moscow, Russia

[3] Far Eastern Federal University, Vladivostok, Russia

[4] Vladivostok State University, Vladivostok, Russia

[5] Peter the Great St. Petersburg Polytechnic University, St. Petersburg, Russia

[6] Perm Military Institute of the National Guard Troops of the Russian Federation, Perm, Russia

[7] Gomel State Medical University, Gomel, Republic of Belarus

✉ roman44@yandex.ru

ABSTRACT

While extensive research has focused on the sound absorption properties of concrete, the effect of external acoustic vibration loads on its hydration process, mechanical performance, and microstructure remains a significant scientific gap. This study investigates the influence of applying acoustic vibrations at varying frequency ranges during the critical hydration period. A conventional concrete mixture was subjected to acoustic vibrations across five frequency ranges for 24 h during hydration, using a setup with two loudspeakers at constant sound intensity. A control sample was cured without any vibrations. The mechanical performance was evaluated through compressive and tensile strength tests at 7, 14, and 28 days Microstructural analysis was conducted using scanning electron microscopy on selected samples. The results demonstrated a clear negative impact on mechanical properties. The control sample achieved the highest compressive (37.2 MPa) and tensile (3.6 MPa) strengths at 28 days. The application of acoustic vibrations generally reduced strength, with the reduction being more severe at higher frequencies. The sample E (10^4–$2{\cdot}10^4$ Hz) showed the most significant decline, with compressive and tensile strengths 42.4 % and 22.2 % lower than the control, respectively. However, the effect was found to be frequency-dependent. Sample C (10^3–$5{\cdot}10^3$ Hz) exhibited a relatively smaller reduction in strength compared to other treated samples, suggesting a less detrimental impact within this specific range. The study concludes that external acoustic vibrations during hydration disrupt the microstructure formation, leading to a decrease in the mechanical strength of concrete. No beneficial effects were observed within the tested parameters.

KEYWORDS

acoustic vibrations • concrete hydration • mechanical properties • compressive strength • tensile strength microstructure • frequency dependence • early-age concrete

Funding. *This work was supported by the Russian Science Foundation, grant № 25-19-00866.*

Citation: Hematibahar M, Kharun M, Fediuk RS, Vatin NI, Lymarev VN, Fediuk GR, Alexeiko LN. Effect of acoustic vibration frequency of concrete during hydration on mechanical properties. *Materials Physics and Mechanics*. 2026;54(2): 129–139.
http://dx.doi.org/10.18149/MPM.5422026_10

Introduction

Concrete is the most common building material in the world [1]. An increase in its mechanical characteristics is achieved by activating various components of this material [2]. Mechanical activation of the binder makes it possible to increase its specific surface area, and hence the hydration zone [3]. Moreover, this method has found application for both cement [4] and cement-free binders [5]. The influence of mechanical activation on the characteristics of glass concrete was studied in [6]. In a recent article [7], the use of sulfate activation was investigated in detail. Another type of increase in the efficiency of the concrete mix is the activation of the mixing water [8]. In [9], it was suggested in-line activation of cementitious materials for 3D concrete printing. It is relevant to use several types of activation, especially those based on various physical processes [10,11]. Ultrasonic activation of the sealed concrete mix was applied in [10], and thermal activation in [11]. In recent years, it has become much easier to predict the mechanical properties of concretes thanks to machine learning [12]. In [13], the wave mechanism of structure formation in cement compositions was investigated. Calcination and mechanical activation of waste clays for low-carbon concrete studied in [14]. The effect of vibration at an early age on the strength of concrete has been proven in [15]. By choosing the rational vibration compaction time, it is possible to improve the strength and microstructure of ultra-high-efficiency concrete [16]. In [17], a simulation of the flow of fresh concrete was carried out taking into account vibration compaction. In [18], a study was carried out on the effect of the vibration process on the density of the concrete mixture in a sliding formwork. In [19], the prediction of the range of action of submersible vibrators based on wave propagation for calculating the rheological behavior during vibration of fresh concrete was studied and described in detail. In [20], a study was conducted on the relationship between the speed of an ultrasonic pulse and the compressive strength of polyurethane foam. According to previous studies, no investigated the effect of acoustic vibration loading on concrete during hydration, and this is a major scientific gap. This study attempts to find out the amount of compressive strength during hydration with five frequency ranges (20–500, 500–1000, 1000–5000, 5000–10000, and 10000–20000 Hz) for 24 h. The research object is conventional concrete subjected to external acoustic vibration over varying frequency ranges during hydration, and the effects on mechanical performance and microstructure are investigated. The aim of the study is to study the effect of the frequency of acoustic vibrations on the mechanical properties of concrete during hydration. The objectives to achieve this aim are to determine the initial and final setting times, as well as compressive and flexural strength.

Materials and Methods

According to Table 1, the concrete mixture used ordinary Portland cement, water, superplasticizer, both fine and coarse aggregates, marble powder, glass powder, and microsilica.

Table 1. Mixture design of concrete, kg/m^3

Sample	Cement	Water	Fine aggregates	Coarse aggregates	Glass powder	Superplasticizer	Micro-silica	Marble powder
Concrete sample	500	190	900	500	100	24.7	100	100

The acoustic vibration load applies to initial setting time (IST) and final setting time (FST) of concrete, 1–4 and 5–10 h, respectively. In fact, concrete is fluid before IST and between IST and FST are in the transection time to hardening [21] (Fig. 1). Due to find effect of acoustic vibrations, six types of concrete have been analyzed:

1. Control sample (CS), without any acoustic vibrations load.
2. A-CS sample with acoustic vibrations load between 20–500 Hz during hydration (24 h).
3. B-CS sample with acoustic vibrations load between 500–1000 Hz during hydration (24 h).
4. C-CS sample with acoustic vibrations load between 1000–5000 Hz during hydration (24 h).
5. D-CS sample with acoustic vibrations load between 5000–10000 Hz during hydration (24 h).
6. E-CS sample with acoustic vibrations load between 10000–20000 Hz during hydration (24 h).

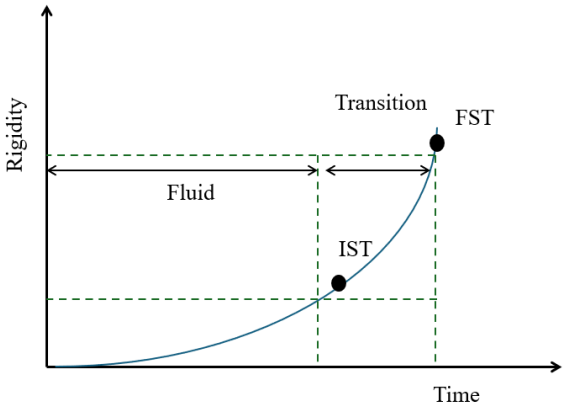

Fig. 1. IST and FST of concrete

The cement setting time is determined using a Vikat device by periodically dipping the needle into a cement paste of standard consistency: the IST is recorded when the needle does not reach the plate by 4 ± 1 mm, and the FST is when the needle is immersed in the paste by no more than 0.5 mm, while the time is counted from the moment of sealing cement with water.

In laboratory conditions, when studying the hydration of cement paste, the distance from the sound source to the center of the test sample is 30 cm when using built-in radiators fixed in a fixed sounding base. The angle of incidence of the sound wave is 45 ± 5° relative to the normal to the sample surface to simulate real-world exposure conditions. Omnidirectional (dodecahedral) loudspeakers are used that meet the requirements of ISO 140-3 and ISO 3382-2 to provide an isotropic sound field. The microphone axis is parallel to the sample plane (at a distance of less than 10 mm). The microphones comply with Classes 0 and 1 according to IEC 60651/IEC 60804. Calibration is performed using a Class 1 acoustic calibrator according to IEC 60942 with a reference level of 114 dB at 1000 Hz. Frequency range of measurements: 50–20 kHz using octave or third octave filters according to IEC 61260.

The samples were cured under normal temperature and humidity conditions for 28 days. Compressive strength testing was performed according to ASTM C109 standard and tensile strength testing was performed according to ASTM C496 standard [22,23]. Compressive strength was determined on cubes with an edge of 70 mm, and axial tensile strength was determined on cylinders with a diameter of 70 mm and a length of 280 mm.

Figure 2 shows the general design of the present study. According to Fig. 2, first the concrete was prepared, then the concrete was placed in the mold and then the acoustic vibration loading was applied. Therefore, to find the mechanical properties, the compressive and tensile strength were analyzed and because of the investigation of the microstructure, the SEM images were also analyzed.

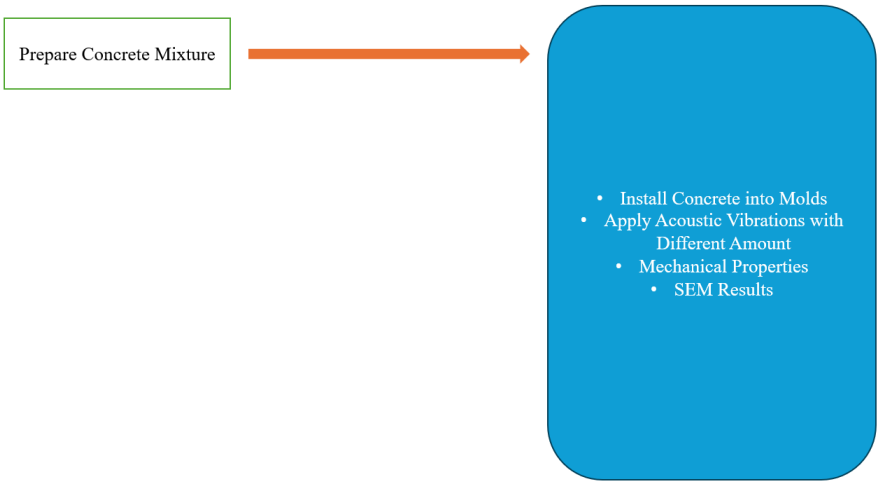

Fig. 2. Scheme of the current study

Figure 3 shows the schematic of the present study under the effect of applying acoustic vibration load to concrete. According to Fig. 3, the concrete is subjected to acoustic vibrations with two loudspeakers with constant sound intensity for all samples. The mechanism of acoustic vibration action on hydrating concrete is the transfer of sound field energy, where the sound intensity determines the density of acoustic energy that initiates cavitation and microcurrents, sound pressure creates cyclic stresses that accelerate the dissolution of clinker minerals and mass transfer, and the spatial distribution of the field ensures uniform activation of the structure, which together intensifies nucleation and growth of hydrate phases.

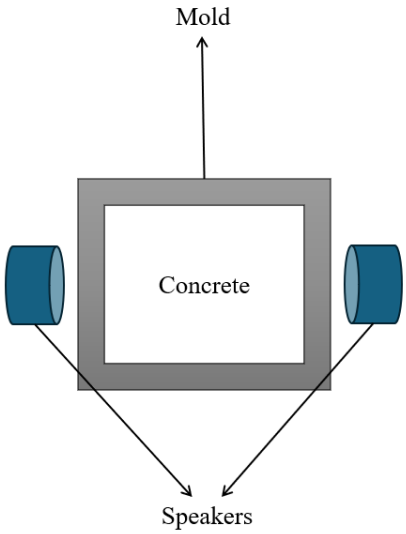

Fig. 3. Apply acoustic vibrations load

Results and Discussion

The compressive strength of concrete samples subjected to acoustic vibrations was investigated illustrated in Table 2 and Fig. 4. The results showed that the control sample (without any noise) had the highest compressive strength in all curing periods (7, 14 and 28 days). With increasing acoustic vibration frequency, the compressive strength of the samples decreased, so that the sample E (with the influence of frequency 10000 to 20000 Hz) showed the lowest resistance in the 28-day period (21.4 MPa). In contrast, sample C (frequency 1000 to 5000 Hz) showed a relative improvement in compressive strength compared to other samples subjected to vibration, which is probably due to the effect of microstructure optimization in this frequency range. These results indicate that high-frequency acoustic vibrations can have a negative effect on the hydration process and, consequently, the compressive strength of concrete.

Table 2. Compressive strength of each sample, MPa

Sample	7 days	14 days	28 days
Control	11.2	18.6	37.2
A	10.5	17.0	33.4
B	9.5	16.8	30.9
C	10.5	16.7	33.5
D	9.5	14.9	28.9
E	6.5	11.1	21.4

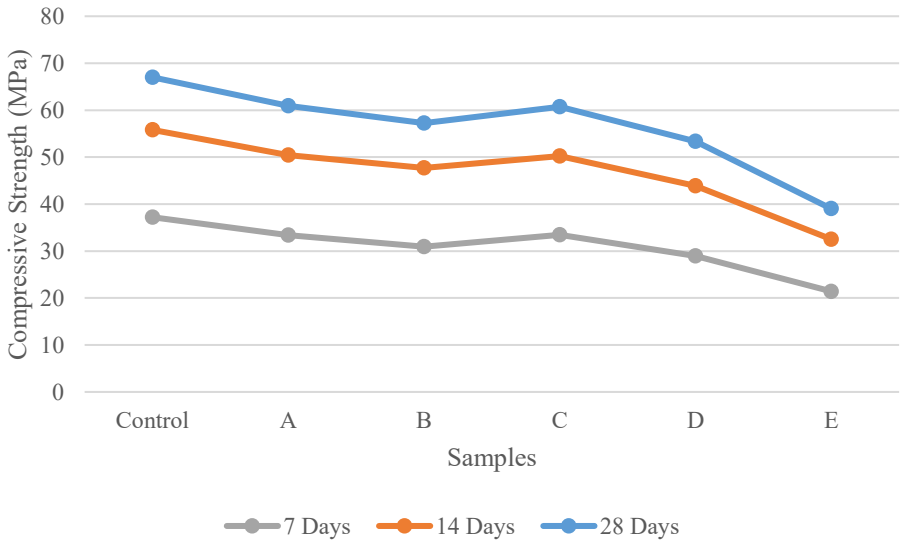

Fig. 4. Compressive strength of each sample

The compressive strength test results after 7, 14 and 28 days of curing for all samples are presented in Table 2 and Fig. 4. According to the results, the control sample achieved the highest compressive strength of 37.2 MPa at the age of 28 days. In addition, the Sample E (affected by frequency 10000 to 20000 Hz) with a strength of 21.42 MPa showed the lowest value among all samples at the age of 28 days. Notably, the relatively better performance of the Sample C (affected by frequency 1000 to 5000 Hz) with a strength of 33.47 MPa is superior to its counterparts (B, D and E) and even surpasses

the sample A (20–500 Hz). This indicates the existence of a "rational frequency range" in which acoustic vibrations may have a positive effect on the microstructure of concrete by improving particle distribution and cement paste compaction to some extent. However, in general, applying vibrations in all frequency ranges studied resulted in a decrease in compressive strength compared to the control sample.

The tensile strength results of the concrete samples subjected to various acoustic vibration frequencies during hydration are presented in Table 3 and Fig. 5. Similar to the trend observed in compressive strength, the control sample (without acoustic vibration) exhibited the highest tensile strength values at all curing ages (7, 14, and 28 days), reaching a maximum of 3.6 MPa at 28 days.

Table 3. Tensile strength of each sample, MPa

Sample	7 days	14 days	28 days
Control	1.95	2.6	3.6
A	1.9	2.5	3.5
B	1.8	2.4	3.3
C	1.9	2.3	3.5
D	1.8	2.2	3.2
E	1.5	1.9	2.8

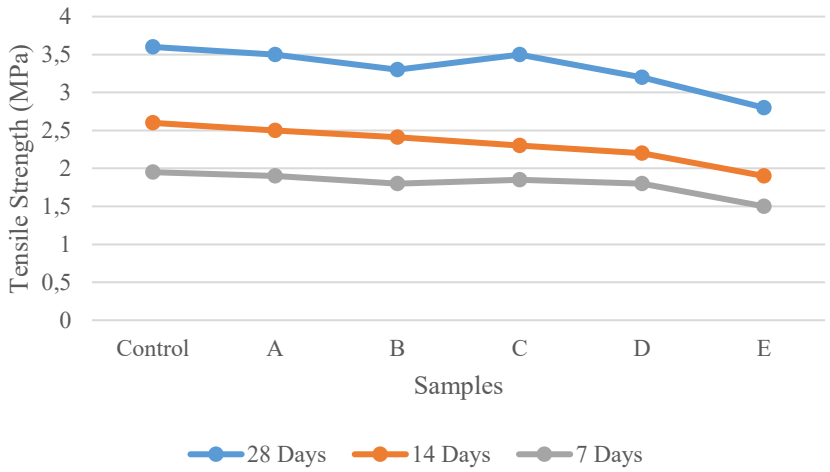

Fig. 5. Tensile strength of each sample

The application of acoustic vibrations led to a general reduction in tensile strength. The strongest decrease in tensile strength was observed in the sample E (10000–20000 Hz), where after 28 days only 2.8 MPa was observed, which is 22.2 % less than in the control sample. This is due to the fact that high-frequency vibrations strongly disrupt the internal microstructure and the connection between the cement mortar and aggregates, which ultimately impairs the ability of concrete to withstand tensile loads. Significantly, the sample A (20-500 Hz) and the sample C (1000–5000 Hz) showed a relatively small decrease in tensile strength after 28 days (3.5 MPa). For example, sample C showed better results than samples exposed to higher frequencies (samples B, D, and E). This further supports the hypothesis proposed in the compressive strength analysis regarding the potential existence of a "rational frequency range" where acoustic vibrations may cause less damage to the concrete's microstructure or even promote a more uniform distribution of

micro-cracks, thereby mitigating the loss in tensile capacity. However, it is crucial to emphasize that no frequency range improved the tensile strength beyond that of the control sample. The overall detrimental effect of acoustic vibrations on tensile strength aligns with the compressive strength findings, indicating that such external energy inputs during the critical hydration period generally compromise the mechanical integrity of concrete.

In this study, it was found that the use of acoustic vibrations during the initial period of hydration of the concrete mixture led to a decrease in mechanical characteristics compared with control samples, which is in full agreement with the data of independent studies [23]. The most pronounced decrease in compressive strength was recorded for the sample E after 28 days of hardening — by 42.4 %, which correlates with previously published results, where the reduction range was 30–50 % [24,25]. The absolute strength values were 21.42 MPa for the sample E versus 37.2 MPa for the control sample, which meets the requirements [26] for minimum values for structural concretes, but indicates a significant technological risk if the acoustic exposure parameters are incorrectly selected.

At the same time, there is a pronounced dependence of the effect on the processing mode: for the sample A, the decrease in strength was only 2.8 % [27], which indicates the presence of a "parameter window" within which acoustic activation can be applied without compromising the final properties of the material. This phenomenon requires detailed consideration from the perspective of the physico-chemical processes occurring in the cement system at the early stages of hydration.

The main mechanism of strength reduction is associated with the intensification of migration of cement particles and aggregates under the influence of an acoustic field. External vibrations contribute to redistribution of the solid phase and violation of the uniformity of the structure, increase in intergranular porosity by preventing dense packing of particles, decrease in adhesion between cement stone and aggregate due to the formation of microgazors at the interface of phases.

A critical aspect is the influence of acoustic vibrations on the formation of hydration products, in particular, the gel of calcium silicate hydrate (C-S-H). At maximum frequencies (> 10 kHz), it is observed: disorientation of crystalline nuclei and disruption of their spatial order, reducing the degree of polymerization of C-S-H gel, which reduces its binding capacity, slowing down the transition of metastable phases into thermodynamically stable modifications.

As noted in [28], these effects are most pronounced at resonant frequencies, when the amplitude of vibrations of cement paste particles reaches critical values that prevent the formation of a dense microstructure. This explains the nonlinear frequency–strength relationship and the need for precise selection of impact parameters for each concrete composition.

One of the most significant conclusions of the study is the confirmation of the hypothesis that reducing the duration of acoustic exposure from 24 h to intervals in the range of minutes can radically change the sign of the effect from destructive to modifying. Short-term fluctuations (from 30 sec to 5 min) contribute to: removal of trapped air without violating the integrity of the emerging structure, increase in effective particle size due to coagulation of colloidal fractions, to prevent the separation of the mixture due to the short duration of the pulse action, which is consistent with [29].

For concretes with ultra-high performance characteristics (UHPC), it has been found that the best results are achieved when exposed for a duration of 5–15 sec, which is consistent with [30]. In this mode, there is an increase in compressive strength by more than 10 % due to improved particle packing and reduced structural defects, improving the rheological properties of the mixture without the use of additional plasticizers, preservation of the uniformity of the composition due to the lack of time for the development of sedimentation processes. This result is of great practical importance: it allows the integration of acoustic activation into existing production lines without significantly increasing the molding cycle time. Table 4 illustrates the need for multiparametric optimization: changing one parameter (for example, frequency) without adjusting others (duration, intensity) can lead to opposite results.

Table 4. Comparative analysis of positive and negative effects

Impact parameter	Positive effect	Negative effect
Duration > 1 h	C-S-H crystallization disorder, porosity increase	-
Duration 5—15 s	-	Air removal, particle packing improvement
Frequency > 10 kHz	Crystal disorientation, reduced adhesion	Intensification of early hydration (with controlled amplitude)
Intensity > 0.1 MPa	Microcracking, stratification	Homogenization of the mixture, reduction of the water-cement ratio

Practical recommendations and technological implications:

1. A differentiated approach to the choice of mode, due to the fact that for conventional structural concretes it is advisable to avoid acoustic effects during the setting period (0–4 h), whereas for UHPC short-term treatment (5–15 sec) immediately after laying can be recommended as a standard operation.
2. Control of the frequency spectrum, due to the fact that the use of narrow-band radiators with the ability to fine-tune the frequency allows you to avoid resonant modes that destabilize the structure.
3. Integration with monitoring systems, which consists in the introduction of built-in acoustic sensors to control the speed of wave propagation and attenuation coefficient, which allows real-time assessment of the degree of structure formation and correction of impact parameters.
4. Economic efficiency due to the fact that despite the initial cost of acoustic activation equipment, reducing cement consumption by 10–15 % by increasing hydration efficiency and reducing structural defects ensures payback within 12–18 months during mass production, which is consistent with [31–33].

The present study has a number of limitations that must be taken into account when interpreting the results:

1. experiments were conducted on laboratory samples of standard sizes; a large-scale transition to structural elements requires additional validation;
2. the long-term effect of acoustic treatment on durability (frost resistance, corrosion resistance, creep) has not been studied;

3. there was no detailed analysis of the effect of the type of cement and chemical additives on the system's response to acoustic effects.

Promising areas for further research include:

1. development of adaptive acoustic activation systems with feedback based on ultrasound monitoring data,
2. study of the synergistic effect of a combination of acoustic vibrations with nanomodifiers and fiber reinforcement,
3. modeling of mass and energy transfer processes in an acoustic field to predict optimal processing modes.

The results obtained confirm the dual nature of the effect of acoustic vibrations on concrete during the hydration period: if the parameters (duration, frequency, intensity) are incorrectly selected, there is a significant decrease in mechanical properties, while optimized short-term modes can improve the structure and performance of the material. The key success factor is the transition from an empirical selection of modes to a scientifically based design of acoustic effects, taking into account the kinetics of hydration, rheology of the mixture and the target properties of the final product. The introduction of the developed approaches into the practice of mass production of concrete products will not only improve technical and economic indicators but also contribute to the development of resource-saving technologies in construction.

Conclusions

This study experimentally investigated the effects of applying acoustic vibration loads at different frequency ranges during the hydration period on the mechanical properties and microstructure of concrete. The following key conclusions can be drawn from the results:

1. The application of acoustic vibrations during hydration generally led to a reduction in both compressive and tensile strength of concrete compared to the control sample (without vibrations). The reduction in strength was more pronounced with increasing frequency. The sample E (10000–20000 Hz) exhibited the most significant decline, with compressive and tensile strength values at 28 days being 42.4 and 22.2 % lower than the control sample, respectively.
2. Despite the overall negative impact, the results indicated that the influence of acoustic vibrations is frequency dependent. The sample C (1000–5000 Hz) demonstrated “a relatively smaller reduction in both compressive and tensile strength compared to other vibrated samples. This suggests that there might be a specific frequency range within which the damaging effects on the concrete's internal structure are less severe, potentially due to a more uniform distribution of energy or a resonance effect with the hydrating particles.
3. The decline in mechanical performance, particularly at high frequencies, can be attributed to the disruption of the normal hydration process and the formation of a less dense microstructure. The vibrations likely interfere with the crystallization of hydration products (like C-S-H gel) and weaken the interfacial transition zone between the cement paste and aggregates, which is critical for achieving high mechanical strength.

4. Contrary to the initial hypothesis that certain vibrations might enhance compaction or homogeneity, none of the tested frequency ranges improved the mechanical properties beyond the performance of the control sample.

CRediT authorship contribution statement

Mohammad Hematibahar: writing – review & editing, writing – original draft; **Makhmud Kharun**: conceptualization, writing – original draft; **Roman S. Fediuk**: investigation, writing – original draft; **Nikolai I. Vatin**: conceptualization, writing – original draft; **Vitaliy N. Lymarev**: supervision, writing – original draft; **German R. Fediuk**: investigation, writing – original draft; **Leonid N. Alexeiko**: conceptualization, writing – original draft.

Conflict of interest

The authors declare that they have no conflict of interest.

References

1. Selyutina NS, Khairetdinova DD. Dynamic fracture of concretes with basalt and limestone aggregate at different temperatures. *Materials Physics and Mechanics.* 2025;53(5): 140–149.
2. Lam TQK, Sreekeshava KS, Kumar S, Bhargavi C, Skanda Kumar BN, Gayathri G, Suresh YR. Structural response of reinforced, steel fiber reinforced and prestressed geopolymer concrete beams subjected to transverse loading. *Materials Physics and Mechanics.* 2025;53(5): 150–163.
3. Fediuk R.S. Mechanical Activation of Construction Binder Materials by Various Mills. *IOP Conference Series: Materials Science and Engineering.* 2016;125(1): 012019.
4. Dvorkin L, Zhitkovsky V, Tracz T, Sitarz M, Mróz K. Mechanical–Chemical Activation of Cement-Ash Binders to Improve the Properties of Heat-Resistant Mortars. *Materials.* 2024;17: 5760.
5. Bawab, J, El-Dieb A, El-Hassan H, Khatib J. Activation of Cementless Binder Based on Volcanic ash and Calcium Carbide Residue. In: *9th International Conference on Civil, Structural and Transportation Engineering, ICCSTE 2024.* Avestia Publishing; 2024.
6. Dobrosmyslov SS, Shakirova VA, Nazirov R, Voronin A, Molokeev MS, Bezrukikh AI, Samoilo AS, Sharonova O. Influence of mechanical activation on the characteristics of glass concrete. *Construction Materials and Products.* 2025;8(4): 4.
7. Selvam P, Purushothaman R, Boomibalan S. Influence of ultrafine slag and sulfate activation on the strength, durability and microstructural performance of high-volume fly ash concrete containing recycled plastic waste aggregate. *Structural Concrete.* 2026;27(1): 891–912.
8. Shyshkina A. Optimization of Water Activation Technology for the Production of Fine-Grained Concrete. *Key Engineering Materials.* 2023;953: 63–68.
9. Ramakrishnan S, Kanagasuntharam S, Sanjayan J. In-line activation of cementitious materials for 3D concrete printing. *Cement and Concrete Composites.* 2022;131: 104598.
10. Korobko O, Vyrovoy V, Grynyova II, Vegera P. Comprehensive material activation of concrete structures. *Budownictwo i Architektura.* 2025;24(2): 57–73.
11. Hasanin T, Alsahli S, Altaleb H, Alshammari B, Tantawy M. Hydration characteristics of cement blended with thermally reactivated recycled concrete demolition waste. *Scientific Reports.* 2026;16: 1499.
12. Vatin N, Hematibahar M, Gebre TH. Chopped and Minibars Reinforced High-Performance Concrete: Machine Learning Prediction of Mechanical Properties. *Frontiers Built Environment.* 2025;11: 1558394.
13. Gorlenko NP, Sarkisov YS, Syryamkin VI, Naumova LB, Pavlova AN, Laptev BI. Wave Mechanism of Structure Formation in Cement Compositions. *IOP Conf. Ser.: Mater. Sci. Eng.* 2019;597: 012030.
14. Jayathiakage RI, Gunasekara C, Law D, Setunge S. Calcination and Mechanical Activation of Waste Clays for Low-Carbon Concrete. In: Dissanayake R, Mendis P, De Silva S, Fernando S, Attanayake U, Gajanayake P.

(Eds.) *Proceedings of the 15th International Conference on Sustainable Built Environment. ICSBE 2024 2024. Lecture Notes in Civil Engineering, vol 652.* Singapore; Springer: 2025. p.451–466.
15. Basler F, Mähner D, Fischer O, Hilbig H. Influence of Early-Age Vibration on Concrete Strength. *Structural Concrete.* 2023;24(5): 6505–6519.
16. Liu J, An M, Huang L, Wang L, Han S. Influence of Vibrating Compaction Time on the Strength and Microstructure of Ultra-High Performance Concrete. *Construction and Building Materials.* 2023;409: 133584.
17. Shin TY, Kim JH. Flow Simulation of Fresh Concrete Accounting for Vibrating Compaction. *Cement and Concrete Research.* 2023;173: 107300.
18. Chai M, Hu C, Cheng M. Study on the Effect of Vibrating Process on the Compactness of Slipform Concrete. *Appl. Sci.* 2023;13(14): 8421.
19. Banfill PF, Teixeira MAOM, Craik RJM. Rheology and Vibration of Fresh Concrete: Predicting the Radius of Action of Poker Vibrators from Wave Propagation. *Cement and Concrete Research.* 2011;41: 932–941.
20. Roobankumar R, Senthil Pandian M. Investigating the Correlation between Ultrasonic Pulse Velocity and Compressive Strength in Polyurethane Foam Concrete. *Scientific Reports.* 2025;15: 23995.
21. Lee T, Lee J. Setting Time and Compressive Strength Prediction Model of Concrete by Nondestructive Ultrasonic Pulse Velocity Testing at Early Age. *Construction and Building Materials.* 2020;252: 119027.
22. American Society for Testing and Materials. ASTM C109/C109M-05. *Standard Test Method for Compressive Strength of Hydraulic Cement Mortars.* ASTM International; 2005.
23. American Society for Testing and Materials. ASTM C496/C496M-17. *Standard Test Method for Splitting Tensile Strength of Cylindrical Concrete Specimens.* West Conshohocken; ASTM International; 2017.
24. Ingle VV, Prem PR. Acoustic emission examination of 3D printed ultra-high performance concrete with and without coarse aggregate under fresh and hardened states, *Journal of Building Engineering.* 2025;111: 113491.
25. Wang Z, Gu Q, Zhong P, Zhang W, Zhang Z, Yang J. Leveraging Weighted peak frequency (WPF)-based acoustic emission to decipher flexural behavior and hybrid effect in ultra-high-performance hybrid fiber-reinforced concrete with aligned steel fiber. *Construction and Building Materials.* 2026;514: 145532.
26. Gao S, Tian M. Flexural damage characterization of lightweight ultra-high performance concrete by recycled powder revealed based on acoustic emission technology. *Journal of Building Engineering.* 2025;114: 114260.
27. Chen L, Chen X, Xiong Z, Lu K, Liu Z. Damage evolution analysis of macro-synthetic fiber reinforced rubber concrete under uniaxial compression using acoustic emission technique. *Journal of Building Engineering.* 2026;118: 114968.
28. Zhang W, Gao D, Guo Y. Flexural failure behavior of ultra-high performance concrete with steel ball aggregates via acoustic emission characterization. *Construction and Building Materials.* 2026;506: 144868.
29. Zhao X, Wang S, Li S, Xu C. Study on size effects and failure precursor characteristics of concrete crack propagation behavior based on digital image correlation and acoustic emission technology. *Structures.* 2026;86: 111357.
30. Korda E, Cousture A, Tsangouri E, Snoeck D, De Schutter G, Aggelis DG. Active SAP desorption control in concrete through acoustic emission for optimized curing. *Cement and Concrete Composites.* 2025;160: 106067.
31. Du S, Liang B, Zhang Y, Lei C, Wang C, Jin Z, Li B, Li X, Liu Y. Mechanical properties and damage characteristics analysis on recycled aggregate concrete with glazed hollow beads after high temperatures by acoustic emission method. *Journal of Building Engineering.* 2024;90: 109429.
32. Chen H, Xu Y. Fracture properties and acoustic emission characteristics of manufactured sand recycled fine aggregate concrete. *Theoretical and Applied Fracture Mechanics.* 2024;133: 104633.
33. Vorozhbit OY, Levkina YV. Improving scoring system of performance indicators of industrial systems at the meso-level. *European Research Studies Journal.* 2017;20(4): 596–603.

Submitted: December 4, 2025 **Revised: February 16, 2026** **Accepted: March 18, 2026**

Topological data analysis and graph signal processing: quantitative defect assessment and localization of structural inhomogeneities in composites from nondestructive testing data

A.I. Borovkov [1] ✉, Kh.M. Vafaeva [1] ✉, N.I. Vatin [1], Zh.S. Nuguzhinov [2]

[1] Peter the Great St. Petersburg Polytechnic University, St. Petersburg, Russia

[2] Kazakhstan Multidisciplinary Institute of Reconstruction and Development Republican State Enterprise on the Right of Economic Use, Karaganda, Republic of Kazakhstan

✉ vafaeva.khm@gmail.com

ABSTRACT

The aim of the study is to develop and perform a preliminary evaluation of a method for diagnosing and locating internal defects in multilayer polymer composite materials using non-destructive testing data. A method combining topological data analysis and graph-signal processing is proposed. To demonstrate the potential feasibility of this method, an analysis of synthetic ultrasonic signals was conducted. A set of 81 ultrasonic signals, representing various locations of internal defects in the composite material, was used. Topological data analysis enabled the identification of informative topological features and distinguished defective from defect-free cases with a silhouette score of 0.471. The results show the potential of using topological data analysis to automate the structural monitoring of internal defects in multilayer polymer composite materials.

KEYWORDS

topological data analysis • graph signal processing • nondestructive testing • composite materials structural inhomogeneities • defect localization • signal interpretation • structural health monitoring

Funding. *This work has been supported by the grant of the Russian Science Foundation (grant No. 24-19-00691).*

Citation: Borovkov AI, Vafaeva KhM, Vatin NI, Nuguzhinov ZhS. Topological data analysis and graph signal processing: quantitative defect assessment and localization of structural inhomogeneities in composites from nondestructive testing data. *Materials Physics and Mechanics.* 2026;54(2): 140–166. http://dx.doi.org/10.18149/MPM.5422026_11

Introduction

Multilayer polymer composite materials and products made from them are used in the aerospace industry, energy sector, civil construction, and other fields [1–3]. The wide use of multilayer polymer composite materials is because of their unique mechanical properties. The manufacturing processes for these materials and products can create hidden defects and structural inconsistencies, which need to be monitored during operation [4,5]. Quantitative evaluation of hidden defects in multilayer polymer composite materials and their spatial distribution remains important, especially for enhancing the reliability of engineering structures [6,7].

To identify hidden structural defects in multilayer polymer composite materials, non-destructive testing methods – including ultrasonic, acoustic emission, thermographic, and radiographic techniques – are used, enabling the collection of large data volumes [8–10]. The listed methods indicate the presence of defects, but traditional analysis of

measurement results often relies on simplified physical models of wave or heat propagation in the material, empirical correlations between signal features and defect types, and the operator's subjective interpretation of the data obtained. Consequently, the accuracy of quantitative assessment of defect parameters (such as size, shape, and morphology) and their spatial location can be significantly diminished, especially when dealing with complex defects or environments with high noise levels [11–13].

Recent advances in the micromechanics of heterogeneous crystalline nanostructures have highlighted the role of misfit-stress relaxation via misfit dislocation formation, providing critical insights into defect generation in composite-like systems, including spherical and cylindrical nanostructures with core-shell or Janus configurations [14]. Complementing this theoretical framework, experimental and numerical investigations of the mechanical properties of porous thermoplastics, including polyacrylonitrile-co-butadiene-co-styrene, polycarbonate, and polyetherimide produced via 3D printing, have revealed a gradual accumulation of plastic strain under cyclic loading. Finite element modeling has validated multilinear isotropic hardening laws that account for porosity-induced variations in stress-strain behavior [15]. These findings collectively underscore the need for integrated analytical approaches, such as topological data analysis combined with graph signal processing, to quantitatively assess and localize structural inhomogeneities in advanced composites materials.

Topological data analysis

Advancements in topological data analysis (TDA) provide mathematical principles for extracting shape and connectivity information that is invariant to continuous deformations and resilient to noise [16,17]. The use of TDA extends beyond mechanical properties. TDA has also been effectively applied to solve heat transfer problems. This method improved temperature uniformity, reducing its variation by 57 %, and successfully eliminated local overheating without increasing energy costs for coolant pumping [18].

In [19], a multi-scale topology optimization method was developed to reduce the vibration response of cellular composites within a specific frequency range. To lower computational costs at the microlevel, Kriging metamodels were employed, enabling quick prediction of the properties of various cell types. At the macro level, the SOMMG method was used to accelerate the calculation of the entire structure's dynamic response. The results facilitate the design of complex 2D and 3D composites with improved dynamic properties and lower vibration levels compared to traditional solutions [19].

An existing topology optimization method was successfully extended and adapted to handle complex multilayer and multicomponent structures in [20]. The results of the study confirmed that the TDA method can be used to create a rigid structure or design uniformly stressed parts [20].

Graph signal processing

Graph signal processing (GSP) continues to evolve. GSP tools facilitate the use of relational information and are effective for describing both local and global dependencies within the structure of materials. In [21], a comprehensive review is presented on how graph signal processing methods are used to analyze geometric data, such as 3D point clouds,

demonstrating that GSP is a useful tool for dealing with irregularly structured data.

Building on the same principles of GSP, in [22], it was presented the "Grid-GSP" framework for data analysis in electrical grids, where the authors model the power system as a graph and show that voltage data behaves as a low-frequency signal on the graph. GSP has been successfully applied to practical problems, such as anomaly detection, data compression, and missing measurement recovery, as demonstrated using real-world power system models [22]. In [23], GSP is applied to develop a computationally efficient structural health monitoring (SHM) algorithm, where data from acceleration sensors are treated as signals on a graph, and damage in the bridge structure causes changes in the smoothness of these signals.

Problem definition

Although TDA and GSP have individually shown potential for solving various scientific and engineering problems [23–25], their combined use for the quantitative analysis and high-precision localization of defects in composite materials based on non-destructive testing data remains an underexplored area. This study aims to develop and preliminarily validate a method that combines topological data analysis and graph signal processing for the quantitative assessment and localization of internal defects in multilayer polymer composite materials using non-destructive testing data.

This goal is achieved by tackling the following tasks, which are designed based on the identified research gap:

1. To analyze the principles of data collection and processing used in non-destructive testing procedures for multilayer polymer composite materials and to identify characteristic defect signatures using synthetic ultrasonic signals as an example.
2. To provide a detailed explanation of the theoretical foundations of topological data analysis and graph-signal processing, including the development of graph models for diagnosing multilayer polymer composite materials.
3. Develop a framework that combines topological data analysis with signal-graph processing to extract meaningful topological features of defects and interpret them within the context of structural monitoring.
4. Demonstrate the capabilities of the proposed method using synthetic ultrasound data modeling different delamination positions, followed by an evaluation of how effectively topological features can be extracted and clustered.
5. Identify areas for further research, such as expanding analysis methods to other defect types and different non-destructive testing data formats.

Materials and Methods

The general flow chart of the methods used in this study is shown in Fig. 1. The third phase (Conceptual Stage, Steps 6–8) represents the planned integration of graph signal processing and nonlinear post-processing; these steps have not been implemented in the present study and are explicitly labelled "future work" in Fig. 1. The research methods are divided into six steps, organized into three main phases. A detailed description of these phases is provided below.

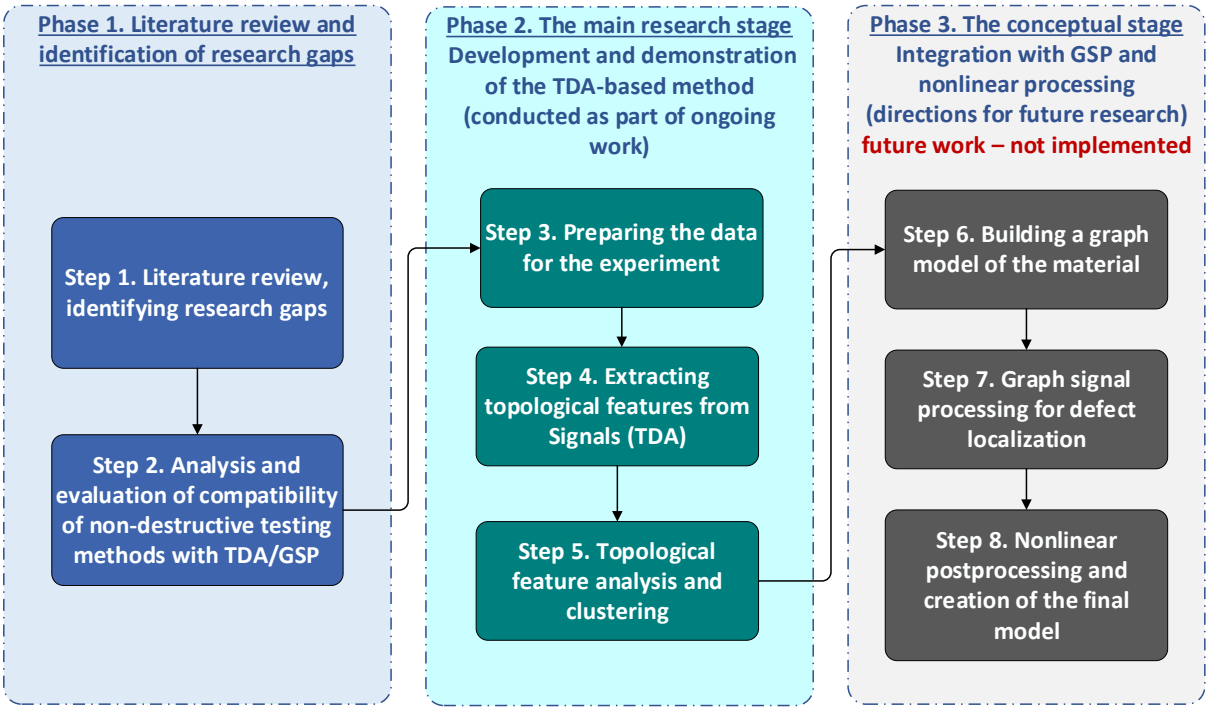

Fig. 1. Research methods flowchart

Preparatory and analytical phase

The preparatory and analytical stage was dedicated to a thorough analysis of the research gap and a justification for the need to develop a new method based on an examination of existing materials publications.

Step 1: Publication analysis and identification of research gaps. This step involved analyzing publications and identifying gaps in prior research. A systematic search and review of scientific literature in the Scopus database was conducted from 2020 to July 2025. Search queries related to topological data analysis (TDA), graph-signal processing (GSP), and non-destructive testing of composites were used. Analyzing 4 072 publications revealed that the combined use of TDA and GSP for the quantitative assessment and localization of defects in composites is an area that is not well understood, confirming the relevance and scientific novelty of the study.

Step 2: Analysis and compatibility evaluation of non-destructive testing methods with TDA/GSP. A comparative analysis of the main non-destructive testing methods (ultrasonic, eddy current, acoustic emission, etc.) was performed. Their operating principles, data formats, and suitability for integration with TDA and GSP were evaluated. It was found that ultrasonic testing (UT), acoustic emission, and infrared thermography are the most promising for integration with TDA/GSP because of their data formats (time series, C-scans, thermal images). These findings are detailed in the following sections.

Main research phase

The primary objective of the main research phase was to demonstrate the functionality of the key component of the proposed method (TDA) by using an example of classifying

defective and non-defective signals.

Step 3: Data preparation for the numerical experiment. Synthetic ultrasound data from the KU Leuven RDR dataset [26,27] were used to demonstrate the method. The dataset includes 81 ultrasound signals that simulate various delamination locations within a composite material.

Step 4. Topological feature extraction from signals (TDA). Each one-dimensional time series was analyzed using TDA with a custom Python script. A detailed description of the topological feature extraction procedure is provided in the "Feature extraction with topological data analysis" section. The process involved the following substeps: the signals were converted into multidimensional point clouds using the Takens method; vietoris-rips complexes were built from the point clouds; stability diagrams showing the "lifetime" of topological features (connected components H0 and cycles H1) were calculated; quantitative topological descriptors (number of points, entropy, and overall stability) were extracted from the diagrams.

Step 5. Analysis and clustering of topological features. The topological feature vectors obtained from all 81 signals were analyzed using the K-means clustering algorithm. The optimal number of clusters was determined through silhouette analysis, achieving a maximum value of 0.471 at $K = 2$. The clustering results were visualized in the principal component analysis (PCA) space.

The successful separation of the signals into two distinct clusters with a silhouette score of 0.471 demonstrates that TDA can extract meaningful topological features suitable for automatic classification of different material states.

Conceptual stage. Future research directions

The goal of this stage is to describe how the developed TDA module will be integrated into a broader system for precise spatial localization of defects. These steps have not been implemented but serve as a plan for future work.

Step 6. Construction of a graph model of the material. Representation of the composite material structure as a graph G=(V,E,W), where vertices are measurement points and edges represent the spatial proximity and/or similarity of signals.

Step 7. Graph-signal processing for defect localization. The topological features obtained in Step 4 will be treated as signals at the graph vertices. Next, GSP tools are used to filter and accurately locate anomaly vertices that correspond to defects.

Step 8. Nonlinear postprocessing and creation of the final model. To enhance accuracy, it is suggested to implement nonlinear processing methods such as wavelets and autoencoders. All features – including topological, graph, and nonlinear – will be combined into a single vector for the final classification and localization of defects.

Results and Discussion

Limitations in quantitative assessment of defects and localization of structural heterogeneities

To identify current limitations in the quantitative assessment of defects and the localization of structural inhomogeneities in composite materials based on non-destructive testing

data, a comprehensive review of existing publications was conducted. The potential application of topological data analysis and graph signal processing for diagnostics and structural integrity monitoring of composite products was also examined analyzed.

A publication search was conducted using the international scientific and analytical database Scopus for the period from 2020 to July 2025. The initial selection of publications was based on the criteria presented in Table 1.

Table 1. Criteria for Selecting Scientific Publications

Selection criteria description	Selection criteria value
Time range	Published between 2020 and 2025 (inclusive)
Publication language	Unrestricted
Source type	Peer-reviewed articles, conference proceedings, reviews
Metadata	Export to RIS format

Using logical operators, search queries were created and applied to the TITLE-ABS-KEY fields. The main search queries and the corresponding number of relevant publications are shown in Table 2. The downloaded data were subsequently combined and analyzed with VOSviewer software.

Table 2. Search results

No.	Search query	Number of documents found
1	Topological data analysis composite	69
2	Graph signal processing composite	30
3	Nondestructive testing composite	1 913
4	Defect localization composite	263
5	Quantitative assessment composite	1 639
6	Structural inhomogeneities composite	158
Total:		**4 072**

Existing non-destructive testing methods

This section offers a brief analysis of the most common non-destructive testing methods for composite materials, including their operating principles, types of detectable defects, data formats, limitations, and an evaluation of their compatibility with topological data analysis and signal-graph processing.

Ultrasonic testing relies on the reflection and scattering of ultrasonic waves as they pass through a material. It allows the detection of internal flaws, such as delaminations, voids, and cracks, by examining variations in the amplitude and timing of reflected signals [28,29]. The data formats for ultrasonic testing results are time series and two-dimensional C-scans. Penetration depth can reach 1 m under ideal conditions (low-attenuating materials), but in composites, it usually does not exceed 50–200 mm.

Eddy current testing employs induced electromagnetic currents to identify surface and subsurface flaws in electrically conductive materials [30–32]. Effective for detecting cracks, corrosion, and other defects at depths of up to 1–10 mm. Eddy current testing data is shown as frequency and amplitude complexes. The method is limited to electrically conductive materials and needs signal transformation to integrate with TDA/GSP.

Acoustic emission (AE) records elastic waves produced during the initiation and

growth of defects under load. It allows for the detection of active cracks, microdefects, and delamination processes throughout the entire thickness of a component; however, precise localization requires a sensor array and triangulation [33–35]. The AE data format consists of a time series of events.

Infrared thermography is a non-destructive testing technique that analyzes the distribution of thermal radiation emitted from a material's surface during localized or uniform heating [36,37]. The technology enables the detection of hidden defects that impact thermal conductivity, such as delamination, pores, voids, and areas of loose contact at depths of 10–20 mm. The data collected is interpreted as two-dimensional or three-dimensional thermograms. The effectiveness of the method depends on external factors like ambient temperature, air flow, and the thermophysical properties of the tested material, especially its thermal characteristics inertia.

Table 3. Brief overview of non-destructive testing methods

NDT method	Operating principle	Defect types	Penetration depth	Data format	Main limitations	TDA/GSP compatibility
Ultrasonic inspection (UT)	Reflection/ scattering of ultrasonic waves	Delamina tions, cracks, voids	Medium to high (up to 1 m, material dependent)	Time series, C-scans	Dependent on input angle, difficulties with curved surfaces	High, as signals lend themselves well to topological and graph analysis
Eddy current Inspection (ET)	Changes in induced current in conduc tors	Surface and subsurface cracks, corrosion	Low (1–10 mm, in conductors)	Frequency/ amplitude complexes	Limited to electrically conductive materials	Limited and requires signal transforma tion into a suitable format
Acoustic emission (AE)	Recording of acoustic waves at defect initiation	Active cracks, delamination growth, microdefects	High (full thickness, but without location without triangulation)	Time series (events)	Difficulty with localization without a sensor array	Spatio-temporal signals are applicable in a graph model
Infrared thermography (IRT)	Thermal response to external excitation	Delamina tions, voids, leaks	Low and medium (10-20 mm)	2D/3D thermal images	Dependent on thermal inertia, noise	Can be analyzed as images through cubic complexes
X-ray/CT	X-ray absorption and trans mission	Internal inclusions, pores, cracks	Very high (up to 100 mm+)	2D/3D voxel images	Expensive, slow, radiation hazardous	Possible through voxel processing and grid graphing

X-ray and computed tomography produce detailed images of a material's internal structure by analyzing how X-rays transmit and are absorbed. They can identify internal inclusions, pores, and cracks at depths of up to 100 mm or more, depending on the material's density and source power [38–40]. The data is in 2D/3D voxel format, which requires significant computing resources and compliance with radiation safety measures.

Despite their widespread use, existing non-destructive testing methods have several significant limitations. They often depend on subjective operator interpretation, struggle to detect small or complex defects, require expensive equipment and highly skilled personnel, and are not always universally suitable for different types of composite materials. To address these issues, a method combining topological data analysis and graph-signal processing is proposed, offering more accurate and objective defect detection.

To evaluate the suitability of existing non-destructive testing methods for TDA/GSP applications, a comparative review was compiled and shown in Table 3. It highlights the key parameters of each method, including defect types detected, penetration depth, data format, limitations, and the capability to integrate with TDA and GSP. Concerning Table 3, it is important to note that the maximum penetration depth is reported under optimal conditions and may vary depending on composite properties such as thickness, density, filler, and binder type).

Table 3 shows that ultrasonic testing, acoustic emission, and infrared thermography are most suitable for integration with TDA and GSP methods because these techniques produce data with the required spatiotemporal features, a regular grid layout, or a continuous intensity scale. This allows for both topological filtering and spectral decomposition on graphs. Meanwhile, radiography and eddy current testing need extra processing steps, like signal transformation, voxel data segmentation, or connected component construction, which make their direct inclusion in a graph model of the material more complicated. However, with proper transformations and graph construction algorithms on a voxel grid, they can also be adapted for the TDA-GSP method.

Collection of non-destructive testing data

Data types and formats. This section provides an analysis of various types of non-destructive testing data that reflect both the temporal and spatial structures of the measured processes, which could be applied with further development of the proposed method. The data types and formats are summarized in Table 4, including the respective measurement types, data presentation, and brief explanations.

Table 4. Data types and formats

Data type	Data format	Description
Ultrasound (UT)	Time series, 2D C-scans	1D: signal amplitude over time (A-scan); 2D: amplitude map over the surface (C-scan)
Eddy current (ET)	Time series, frequency spectra	Induced current signals over time and/or spectral domain
Acoustic emission (AE)	Time series of events	Bursts of pulses (time, amplitude, coordinates); event-based format with detection threshold
Infrared thermography (IRT)	2D/3D thermal images	Spatial temperature distribution on a surface or in a volume
X-ray/CT	2D/3D voxel images	2D X-ray or 3D tomography voxel data

To ensure compatibility with graph-topology processing, time series should be in .csv, .tdms, or .mat formats and contain numerical tables with time and amplitude data. Raster images should be in .png, .tif, or .dcm formats and include two-dimensional and three-dimensional visual data suitable for analysis with cubic complexes. Hybrid datasets can include time signals synchronized with the spatial coordinates of sensors. The use of these formats will provide flexibility, allowing TDA and GSP to be applied to a wide range of signals and images typical for structural applications diagnostics.

Feature extraction with topological data analysis. Topological data analysis offers a formal way to extract invariant structural features that represent the geometry and shape of data across various scales. The main tool of TDA is persistent homology, which provides a quantitative way to describe how topological objects appear and disappear as the filtering scale varies. It examines features that are resilient to noise and allows for comparing complex structures based on their overall topology (Table 5).

Table 5. Topological features

Topological feature	Brief description
0D – dimension 0 (β_0)	Individual clusters or regions that may correspond to local defects, such as pores or inclusions. In the context of Takens embedding of a 1D time series, β_0 reflects the density and fragmentation of points in the reconstructed phase space. High NumPoints_H0 and Entropy_H0 indicate noise-induced fragmentation or amplitude anomalies caused by defects.
1D – dimension 1 (β_1)	Closed contours or loops reflecting structures such as cracks or delamination boundaries.
2D – dimension 2 (β_2)	Spatial voids or inclusions characteristic of large defects in composites.

Applying H0 to Takens-embedded time series allows for a direct assessment of point cloud density and connectivity. As the filtration radius ϵ expands, H0 tracks the transition from isolated points to clusters, effectively capturing noise-induced fragmentation. While a point cloud of length L starts with NumPoints_H0 near L, it is the Entropy_H0 that reveals the underlying uniformity of the distribution. Although H1 remains the primary tool for detecting delamination via wave interference, H0 provides critical context regarding density anomalies. Combining both descriptors ensures the feature vector is robust enough for reliable clustering. The way of extracting topological features depends on the data source (time series or image).

Time series processing. For one-dimensional signals such as ultrasound, eddy currents, and acoustic emission, the following steps are used:

1. Embedding into phase space. The Takens embedding method is used, in which the signal $x(t)$ is transformed into a point cloud: $X_t = [x(t), x(t+t), x(t+2\cdot t), \ldots, x(t+(d-1)t)]$, where $x(t)$ is the original time signal, τ is the time delay, d is the embedding dimension, X_t is the vector in phase space corresponding to time t.

2. After transforming the time signal into phase space (using Takens' method), we obtain a set of points X_t in a dimensional space d. Next, a Vietoris-Rips complex is constructed, which reflects the topological structure of these points to understand which points are connected and how they form geometric structures (line segments, triangles, etc.). For each pair of points X_t and X_j in phase space, the Euclidean distance is calculated:

$d(X_i, X_j) = \sqrt{\sum_{k=1}^{d}(X_i^{(k)} - X_j^{(k)})^2}$, where d is the dimension of the phase space, $X_i^{(k)}$ is k-th coordinate of the point X_i . Two points X_i and X_j are connected by an edge if the distance between them does not exceed the radius ε: $d(X_i, X_j) \leq \varepsilon$.

A set of $k+1$ points forms a k-simplex if all pairs between them are pairwise connected, that is, the distance between each pair does not exceed ε: $d(X_i, X_j) \leq \varepsilon \quad for\ all \quad i < j \quad from \ \{0,1,\ldots,k\}$. The entire complex at a fixed level ε can be denoted as: $VR(X, \varepsilon)$, where X is a set of points, ε is the filtration radius (threshold distance).

Although H1 (cyclicity) is the primary indicator of defects (stable loops appear due to wave interference at delamination), H0 is not redundant. In the Takens-embedded point cloud H0 quantifies sample density: defects change the local amplitude distribution, increasing fragmentation (higher NumPoints_H0) or altering uniformity (Entropy_H0). Thus, the full feature vector {NumPoints_H0, Entropy_H0, NumPoints_H1, Entropy_H1, Amplitude_H0, Amplitude_H1} provides complementary information and improves clustering robustness.

3. Calculating persistence diagrams is a graph that displays all topological objects (components, cycles, etc.) with their birth and death times (depending on ε). Each object corresponds to a point (b, d), where b is the value of ε, at which the object appeared, and d is the value of ε, at which it disappeared. If $d - b$ is large, then the object is considered significant, and if $d \approx b$, then it is most likely noise. That is, the further the point is from the diagonal $b = d$, the more significant the topological structure.

4. After constructing the persistence diagram, a quantitative assessment of the topological features is performed. These numerical characteristics are called topological descriptors and serve as features for analysis or machine learning (Table 6).

Table 6. Topological descriptors

No.	Descriptor	Designation	Description
1	Number of components	β_0	Number of distinct regions in the data
2	Number of cycles	β_1	Number of cycles (loops)
3	Object stability	$Persistence_i = d_i - b_i$	"Lifetime" of a topological object
4	Average stability	$Persistence_{avg} = \frac{1}{N}\sum_{i=1}^{N}(d_i - b_i)$	Average importance of all objects
5	Diagram entropy	$H = -\sum_{i=1}^{N}(p_i \cdot log(p_i))$	Complexity/diversity of topological structures
6	Object share	$p_i = \frac{d_i - b_i}{\sum_{j=1}^{N}(d_j - b_j)}$	Used in entropy calculations
7	Maximum stability	$Persistence_{max} = max_i(d_i - b_i)$	The longest-lived object
8	Total stability	$Persistence_{total} = \sum_{i=1}^{N}(d_i - b_i)$	The sum of all lifetimes

Image processing with TDA. For 2D and 3D images (e.g., ultrasound C-scans, thermography heat maps, CT tomographic data), topological feature extraction is carried out by constructing cubic complexes.

1. Image preparation (binarization). Before constructing topological objects, the image is converted into a binary mask, where each pixel (or voxel) takes the value 1 (object) or 0 (background): $I(x,y) = \begin{cases} 1, & \text{if } f(x,y) \geq T \\ 0, & \text{if } f(x,y) < T \end{cases}$, where $f(x,y)$ is the intensity at an image point, T is the selected threshold, $I(x,y)$ is the binarized image.

2. Construct a cubic complex. Each pixel (in 2D) or voxel (in 3D) with a unit value corresponds to a vertex (0-simplex). Vertices are connected by edges (1-simplexes) if they are adjacent on the grid (e.g., 4-neighborhood or 8-neighborhood in 2D): $K = CubicalComplex(I)$, where K is the set of all simplexes constructed from a binary image I.

3. Filtering by intensity level. To analyze inhomogeneities, filtering is used, i.e., successively lowering the T threshold, which binarizes the image, creating a hierarchy of nested complexes: $K_1 \subseteq K_2 \subseteq \cdots \subseteq K_n$, where K_i is the cubic complex obtained by binarization with the T_i threshold. Each subsequent T_{i+1} level is lower than the previous one: $T_1 > T_2 > \ldots > T_n$.

4. Calculating stability diagrams. For each filtering level, the creation and disappearance of topological objects (clusters, holes, cavities) is tracked. The resulting stability diagram records: β_0 is the number of connected components; β_1 is the number of closed contours (loops); β_3 is the number of voids (for 3D).

5. Similar to time series (Table 6), descriptors are extracted from the image stability diagrams. Image processing using TDA enables the quantitative evaluation of the shape, connectivity, and heterogeneity of the structure, which is especially important for analyzing microporosity, delamination, and cracks observed in thermal images or tomograms.

Construction of a graph model of the material. The construction of the graph model and GSP are described as conceptual steps for analyzing spatial dependencies. Nonlinear processing involves using wavelets and autoencoders but is not implemented in the current study. These steps will be tested in future work (the Conclusion section).

The graph model enables formalizing the structure of a material or system as a mathematical graph that considers spatial and/or functional relationships between measured points, microstructure grains, sensors, or pixels clusters.

1. Each graph vertex corresponds to a specific spatial element: a sensor coordinate, a grain or phase center, an image pixel cluster, or a measurement point (e.g., in ultrasound or CT). The set of vertices is denoted as $V = \{v_1, v_2, \ldots, v_N\}$, where N is the total number of points used to construct the graph.

2. Definition of graph edges. Edges are established between vertices based on spatial proximity (e.g., connecting nearest neighbors) and signal similarity (e.g., correlating signals from different sensors). Distance-based connection condition: $e_{ij} \in E, \quad if\ d(v_i, v_j) \leq \varepsilon$, where e_{ij} is the edge between vertices $v_i$and v_j, $d(v_i, v_j)$ is the Euclidean distance between vertices, ε is the distance threshold.

3. Defining edge weights. An edge weight is a number reflecting the degree of "connection" between two vertices. It can be determined in different ways:

(a) by distance (exponential decay): $w_{ij} = exp\left(-\frac{d(v_i,v_j)^2}{\sigma^2}\right)$, where σ is the scaling parameter (the width of the Gaussian);

(b) by correlation between signals: $w_{ij} = corr(s_i, s_j)$, where s_i, s_j are the signals measured at the vertices i, j;

(c) by topological similarity: $w_{ij} = exp\left(-\frac{||T_i - T_j||^2}{\gamma^2}\right)$, where T_i, T_j are the vectors of topological descriptors (e.g., β_0, β_1, entropy) and γ is the scaling parameter.

4. A weighted undirected graph $G = (V, E, W)$ is formed, where V is the set of vertices, E is the set of edges, and W is the edge weight matrix.

Graph-signal processing. The GSP method enables analysis of data not on a regular grid, like in traditional signal processing, but on graph vertices. In non-destructive testing, this could include signal amplitudes from sensors, topological descriptors, or energy parameters derived from images or signals over time series. A graph signal is a function defined on the vertices of a graph $f = [f(v_1), f(v_2), \dots, f(v_N)]^T$, where $f(v_i)$ is the signal value at a vertex v_i, and N is the number of vertices.

The graph Laplacian is a key matrix describing the structure of the graph $L = D - W$, where D is the diagonal degree matrix of $D_{ii} = \sum_j w_{ij}$; W is the edge weight matrix of $W_{i_j} = w_{ij}$.

1. Spectral decomposition of the signal. The graph signal f is decomposed in terms of the graph's eigenvectors (analogous to the Fourier transform): $Lu_k = \lambda_k u_k$ $f = \sum_{k=1}^{N} \hat{f}(\lambda_k) u_k$, where λ_k are the eigenvalues (graph "frequencies"), u_k are the eigenvectors (graph "harmonics"), $\hat{f}(\lambda_k)$ are the spectral coefficients of the signal.

2. Graph filtering. Filtering is used to suppress noise or highlight abrupt changes (anomalies). A low-pass filter (signal smoothing) is defined by: $f_{low} = \sum_{\lambda_k \le \lambda_c} \hat{f}(\lambda_k) u_k$, and a high-pass filter (amplifying abrupt transitions): $f_{high} = \sum_{\lambda_k > \lambda_c} \hat{f}(\lambda_k) u_k$, where λ_c is the cutoff threshold.

3. Anomaly detection. Localization by graph derivative. Nodes with abrupt signal changes relative to their neighbors can be found using the graph gradient: $\nabla_G f = Lf$, where $(Lf)_i$ indicates how much the value at node v_i differs from its neighbors. High values indicate anomalies or defects.

In practice, GSP is implemented using open-source libraries. PyGSP handles spectral filtering and graph analysis, NetworkX allows for graph construction and manipulation, and SciPy and NumPy are used for linear algebra and eigenfactorization. Scikit-learn is employed for clustering and feature-based machine learning tasks.

Nonlinear post-processing. The final stage of data processing involves using a combination of nonlinear methods to extract meaningful features, reduce noise, and organize signal information. One fundamental method is the wavelet transform, which enables signal decomposition across the time-frequency spectrum, preserving details about both overall and local features. After transformation, insignificant coefficients are set to zero, and the signal is reconstructed with less noise.

A method utilizing autoencoders (specialized symmetric neural networks) trained to reconstruct input data is also proposed. After training, the central layer (bottleneck) contains a compressed representation of features, free from noise and redundant information, which can be used as input for subsequent processes analysis.

The final step involves combining all the extracted features into a single vector, normalizing them, and inputting them into machine learning or visualization algorithms. This helps ensure compatibility across different data types (signals, images, graphs) and enhances the interpretability of the results. An overview of the proposed methods and key steps for their practical implementation are provided in Table 7.

Table 7. Stages of nonlinear post-processing of signals and images

No.	Method	Objective	Main steps	Tools
1	Wavelet transform	Extracting local signal features	1. DWT transform of the signal 2. Zeroing out small coefficients 3. Inverse DWT transform	PyWavelets, SciPy
2	Local PCA	Dimensionality reduction in a local neighborhood	1. Forming a local window around each point 2. PCA in this region 3. Using 1–2 principal components as new features	scikit-learn, NumPy
3	Autoencoders	Noise removal and compact coding	1. Training a network to reconstruct input features 2. Extracting features from the bottleneck layer 3. Using them as output	Keras, PyTorch, TensorFlow
4	Feature fusion	Preparing data for ML/clustering	1. Normalizing all features 2. Combining into a single vector 3. Clustering or classification	NumPy, Scikit-learn

Results of the literature review. A review and analysis of the literature in the Scopus database (2020 – July 2025) identified key trends and current limitations in the non-destructive testing of composite materials. The total number of relevant publications was 4 072, as shown in Table 2, based on the search queries.

Figure 2 displays word clouds generated from publication abstracts and keywords. The figure on the left shows the most common keywords, such as "Non-destructive testing", "Non-destructive examination", "Carbon fiber", "Composite material", "Ultrasonic testing", "Fiber reinforced", and "Damage detection". This highlights the main research areas in the field of non-destructive testing of composite materials, focusing on methods and research objects.

Fig. 2. Word clouds for annotations and keywords

The figure on the right, a word cloud of abstracts, displays terms from the abstracts, including "method", "material", "structure", "composite", and "inhomogeneity", highlighting the focus on methods, material properties, structural analysis, and inhomogeneity issues composites.

Figure 3 illustrates the distribution of publications across different fields of knowledge. The highest number of publications is in "Engineering" (over 2,000), followed by "Materials Science" (around 1 500), and "Physics and Astronomy" (around 1,000), highlighting the interdisciplinary nature of research in nondestructive testing of composites, with a strong focus on engineering and materials science.

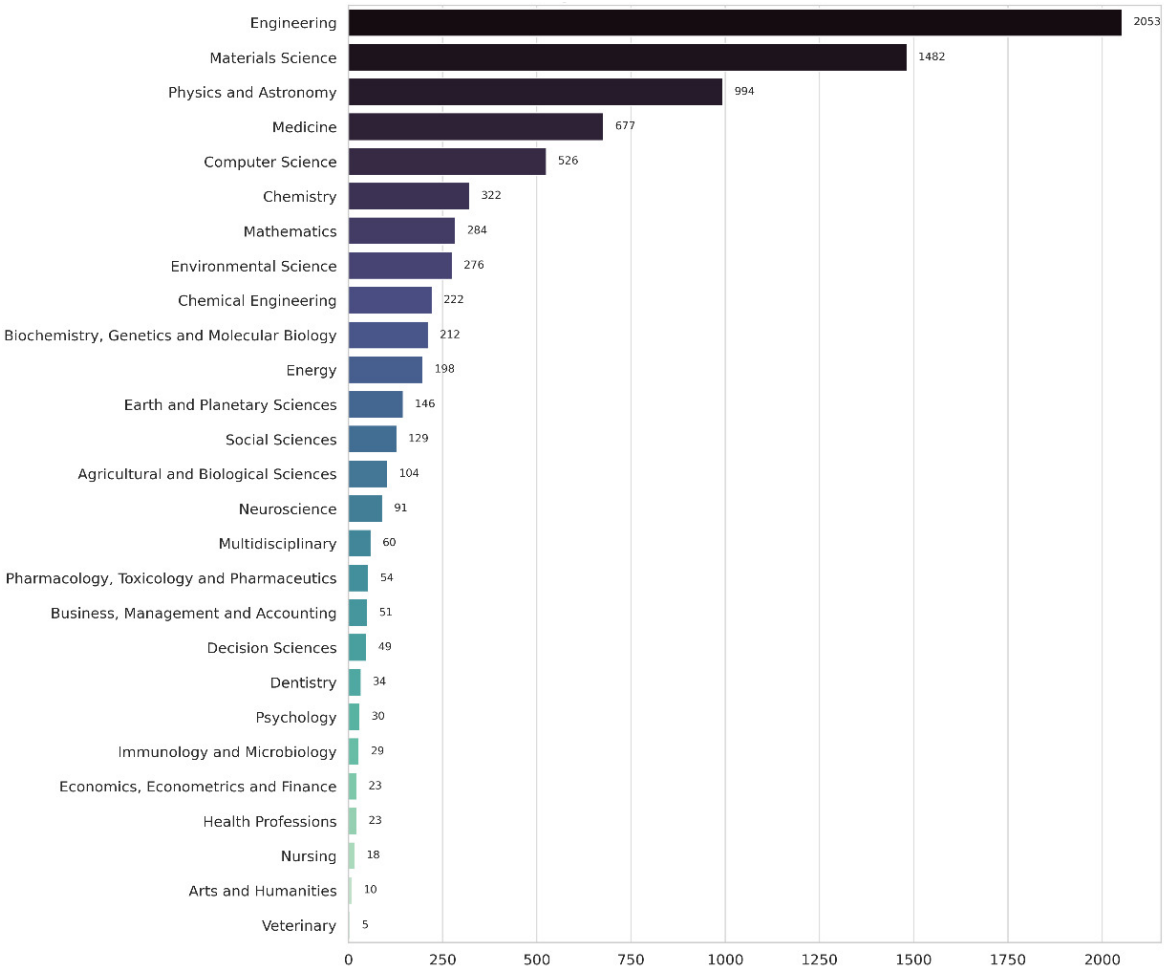

Fig. 3. Distribution of publications by industry

Figure 4 illustrates the trends in the top 15 keywords from 2020 to 2025. A significant rise in publications is observed from 2021 to 2023, followed by a decline in 2024 and 2025 (due to incomplete data for 2025). Among the most common keywords are "Carbon composites", "Carbon fiber reinforced plastics", "Composites material", "Damage detection", "Deep learning", "Defect detection", "Delamination", "Non-destructive", "Non-destructive testing", "Non-destructive examination", "Thermography (imaging)", "Ultrasonic testing", and "Ultrasonic waves", showing steady interest in various aspects of non-destructive testing and defect diagnostics in composites, as well as the increasing importance of machine learning in this field.

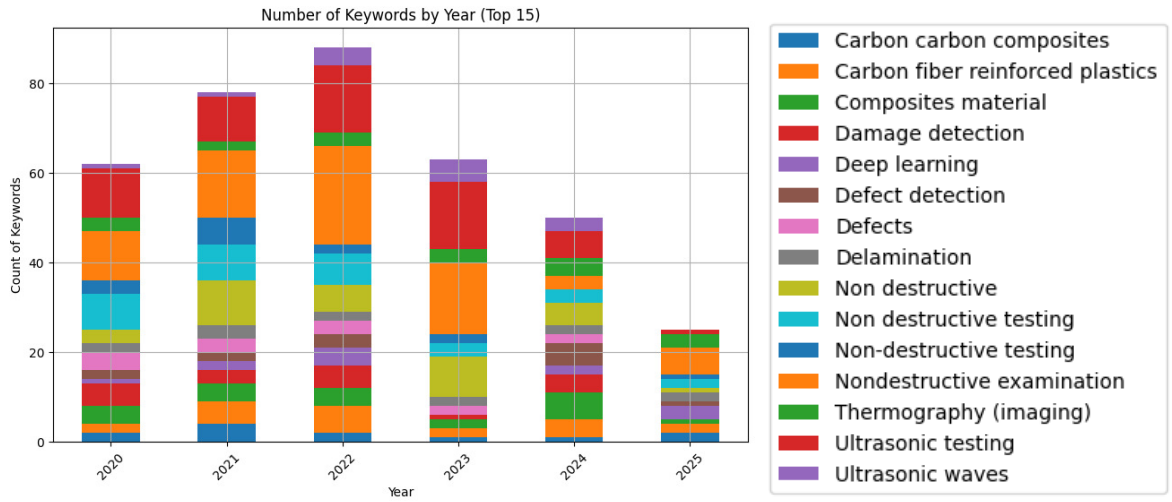

Fig. 4. Top 15 most frequently used keywords

Figure 5 shows the total number of publications by year in more detail. It is clear that the number of publications rose sharply from 2020 to 2023, peaking in 2023 with over 750 publications. A decline appears in 2024 and 2025, which may be due to incomplete data for 2025.

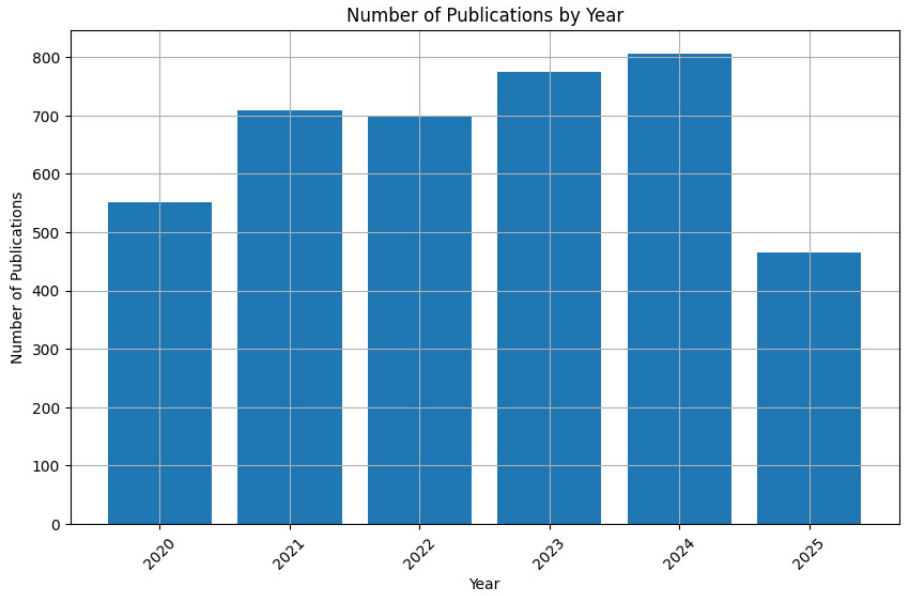

Fig. 5. Dynamics of the number of publications by year

Figure 6 displays the results of a keyword cluster analysis conducted with VOSviewer. Three main clusters (Cluster 1, Cluster 2, Cluster 3) are visible in the image. The analysis identified four major thematic clusters, representing research areas in non-destructive testing and composite material analysis. The first cluster, including terms like "composite materials", "carbon fiber", "reinforced plastics", and "delamination", focuses on composite properties and defects. The second cluster, with keywords such as "ultrasonic testing", "acoustic emission", and "defect detection", highlights non-destructive testing techniques. The third cluster, containing "deep learning", "feature extraction", and

"convolutional neural networks", shows the use of artificial intelligence in data analysis. The fourth cluster, with terms like "compression testing", "compressive strength", and "mechanical failure", concentrates on the mechanical properties and testing of materials.

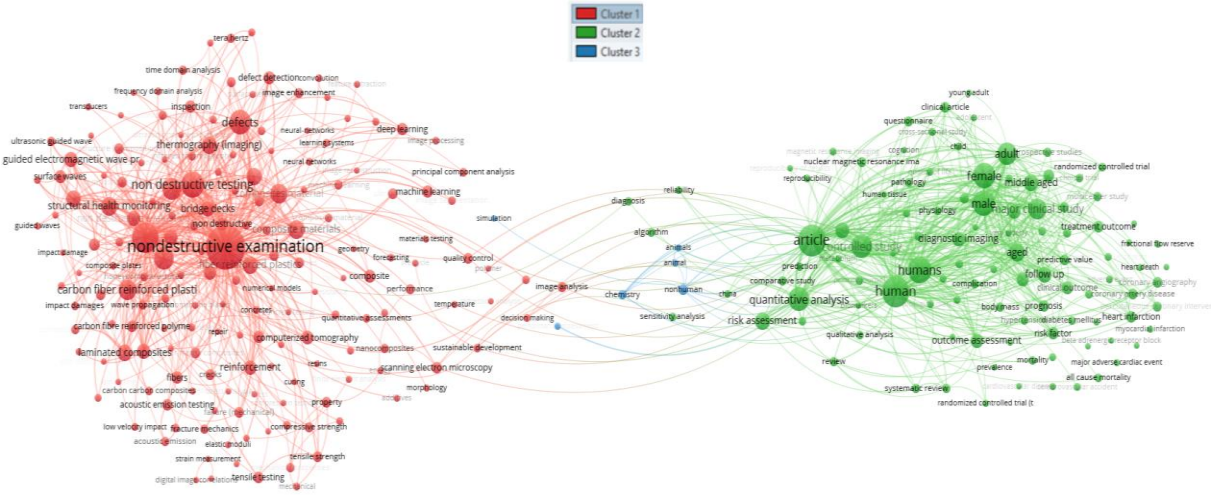

Fig. 6. General view of analytics results in VOSviewer

The relationship between the clusters illustrates how testing methods, data analysis, and composite property studies work together to enhance reliability and efficiency in various industries. An analysis of the selected publications identified some limitations of existing nondestructive testing and data processing methods:

1. Topological data analysis and graph signal processing methods are virtually absent in current research on nondestructive testing of composites. Only 69 papers on TDA and 30 papers on GSP in the context of composites have been published in the past five years. This highlights a significant research gap and untapped potential for combining TDA and GSP methods to address diagnostics and structural integrity monitoring challenges. Most of this work remains primarily theoretical nature.
2. Most work on nondestructive testing data analysis depends on traditional signal processing techniques (e.g., spectral analysis, PCA, standard filters) and machine learning methods. While these approaches yield certain results, they often lack interpretability, particularly when dealing with high-dimensional and noisy data typical of nondestructive testing.
3. Quantitative defect assessment methods based on traditional approaches show low noise immunity and high sensitivity to model parameters, which diminishes their reproducibility and reliability in real-world applications where non-destructive testing data always contains some level of noise.

Demo example on synthetic data

To partly demonstrate the effectiveness and advantages of the developed method, a series of experiments was conducted on synthetic and real non-destructive testing data. The data used to showcase the performance of the proposed method is shown in Table 8. The experiments involved synthetic ultrasound data ("Averaged 10dB normalized delamination damage position at 0 to 1.csv", KU Leuven RDR), including 81 signals with

normalized delamination positions [0, 1] and an SNR of 10 dB [26]. Each signal consists of 1122 points normalized to the amplitude range [-1, 1]. Graph signal processing and nonlinear post-processing were not implemented in the present study.

Table 8. Data sets used for demonstration

Dataset	Type	Source
KU Leuven RDR – delamination [26]	Ultrasound	Lu, Houyu; Cantero Chinchilla, Sergio; Yang, Xin; Gryllias, Konstantinos; Chronopoulos, Dimitrios, 2024, «Multiple ultrasonic-guided wave signals generated by wave propagation model: focused on delamination damage location variations in cross-ply composite beams», *https://doi.org/10.48804/JAIG58*, KU Leuven RDR, V1

Topological data analysis. Visualization and results. Topological data analysis was used to extract invariant structural features that reflect the geometry and shape of the non-destructive testing data across multiple scales, as described in the "Feature extraction with topological data analysis" section.

This section provides diagnostic plots for several of the studied signals, illustrating their main characteristics. Each set of plots includes a signal time series that shows how the signal amplitude changes over time; an amplitude histogram that displays the distribution of amplitude values to estimate frequently occurring levels; and a power spectrum that illustrates how the signal's power is distributed across different frequencies. Peaks in the power spectrum highlight dominant frequency components, which are important for identifying hidden periodicities and evaluating the overall frequency content.

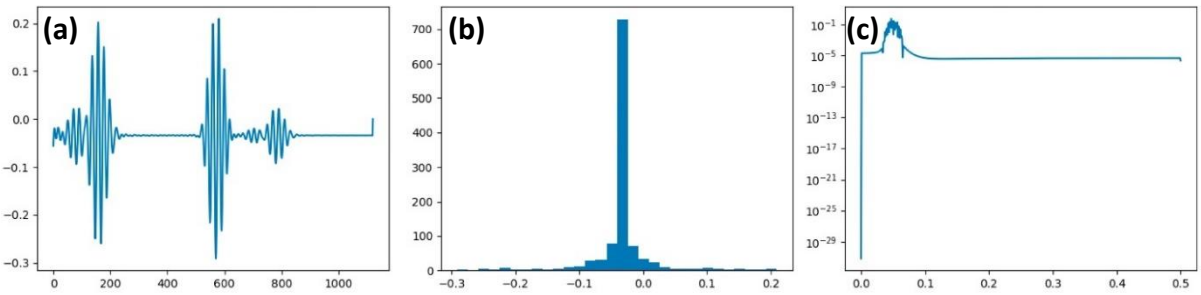

Fig. 7. Signal 1 diagnostics: (a) time series; (b) histogram; (c) power spectrum

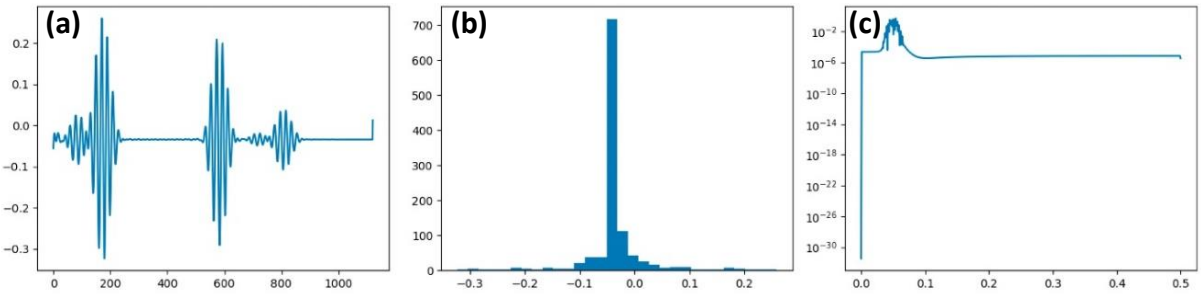

Fig. 8. Signal 2 diagnostics: (a) time series; (b) histogram; (c) power spectrum

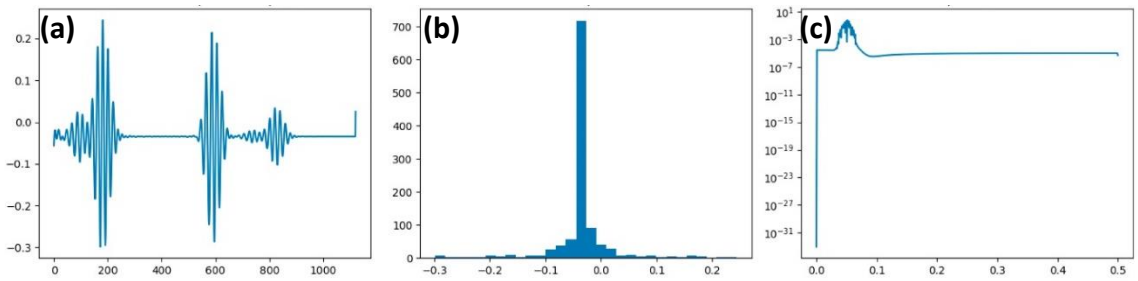

Fig. 9. Signal 3 diagnostics: (a) time series; (b) histogram; (c) power spectrum

All input data for TDA had the shape (81, 1122), meaning 81 individual time series, each consisting of 1122 data points. Diagnostic plots (time series, amplitude histogram and power spectrum) for three representative ultrasonic signals are shown in Fig. 7–9. The corresponding diagnostic descriptions are given in Tables 9–11.

A preliminary analysis of the time series, histograms, and power spectra shows that the signals 2 and 3 have similar characteristics, indicating a more uniform state, while the signal 1 displays greater high-frequency content activity.

Table 9. Signal 1 diagnostics

Time series	Signal 1 shows an oscillating, noise-like pattern without sharp anomalies at this scale. The amplitude varies roughly from -0.25 to 0.2. The lack of strong peaks or dips suggests a relatively stable material or background noise in the absence of a defect.
Histogram	The signal amplitude distribution is almost symmetrical, with most values near zero, which is typical of random noise or signals oscillating around a mean value. The histogram shape shows no bimodality or strongly shifted peaks, which could indicate obvious defects or consistent signal offsets.
Power spectrum	The power spectrum shows a fairly broad frequency range with several noticeable but not dominant peaks at lower frequencies. The lack of very high peaks at specific frequencies suggests the signal does not have strong periodic components, which might be typical of background noise or a complex mix of weak oscillations.

Table 10. Signal diagnostics 2

Time series	The time series of Signal 2 also shows an oscillatory pattern, but with a slightly lower amplitude compared to Signal 1 (roughly from -0.2 to 0.15). Visually, it looks smoother or has less high frequency than Signal 1.
Histogram	The histogram, like Signal 1, is centered around zero and has a symmetrical distribution, but with a more prominent peak, suggesting a smaller spread of amplitude values and possibly less random noise.
Power spectrum	The power spectrum of Signal 2 shows significantly less overall power than Signal 1, especially at higher frequencies, confirming the visual observation of a smoother signal and the lack of pronounced high-frequency components often linked to sudden changes or impulsive events.

Table 11. Signal 3 diagnostics

Time series	Signal 3 is an oscillatory time series, similar in amplitude and overall appearance to Signal 2 (ranging from approximately -0.2 to 0.15). It also shows no obvious sharp anomalies or high-amplitude pulses.
Histogram	The histogram of Signal 3 shows a peak near zero and looks symmetrical, indicating a similar statistical distribution of amplitudes.
Power spectrum	The power spectrum of Signal 3 shows relatively low overall power and no distinct peaks at high frequencies, similar to Signal 2, which may suggest similar underlying processes.

For each data time series, a phase-space embedding step was performed using the Takens embedding method. The embedding dimension and time delay $\tau = 10$ were chosen as the embedding parameters, allowing the one-dimensional signals to be transformed into multidimensional point clouds. Vietoris-Rips complexes were then constructed for the resulting point clouds, which serve as the basis for calculating topological characteristics. The corresponding stability diagrams (persistence diagrams) for these three signals are presented in Fig. 10.

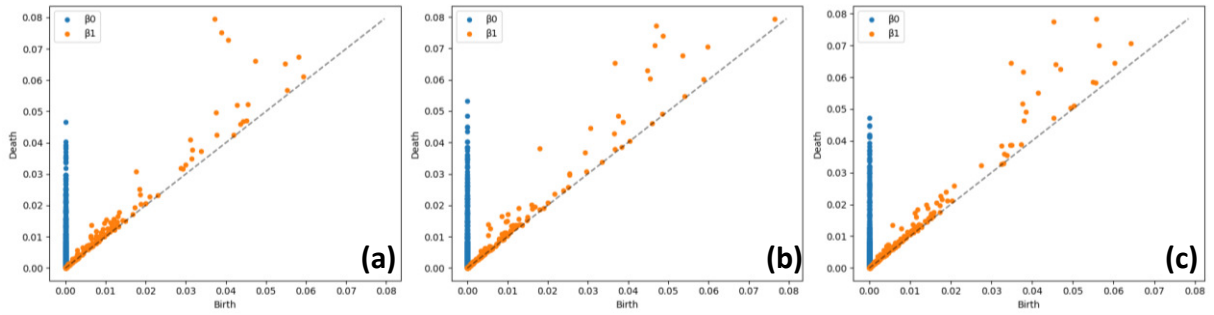

Fig. 10. Stability diagrams of three signals: (a) signal 1; (b) signal 2; (c) signal 3

Table 12. Stability diagrams

Signal stability diagram number	**β_0 (connected components, blue dots)**	**β_1 (cycles, orange dots)**
Signal stability diagram 1	A large number of blue dots are visible, located close to b = d. This indicates numerous short-lived connected components that quickly form and disappear with a slight increase in the epsilon radius. Such dots typically correspond to noise fluctuations or minimal, transient data features that are not structurally significant. However, there are also individual β_0 dots with longer lifetimes (far from the diagonal), which may indicate stable, well-separated clusters inherent in the signal structure.	The presence of many orange dots with relatively long lifetimes (far from the diagonal) is a key feature of this diagram. These dots depict stable closed loops in the reconstructed phase space of the signal. Their presence suggests complex topological structures that could indicate defects such as cracks or delaminations, which form loops in the signal's phase space due to nonlinear interaction dynamics. One of these dots has considerably greater stability (a large distance from the diagonal) highlighting a highly significant topological cycle.
Signal stability diagram 2	Similar to signal 1, short-lived β_0 components close to the diagonal dominate. The number of more stable β_0 points is presumably lower than for signal 1, which may reflect less clustering or a more uniform distribution of points in phase space.	The number of orange β_1 points in this diagram is significantly smaller compared to signal 1, and their distance from the diagonal is also smaller. This indicates that fewer stable cycles are formed in the phase space of signal 2. The reduced number and significance of cycles are consistent with the hypothesis that this signal arises from a less damaged region.
Signal stability diagram 3	The distribution of β_0 points is similar to signal 2, indicating a predominance of noise-like or short-term connected components.	As with signal 2, the number and lifetime of β_1 points in this diagram are low, confirming that signal 3 also contains fewer stable topological cycles.

A comparative analysis of the stability diagrams of the three signals demonstrates that signals related to defective regions are characterized by the presence of stable first order β_1 cycles with a long lifetime. These cycles correspond to closed anomalies in the reconstructed signal dynamics, which is a powerful indicator of damage. A detailed description of the stability diagrams is given in Table 12.

Signals from defect-free zones (represented by Signals 2 and 3) predominantly contain short-lived zero-order β_0, components reflecting noise fluctuations and significantly fewer or no stable β_1 cycles, providing direct evidence of TDA's ability to effectively differentiate different material states based on their internal topological structure.

Based on the calculated stability diagrams, quantitative topological descriptors were derived. These descriptors provide a numerical representation of the topological properties of the data and are used as features for further analysis or machine learning (Table 6). The first five rows of the extracted topological descriptor matrix are shown in Table 13.

Table 13. Topological descriptors (first five rows)

NumPoints_H0	NumPoints_H1	Entropy_H0	Entropy_H1	Amplitude_H0	Amplitude_H1
0	1101	307	8.597069	0.135013	0.038029
1	1101	299	8.546403	0.147386	0.036210
2	1101	308	8.539554	0.145726	0.035309
3	1101	289	8.491680	0.131108	0.033008
4	1101	268	8.560095	0.129314	0.038186

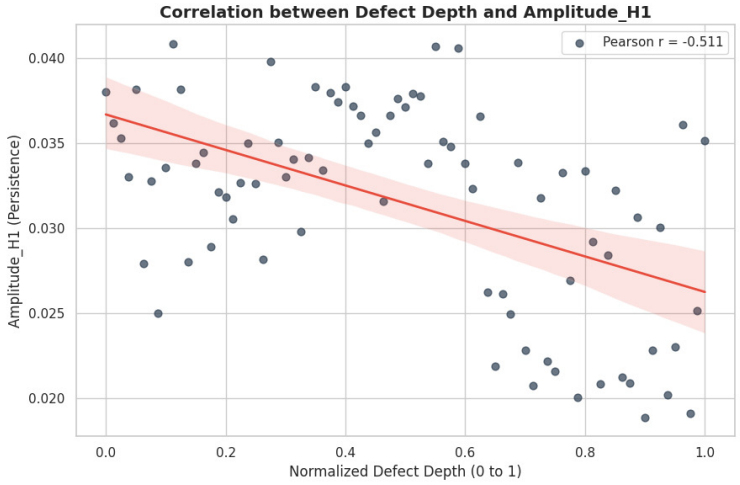

Fig. 11. Correlation between normalized delamination position (defect depth) and Amplitude_H1 topological descriptor (Pearson r ≈ -0.51, p < 0.001). Blue points – individual signals; red line – linear regression trend

The dependence is visualized in Fig. 11. Analysis of the KU Leuven RDR dataset showed a moderate negative correlation (Pearson $r \approx -0.51$, $p < 0.001$) between the normalized delamination position (0–1, interpreted as relative defect depth along the beam) and the topological descriptor Amplitude_H1 (total lifetime of persistent H1 cycles). This indicates that shallower delaminations (lower position values) produce longer-lived topological cycles in the reconstructed phase space. Physically, this is explained by stronger nonlinear scattering and mode conversion at the defect interface when the delamination is closer to the excitation/sensor surface; deeper positions lead

to greater attenuation and weaker phase-space distortion, shortening the lifetime of the detected H1 loops. Thus, the Amplitude_H1 metric not only distinguishes defective from defect-free signals but also carries quantitative information about defect depth, which will be crucial for future spatial localization with graph signal processing. A detailed interpretation of all topological descriptors used in the analysis is provided in Table 14.

Table 14. Topological descriptors

Descriptor	**Brief description of the topological descriptor**
NumPoints_H0	The number of connected components detected in 0-dimensional homology. In the context of Takens embedding applied to time series, this descriptor primarily reflects the density of points in the reconstructed phase space. It begins with a value close to the number of embedded points L (as each point initially forms its own component) and thereby provides a measure of noise-induced fragmentation versus underlying signal structure. Higher values typically indicate finer-scale clustering attributable to noise or detailed signal features, while lower values after merging point to more coherent topological organization.
NumPoints_H1	The number of cycles (holes) detected in 1-dimensional homology is a key feature for identifying defects like cracks or delaminations, which appear as stable closed structures in phase space. The higher this value, the more such structures there are.
Entropy_H0 Entropy_H1	Entropy of the stability diagram for 0th and 1st homology, respectively. High entropy indicates a broad range of «lives» (stability) for topological objects, which may result from the complexity or chaos of the signal's internal structure. For defective regions, increased entropy is expected in H_1, reflecting the diversity and complexity of the defects.
Amplitude_H0 Amplitude_H1	Stability amplitude (or total stability) for 0th and 1st homology, respectively. These values reflect the overall significance of all topological objects in a given measurement. High amplitude, especially for H_1, indicates the presence of strong, long-lasting topological features characteristic of pronounced defects.

Table 14 shows that NumPoints_H0 for the first five signals remains constant (1101), likely representing the number of data points in each time series. More important for classification are variations in NumPoints_H1, Entropy_H0, Entropy_H1, Amplitude_H0, and Amplitude_H1. For instance, signal 0 has NumPoints_H1=307 and Amplitude_H1=0.038029, whereas signal 4 has NumPoints_H1=268 and Amplitude_H1=0.038186. These detailed differences in topological features can be used to accurately distinguish material states.

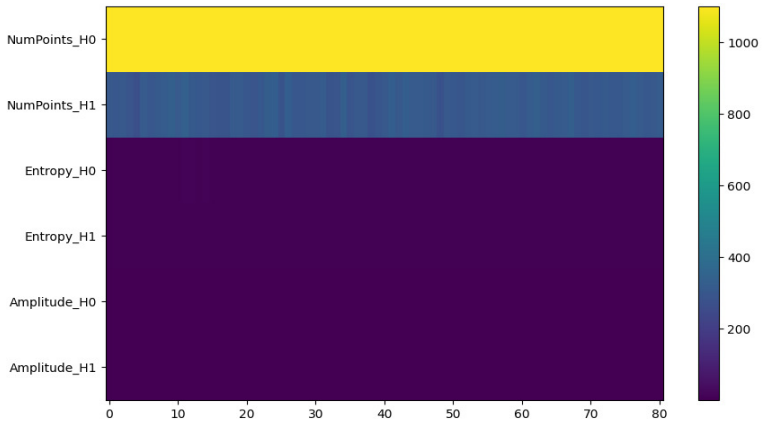

Fig. 12. Heat map of topological features

The topological feature heatmap, which visualizes the values of each of the six extracted descriptors for all 81 signals under study, is shown in Fig. 12. The x-axis represents the signal indices, and the y-axis displays the names of the topological features. The color scale (ranging from blue to yellow/light green) indicates the normalized feature values. Brighter colors (yellow, light green) represent high values, while darker colors (violet, blue) signify low values.

The heatmap shows horizontal bands and vertical patterns. Each row represents a specific topological feature, and each column represents a specific signal. Visually, groups of signals (columns) with similar topological characteristics can be identified. For example, the NumPoints_H1, Entropy_H1, and Amplitude_H1 features (bottom three rows) display more noticeable variations and contrasting areas compared to NumPoints_H0 and Entropy_H0. Although H1 features dominate the separation (see stability diagrams), H0 descriptors also contribute: defective signals show higher variation in NumPoints_H0 and Entropy_H0 (visible as brighter vertical bands in the upper rows of the heatmap).

If we assume that defective signals are characterized, for example, by high NumPoints_H1 values (more cycles) and Amplitude_H1 (more stable cycles), then such signals will be highlighted on the heatmap by brighter vertical columns in the corresponding rows. The image indeed shows areas of increased and decreased feature values, forming clear boundaries. This confirms that topological descriptors effectively generate distinguishable patterns for defective and defect-free areas. Such visually distinguishable clusters on the heat map provide direct evidence of the suitability of these features for automatic defect classification or segmentation.

To further identify hidden structures in the data and automatically segment defective and defect-free areas, K-Means clustering was applied based on the extracted topological feature vectors. The clustering results are summarized in Table 15.

Table 15. Clustering results

Clustering results
K = 2, silhouette score=0.471
K = 3, silhouette score=0.334
K = 4, silhouette score=0.336
K = 5, silhouette score=0.300
Optimal number of clusters: 2 with a silhouette score of 0.471

The silhouette score is a metric used to assess clustering quality. It measures how similar an object is to its own cluster compared to other clusters. Silhouette score values range from -1 to 1, with values close to 1 indicating well-separated and dense clusters, and values close to 0 or negative values indicating overlapping or poorly formed clusters.

In this case, the highest silhouette score of 0.471 was achieved with K = 2. This strongly indicates that the dataset has the most natural and well-separated division into two main signal categories. This binary division is ideal for non-destructive testing tasks, where it is essential to distinguish between defects and the absence of defects.

The graph in Fig. 13 shows the results of topological feature clustering after reducing the dimensions to two using principal component analysis (PCA) for easier visualization. Each point on the graph represents a single signal, and the color of each point indicates its cluster membership, as determined by K-means algorithm.

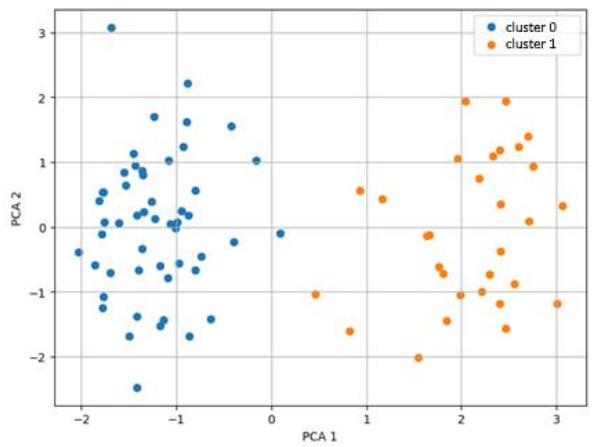

Fig. 13. Clusters by topological features (PCA)

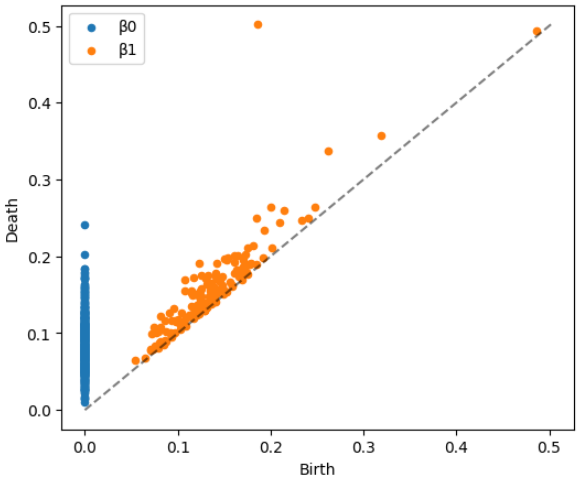

Fig. 14. Synthetic signal stability diagram (points on the synthetic signal diagram: 637)

The graph shows two distinct, well-defined groups of points, colored differently (blue and orange), representing two optimal clusters based on the silhouette score. These clusters have minimal overlap in the two-dimensional principal component space, indicating significant and statistically meaningful differences in the topological features between signals from different clusters.

Since topological features were extracted to distinguish defective from defect-free regions, this clear separation into two clusters confirms that the TDA method successfully detects internal structural differences in the data. This allows for automatic classification of signals based on their topological characteristics, such as those from defective regions (characterized by the presence of stable cycles, as shown by stability diagrams) and those from healthy regions (with a predominance of noise-like components).

To benchmark the proposed TDA approach against conventional linear techniques, the same 81 ultrasonic signals were processed using two standard baseline methods: Fast Fourier Transform (FFT) and Discrete Wavelet Transform (DWT, Daubechies 4, level 5) followed by an identical K-Means clustering and silhouette evaluation routine. While the FFT feature vectors comprised total power, dominant frequency, and sub-band power distribution, and the DWT approach relied on the energy of detail coefficients, both methods yielded significantly lower silhouette scores than the 0.471 achieved through TDA. This performance gap is clearly explained by the diagnostic plots in Fig. 7–9, which show that at a 10 dB noise level, the power spectra of defective and healthy regions overlap so heavily that frequency- and wavelet-domain features cannot reliably differentiate between them. In contrast, TDA identifies persistent H1 topological cycles that remain stable despite the noise, effectively capturing the physical delamination interface within the reconstructed phase space and proving far more robust than classical signal processing in such challenging signal-to-noise conditions.

To fundamentally validate the TDA's ability to reliably identify known topological structures, a test was performed on a synthetic signal (Fig. 14). For this, a simple sinusoidal signal with some random noise was generated. It is known that such a signal, when embedded in phase space using the Takens method, should form a clearly defined topological structure loop.

The synthetic signal plot (Fig. 14) clearly shows a dominant orange dot β_1, indicating a very stable topological cycle. Its location far from the diagonal confirms the cycle's significant lifetime. This fact demonstrates that the TDA algorithm accurately finds and describes closed structures, or loops, in the signal's phase space, even in the presence of noise.

TDA was applied to 81 signals using the Takens embedding (m = 3, τ = 1) and Vietoris-Rips complexes. Stability diagrams (Fig. 10) show that signals with delaminations (e.g., signal 1) contain stable H1 cycles (orange dots far from the diagonal), corresponding to anomalies caused by delaminations in the composite beam. Signals without defects (signals 2 and 3) have more short-lived H0 components, reflecting noise. Table 14 shows the descriptors (NumPoints_H1, Amplitude_H1) varying depending on the delamination position. Clustering (Table 15, Fig. 13) divided the signals into defective and defect-free clusters (silhouette score 0.471).

The mathematical logic of the TDA pipeline is as follows:

1. For each ultrasonic signal s_i ∈ $\mathbb{R}^{1122}$: P_i = TakensEmbedding(s_i, *m* = 3, τ = 1).
2. Construct Vietoris-Rips complex VR (P_i, ε) for ε ∈ [0, ε_max].
3. Compute persistence diagram D_i = Pers(VR) in dimensions 0 and 1.
4. Extract feature vector F_i = {NumPoints_H0, NumPoints_H1, Entropy_H0, Entropy_H1, Amplitude_H0, Amplitude_H1}.
5. Form matrix F ∈ ℝ^{81×6}, standardize, and apply K-Means for k = 2…10.
6. Select optimal k by maximum silhouette score.
7. Validation on synthetic sinusoidal signal with known H1 cycle.

The results showed that TDA can identify basic topological features and that these features remain stable even with background noise, making them distinguishable from random fluctuations. These early findings can lay the groundwork for applying the method to real-world nondestructive testing signals, where defects may appear as similar topological features in the signal's phase space. Detecting these with TDA allows for accurate damage assessment diagnosis.

Conclusions

A non-destructive testing method for composite materials has been developed that combines topological data analysis and graph signal processing. This study emphasizes applying topological data analysis to synthetic ultrasonic data, marking a first step toward integrating these approaches processing.

The results obtained allow the following conclusions to be drawn:

1. Topological data analysis allows the extraction of noise-resistant features, such as the number of first-order cycles (H1), the entropy of stability diagrams, and the stability amplitude from synthetic ultrasonic data (Table 14). First-order cycles indicate structural anomalies associated with delaminations in composite materials, thereby helping distinguish defective from defect-free signals.
2. The K-means algorithm divided the signals into two clusters, corresponding to defective (containing delaminations) and defect-free regions, with a silhouette score of 0.471, demonstrating topological data analysis's ability to identify differences in the signal structure related to physical aspects of defects.

3. A test on a noisy sinusoidal signal demonstrated that TDA reliably detects topological structures (stable cycles), even amidst noise, highlighting its robustness.

In this study, the analysis is limited to applying topological data analysis to synthetic data, without employing graph signal processing. Validation on real non-destructive testing data was not conducted, which limits the conclusions about the method's practical applicability. The computational complexity of topological data analysis necessitates optimization to enable real-time use. The results obtained provide a foundation for future integration with graph-signal processing and will enhance the accuracy of quantifying and localizing defects in complex composite structures.

Future research directions include:

1. Application of graph signal processing for spatial dependency analysis and defect localization in synthetic and real non-destructive testing data.
2. Conducting tests on diverse datasets, including different types of composite materials and defects (such as delaminations, pores, and cracks), to verify the scalability of the method.
3. Refinement of computational algorithms for topological data analysis and graph signal processing using parallel computing to accelerate processing and adapt to industrial environment conditions.

Integration of the proposed method with graph neural networks to automate defect classification and enhance the interpretability of results.

CRediT authorship contribution statement

Alexey I. Borovkov: writing – review & editing, supervision; **Khristina M. Vafaeva**: writing – original draft, conceptualization; investigation; data curation; **Nikolay I. Vatin**: writing – review & editing, supervision; **Zhmagul S. Nuguzhinov**: writing – review & editing, supervision.

Conflict of interest

The authors declare that they have no conflict of interest.

References

1. Li Y, Cheng S, Wang S, Yuan C, Luo Z, Zhu Y, Hu J, He J, Li Q. Multilayered ferroelectric polymer composites with high energy density at elevated temperature. *Composites Science and Technology.* 2021;202: 108594.
2. Bastovansky R, Smetanka L, Kohar R, Mishra RK, Petru M. Comparison of mechanical property simulations with results of limited flexural tests of different multi-layer carbon fiber-reinforced polymer composites. *Polymers.* 2024;16(11): 1588.
3. Gilys L, Griškonis E, Griškevičius P, Adlienė D. Lead-free multilayered polymer composites for radiation shielding. *Polymers.* 2022;14(9): 1696.
4. Berretti S, Thomas J-B, Hayat K, Abdollahi-Mamoudan F, Ibarra-Castanedo C, Maldague XPV. Non-destructive testing and evaluation of hybrid and advanced structures: a comprehensive review of methods, applications, and emerging trends. *Sensors.* 2025;25(12): 3635.
5. Wiener J, Arbeiter F, Kolednik O, Pinter G. Influence of layer architecture on fracture toughness and specimen stiffness in polymer multilayer composites. *Materials & Design.* 2022;219: 110828.
6. Feng M, Feng Y, Zhang T, Li J, Chen Q, Chi Q, Lei Q. Recent advances in multilayer-structure dielectrics for energy storage application. *Advanced Science.* 2021;8(23): 2102221.
7. Huang X, Su S, Xu Z, Miao Q, Li W, Wang L. Advanced composite materials for structure strengthening and resilience improvement. *Buildings.* 2023;13(10): 2406.

8. Kumpati R, Skarka W, Ontipuli SK. Current trends in integration of nondestructive testing methods for engineered materials testing. *Sensors.* 2021;21(18): 6175.
9. Mortada H, El Mousharrafie S, Mahfoud E, Harb M. Noncontact nondestructive ultrasonic techniques for manufacturing defects monitoring in composites: a review. *Structural Health Monitoring.* 2024;23(3): 1969–1997.
10. Gupta R, Mitchell D, Blanche J, Harper S, Tang W, Pancholi K, Baines L, Bucknall DG, Flynn D. A review of sensing technologies for non-destructive evaluation of structural composite materials. *Journal of Composites Science.* 2021;5(12): 319.
11. Sabry AH, Ungku Amirulddin UAB. A review on fault detection and diagnosis of industrial robots and multi-axis machines. *Results in Engineering.* 2024;23: 102397.
12. Zhang J, Peng L, Wen S, Huang S. A review on concrete structural properties and damage evolution monitoring techniques. *Sensors.* 2024;24(2): 620.
13. Kosova F, Altay Ö, Ünver HÖ. Structural health monitoring in aviation: a comprehensive review and future directions for machine learning. *Nondestructive Testing and Evaluation.* 2025;40(1): 1–60.
14. Gutkin MYu, Kolesnikova AL, Krasnitckii SA, Mikaelyan KN, Petrov DA, Romanov AE, Smirnov AM. Micromechanics of misfit stress relaxation in heterogeneous crystalline nanostructures: a review. *Materials Physics and Mechanics.* 2025;53(5): 1–34.
15. Keresten IA, Pirozhnikov PB, Suranov IS, Erofeev DA, Titov AG. Experimental and numerical determination of mechanical properties of porous thermoplastic. *Materials Physics and Mechanics.* 2025;53(4): 66–75.
16. Wang Z, Jia Z, Ren J, Wang L, Lan D, Zhang S, Shi X, Liu X, Gao Z, Wu G. Multi-topological network engineering of Co/MnO composites for electromagnetic wave absorption. *Journal of Materials Science & Technology.* 2025;235: 81–90.
17. Al-Dayel I, Nadeem MF, Khan MA. Topological analysis of tetracyanobenzene metal–organic framework. *Scientific Reports.* 2024;14: 1789.
18. Sun C, Wang W, Tian XW, Zeng X, Qian SH, Cai YZ, Wang XH. Thermal design of composite cold plates by topology optimization. *International Journal of Mechanical Sciences.* 2023;259: 108594.
19. Liu X, Gao L, Xiao M. An efficient multiscale topology optimization method for frequency response minimization of cellular composites. *Engineering with Computers.* 2025;41: 267–291.
20. Alfouneh M, Hoang VN, Luo Z, Luo Q. Topology optimization for multi-layer multi-material composite structures. *Engineering Optimization.* 2023;55(5): 773–790.
21. Hu W, Pang J, Liu X, Tian D, Lin CW, Vetro A. Graph signal processing for geometric data and beyond: theory and applications. *IEEE Transactions on Multimedia.* 2022;24: 3961–3977.
22. Ramakrishna R, Scaglione A. Grid-graph signal processing (grid-gsp): a graph signal processing framework for the power grid. *IEEE Transactions on Signal Processing.* 2021;69: 2725–2739.
23. Cheema MA, Sarwar MZ, Gogineni VC, Cantero D, Rossi PS. Computationally efficient structural health monitoring using graph signal processing. *IEEE Sensors Journal.* 2024;24(7): 11895–11905.
24. Zhao Z, Chen NZ. Spatial-temporal graph convolutional networks (STGCN)-based method for localizing acoustic emission sources in composite panels. *Composite Structures.* 2023;323: 117496.
25. Vasudevan A, Prieto JZ, Zorkaltsev S, Haranczyk M. TDA-segmentor: a tool to extract and analyze local structure and porosity features in porous materials. *Computer Physics Communications.* 2024;305: 109344.
26. Lu H, Cantero-Chinchilla S, Yang X, Gryllias K, Chronopoulos D. Multiple ultrasonic-guided wave signals generated by wave propagation model: focused on delamination damage location variations in cross-ply composite beams. *KU Leuven RDR.* 2024; V1.
27. Lu H, Cantero-Chinchilla S, Yang X, Gryllias K, Chronopoulos D. Deep learning uncertainty quantification for ultrasonic damage identification in composite structures. *Composite Structures.* 2024;338: 118087.
28. Lin Y, Liu H, Yu J, Cheng Z, Song Y, Zeng L, Ji X. Non-destructive testing of metal/CFRP composite defects using continuous-wave laser ultrasonic technique. *Optics & Laser Technology.* 2025;189: 113113.
29. Zarei A, Pilla S. Laser ultrasonics for nondestructive testing of composite materials and structures: a review. *Ultrasonics.* 2024;136: 107163.
30. Machado MA. Eddy currents probe design for NDT applications: a review. *Sensors.* 2024;24(17): 5819.
31. Cheng J, Zhu Y, Wang B, Liu M, Xu D, Qiu J, Takagi T. Noncontact visualization of multiscale defects in CFRP composites using eddy current testing with T-R probe. *NDT & E International.* 2024;145: 103138.
32. Guo Z, Lee KM, Yu H, Xiong Z. Magnetic field-based eddy-current probe design, modeling, and computing methods for edge defect detection. *IEEE Sensors Journal.* 2024;24(12): 18889–18902.

33. Sharma S, Vishnu VG, Srivastava V. Detection of failure in materials under tensile testing using acoustic emission technique. *e-Journal of Nondestructive Testing*. 2025;30(6).
34. van de Velde M, Vandecruys E, Verstrynge E, Reynders E, Lombaert G. Vibration monitoring and acoustic emission sensing during progressive load tests of corroded reinforced concrete beams. *Engineering Structures*. 2024;306: 117851.
35. Melchiorre J, D'Amato L, Agostini F, Rizzo AM. Acoustic emission onset time detection for structural monitoring with U-net neural network architecture. *Developments in the Built Environment*. 2024;18: 100449.
36. Hsiao TY, Sfarra S, Liu Y, Yao Y. Two-dimensional Hilbert-Huang transform-based thermographic data processing for non-destructive material defect detection. *Quantitative InfraRed Thermography Journal*. 2025;22(4): 297–312.
37. Tang S, Gao X, Tian K, Zhang Q, Zhang X, Peng J, Guo J. Non-destructive evaluation of weld defect with coating using electromagnetic induction thermography. *Nondestructive Testing and Evaluation*. 2024;39(2): 347–365.
38. Evans EE, Brooks RA, Liu J, Hall ZEC, Liu H, Lowe TJE, Withers PJ, Kinloch AJ, Dear JP. Comparison of X-ray computed tomography and ultrasonic C-scan techniques and numerical modelling of impact damage in a CFRP composite laminate. *Applied Composite Materials*. 2024;31: 249–264.
39. Brewer CE, Poovathingal SJ. Pyrolysis front detection in carbon phenolic composites using X-ray computed tomography. *Composites Part A: Applied Science and Manufacturing*. 2024;187: 108444.
40. Li C, Xia T, Gao S, Yan M, Chen Y, Wan B, Li J, Wan F. Microstructure analysis of quartz fiber reinforced SiO_2 matrix composites by X-ray computed tomography. *Materials Characterization*. 2024;209: 113745.

MATERIALS PHYSICS AND MECHANICS RESEARCH ARTICLE

Submitted: July 4, 2025 **Revised: November 26, 2025** **Accepted: March 10, 2026**

CFD evaluation of the hydrodynamic and thermal performances of a counter-flow heat exchanger

R. Nebatti [1] ✉, M. Kadja [1], F. Mechighel [2]

[1] University of Brothers Mentouri Constantine 1, Constantine, Algeria

[2] Badji Mokhtar University – Annaba, Annaba, Algeria

✉ nebbatirabah@yahoo.com

ABSTRACT

A heat exchanger is a device that facilitates the transfer of energy between two fluids through a solid barrier. Simulations were performed in a turbulent flow regime to investigate the two-dimensional forced convective heat transfer of the nanofluid water / Al_2O_3 within a counter-flow heat exchanger. This study is numerical and was conducted using a single-phase approach with constant thermophysical properties. Conduction through the interface was taken into account in the computations. The results unequivocally showed an improvement in the overall coefficient of heat transfer depending on the Reynolds number along with the type of fluid. The use of nanofluid significantly increases total heat transfer in contrast to the pure base fluid; however, this is accompanied by an increase in friction coefficients, leading to higher pumping costs.

KEYWORDS

computational fluid dynamics • fully developed turbulent flow • double tube heat exchanger numerical convective heat transfer • overall heat transfer coefficient

Citation: Nebatti R, Kadja M, Mechighel F. CFD evaluation of the hydrodynamic and thermal performances of a counter-flow heat exchanger. *Materials Physics and Mechanics*. 2026;54(2): 167–180.
http://dx.doi.org/10.18149/MPM.542202612

Introduction

The thermal energy exchanger is one of the key instruments of the thermal engineer or energy engineer, whether its goal is the manufacture of a product whose development passes through a set of cycles where temperature and pressure vary [1], or whether it involves the production of mechanical (or electrical) energy from thermal energy [2]. Essentially, a hot fluid circulates from an inlet of the exchanger to its outlet by transferring part of its enthalpy to a cold fluid which also circulates between an inlet and an outlet distinct from those of the hot fluid.

Heat exchangers are mainly used in various industrial sectors, including chemicals, petrochemicals, steel, agri-food, and energy production, along with transportation (automobile, aeronautics) and residential and tertiary sectors (heating, air conditioning, etc.) [3,4]. The selection of a heat exchanger for any application is influenced by numerous factors: the temperature and pressure ranges of the fluids, their physical characteristics and corrosiveness, maintenance considerations, and size. It is evident that a well-suited, correctly sized, robust, and efficiently operated exchanger contributes to improved process efficiency and energy utilization [5]. Due to their importance in industry many recent studies have been published by researchers, whether theoretical or numerical, on these devices. In the work of Pathak et al. [6], a concentric pipe counterflow heat

Publisher: Peter the Great St. Petersburg Polytechnic University

exchanger (CPCFHEx) is examined to enhance its performance under various conditions. Velocity, pressure, temperature, and turbulence profiles are analyzed in pipes using the CFD (computational fluid dynamics) simulation method. The analysis encompasses pressure drops, velocity variations, total heat transfer coefficients, and effectiveness for CPCFHEx. The study includes an examination of entropy, exergy, and entransy across various flow rates and internal pipe materials to identify the best operating conditions. Following the analysis, the results indicate that copper achieves a maximum temperature difference of 4.688 K and an effectiveness of 0.1562 for the cold fluid at low flow rates (0.081 and 0.19 kg/s). On the other hand, steel shows a maximum temperature difference of 1.595 K for the hot fluid at higher flow rates (0.1 and 0.22 kg/s). The analysis reveals that at high flow rates, copper achieves a maximum heat transfer rate of 1.603 W and a total heat transfer coefficient of 3.160 W/m^2 K, alongside maximum entropy generation rates of 1.144 J/s and exergy destruction at 343.2 J/s. Conversely, steel displays a minimum entransy dissipation rate of 19874.925 JK/s and an entransy dissipation number of 0.4516 at these flow rates. To achieve better heat exchanger performance in terms of rate heat transfer, effectiveness, entropy generation, as well as exergy destruction, selecting high-conductivity materials for the pipes and maintaining low fluid flow rates is advisable.

Incorporating nanoparticles into traditional heat transfer fluids enhances the thermal properties and stability of the suspension was proposed by Choi and Eastman [7] in 1995. Maryam Mousavi et al. [8] experimentally investigated the effect of singular, binary hybrid and ternary hybrid nanofuids including (water / CuO, water / $CaCO_3$ and water / SiO_2) on fully developed convective heat transfer and pressure loss in circular tube. The findings indicated a notable improvement in heat transfer rate and a significant decrease in pressure drop.

Ali et al. [9] investigated the efficiency of double pipe heat exchangers using different materials. The heat exchanger harnesses heat from steam waste recovery in a refinery process. Design of the double pipe heat exchangers is carried out using CATIA and GAMBIT, while CFD analysis is performed with ANSYS Fluent. Results are derived using three different materials: copper, steel, and aluminum. Parallel and counter-current flow heat exchangers were also numerically investigated by Dhoria et al. [10]. It was utilized ANSYS FLUENT 17.1 software, alongside theoretical calculations, to assess temperature drops in relation to inlet velocity as well as inlet temperature, investigating their variations. Design and simulation encompassed both parallel flow as well as counterflow heat exchanger models. Calculated outlet temperatures for parallel and counterflow heat exchangers, based on the inlet velocity and inlet temperature of the fluid medium, were utilized to determine the total coefficient of heat transfer. Values obtained after experiments on the heat exchanger setup for parallel and counterflow heat transfer are used for theoretical calculations. In the study of Ahmed et al. [11], CFD analysis was performed on parallel, counterflow shell-and-tube heat exchangers. The research explored multiple factors, including temperature, turbulence, kinetic energy, pressure drop, velocity, and the length of the heat exchanger's length was considered, with hot water flowing through the tube side and cold water through the shell side. As the cold water traveled along the shell side, its temperature gradually increased. Conversely, the temperature of the hot water on the tube area reduced along the length of the tube. This effect was more pronounced in the

counterflow configuration compared to the parallel flow. Additionally, the velocity on the shell side exhibited greater fluctuations due to the presence of baffles. As a result, pressure loss was higher in the cold water at the shell side than in the hot water at the tube side. To assess the impact of turbulence, turbulence kinetic energy was measured. Turbulence decreased in the initial section of the shell-and-tube heat exchangers, whereas it increased in the subsequent sections. All these observations and results were evaluated and subsequently analyzed. In the same year, Rabienataj Darzi et al. [12] also investigated the hydrodynamic and thermal characteristics of double-pipe heat exchangers (DPHEs). This experimental study aimed to explore the effects of an Al_2O_3 nanofluid with an average particle diameter of 20 nm on heat transfer, pressure drop, and thermal performance in a double pipe heat exchanger. The experiments were conducted for Reynolds numbers ranging from approximately 5,000 to 20,000 and for nanoparticle concentrations up to 1 % by volume. The results indicated that adding nanoparticles within the studied ranges has significant potential to enhance the thermal performance of the heat exchanger without causing a substantial increase in pressure drop. Ebrahim Tavousi et al. [13] provided a critical analysis of the impact of various passive methods on improving heat transfer rates, fluid flow characteristics, and friction factor enhancement in double-pipe heat exchangers. These methods included the use of turbulator inserts, extended surfaces (fins), changes in tube geometry, nanofluids, and combinations of these techniques. They concluded that combining turbulator inserts with nanofluids is the most effective approach for increasing heat transfer rates. Some researchers focused on modifying geometry and inserting elements into the inner and outer tubes [14,15]. Chun et al. [16] investigated the convective heat transfer coefficient of oil/alumina nanofluids in different volume fractions in a double pipe heat exchanger under laminar regime. They reported that the reason of heat transfer enhancement of nanofluids is the concentration of nanoparticles in thermal boundary layer near walls and particles motion. Dariush Mansourya et al. [17] experimentally studied a shell & tube heat exchanger and a plate heat exchanger under turbulent flow conditions using distilled water and water / Al_2O_3 nanofluid with 0.2, 0.5, and 1 % particle volume concentrations. Their results show, the double pipe heat exchanger revealed the best outcome for the heat transfer coefficient with a maximum enhancement of 60 % while a maximum enhancement in the heat transfer coefficient of 11 % was reported for the plate heat exchanger. Utilizing a nanofluid represented the lowest penalty in the pressure drop with a maximum enhancement of 27 % for the plate heat exchanger while the highest penalty in the pressure drop with a maximum enhancement of 85 % was observed in the double pipe and shell and tube heat.

The convective heat transfer performance and the flow characteristics of water / Al_2O_3 nanofluid flowing in heat exchangers, namely parallel flow, counter flow and shell and tube heat exchangers, have been experimentally investigated under laminar flow conditions by R. Dharmalingam et al. [18]. The effect of Al_2O_3 nanoparticle and the Reynolds number on the heat transfer performance and flow behavior of the nanofluid and water have been compared. It is concluded that for R_e = 1200, the ratio of overall heat transfer coefficient of water / Al_2O_3 nanofluid with that of water is 1.161 for parallel flow, 1.146 for counter flow, 1.171 for shell and tube heat exchangers. Zarringhalam et al. [19] experimentally investigated the convection heat transfer coefficient of water / CuO nanofluid with different volume fractions of turbulent flow

through a counter flow double pipe heat exchanger. They figured out that by increasing Reynolds number and volume fraction of nanoparticles to 2 %, the convection heat transfer enhances to 57 %.

Others investigated different fin shapes, while some explored the use of various working fluids, such as nanofluids [16,20]. In their study, Bouazizi and Turki [21]. numerically investigated forced convection flows in a horizontal channel through a porous medium. The results showed that in the absence of Brownian motion, the mean Nusselt number increases as the nanoparticle volume fraction φ increases. Investigation of gas dynamics in a heat exchanger turbulator with and without a lattice structure was examined numerically by Pulin et al. [22]. It was shown that the use of turbulators not only increases the efficiency of heat exchange processes, but also their resistance.

This study focuses on modeling a double-tube heat exchanger that operates with counter-flow, in which the fluids enter from opposite ends of the exchanger, with opposite flow directions, and exit the device through opposite ends.

Mathematical formulation

Geometric analysis and equation formulation

The investigated heat exchange challenge consists of circulating two fluids through conduits, which bring them into thermal contact. The illustrative schematic of the domain investigation is shown in Fig. 1, which shows that the two fluids are brought into thermal contact through a metallic wall, which promotes heat exchange. We have hot fluid, which transfers heat to cold fluid. The two fluids exchange heat through the wall. The inner pipe diameter of 15 mm has a thickness of 2 mm while the outer pipe diameter is 32 mm. Both pipes have a length of 1000 mm. The double tube heat exchanger is made of high heat conductive copper.

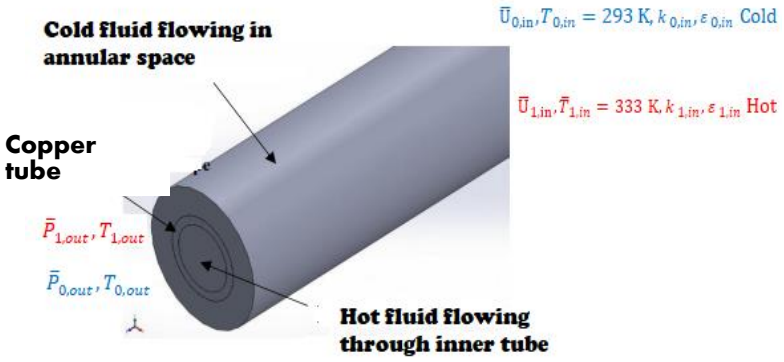

Fig. 1. Approached view of the double tube heat exchanger studied

The quantity of heat transferred depends on the exchange surface between the two fluids, but also on many other parameters, which makes a precise study of these devices quite complex [23]. Heat transfer is determined by the inlet temperature, the thermal characteristics of the fluids (including specific heat, thermal conductivity, dynamic viscosity, etc.), and the convection exchange coefficients (Table 1).

Table 1. The properties of the fluids and the material used

Fluide	Hot water at 333 K	Cold water at 293 K	Nano-fluid water / Al_2O_3 (φ = 3 %)	Copper
Density ρ, kg/m³	982.9	998.3	1086.9	8978
Specific heat C_p, JK/kg	4183	4181	3804.78	381
Thermal conductivity, W/mK	0.65	0.60	0.653	387.6
Dynamic viscosity, kgs/m	0.000472	0.00101	0.00113	-

This study assumed that the nanofluid possessed a uniform and stable composition, was incompressible, and maintained constant thermo-physical properties. The solid walls are made of copper with thermo-physical properties constants. Assuming the flow to be turbulent and steady with forced convection, the problem was analyzed in a 2D cylindrical coordinate system. Under these conditions, the modelled equations are presented in vector format as shown below:

1. conservation of mass $\frac{\partial \overline{U}_i}{\partial x_i} = 0,$ (1)

2. conservation of momentum $\overline{U}_j \frac{\partial \overline{U}_j}{\partial x_i} = -\frac{1}{\rho_{\mathrm{nf}}} \frac{\partial \overline{P'}}{\partial x_i} + \frac{\partial}{\partial x_j}\left(\left(\nu_{nf} + \nu_t\right)\frac{\partial \overline{U}_j}{\partial x_i}\right),$ (2)

where $\overline{P'} = \overline{P} - \frac{2}{3}\rho_{\mathrm{nf}} \cdot k,$

3. conservation of energy $\overline{U}_J \frac{\partial \overline{T}}{\partial x_j} = \frac{\partial}{\partial x_j}\left(\left(\frac{\nu_{nf}}{Pr_{nf}} + \frac{\nu_t}{Pr_t}\right)\frac{\partial \overline{T}}{\partial x_j}\right).$ (3)

Given that the nanofluid was considered a single-phase homogeneous fluid, the $k-\varepsilon$ turbulent model developed by [24] was used to define the turbulent viscosity, $\mu_t = \left(\rho C_\mu k^2\right)/\varepsilon$, through both additional equations for turbulent kinetic energy (k) and its dissipation rate (ε). These equations are formulated as follows:

$$\overline{U}_J \frac{\partial k}{\partial x_j} = \nu_t \left(\frac{\partial \overline{U_i}}{\partial x_j} + \frac{\partial \overline{U_J}}{\partial x_i}\right)\frac{\partial \overline{U_i}}{\partial x_j} + \frac{\partial}{\partial x_j}\left(\left(\nu_{nf} + \frac{\nu_t}{Pr_k}\right)\frac{\partial \kappa}{\partial x_j}\right) - \varepsilon, \quad (4)$$

$$\overline{U}_J \frac{\partial \varepsilon}{\partial x_j} = \nu_t C_{\varepsilon 1} \frac{\varepsilon}{k}\left(\frac{\partial \overline{U_i}}{\partial x_j} + \frac{\partial \overline{U_J}}{\partial x_i}\right)\frac{\partial \overline{U_i}}{\partial x_j} + \frac{\partial}{\partial x_j}\left(\left(\nu_{nf} + \frac{\nu_t}{Pr_\varepsilon}\right)\frac{\partial \varepsilon}{\partial x_j}\right) - C_{\varepsilon 2}\frac{\varepsilon^2}{k}. \quad (5)$$

The various empirical constants of the model are as follows [24]:

$$C_\mu = 0.09,\ C_{\varepsilon 1} = 1.44,\ C_{\varepsilon 2} = 1.92,\ Pr_k = 1.0,\ Pr_\varepsilon = 1.3,\ \mu_{\mathrm{eff}} = \mu_{\mathrm{nf}} + \mu_{\mathrm{t}}. \quad (6)$$

Boundary conditions

This study involves a temperature labeled $T_{1,in} = 333$ K and a velocity which varies according to the Reynolds number were imposed at the inlet of the inside tube where

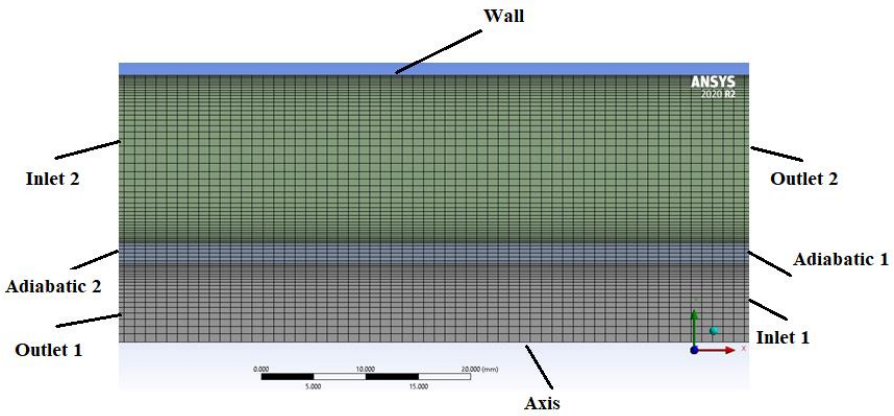

Fig. 2. The heat exchanger mesh and the naming of the boundaries

the hot fluid circulates while at the inlet of the outside tube, the cold fluid enters at a temperature of $T_{0,in} = 293$ K and a velocity which varies according to the Reynolds number. The mesh and the boundaries of the heat exchanger are illustrated in Fig. 2.

The other boundary conditions are as follows: $k = k_{in}$, $k_{in} = \frac{3}{2}(\overline{\mathrm{U}}_{\mathrm{in}}\mathrm{I})^2$, $\varepsilon = \varepsilon_{in}$, $\varepsilon_{in} = C_\mu^{3/4}\frac{k^{3/2}}{\mathrm{L}}$, $L = D_h$ and the turbulent intensity is $I = \frac{u'}{\bar{U}_{mean}} \cdot 100\% =$ $= 0.16\left(R_{e_{D_h}}\right)^{-1/8}$, where $\bar{P}_{out,h}$ is the hot fluid outlet, $\bar{P}_{out,c}$ is the cold fluid outlet, and the exterior wall is adiabatic. Interior and exterior walls of the copper tube (fluid-solid interfaces). Right side wall (adiabatic 1) and left side wall of the copper tube (adiabatic 2) are adiabatic.

Nanofluid properties models

The density [25], specific heat [26], thermal conductivity [27], and dynamic viscosity of the nanofluid [28] were calculated using the thermo-physical properties of water and nanoparticles measured on the inlet temperature $\bar{T}$ = 293 K.

In the formulas that follow, the indices (*p*, *f*, and *nf*) correspond to particles, base fluid, and nanofluid, respectively.

Density is:

$$\rho_{nf} = (1-\varphi)\rho_f + \varphi\rho_s. \tag{7}$$

Specific heat is:

$$\left(\rho C_p\right)_{nf} = (1-\varphi)\left(\rho C_p\right)_f + \varphi\left(\rho C_p\right)_s. \tag{8}$$

Thermal conductivity is:

$$\frac{K_{nf}}{K_f} = \frac{K_s+(n-1)K_f-(n-1)(K_f-K_s)\varphi}{K_s+(n-1)K_f+(K_f-K_s)\varphi}. \tag{9}$$

The empirical shape factor φ is expressed as 3Ψ, where Ψ denotes the sphericity, $n = 1$ for spherical nanoparticles, $n = 6$ for cylindrical nanoparticles.

Dynamic viscosity is:

$$\mu_{nf} = \mu_f\,(123\varphi^2 + 7.3\varphi + 1). \tag{10}$$

Principal factors of the problem

This issue of forced convection heat transfer of a nanofluid in fully developed flow can be described by a range of parameters that impact heat transfer and fluid movement within the double-tube counter-current flow heat exchanger, specifically: Prandtl number is $P_{r_{nf}} = \mu_{nf}.C_{p_{nf}}/k_{nf} = \nu_{nf}/\alpha_{nf}$, Reynolds number is $\mathrm{Re} = \frac{\rho_{nf}\,\bar{V}\,D_h}{\mu_{nf}}$, which ranges from 10000 to 50000; the nanoparticle volume fraction within the nanofluid was maintained at 30 %, while the hydraulic diameter was determined using the following formula: $D_h = \frac{4A}{P}$.

Heat transfer is quantified by the Nusselt number, which is calculated using the following formula:

$$Nu = \frac{hD_h}{K_{nf}}. \tag{11}$$

For forced convective heat transfer (in case of plane flow) $N_u = 0.66 \cdot pr^{\frac{1}{3}} \cdot Re^{\frac{1}{2}}$, $R_e < R_{ec}$ in laminar flow and $Nu = 0.036 \cdot pr^{\frac{1}{3}} \cdot Re^{\frac{4}{5}}$, $R_e > R_{ec}$ in turbulent flow.

The Nusselt number average $\overline{Nu} = \frac{\bar{h}.D_h}{k_{nf}}$ and the mean heat transfer coefficient $\bar{h} = k_{nf} \times \overline{Nu}/D_h$ are an indicator of the effectiveness of heat transfer between the two fluids.

The friction coefficient utilized is based on the formulation introduced by Haaland [29], which provides an explicit approximation of the Colebrook-White equation:

$$\frac{1}{\sqrt{f}} = -1.8 \log\left[\left(\frac{\frac{\epsilon}{D_h}}{3.7}\right)^{1.11} + \frac{6.9}{R_e}\right]. \quad (12)$$

The formula for the pressure loss is as follows:

$$\Delta\bar{P} = f \frac{L}{D_h} \frac{\rho_{nf} U^2}{2}. \quad (13)$$

The heat transfer rate (Q) in a double tube heat exchanger can be calculated by following formula [30]:

$$Q = U\, A\, LMTD = \dot{m} C_p \Delta\bar{T}, \quad (14)$$

where $\Delta\bar{T} = \bar{T}_{out} - \bar{T}_{in}$ indicates the variation in temperature of the fluid between the inlet and outlet.

The goal of this numerical study is to evaluate the impact of the Reynolds number and the chosen heat transfer fluid on the flow dynamics and heat transfer within a double-tube exchanger used to cool hot water to 333 K. Two fluids were used: water and the nanofluid water / Al_2O_3. The numerical results obtained using Ansys Fluent software 2020 R2 were graphically represented and discussed. The plotted graphs show the temperature fields, the pressure fields as well as the friction factor, the total exchange coefficient, the rate of heat transfer and the mean Nusselt number following the streamlines of the exchanger for a Reynolds number of 20000, of both cases cold water and nanofluid.

Simulation method

This numerical study utilizes the finite volume method S. Patankar [31] to solve the equations embedded in the commercial code Ansys Fluent software 2020 R2. The methods used are: The pressure field is determined using SIMPLE (Semi-Implicit Method for Pressure-Linked Equations), while the convection term in the governing equations is approximated with an upstream second-order scheme. The resulting systems of algebraic equations are solved using a line-by-line procedure alongside the Gauss-Seidel iterative technique convergence of the solution is achieved as the normed residual of every algebraic equation falls below 10^{-4} for the continuity equations and momentum, yet below 10^{-6} for the energy equation.

Results and commentary

Code validation

The computational code was validated by contrasting the computed pressure drop results against the analytical ones (see Fig. 3 and 4). The analytical values of the pressure drop were obtained from Eq. (12) for heat transfer in turbulent forced convection involving hot and cold water. The present numerical predictions closely match the analytical values, with differences so negligible that the results appear virtually the same.

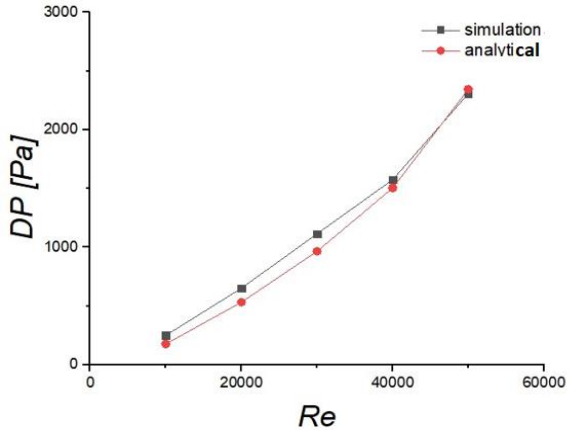

Fig. 3. Comparison of pressure loss between simulated and analytical results of the hot fluid as function of Reynolds number

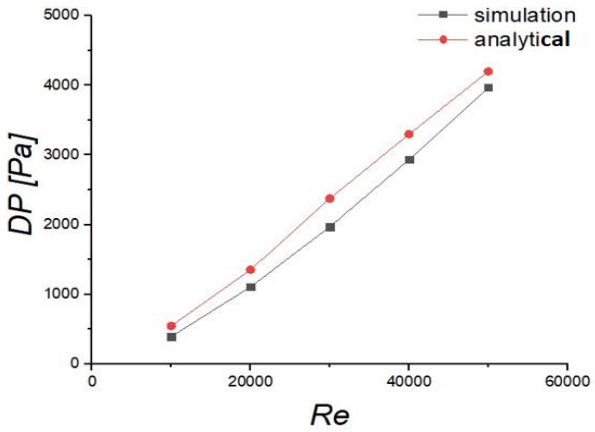

Fig. 4. Comparison of pressure loss between simulated and analytical results of the cold fluid as function of Reynolds number

Thermal field

Figures 5 and 6 present the temperature contours in an r-z plane along the exchanger. It is observed that, in the case where cold water is present in the outer tube, the thermal distribution within the inner tube reveals that the hot water has a high temperature, thus indicating a transfer of heat from the inside towards the outside. The temperature gradually decreases along the inner tube due to heat exchange with the cold water in the outer tube whose temperature gradually increases along the tube. When the nanofluid flows into the outside tube, the temperature decreases faster along the heated tube, and the temperature of the nanofluid gradually increases along the tube. This enhancement

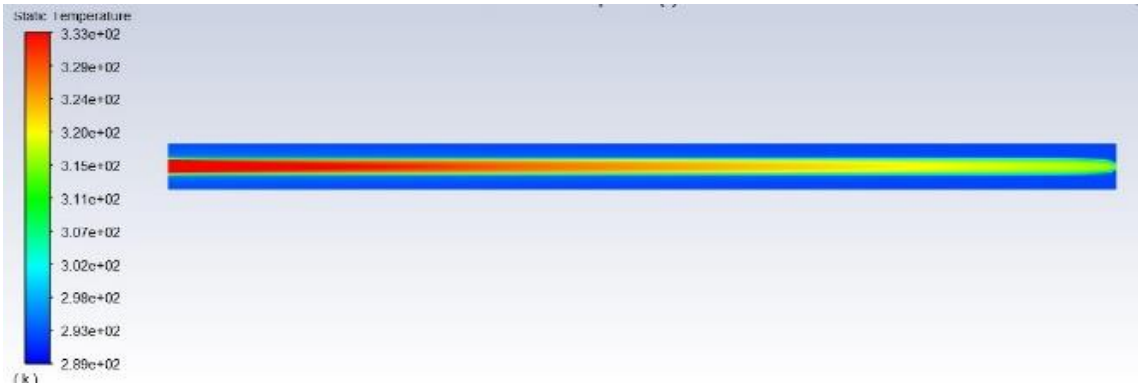

Fig. 5. Temperature contours in a r-z plane, for Reynolds number of 20000 when using cold water

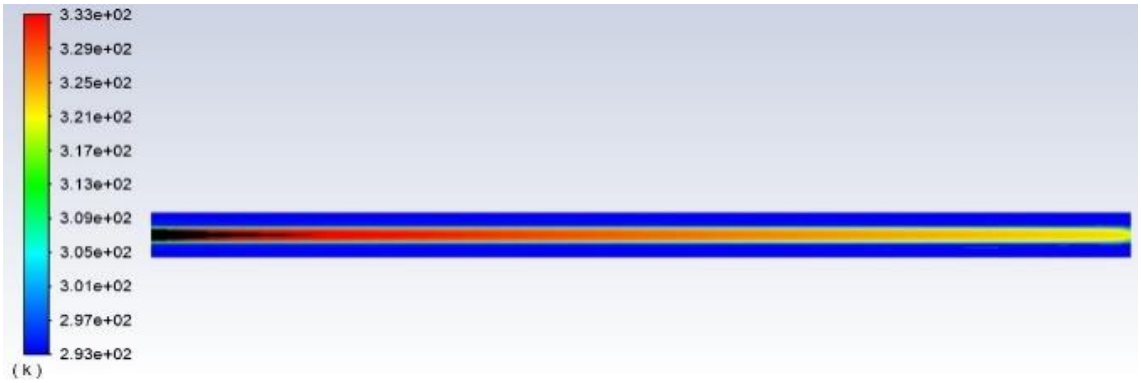

Fig. 6. Temperature contours in a r-z plane, for Reynolds number of 20000 when using nanofluid

is more evident than with cold water, attributable to the nanofluid's excellent thermal conductivity. Differences in heat performance between the two cases can also be observed through the distribution and variation of temperatures along the heat exchanger.

Figure 7 shows the variation in the temperature of the hot water at the exit of the inner tube. When cold water is utilized in the outer tube, the hot water temperature is expected to be higher at the end of the inner tube due to the low overall exchange coefficient. In contrast, when the nanofluid is used in the outer tube, the high thermal conductivity can improve the heat exchange efficiency by increasing the *U* value, resulting in more efficient cooling of the hot water at the outlet of the internal tube.

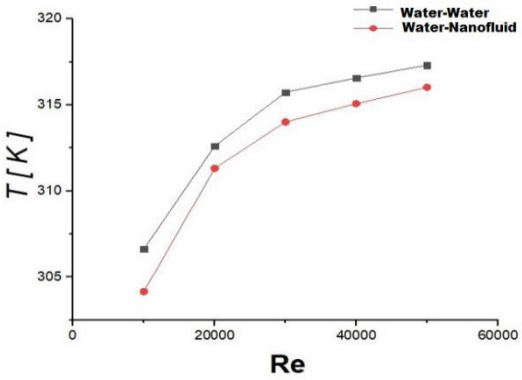

Fig. 7. Temperature variation of the hot water at the outlet of the inner tube with respect to the Reynolds number in both cases

However, a decrease in the cooling rate of hot water can occur with increasing Reynolds number, due to increased flow rates of the fluid passing through the exchanger. This conclusion can be drawn using the formula for the quantity of heat exchanged, which is: $\mathrm{Q} = \mathrm{U\ A\ LMTD} = \dot{m}\ C_p\ \Delta\bar{T}$. Thus, we can see from Fig. 7 that $\Delta\bar{T}_{Re=10000} > \Delta\bar{T}_{Re=20000} > \Delta\bar{T}_{Re=30000} > \Delta\bar{T}_{Re=40000} > \Delta\bar{T}_{Re=50000}$.

Flow field

Figures 8 and 9 reflect the changes in the flow of dynamics along the heat exchanger. It can be noticed from these figures that, in the case where cold water is present in the outer tube, the contour of the stream function shows a lower maximum value than in

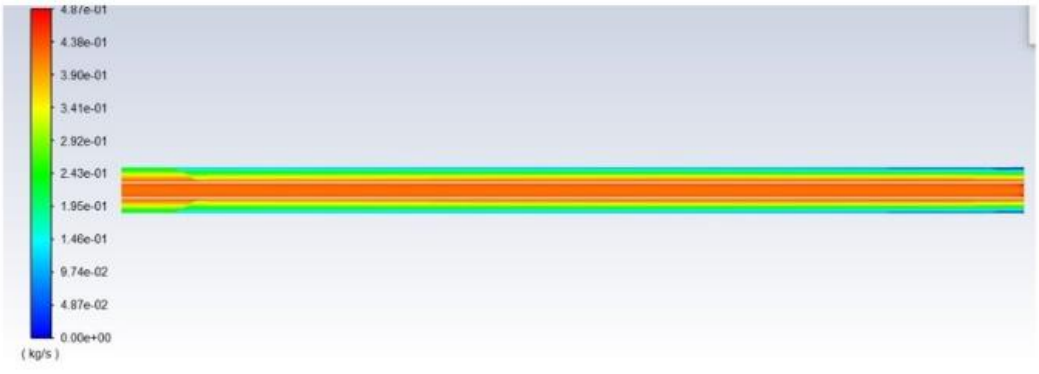

Fig. 8. Contours of the stream function ψ (kg/s) in an r-z plane along the exchanger for Reynolds number of 20000, for the water-water exchanger

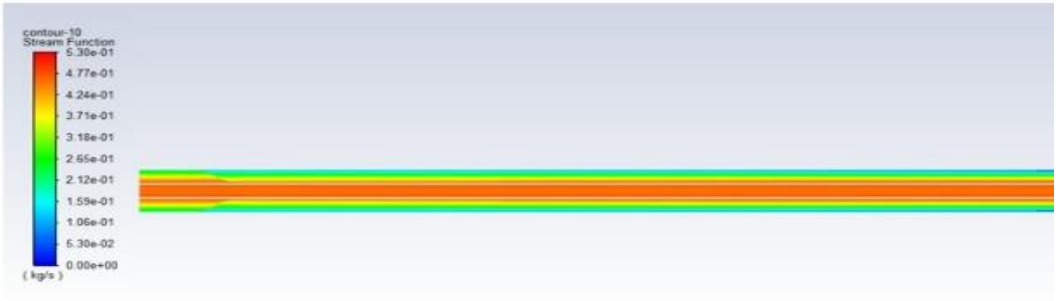

Fig. 9. Contours of the stream function ψ (kg/s) in an r-z plane along the exchanger for Reynolds number of 20000, for the nanofluid-water exchanger

the case of the nanofluid. This is because of the nanofluid's density which is higher than that of water. Indeed, the value of the stream function is given by the formula:

$$\psi = \psi_0 + \rho \int_{y_p}^{y=0} Urdr \text{ with } \psi_0 = 0 \quad (15)$$

These figures also indicate that the velocity profile changes along the inner tube from a uniform profile at the inlet ($\overline{U} = \overline{U}_{1,in}, \overline{V} = 0$) towards a profile developed at a distance $\mathrm{Z} = 4.4.\,\mathrm{Re}^{1/6} = 22.92,\ \mathrm{D} = 344\ \mathrm{mm}$ from the entrance. Beyond this value the profile remains constant $\left(\frac{\partial \overline{U}}{\partial z} = \frac{\partial \overline{V}}{\partial z} = 0\right)$. However, the velocity profile along the outer annular pipe changes from a uniform profile at the inlet ($\overline{U} = \overline{U}_{0,in},\ \overline{V} = 0$) but does not reach the developed state.

Pressure fields reach

Figure 10 presents the pressure contours for the case where cold-water flows in the outer tube. The results show a maximum pressure drop ($\Delta\overline{P}$) of 5.34 Pa across the two tubes. In contrast, Fig. 11 illustrates the case of nanofluid circulating in the outer tube, where the maximum pressure drops ($\Delta\overline{P}$) reaches 454 Pa. This indicates that the pressure loss due in the case of the nanofluid, the heat exchanger shows increased performance which implies greater pumping power when used as a cooling fluid. The cause of this difference is the high viscosity of the nanofluid, which leads to: $\tau_{p\ \text{nanofluid}} = 8.356 > \tau_{p\ \text{cold water}} = 5.92$.

Fig. 10. Pressure contours in an r-z plane along the exchanger for a Reynolds number of 20000 for the water-water exchanger

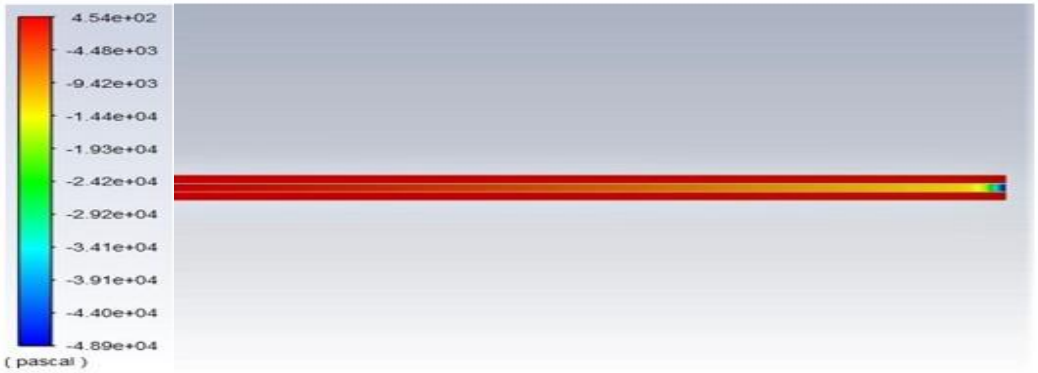

Fig. 11. Pressure contours in an r-z plane along the exchanger for a Reynolds number of 20000, for the nanofluid-water exchanger

Overall heat exchange coefficient

Figure 12 illustrates the change in the total heat transfer coefficient (*U*) along the tube. When using the nano fluid within the outer tube, an increase in the coefficient of total heat transfer is measured over the entire Reynolds number range compared with cold water. This indicates increased efficiency in heat transfer through the heat exchanger when using the nano fluid.

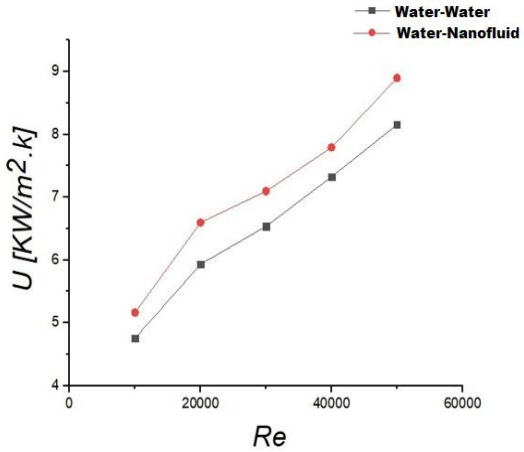

Fig. 12. Variation t of the total heat transfer coefficient *U* throughout the tube *U* as a function of the Reynolds number in both cases

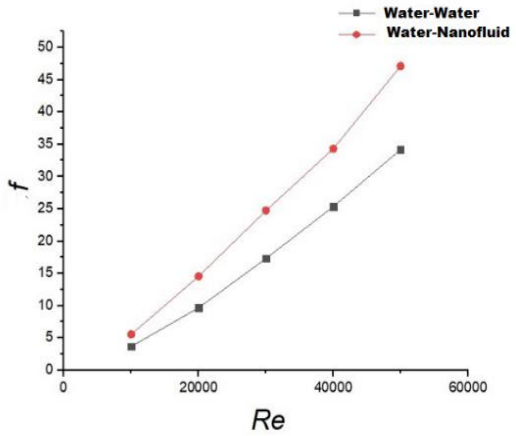

Fig. 13. Variation of the friction coefficient (*f*) with respect to the Reynolds number in both cases

Friction coefficient

Figure 13 presents the change in the friction coefficient ƒ throughout the tube. A rise in the friction coefficient is noted when utilizing the nanofluid compared to cold water for the entire Reynolds number range. This increase can be linked to the increased value of the viscosity of the nanofluid in comparison with that of water. Indeed, high viscosity results in greater resistance τ to the flow.

Rate of heat transfer

The curves in Fig. 14 indicate an improvement in the heat transfer rate when employing a nanofluid compared to cold water for the entire range of Reynolds numbers. This is due to the increase in coefficient of convective exchange as a function a Reynolds number. Raising the number of Reynolds signifies higher velocities close to the fluid-copper wall interfaces, which promotes convective heat transfer across these interfaces.

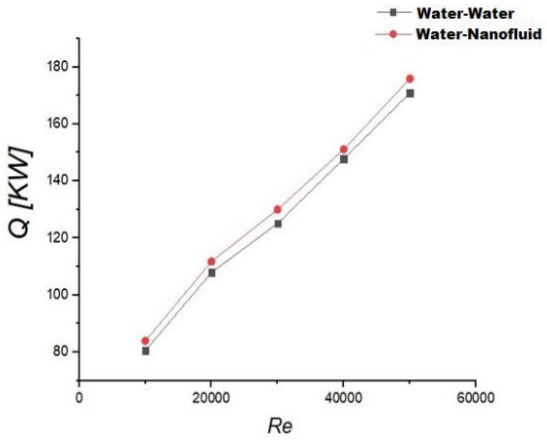

Fig. 14. Variation of the heat transfer rate Q in relation to the Reynolds number in both cases

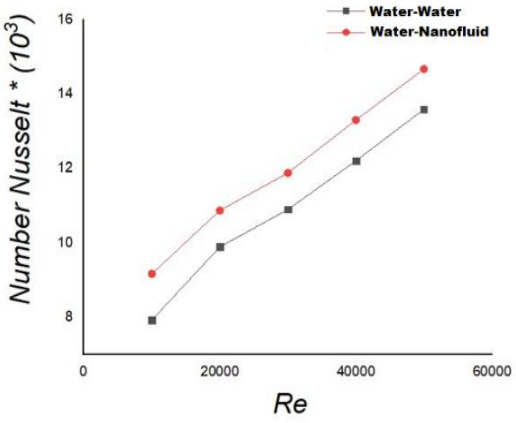

Fig. 15. Variation of the Nusselt number as a function of the Reynolds number in both cases

Nusselt number

Figure 15 illustrates the change in the Nusselt number Nu at the hot fluid-copper wall interface. When using the nano fluid in the outer tube an increase in the Nusselt number across the scale of Reynolds numbers is observed compared to cold water. One can also note from Fig. 15 that the difference between the Nusselt numbers for the water-water and the water-nanofluid exchangers remains constant as the Reynolds number rises.

Conclusions

The numerical investigation of flow and heat transfer in a double-tube heat exchanger was carried out considering the impact of the Reynolds number and the fluid type on temperature of the hot water, on the total convective exchange coefficient, on the friction coefficient, on the rate of heat transfer and its Nusselt number. The ANSYS-Fluent 2020.R2 calculation code was employed to solve the transport equations.

The aim of this study is to compare the nano fluid and cold water in terms of performance which is measured by the performance of the heat exchanger and the pressure drop within it.

Key findings from this study are summarized as follows:

1. An increase in Reynolds' number produces a significantly higher transfer rate.
2. The best improvement in the performance of the heat exchanger was obtained by using the nanofluid.
3. The friction coefficient is greater for the nanofluid

CRediT authorship contribution statement

Rabah Nebatti: writing – review & editing, writing – original draft, conceptualization, investigation, supervision, data curation; **Mahfoud Kadja**: writing – review & editing, writing – original draft, conceptualization, supervision; **Farid Mechighel**: writing – review & editing, investigation.

Conflict of interest

The authors declare that they have no conflict of interest.

References

1. Bergman TL, Lavine AS, Incropera FP, DeWitt DP. *Fundamentals of Heat and Mass Transfer.* New York: John Wiley & Sons; 1996.
2. Cengel YA, Boles MA. *Thermodynamics: An Engineering Approach.* New York: McGraw-Hill; 2002.
3. Shah RK, Sekulić DP. *Fundamentals of Heat Exchanger Design.* Hoboken (NJ): John Wiley & Sons; 2003.
4. Kakaç S, Liu H, Pramuanjaroenkij A. *Heat Exchangers: Selection, Rating, and Thermal Design.* Boca Raton (FL): CRC Press; 2002.
5. Bejan A. *Advanced Engineering Thermodynamics.* Hoboken (NJ): John Wiley & Sons; 2016.
6. Pathak R, Geete A. Thermal performance analyses of concentric pipe counter flow heat exchanger at different operating conditions by CFD. *i-Manager's Journal on Mechanical Engineering.* 2019;9(1): 1–12.
7. Choi SUS. Enhancing thermal conductivity of fluids with nanoparticles. In: *1995 ASME International Mechanical Engineering Congress and Exposition: Proceedings of the ASME Materials Division, 12–17 November 1995, San Francisco, California.* New York: American Society of Mechanical Engineers; 1995. p.95–105.
8. Mousavi M, Darvishi P, Pouranfard A. Comparative study of heat transfer and pressure drop in turbulent flow of a singular and hybrid nanofluids into a horizontal pipe. *Journal of Thermal Analysis and Calorimetry.* 2023;148:14375–14384.
9. Ali S, Krishna K, Reddy S, Ali S. Thermal analysis of double pipe heat exchanger by changing the materials using CFD. *International Journal of Engineering Trends and Technology.* 2015;26(2): 95–102.
10. Dhoria SH, Kumar EM, Yeswanth IVS, Jayanti L. CFD analysis on concentric tube heat exchanger in parallel and counter flow direction. *International Journal of Engineering Research and Applications.* 2018;8(6): 20–25.
11. Ahmed F, Sumon MM, Fuad M, Gugulothu R, Mollah AS. Numerical simulation of heat exchanger for analyzing the performance of parallel and counter flow. *WSEAS Transactions on Heat and Mass Transfer.* 2021;16: 145–152.
12. Darzi AAR, Farhadi M, Sedighi K. Heat transfer and flow characteristics of Al_2O_3–water nanofluid in a double tube heat exchanger. *International Communications in Heat and Mass Transfer.* 2013;47: 105–112.
13. Tavousi E, Perera N, Flynn D, Hasan R. Heat transfer and fluid flow characteristics of the passive method in double tube heat exchangers: a critical review. *International Journal of Thermofluids.* 2023;17: 100282.
14. Naphon P. Heat transfer and pressure drop in the horizontal double pipes with and without twisted tape insert. *International Communications in Heat and Mass Transfer.* 2006;33(2): 166–175.
15. Córcoles JI, Moya-Rico JD, Molina A, Almendros-Ibáñez JA. Numerical and experimental study of the heat transfer process in a double pipe heat exchanger with inner corrugated tubes. *International Journal of Thermal Sciences.* 2020;158: 106526.
16. Chun B-H, Kang H-U, Kim S-H. Effect of alumina nanoparticles in the fluid on heat transfer in double-pipe heat exchanger system. *Korean Journal of Chemical Engineering.* 2008;25: 966–971.
17. Mansoury D, Ilami Doshmanziari F, Kiani A, Chamkha AJ, Sharifpur M. Heat transfer and flow characteristics of Al_2O_3/water nanofluid in various heat exchangers: experiments on counter flow. *Heat Transfer Engineering.* 2020;41(3): 220–234.
18. Dharmalingam R, Sivagnanaprabhu KK, Yogaraja J, Gunasekaran S, Mohan R. Experimental investigation of heat transfer characteristics of nanofluid using parallel flow, counter flow and shell and tube heat exchanger. *Archive of Mechanical Engineering.* 2015;62(4): 509–522.
19. Zarringhalam M, Karimipour A, Toghraie D. Experimental study of the effect of solid volume fraction and Reynolds number on heat transfer coefficient and pressure drop of CuO–water nanofluid. *Experimental Thermal and Fluid Science.* 2016;76: 342–351.

20. Braga CVM, Saboya FEM. Turbulent heat transfer, pressure drop and fin efficiency in annular regions with continuous longitudinal rectangular fins. *Experimental Thermal and Fluid Science.* 1999;20(2): 55–65.
21. Bouazizi L, Turki S. Combined effects of viscous dissipation and Brownian motion on temperature distribution and heat transfer of Al_2O_3/water nanofluid flow through a porous medium. *Materials Physics and Mechanics.* 2021;47(6): 921–936.
22. Pulin AG, Laptev MA, Alisov KA, Barskov VV, Rassokhin VA, Gong B, Kotov VS, Roshchenko GA, Balakin AM, Golubtsov M, Nurkov IR, Basati Panah M. Heat exchanger and the influence of lattice structures on its strength. *Materials Physics and Mechanics.* 2024;52(6): 61–80.
23. Taourit F. Étude du comportement dynamique et thermique de deux écoulements du fluide dans un échangeur de chaleur (comparaison entre le cas simple et le cas avec ailettes). *Université Abou Bekr Belkaïd Tlemcen.* Tlemcen (Algeria): Mémoire de master (option génie énergétique); 2013.
24. Launder BE, Spalding DB. The numerical computation of turbulent flows. *Computer Methods in Applied Mechanics and Engineering.* 1974;3(2): 269–289.
25. Pak BC, Cho YI. Hydrodynamic and heat transfer study of dispersed fluids with submicron metallic oxide particles. *Experimental Heat Transfer.* 1998;11(2): 151–170.
26. Xuan Y, Roetzel W. Conceptions for heat transfer correlation of nanofluids. *International Journal of Heat and Mass Transfer.* 2000;43(19): 3701–3707.
27. Hamilton RL, Crosser OK. Thermal conductivity of heterogeneous two-component systems. *Industrial & Engineering Chemistry Fundamentals.* 1962;1(3): 187–191.
28. Maiga SEB, Palm SJ, Nguyen CT, Roy G, Galanis N. Heat transfer enhancement by using nanofluids in forced convection flows. *International Journal of Heat and Fluid Flow.* 2005;26(4): 530–546.
29. Haaland SE. Simple and explicit formulas for the friction factor in turbulent pipe flow. *Journal of Fluids Engineering.* 1983;105(1): 89–90.
30. Kakaç S, Liu H, Pramuanjaroenkij A. *Heat Exchangers: Selection, Rating, and Thermal Design.* 3rd ed. Boca Raton (FL): CRC Press; 2012.
31. Patankar SV. *Numerical Heat Transfer and Fluid Flow.* New York: McGraw-Hill; 1980.

MATERIALS PHYSICS AND MECHANICS RESEARCH ARTICLE

Submitted: September 15, 2024 **Revised: March 12, 2025** **Accepted: April 17, 2025**

Structural health monitoring of two storey steel frame using accelerometer sensor: a numerical and experimental study

K. Mohit ✉, **S.K. Singh**, **A. Mishra**

Institute of Engineering and Technology Lucknow, Lucknow, India

✉ ce22mohit@gmail.com

ABSTRACT

External forces generated due to earthquakes, wind, and blasts cause damage to the structure by which its structural integrity gets compromised. A method is to be developed to find the current state of the structure after the damage has occurred. This can be done by finding the natural frequency of the structure using modal analysis. In this study, a two-storey steel frame bolted structure has been studied experimentally on a one-dimensional shake table. Results obtained through the experiment have been verified using the numerical study of the same structure. COMSOL Multiphysics was used for additional numerical analysis, and the various eigenfrequencies and mode shapes were identified. Additionally, numerical research was carried out to simulate damages ranging from 10 mm to 20 mm, and the findings indicate that the natural frequencies decrease as the damage increases. Thus, Modal analysis can be used to determine the current state of the structure. For various mode shapes, the experimental and numerical frequency variations are 0.37, 1.61, and 3.16 %, respectively.

KEYWORDS

experimental modal analysis • COMSOL Multiphysics • shake table • accelerometer • damage study numerical study

Citation: Mohit K, Singh SK, Mishra A. Structural health monitoring of two storey steel frame using accelerometer sensor: a numerical and experimental study. *Materials Physics and Mechanics.* 2026;54(2): 181–196.
http://dx.doi.org/10.18149/MPM.5422026_13

Introduction

The condition of the civil infrastructure has been carefully monitored through the implementation of the structural health monitoring (SHM) system [1,2]. Different methods of SHM have been developed to detect damage in various kinds of steel structures [3–7]. An intelligent method was created to detect structural damage, such as cracking in steel gusset plate joints. It is argued that bolt joint loosening and cracking are two of the most common types of damage in bolted steel frames [8]. For steel frames, connection stiffness is important because it affects the structure's overall integrity and dynamic responsiveness. The impact of bolt loosening on the mechanical behaviour of steel frames has been examined in numerous studies. A reduced-order numerical modal for damage diagnosis upon loss of the frame connecting bolt was suggested in [9]. In [10], a technique is provided based on variations in the intrinsic frequencies of the structure to identify defects, such as the loosening of bolted connections, in space frame construction with L-shaped beams. Based on piezoelectric impedance frequency shifting, a bolt looseness detection system was created by Shao et al. [11]. Consequences of joint damage in steel frame structures under seismic excitations were investigated in [12]. In [13], it was developed a model that detects changes in modal parameters and compares them to a reference state, giving a way to anticipate structural defects in steel frames.

Publisher: Peter the Great St. Petersburg Polytechnic University

System identification principles were the foundation for early operational and experimental modal analysis research. Numerous studies have been done on system identification [14–20]. Assessing how vibrations affect structures and how they behave has rapidly grown in recent years, both domestically and internationally. Since many historically significant buildings are situated in seismically active zones, more research is being carried out on how buildings react to vibrations, particularly after earthquakes. Currently, researchers utilize soft computing techniques such as genetic algorithms [20], artificial neural networks (ANN) [21–23], fuzzy logic [24], etc., for this purpose. Many older buildings have experienced significant damage due to design flaws, construction errors, natural disasters, and excessive loads. Given our country's active seismic zones and large population, evaluating such damage is crucial. Structures are continually exposed to vibrations from wind, earthquakes, waves, explosions, and vehicular traffic, which can result in cracks or severe damage. Understanding how a structure behaves under these conditions is essential for its longevity and often requires experimental studies, as numerical models may not entirely capture real-world behaviour. Structural design generally starts with developing Numerical models for static and dynamic analyses under various loads. However, these modals often do not accurately represent actual building behaviour. With advanced technologies, it is now possible to create safer structures and also continuously monitor them. To accurately determine dynamic parameters, it is essential to correctly define the structure's parameters.

Many studies have found discrepancies between the dynamic parameters derived from operational modal analysis and the steel frame structure finite element model. The permissible range for these variances is usually between 2 to 5 %. The range greater than this is due to finite element model flaws. Errors in the finite element model usually stem from incorrect material properties, dimensional measurement inaccuracies, etc. Measurement errors can be due to issues such as improper placement of accelerometers and other environmental effects, such as noise. In this study, special care was taken to avoid errors in both the operational modal analysis measurement and the finite element model, which were positively reflected in the outcomes. To bridge this gap, comparing dynamic parameters offers a practical solution [25]. Many structures in earthquake-prone regions endure various forms of damage from seismic loads, especially column damage during earthquakes. Strengthening columns without increasing the overall structure's mass is essential for improving building performance during seismic events. This requires examining technical repair and strengthening methods concerning column capacity. Ongoing research aims to optimize structural performance under seismic loads from different angles. In civil engineering, reinforced cement concrete, engineered wood, structural steel, and fiber-reinforced plastic are examples of materials used in framing, determining how structures behave when they vibrate, and impacting their longevity. It is possible to accurately evaluate a structure's behavior under vibration through numerical and experimental research. Operational modal analysis is frequently used to assess the vibration of existing structures. It also serves to confirm the assumptions made during the construction of the finite element model, update the initial numerical model of existing structures based on experimental data, and identify those dynamic properties of structures. In cases where numerical model is not possible, the structural health monitoring process is used to monitor the structures [26–30].

Numerical and experimental modal analysis for the dynamic properties of the structure work was carried out for this aim, and a 3D finite element Model of the building was produced based on the design drawings. Using ground-level recorded microtremor ambient vibration data, ambient excitation was produced. For output-only Modal identification, enhanced frequency domain decomposition was used. The structure is first represented by numerical Modal, which are then subjected to static and dynamic study under various loading scenarios. Nonetheless, the majority of the time, the numerical Model falls short of accurately describing the building's actual behaviour. Differentiations in building behaviour can be effectively identified and addressed by comparing dynamic metrics. Due to seismic loads, the majority of structures in earthquake-prone areas sustained various types of damage. Particularly affecting parts of the building, such as the columns. Considering the performance of buildings during seismic events, it is essential to strengthen the columns without increasing the overall building mass. This necessity highlights the importance of investigating the relationship between technical repair or strengthening methods and column capacity. Condition assessment can be accomplished by evaluating the dynamic and static characteristics of the structure, such as its inherent frequency [31,32] and degrees of stiffness [33,34] or flexibility [35]. Nevertheless, these kinds of techniques usually require computational measurement of the transfer function or experimental modal analysis. Therefore, online damage detection is unsuitable for in-service structures, requiring manual processes or equipment to obtain experimental measurements. Global-based damage detection involves numerical methods that use the overall vibration characteristics of a structure, such as mode shapes and natural frequencies, to identify damage. This approach was initially developed with the advent of structural monitoring systems capable of collecting response time histories from the structure. However, due to the high cost of structural monitoring systems, most installations involve a low number of sensors, typically only 10–20 per structure. This limited sensor density is often inadequate for capturing localized damage behaviour, and implementing globe-based damage detection is challenging. This problem is particularly severe for structures subjected to various operational and environmental pressures, such as civil structures (bridges, buildings, dams), where it becomes even more difficult to detect deterioration using global vibration characteristics.

Modal parameter extractions

The basic frequency domain (BFD) methodology, commonly called the Peak-Picking technique, is expanded upon by the frequency domain decomposition (FDD) method. This method is based on the idea that, under the assumption of white noise input and a lightly damped structure, modes can be predicted from the computed spectral densities. As a non-parametric method, FDD directly derives modal parameters through signal processing. It estimates modes by applying singular value decomposition (SVD) to every measurement data collection. For any single value, this decomposition enables a Single Degree of Freedom (SDOF) identification of the measured system [36]. The FDD approach is expanded upon by the enhanced frequency domain decomposition (EFDD) technique. EFDD is a simple, easy-to-use method that locates the modes in singular value decomposition (SVD) plots created from the responses' spectral density Spectra, making

mode identification easier. EFDD offers better accuracy in predicting natural frequencies and can manage situations with modal damping, in contrast to FDD, which depends on a single frequency line from fast Fourier transform (FFT) analysis and does not account for modal damping.

Conversely, the EFDD provides a more sophisticated approximation of the natural frequencies, mode shape, and damping ratio [37]. The inverse discrete Fourier transform (IDFT) is used in that EFDD approach to return the single degree of freedom (SDOF), power spectral density (PSD) functions, which are located close to a resonance peak, to the time domain [38]. The function of time is used to count zero crossings to calculate the eigen frequency.

The study presented in this paper shows the experimental and numerical modal analysis of the two-storey steel frame structure. The results obtained from the analysis were verified numerically. After that, a damage study was done on the structure to detect the pattern in the structure's natural frequencies as the damage increased.

Materials and Methods

Description of steel frame structure and shake table

The steel frame structure height is 1.1 m. As shown in Fig. 1, a 3D steel frame was built in the laboratory. The height of each floor is 550mm, and the plan of the frame structure is 530 × 550 mm^2. The steel angle structure profile was selected for the columns and beams of the steel frame shown in Table 1, while the Indian Standard Angle (ISA) 24.4 × 24.4 × 2 mm^3 profile was used for the joints. M6 bolts are used in all the column-beam joints. E250 grade steel was chosen as the material, with nonlinear material properties represented in Table 2. The frame is connected to the Shake Table, with each beam secured by five M10 bolts and a 2 mm-thick angle.

Uniaxial bench-scale shake table used for the analysis of the steel frame structures shown in Fig. 2. Time history data acquired through the data acquisition system (DAQ) is used to extract accelerometer data from the shake table. It works well for a wide range of civil engineering Modal and structural experiments. Table 3 gives the specifications for the shake table.

Fig. 1. Two storey steel moment frame

Fig. 2. Shake table

Table 1. Physical property of the steel frame structure

Physical properties	Parameter	Values, mm
Front beam dimension	Length	530
	Width	24.4
	Thickness	2.0
Side beam dimension	Length	550.0
	Width	24.4
	Thickness	2.0
Column dimension	Length	1100.0
	Width	24.4
	Thickness	2.0

Table 2. Material characteristics of the steel frame structure

Material properties	Parameter	Values
Structural steel	Young's modulus, GPa	18.0
	Density, kg/m^3	7850.0
	Poisson ratio	0.3

Table 3. Shake table specifications

Parameters	Values
Model mounting table size, mm^2	900 × 1500
Maximum specimen mass, kg	500
Material thickness, mm	16
Temperature resistance, ºC	50
Automation type	Automatic
Material	Mild steel
Shape	Rectangular

Two-storey steel frame building was set up on the shake table with four bottom beams connected with columns were positioned and fastened to the shaking table by using twenty M10 bolts. Beam-column Joints were fastened at corners by using twenty-four M6 bolts. Accelerometers were installed at the mid beam. After fixing the accelerometer on the beam, DAQ was used to acquire time history.

Numerical analysis

Numerical studies are an essential tool for monitoring structural health and ensuring its durability and safety. Because numerical studies offer a comprehensive and accurate examination of the structure's performance, they are employed in the structural health monitoring of steel frame structures. In addition, it ensures the longevity and safety of the construction while being cost-effective. Using the software program COMSOL Multiphysics 6.2 (2023), the finite element (FE) model of the three-dimensional, two-storey steel frame test specimen was modelled. The FE models are categorized into the following groups, beginning with the definition of the geometry of the steel frame structure. This involves specifying the dimensions and shapes of beams, columns, and other structural elements. Assign material properties to the elements. For steel, we need to input properties such as Young's modulus, Poisson's ratio, density, and yield strength [39–41]. For structural analysis, the Solid Mechanics or Shell interface is typically used,

depending on the nature of the frame elements. Define the study type (e.g., static, dynamic, eigen-frequency, buckling) and configure the solver settings. Discretize the geometry into finite elements. Choose an appropriate mesh size that balances accuracy and computational efficiency. A finer mesh generally provides more accurate results but requires more computational resources. Apply boundary conditions to the model, which includes constraints (Fixed supports), and determine the mode shape. After running the simulation, the results analyses. This may include stress and strain distributions, deformation, patterns, Modal shapes, and natural frequencies.

Other methods for SHM were also formulated numerically such as, the electro-mechanical impedance (EMI) technique in which real component of the impedance obtained from the coupled-field FE model and the finite element analysis (FEA)-based impedance model (semi-analytical) was compared with the experimental results [40]. Applying a thermoelastic analogy and using FEA codes that are widely available and incorporate a formulation for a piezoelectric element, they used the commercial program COMSOL Multiphysics 6.2 to perform dynamic FEA of ring and steel structures to predict the structural response that arises from induced strain actuation. Fairweather created an impedance Model based on finite element analysis. This Model utilizes finite element method (FEM) to calculate the mass-normalized eigenfrequency and eigenvalues to determine the host structure's impedance. using the impedance-based electromechanical coupling equation, the mechanical impedance acquired for the EMI approach could be utilized to calculate the Admittance signature of the bonded piezoelectric lead zirconate titanate (PZT) patch as if measured by an impedance analyzer. These models were initially applied to relatively low-frequency simulation, usually below. 1KHz. For a 1D thin beam construction [13,15,17,19], research investigated simulating several SHM approaches using a PZT sensor using FE Modals. It was researched basic models, such as a 1D beam with a PZT patch and a free piezo patch of various forms to simulate the EMI approach. A long beam with many PZT patches that were simulated by tone burst signals to propagate elastic waves along the beam, with echo reflections caused by fractures, was employed. Bhalla [42] used 3D FE modelling to simulate the PZT–concrete interaction. The three-dimensional numerical Model of the host structure, A concrete block, was connected with a one-dimensional impedance Modal. The integrated crack propagation scheme in ANSYS was used to simulate damage. A reasonably good agreement of electrical impedance between experiment and the FEA-based impedance Model for an aluminium beam, truss, and concrete cube was demonstrated [43]. This paper also studies the further improvement of modelling by introducing the definition of effective impedance, thereby enhancing the interaction simulation. Because they coupled the FE output of the structural displacement response with the impedance-based numerical model without incorporating the coupled field theory into the FE formulations, these models were semi-analytical [39]. demonstrated that FEM could yield fairly accurate results for dynamic harmonic problems, even up to frequencies in the gigahertz range. With these developments, FEM's ability to Model the EMI technique's PZT-structure interaction has greatly enhanced.

The research methodology is constructed as follows to use accelerometer to evaluate the structural health of a two-storey steel frame structure as shown in Fig. 3. To accurately depict the size and layout of the building, the first step is to define

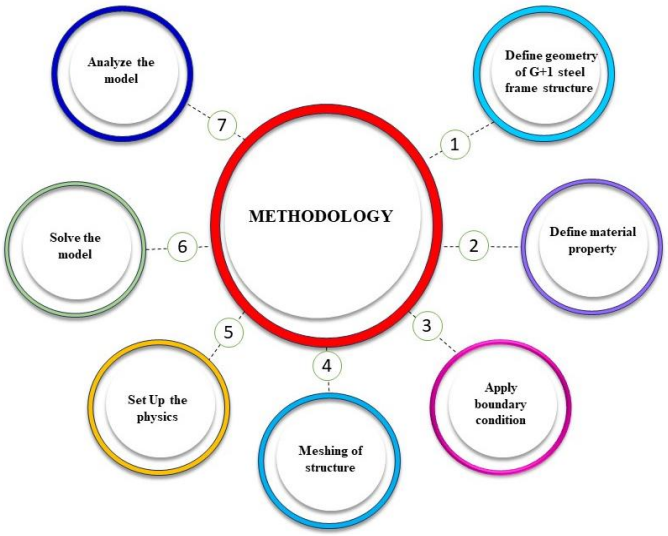

Fig. 3. Methodology of numerical study

the geometry of the two storey steel frame structure shown in Fig. 4. This involves defining how the floors, beams, and columns are arranged. The mechanical properties of the steel material, such as its density, yield strength, and Young's modulus, are then entered into the Modal to determine the steel frame's material properties. Then, suitable boundary conditions—such as fixed support at the base and constraints resulting from connections—are imposed to replicate the restrictions and support conditions of the structure as they exist in real life. Through the meshing process (Fig. 5), the structure is discretized into a finite element model once the geometry, material properties, and boundary conditions shown in Fig. 6 are established. This entails breaking down

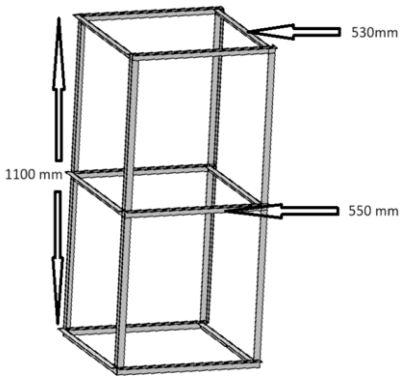

Fig. 4. Geometry of steel frame structure

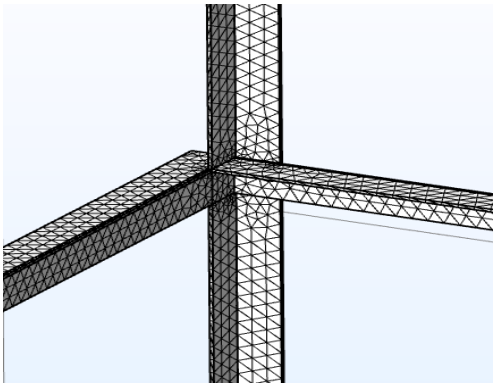

Fig. 5. Meshing of the steel frame modal

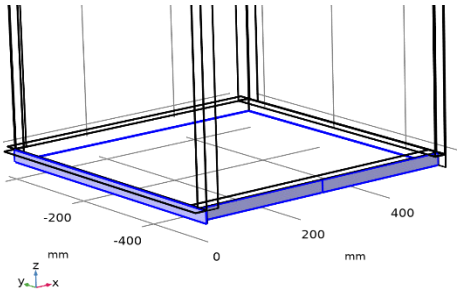

Fig. 6. Fixed support of the steel frame in FEM analysis

the structure into smaller components in order to precisely represent the behaviour of the complete frame under various loading scenarios. Physics of the problem are established following meshing, including the application of loads and external factors that the structure will encounter, like dynamic loads or vibrations [38]. After the model is completely defined, the finite element model must be solved to get information about the structural reactions, including displacements, stresses, and natural frequencies. In order to evaluate the structural soundness of the two-storey steel frame, the Modal results are finally examined. As part of this research, real accelerometer sensor values are compared with the simulated data to look for any anomalies or discrepancies that might point to possible structural problems. This all-encompassing method guarantees a precise assessment of the structural soundness and the efficiency of accelerometer sensors in keeping an eye on the structural integrity of the steel frame building.

Steel frame of a two-storey building geometry design in COMSOL Multiphysics, which includes defining the angle, beam, and column lengths, widths, and heights. In the Materials section, select steel from the Material Library and describe the material properties of steel, including Poisson's ratio and Young's modulus, and density. Define the fixed support at the bottom beam. With the help of a conversion study, define the mesh size.

Results and Discussion

Experimental modal analysis of steel frame structure

The ambient vibration measurements were carried out using two accelerometer sensors capable of measuring vibrations in both X and Y directions, as shown in Fig. 7. One accelerometer was used as a reference sensor and was permanently positioned on the beam, while the other sensors acted as roaming sensors. Two distinct measurement datasets were recorded, each with a duration of 20 sec. The acquired accelerometer signals were used to generate the ambient excitation data through the data acquisition (DAQ) system, as shown in Fig. 8. Data acquisition and preliminary processing were performed using a dual-computer system, where one system continuously collected data and the second system handled data processing. Quality control procedures were applied to ensure data reliability, and datasets showing signal drift, noise contamination, or corruption were discarded and re-measured. Eigenfrequencies were identified using the peak-picking method (PPM) based on nonparametric spectral density estimation. However, due to the limitations of PPM in the presence of closely spaced modes and noise, frequency domain operational modal analysis (OMA) techniques were employed for more reliable modal parameter extraction. The experimentally obtained modal parameters were subsequently used for validation of the finite element model developed in COMSOL Multiphysics 6.2.

Vibration sensors are extensively used in various products, including automobiles, aircraft, circuit boards, suspension bridges, and buildings, for vibration measurements and to study the dynamic behavior of structures, such as through defined Modal analysis. Accelerometers, a type of vibration sensor, are employed to evaluate responses to outside pressures, validate the modal that simulation programs employ, and forecast reactions in

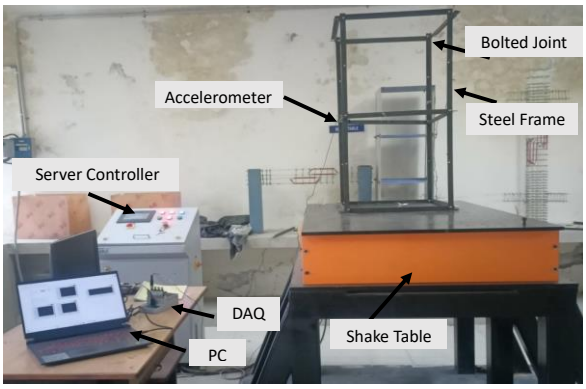

Fig. 3. Lab setup

Fig. 8. DAQ with sensor

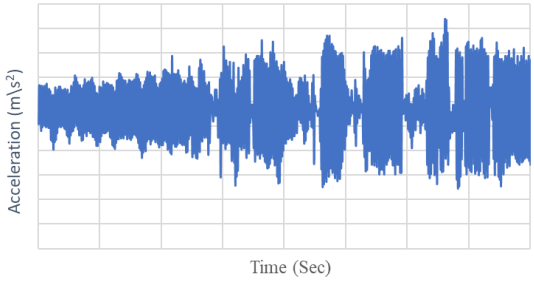

Fig. 9. Accelerometer data through shake table

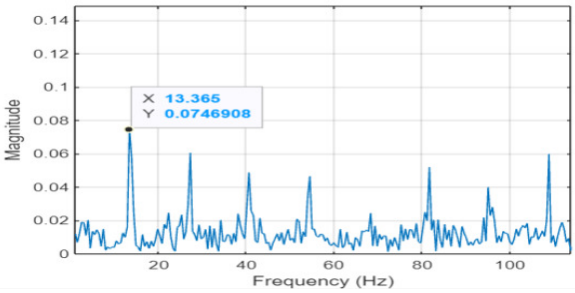

Fig. 10. FFT analysis data from the MATLAB software

various operational scenarios. Vibration sensor monitoring has emerged as the most widely used method for evaluating the condition of major machinery and buildings in both the industrial and civil sectors. Vibration trends over time can be used to forecast when deterioration will start and to take corrective action before failure happens. “Predictive maintenance” is the term for this type of ongoing or sporadic observation of a plant’s operational state. An accelerometer works by measuring the inertia of a mass that is being accelerated. A sensor measures the displacement of the mass for the device’s permanent structures while it is suspended by an elastic element. Because of its inertia, the mass accelerates and moves from its rest position according to the acceleration that is sensed. The displacement is transformed by the sensor into an electrical signal that contemporary measurement equipment can obtain. Various types of sensors have been developed based on this principle. Data obtained from the accelerometer sensor with the help of LabVIEW software is shown in Fig. 9. The obtained mode shape frequency results through FFT analysis are shown in Fig. 10.

Convergence study

Finding a reasonably decent final solution through numerous separate optimization runs is a typical method in metaheuristic structural optimization. while this approach is often feasible for a small-scale design optimization problem, it is typically not feasible computationally for more complicated cases like steel frames that are the actual size. This is clear from the present literature on structural optimization, where the large computing cost of the examples usually results in the final Optimal solution being reported based on a small number of optimization runs. being investigated. In Fig. 11, the Convergence study showed that as the increment in the number of elements increased,

the eigen frequency decreased. After an optimum number of elements, the value of the eigen frequency is approximately constant or varies with very small percentages.

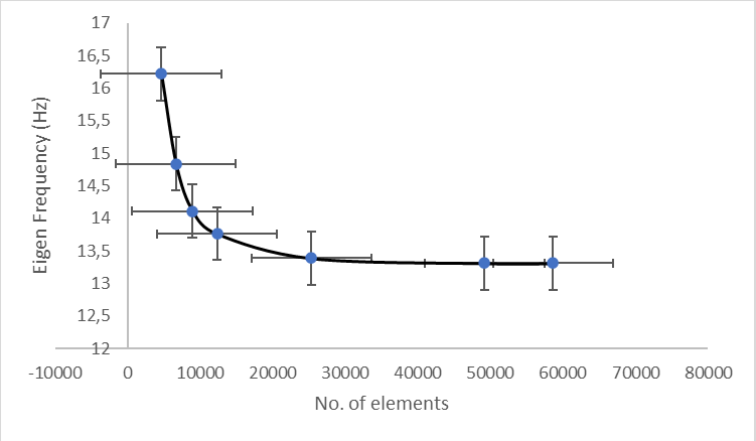

Fig. 11. Convergence study

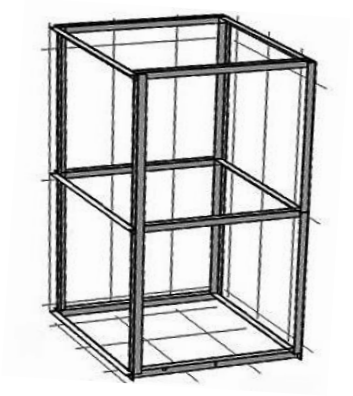

Fig. 12. Finite element model of steel frame structure

Eigenfrequency of the steel frame. Modal is added to the software relevant to physics. Utilize the Study section to specify the type of analysis and execute the Modal. This could include a static study for analysing displacement and stress, a frequency study for determining natural frequencies, or a transient study for investigating time-dependent behaviour. The frame system is modal as depicted in Fig. 12. Two equal spaces separate the outside surface of the L24.4x24.4x2 profile arms in the joints. These outside surfaces were divided into frictionless sections. And the terminal portions were chosen under a tie constraint. Furthermore, normal contact qualities were simulated using hard contacts. Surface-to-surface contact was used to modal the interaction between the beam and column connection as frictionless. To avoid Anomalies, the junction regions of the system mesh were meticulously partitioned. field-variable-dependent conductivity elements, each with eight nodes and three degrees of freedom, were used to mesh the Modal. The mesh was improved close to the connections. for the computation, reduced integration was employed. The Modal was initially subjected to gravity loads, which include applied load and self-weight. Dynamic parameters were obtained through implicit analysis.

Analysis results

In Fig. 13, FEM analysis fixed support created at the bottom beam in the steel frame structures. During the analysis, the effect of rotation in the frame systems is rigid. Semi-rigid. The joint was explained. The outcomes revealed an increase in displacement for eigen frequency 13.30 in the joint regions, as shown in Fig. 9. The rotation impact on the joints was amplified by the greatest tension at the mode.

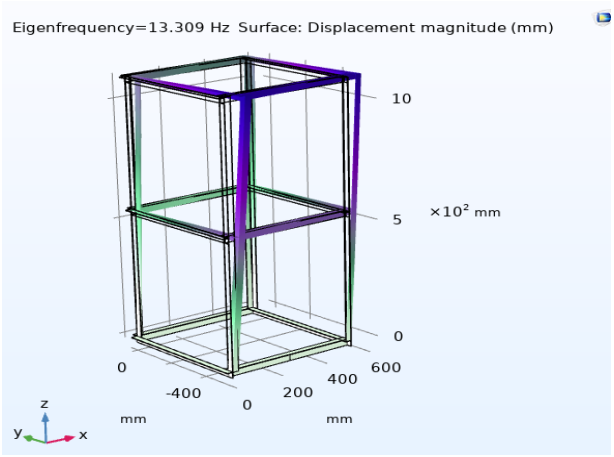

Fig. 13. Displacement for mode shape I

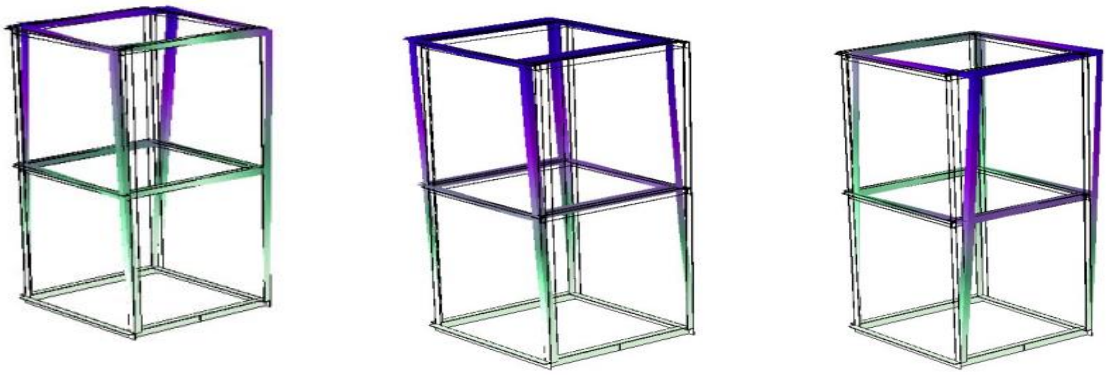

(a) (b) (c)

Fig. 14. Numerical analysis mode shape for two storey frames: (a) mode-1 (13.309), (b) mode-2 (26.79), (c) mode-3 (39.25)

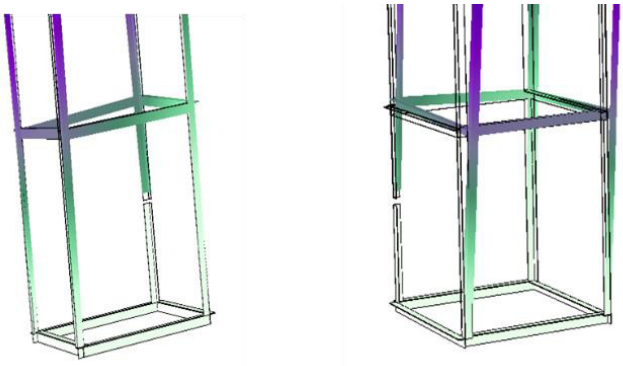

(a) (b)

Fig. 15. Damage column front and back side: (a) 10 mm damage, (b) 20 mm damage

Natural frequencies and vibration modes significantly affect essential dynamic attributes and the dynamic performance of structures. Three natural frequencies in all, 13.31, 22.21, and 28.85 Hz, of the structure were obtained, which are shown in Fig. 14 and developed beam damage shown in Fig. 15.

Damage analysis

This section's goal is to investigate how cracking affects the frame's mechanical response. As seen in Fig. 15, the crack is inserted into the structure's three columns. Frequency is measured from the accelerometer sensor, and the accelerometer sensor is placed in the sensing location shown in Fig. 16. First, the damage condition is analysed without the bolts being removed or loosened. After that, the outcomes for strain and acceleration are compared to examine how cracking affects the behaviour of the frame. Determining whether the eigenfrequency and acceleration are more susceptible to damage of the type Fractures is the specific goal of this section. When cracking is introduced to the first three columns, the first mode shape frequency for partial damage column of 10 and 20 mm are 13.30, 13.28, 13.26, 13.29, 13.27, and 13.24 Hz, respectively shown in Table 4. First mode shape frequency for fully damaged columns of 10 and 20 mm are 9.22, 4.62, 0.55, 9.22, 4.63, and 0.56 Hz, respectively, as shown in Table 5.

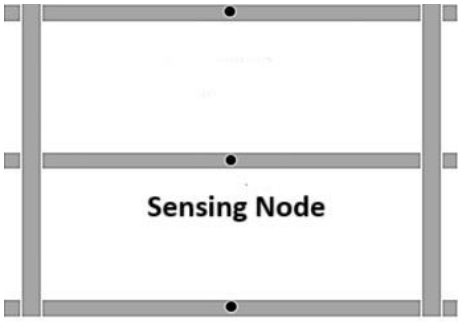

Fig. 16. Sensor place at the sensing node

Table 1. Mode shape frequency for partial damage

Damage level	Mode-1, Hz	Mode-2, Hz	Mode-3, Hz
10 mm	13.30	21.95	28.35
10 × 10 mm^2	13.28	21.91	28.35
10 × 10 × 10 mm^3	13.26	21.74	27.77
20 mm	13.29	21.92	28.34
20 × 20 mm^2	13.27	21.86	28.32
20 × 20 × 20 mm^3	13.24	21.70	27.69

Table 2. Mode shape frequency for partial damage

Damage level	Mode-1, Hz	Mode-2, Hz	Mode-3, Hz
10 mm	9.22	17.00	23.77
10 × 10 mm^2	4.62	7.61	19.80
10 × 10 × 10 mm^3	0.55	2.07	4.99
20 mm	9.22	17.00	23.78
20 × 20 mm^2	4.63	7.63	19.86
20 × 20 × 20 mm^3	0.56	2.07	5.01

Table 3. Variation in frequency of first mode shape

Damage level	Partial damage, Hz	Full damage, Hz	Percentage variation
10 mm	13.30	9.22	30.62
10 × 10 mm^2	13.28	4.62	65.21
10 × 10 × 10 mm^3	13.26	0.55	95.85
20 mm	13.29	9.22	30.62
20 × 20 mm^2	13.27	4.63	65.10
20 × 20 × 20 mm^3	13.24	0.56	95.77

Table 4. Eigen frequency value comparison between experimental and numerical data

Mode shape	1	2	3
Experimental frequency, Hz	13.36	27.22	40.49
Numerical frequency, Hz	13.31	26.79	39.25
Percentage variation	0.37	1.61	3.16

The percentage variation in the first mode shape of partial and full damage for the first three columns is shown in Table 6. 30.62, 65.21, 95.85 % variation in 10 mm damage in column, 30.62, 65.10, 95.77 % variation in 20 mm damage in column are shown in Table 6. Experimental frequency and numerical frequency variation are shown in Table 7 and Fig. 17. The generated finite element model was validated by comparing the findings of numerical modal analysis and experimental modal analysis. The comparison between numerically calculated eigenfrequencies from the finite element model and experimentally acquired natural frequencies from ambient vibration testing is shown in Table 7. For Mode 1, Mode 2, and Mode 3, the percentage difference between experimental and numerical frequencies was 0.37, 1.61, and 3.16 %, respectively. There is a high agreement between the experimental and numerical results, as these fluctuations fall within the permissible range (usually 2–5 %) stated in the structural dynamics literature. This high degree of agreement confirms the accuracy of the finite element modeling, the assignment of material properties, the boundary condition determination, and the operational modal analysis method. In order to validate the model through ambient vibration testing, experimental investigations were restricted to the healthy structure. To simulate cracking and stiffness deterioration, damage scenarios were then numerically added to the verified finite element model. Therefore, rather than being experimental damage testing, the partial and full damage studies are model-based prediction simulations.

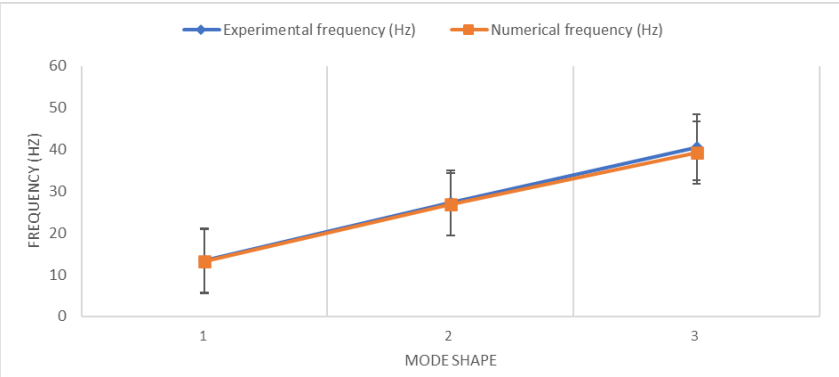

Fig. 17. Variation in experimental and numerical data

Conclusions

The modal analysis of a steel moment frame is presented in this study using both experimental and numerical methods. First mode shape frequency for partial damage column of 10 and 20 mm are 13.30, 13.28, 13.26, 13.29, 13.27, and 13.24 Hz, respectively. The variation in frequency in the first mode shape is very small compared to other higher mode shapes. These variations are due to inaccurate modelling of the experimental steel-framed structure in the FE numerical package. The unwanted noise captured by the accelerometer during the experimental data acquisition is also one of the reasons for it. The noise can be due to any physical environmental forces near the structure. The study shows that the structure's natural frequency gets reduced by increasing the damage. This is due to the reduction in the stiffness of the structure. When damage is induced in the structure, its moment of inertia changes, which is responsible for the reduction in stiffness. For various mode shapes, the experimental and numerical frequency variations are 0.37, 1.61, and 3.16, respectively.

CRediT authorship contribution statement

Kumar Mohit: investigation, writing – investigation review & editing, writing – original draft; **Sachin K. Singh**: data curation, validation, software, resources, methodology, formal analysis, supervision; **Abhishek Mishra**: validation, software, resources, methodology, formal analysis, supervision.

Conflict of interest

The authors declare that they have no conflict of interest.

References

1. Lynch JP, Loh KJ. A summary review of wireless sensors and sensor networks for structural health monitoring. *The Shock and Vibration Digest.* 2006;38(2): 91–128.
2. Chiang CC, Lee JR, Bang HJ. Structural health monitoring for a wind turbine system: a review of damage detection methods. *Measurement Science and Technology.* 2008;19(12): 122001.
3. Doebling SW, Charles RF, Michael BP, Daniel WS. *Damage identification and health monitoring of structural and mechanical systems from changes in their vibration characteristics: a literature review*. Los Alamos National Laboratory; 1996. Report No.: LA-13070-MS.
4. Alavi AH, Hasni H, Lajnef N, Chatty K, Faradizer F. An intelligent structural damage detection approach based on self-powered wireless sensor data. *Automation in Construction.* 2016;62: 24–44.
5. Li HN, Ren L, Jia ZG, Yi TH, Li DS. State-of-the-art in structural health monitoring of large and complex civil infrastructures. *Journal of Civil Structural Health Monitoring.* 2016;6(1): 3–16.
6. Amezquita-Sanchez JP, Adeli H. Signal processing techniques for vibration-based health monitoring of smart structures. *Archives of Computational Methods in Engineering.* 2016;23(1): 1–15.
7. Hasni H, Alavi AH, Jiao P, Lajnef N. Detection of fatigue cracking in steel bridge girders: a support vector machine approach. *Archives of Civil and Mechanical Engineering.* 2017;17(3): 609–622.
8. Meneghetti G, Guzzella C, Atzori B. The peak stress method combined with 3D finite element models for fatigue assessment of toe and root cracking in steel welded joints subjected to axial or bending loading. *Fatigue & Fracture of Engineering Materials & Structures.* 2014;37(7): 722–739.
9. Yang JN, Xia Y, Loh CH. Damage identification of bolt connections in a steel frame. *Journal of Structural Engineering.* 2014;140(3): 04013064.

10. Zhu WD, He K. Detection of damage in space frame structures with L-shaped beams and bolted joints using changes in natural frequencies. *Journal of Vibration and Acoustics.* 2013;135(5): 051001.
11. Shao J, Wang T, Yin H, Yang D, Li Y. Bolt looseness detection based on piezoelectric impedance frequency shift. *Applied Sciences.* 2016;6(10): 298.
12. Lei Y, Li Q, Chen F, Chen Z. Damage identification of frame structures with joint damage under earthquake excitation. *Advances in Structural Engineering.* 2014;17(8): 1075–1087.
13. Döhler M, Hille F. Subspace-based damage detection on steel frame structure under changing excitation. In: Wicks A. (Eds.) *Structural Health Monitoring, Volume 5. Conference Proceedings of the Society for Experimental Mechanics Series*. Cham: Springer; 2014. p.167–174.
14. Tuhta S, Günday F. MIMO System Identification of Industrial Building Using N4SID With Ambient Vibration. *International Journal of Innovations in Engineering Research and Technology.* 2019;6(8): 1–6.
15. Tuhta S, Günday F, Aydin H, Alalou M. MIMO System Identification of Machine Foundation Using N4SID. International *Journal of Interdisciplinary Innovative Research Development.* 2019;04(01): 27–36.
16 Tuhta S, Günday F. Multi Input – Multi Output System Identification of Concrete Pavement Using N4SID. *International Journal of Interdisciplinary Innovative Research Development.* 2019;04(01): 41–47.
17. Tuhta S, Günday F. Analytical Modal Analysis of RC Building Retrofitted with CFRP using Finite Element Method. *International Journal of Latest Technology in Engineering, Management & Applied Science.* 2020;9(2): 78–82.
18. Tuhta S, Günday F. System Identification of RC Building Using N4SID. *International Journal of Research and Scientific Innovation.* 2019;6(11): 100–106.
19. Tuhta S, Alameri I, Günday F. Numerical Algorithms N4SID For System Identification of Buildings. *International Journal of Advanced Research in Engineering Technology & Science.* 2019;6(1): 7–15.
20. Tuhta S, Günday F, Aydin H. Subspace Identification Using N4SID Methods Applied to Model Concrete Chimney. *Journal NX.* 2020;6(6): 415–423.
21. Tuhta S, Günday F. Modal Parameters Determination of Steel Benchmark Warehouse by System Identification Using ANN. *International Journal of Research and Innovation in Applied Science.* 2019;6(12): 8–12.
22. Lus H, De Angelis M, Betti R, Longman RW. Constructing second-order models of mechanical systems from identified state space realizations. Part I: Theoretical discussions. *Journal of Engineering Mechanics.* 2003;129(5): 477–488.
23. Tuhta S, Günday F. Artificial Neural Network Based System Identification Usage for Steel Sheds. *International Journal of Innovations in Engineering Research and Technology.* 2020;7(10): 22–30.
24. Tuhta S, Günday F, Aydin H. System Identification of Model Steel Bridge with Fuzzy Logic. *International Journal of Research and Innovation in Applied Science.* 2020;5(1): 50–54.
25. Hadi MN, Almalome MH, Yu T, Rickards WA. Flexural behaviour of beams reinforced with either steel bars, molded or pultruded GFRP grating. *Steel and Composite Structures.* 2020;34(1): 17–34.
26. Roeck GD. The state-of-the-art of damage detection by vibration monitoring: the SIMCES experience. *Journal of Structural Control.* 2003;10(2): 127–134.
27. Tuhta S, Günday F. Application of Oma on The Bench-scale Aluminium Bridge Using Micro Tremor Data. *International Journal of Advance Research and Innovative Ideas in Education.* 2019;5(5): 912–923.
28. Tuhta S, Aydin H, Günday F. Updating for Structural Parameter Identification of the Model Steel Bridge Using OMA. *International Journal of Latest Technology in Engineering, Management & Applied Science.* 2020;9(3): 59–68.
29. Tuhta S, Günday F, Aydin H. Update of Structural Parameters on the Bench-Scale Aluminium Bridge Model Using Ambient Vibration. *International Journal of Latest Technology in Engineering, Management & Applied Science.* 2020;9(4): 10–18.
30. Kasimzade AA, Tuhta S, Günday F, Aydın H. Obtaining Dynamic Parameters by Using Ambient Vibration Recordings on Model of The Steel Arch Bridge. *Periodica Polytechnica Civil Engineering.* 2021;65(2): 608–618.
31. Zhang J, Guo SL, Zhang QQ. Mobile impact testing for structural flexibility identification with only a single reference. *Computer-Aided Civil and Infrastructure Engineering.* 2015;30(9): 703–714.
32. Lei Y, Zhou H, Lai ZL. A computationally efficient algorithm for real-time tracking the abrupt stiffness degradations of structural elements. *Computer-Aided Civil and Infrastructure Engineering.* 2016;31(6): 465–480.
33. Cheng J, Xu RM, Tang XY, Sheng VS, Cai CT. An abnormal network few feature sequence prediction approach for DDoS attacks detection in big data environment. *Computer Materials Continua.* 2018;55(1): 95–119.
34. Sanaz R, Armen DK. A stochastic ground motion model with separable temporal and spectral nonstationarities. *Earthquake Engineering & Structural Dynamics.* 2012;41(11): 1549–1568.
35. Yan WJ, Ren WX. Operational modal parameter identification from power spectrum density transmissibility. *Computer-Aided Civil and Infrastructure Engineering.* 2012;27(3): 202–217.

36. Brincker R, Zhang L, Andersen P. Modal Identification from Ambient Responses using Frequency Domain Decomposition. In: *Proceedings of the International Modal Analysis Conference, IMAC 18, San Antonio, Texas, USA, 7–10 February, 2000.* 2000. p.625–630.
37. Jacobsen NJ, Andersen P, Brincker R. Using enhanced frequency domain decomposition as a robust technique to harmonic excitation in operational modal analysis. In: Sas P, De Munck M. (eds.) *Proceedings of International Conference on Noise & Vibration Engineering, ISMA 2006, 18–20 September 2006. Heverlee, Belgium.* New York: Curran Associates, Inc.; 2006. p.3129–3140.
38. Peeters. B. *System identification and damage detection in civil engineering.* Katholieke Universiteit Leuven, Leuven, Belgium; 2000.
39. Afane NEB, Zahaf S, Dahmane M, Belaziz A, Noureddine R. Modal and harmonic analysis of the rotor system involving four different materials by finite element code: Ansys workbench. *Materials Physics and Mechanics.* 2023;51(7): 63–98.
40. Sheinerman AG, Shevchuk RE. Toughening of nanocrystalline alloys due to grain boundary segregations: finite element modeling. *Materials Physics and Mechanics.* 2023;51(7): 34–41.
41. Borovkov AI, Maslov LB, Zhmaylo MA, Tarasenko FD, Nezhinskaya LS. Finite element analysis of elastic properties of metamaterials based on triply periodic minimal surfaces. *Materials Physics and Mechanics.* 2024;52(2): 11–29.
42. Moharana S, Bhalla S. Numerical investigations of shear lag on PZT-structure interaction: review and application. *Current Science.* 2012;103(6): 678–688.
43. Lim YY, Soh CK. Towards more accurate numerical modelling of impedance based high frequency harmonic vibration. *Smart Materials and Structures.* 2014;23(3): 035017.

MATERIALS PHYSICS AND MECHANICS

54 (2) 2026

УЧРЕДИТЕЛИ

Санкт-Петербургский политехнический университет Петра Великого
Адрес: 195251, Санкт-Петербург, Политехническая ул., д. 29

Институт проблем Машиноведения Российской академии наук
Адрес: 199178, Санкт-Петербург, Большой пр-кт В.О., д. 61

ИЗДАТЕЛЬ

Санкт-Петербургский политехнический университет Петра Великого
Адрес: 195251, Санкт-Петербург, Политехническая ул., д. 29

Журнал зарегистрирован в Федеральной службе по надзору в сфере связи, информационных технологий и массовых коммуникаций (РОСКОМНАДЗОР), свидетельство ПИ №ФС77-69287 от 6 апреля 2017 года.

АДРЕС И ТЕЛЕФОН РЕДАКЦИИ

199178, Санкт-Петербург, Большой пр-кт В.О., д. 61

Тел. редакции: +7(812)552 77 78, доб. 224

E-mail редакции: mpmjournal@spbstu.ru

Компьютерная верстка Л.И. Гузилова

Подписано в печать 21.05.2026 г. Выход в издания в свет: 01.06.2026 г.
Формат 60x84/8. Печать цифровая
Усл. печ. л. 10,0. Тираж 100. Заказ___.
Цена: Бесплатно

Отпечатано в **Издательско-полиграфическом центре Политехнического университета Петра Великого**
Адрес: 195251, Санкт-Петербург, Политехническая ул., 29
Тел.: +7(812)552 77 17

MPM, Vol. 54, No. 2, 2026

MPM SCIENTIFIC JOURNAL